JOINT TRANSPORTATION
RESEARCH PROGRAM
INDIANA DEPARTMENT OF TRANSPORTATION
AND PURDUE UNIVERSITY

Reduction of Bridge Construction and Maintenance Costs through Coupled Geotechnical and Structural Design of Integral Abutment Bridges

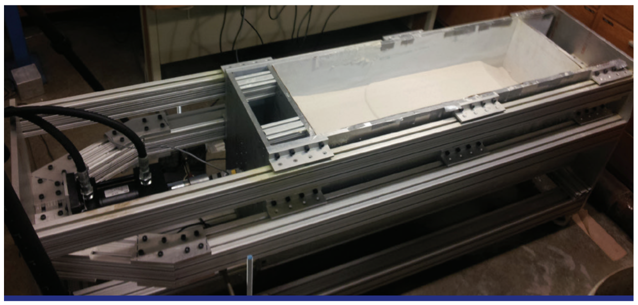

Robert J. Frosch

Antonio Bobet

Yazen Khasawneh

SPR-3318 • Report Number: FHWA/IN/JTRP-2014/06 • DOI: 10.5703/1288284315500

RECOMMENDED CITATION

Frosch, R. J., Bobet, A., & Khasawneh, Y. (2014). *Reduction of bridge construction and maintenance costs through coupled geotechnical and structural design of integral abutment bridges* (Joint Transportation Research Program Publication No. FHWA/IN/JTRP-2014/06). West Lafayette, IN: Purdue University. http://dx.doi.org/10.5703/1288284315500

AUTHORS

Robert J. Frosch, PhD
Professor of Civil Engineering
Lyles School of Civil Engineering
Purdue University
(765) 494-5904
frosch@purdue.edu
Corresponding Author

Antonio Bobet, PhD
Professor of Civil Engineering
Lyles School of Civil Engineering
Purdue University
(765) 494-5033
bobet@purdue.edu
Corresponding Author

Yazen Khasawneh
Graduate Research Assistant
Lyles School of Civil Engineering
Purdue University

JOINT TRANSPORTATION RESEARCH PROGRAM

The Joint Transportation Research Program serves as a vehicle for INDOT collaboration with higher education institutions and industry in Indiana to facilitate innovation that results in continuous improvement in the planning, design, construction, operation, management and economic efficiency of the Indiana transportation infrastructure. https://engineering.purdue.edu/JTRP/index_html

Published reports of the Joint Transportation Research Program are available at: http://docs.lib.purdue.edu/jtrp/

NOTICE

COPYRIGHT

Print ISBN: 978-1-62260-307-7
ePUB ISBN: 978-1-62260-308-4

TECHNICAL REPORT STANDARD TITLE PAGE

1. Report No. FHWA/IN/JTRP-2014/06	**2. Government Accession No.**	**3. Recipient's Catalog No.**

4. Title and Subtitle Reduction of Bridge Construction and Maintenance Costs through Coupled Geotechnical and Structural Design of Integral Abutment Bridges	**5. Report Date** June 2014
	6. Performing Organization Code
7. Author(s) Robert J. Frosch, Antonio Bobet, Yazen Khasawneh	**8. Performing Organization Report No.** FHWA/IN/JTRP-2014/06
9. Performing Organization Name and Address Joint Transportation Research Program Purdue University 550 Stadium Mall Drive West Lafayette, IN 47907-2051	**10. Work Unit No.**
	11. Contract or Grant No. SPR-3318
12. Sponsoring Agency Name and Address Indiana Department of Transportation State Office Building 100 North Senate Avenue Indianapolis, IN 46204	**13. Type of Report and Period Covered** Final Report
	14. Sponsoring Agency Code

15. Supplementary Notes

Prepared in cooperation with the Indiana Department of Transportation and Federal Highway Administration.

16. Abstract

Elimination expansion joints in the superstructure of integral abutment bridges offers the advantage of reducing the initial and life cycle costs of the structure. However, such elimination may have an adverse effect on the displacement demand at the pile-abutment connection and on the earth pressures on the abutment wall due to the thermal expansion/contraction cycles of the bridge. These adverse effects have resulted in regulations that impose restrictions on the maximum length and skew angle of integral abutment bridges. This research consisted of a deep analysis of the problem by considering soil-structure interaction. The approach was multifaceted as it included experimental and numerical analysis. Upon calibration and verification of the constitutive model, it was used as part of a parametric analysis to provide recommendations for the design limits of integral abutment bridges.

The analysis results showed that active state earth pressure is reached after the first contraction cycle. The displacement demand on piles is a function of the abutment wall displacement. Larger displacement demand of the pile at the acute corner when compared to the obtuse corner was observed during expansion and contraction cycles. The inflection point of the piles deformed shape was found to be at relatively shallow depth. Concrete shrinkage and sequence of loading affected significantly the displacement demand of the supporting piles, lower displacement demand of piles during the expansion cycle and larger displacement demand during contraction cycles. The analysis showed that a 500 ft bridge with 60° skew will provide acceptable long term performance.

17. Key Words integral abutment bridges, soil-structure interaction, piles, constitutive models, numerical analysis, coupled thermal-displacement, larger scale test, physical model	**18. Distribution Statement** No restrictions. This document is available to the public through the National Technical Information Service, Springfield, VA 22161.

19. Security Classif. (of this report)	**20. Security Classif. (of this page)**	**21. No. of Pages**	**22. Price**
Unclassified	Unclassified	176	

Form DOT F 1700.7 (8-69)

EXECUTIVE SUMMARY

REDUCTION OF BRIDGE CONSTRUCTION AND MAINTENANCE COSTS THROUGH COUPLED GEOTECHNICAL AND STRUCTURAL DESIGN OF INTEGRAL ABUTMENT BRIDGES

Introduction

Eliminating bearings and expansion joints in the superstructure of integral abutment bridges has many advantages in reducing both initial and life cycle costs. However, elimination of these elements has an adverse effect on displacement demands at the pile-abutment connection and on the resulting earth pressure on the abutment wall due to thermal expansion/contraction cycles of the bridge. This effect on the displacement demand at the pile-abutment connection and on the earth pressure behind the abutment wall has resulted in imposed restrictions on the maximum length and skew angle of integral abutment bridges.

Several studies have been conducted to quantify these limitations. The studies focused primarily on the structural or soil component of the problem. This study utilized a coupled thermal-displacement analysis along with soil-structure interaction. An experimental-based numerical analysis approach was followed in this study. The experimental portion of the study consisted of laboratory-scale tests and large-scale tests. The laboratory-scale tests were conducted on sand using a specially designed apparatus that simulates the abutment movement with different skew angles and surface conditions. The large-scale tests were conducted on a ¼scale bridge of SR 18 over the Mississinewa River. The numerical simulation consisted of developing a soil constitutive model, verification and calibration of the model, and a parametric study to cover a range of bridge lengths and skew angles. The developed constitutive soil model was an elastoplastic model using the Drucker-Prager Yield criteria and an unloading/ reloading algorithm. The model was verified and calibrated using element tests from the literature, the results from the laboratory-scale tests conducted in this study, results from the large-scale test, and monitoring data of a full-scale bridge. Finally, a parametric study was conducted for eighteen cases and investigated bridge length, skew angle, foundation stiffness, abutment wall stiffness, existence of wing wall, and shrinkage and loading sequence effects.

Findings

The results from the large-scale tests showed that skew angle imposes transverse and rotational movements to the deck in addition to longitudinal movements expected from expansion/ contraction due to thermal effects. The presence of backfill introduces friction between the soil and abutment which reduces the rotational and transverse movements during expansion cycles. Settlement in the backfill at the abutment wall is an indication of active wedge formation during the contraction phase and was observed during summer testing. Soil pressures at the obtuse corner of the abutment are larger than at the acute corner due to the larger degradation of the stiffness at the acute corner caused by rigid body rotation during expansion. During winter testing, frozen soil was observed which resulted in a gap during contraction cycles and subsequently the absence of soil pressure.

Calibration and verification of the soil constitutive model showed that the model performed well under a wide range of stress levels and various length scales. The model has acceptable predictive capabilities. Escalation of earth pressure behind the abutment with number of cycles was captured. The semi-linear response of earth pressure upon reloading under lateral loading was also captured. The model performed well replicating the magnitude of pile deformation and in calculating the inflection point.

The parametric study results indicate that shrinkage and loading sequence significantly affects the performance of integral abutment bridges. Furthermore, the effect of the abutment wall stiffness, for the range of practical wall thickness typically used on integral abutment bridges, is not significant. An integral abutment bridge of 500 ft with a 60° skew on soft to firm foundation soils resulted in displacement demands of the piles less than 2.0 in. For a 1000 ft bridge with a 60° skew, displacements greater than 2 in. are developed and reached 3 in. To achieve these larger displacements, confining reinforcement as recommend by Frosch et al. (2009) is required. The stiffness of the foundation may have an adverse effect on the displacement demand on piles in the case of long bridges (>1000 ft) on soft foundation soils. For this case, a full soil-structure analysis should be conducted.

Implementation

This study was a continuation of research conducted at Purdue University on integral abutment bridges (Frosch et al. (2006, 2009), Frosch & Lovell (2011)). This research supports the conclusions provided by Frosch and Lovell (2011) and agrees with the recommendations already provided in the INDOT bridge design manual. This research indicates that it may be possible to increase the maximum bridge lengths for skew angles greater than 30°. For soft to very soft foundation soils and for long bridges (>1000 ft), bridge-specific analyses should be conducted utilizing soil-structure interaction.

CONTENTS

LIST OF TABLES

LIST OF FIGURES

1. INTRODUCTION

Integral abutment bridges are a form of bridge construction that eliminates the necessity of bearings and expansion joints by integrally connecting the superstructure to the substructure at the abutment. Through elimination of these assemblies, significant benefits result including a decrease in initial as well as life cycle costs (Wasserman & Walker, 1996). In addition, these structures exhibit inherent seismic resistance (Wasserman & Walker, 1996), which can provide for increased safety to the traveling public.

While the concept of integral abutment construction has been in use for some time, significant design limitations have been imposed on this construction type due to a lack of understanding of its behavior. For instance, many states, including Indiana, provide design limitations on the overall length and skew of bridges that utilized this structural system.

To eliminate arbitrary design limits, research was initiated by various Departments of Transportation including the Indiana Department of Transportation (INDOT) to evaluate the appropriateness of design limits and develop more rational design procedures and limits. Literature Review was conducted to identify caps in the current knowledge, the literature review is attached as Appendix A. Through research (e.g., Frosch & Lovell (2011)), design recommendations were provided for an increase in the overall structural length such that bridges could be designed with a length of up to 500 ft using standardized abutment details and a maximum skew angle of 30°. While specific recommendations were given, several areas of research were still needed to provide comprehensive and rational design guidelines outside of the ranges recommended.

2. PROBLEM STATEMENT

Most of the conducted research for evaluating the integral abutment bridge performance used numerical simulations focusing on the structural elements, with soil structure interaction, typically incorporated through the use of linear springs. The lack of comprehensive guidelines based on soil-structure interaction analysis motivated the research work presented in this thesis. Specifically, an improved understanding of thermal induced displacement coupled with soil-structure interaction is needed to evaluate the long-term performance of the integral abutment bridge as well as to obtain an improved understanding of the effects of length, skew, foundation stiffness, abutment wall stiffness, wing walls, concrete shrinkage, and sequence of loading.

3. OBJECTIVE AND SCOPE

The objective of this study is to provide guidelines that assist in the design of integral abutment bridges and potentially increase the currently imposed limits on maximum length and skew. This objective is achieved using an enhanced understanding of soil-structure interaction through testing and numerical modeling.

The scope of the work is as follows:

1. Large-scale test on a ¼ scale bridge.
2. Laboratory tests on sands using a specially designed apparatus that simulates abutment wall movement.
3. Development and calibration of a constitutive model that captures the behavior observed in field and laboratory tests.
4. Numerical simulations of instrumented bridge in Indiana using three-dimensional models.
5. Parametric study using three-dimensional numerical simulations.
6. Development of design guidelines.

4. FINDINGS AND DELIVERABLES

4.1 Large Scale Tests

Large scale tests were conducted on a bridge that was a ¼ scale replicate of the SR 18 Bridge over the Mississinewa River in Indiana with the exception that the bridge's skew was increased. Details of the test and findings are provided in Appendix B. The SR 18 Bridge skew angle is 8° while the ¼ scale bridge skew angle was 45°. The bridge was constructed at Bowen Laboratory at Purdue University as part of a previous INDOT project (Frosch & Lovell, 2011). The bridge was single span, 28.4 ft long and 12.5 ft wide. The abutment was 2.1 ft thick and 3 ft high. The bridge deck was divided into two halves with a 4.5 ft gap where displacements were imposed through two hydraulic actuators. The deck was 4 in. thick and was supported by three reinforced concrete girders, 1.3 ft × 0.83 ft in cross section. Transfer beams (W14 × 68) were used to bridge the gap between the two halves and compensate for stiffness loss. Each bridge abutment was supported by five (5) concrete filled tube (CFT) piles, with a 6 in. diameter and 0.25 in. wall thickness. The length of the piles ranged from approximately 18 ft to 20 ft. The piles were driven in predominantly medium dense to dense granular soils. The water table at the site was approximately 9 ft below the ground surface.

The bridge was instrumented to monitor deck displacements, pile deformation, hydraulic actuators pressure, and earth pressure of the soil in contact with the abutment. Displacements were monitored by potentiometers at the gap and at each of the bridge corners. Displacement measurements were taken at two depths: at the deck and at ground level. Lateral earth pressure was monitored at two locations: at the obtuse and acute corners of each abutment. The two piles closer to the obtuse and acute corners were monitored for deformations. A conventional survey of the corners of the deck (at the bridge deck level) with a total station was conducted for redundancy.

Three tests were conducted on the bridge: one with no backfill and two with backfill. The test with no backfill was performed in November 2010, and the tests with back fill were conducted in December 2010 and June 2011. The backfill was INDOT #4 structural backfill and placed in three layers, each compacted using a plate compactor. The displacements applied at the gap consisted of cycles of increasing amplitude. The amplitudes ranged from +/−0.25 in. to +/−2.5 in.

Rigid body movements of the bridge associated with the displacements imposed at the gap were calculated and plotted for the three tests as a function of gap opening/closing. Rigid body movements consisted of translation in the longitudinal and transverse directions and rotation. During expansion, the longitudinal displacement was in the direction of elongation while the transverse movement and rotation were toward the obtuse corner. During contraction, the longitudinal displacement was in the direction of shortening while transverse movement and rotation were toward the acute corner. It was found that the existence of backfill significantly restrained the transverse translational and rotational movements of the deck and that the restraint was more significant during expansion than during contraction. The results also showed that the longitudinal deformations of the deck were not significantly affected by the existence of the backfill. The transverse and rotational movements, however, were reduced due to the existence of backfill.

The piles at the acute corner had larger displacement demands during both expansion and contraction than at the obtuse corner. The displacement demand on the pile at the acute corner was larger during contraction than during expansion. The opposite behavior occurred for the pile at the obtuse corner. In addition, the backfill worked as an effective restraint, reducing the displacement demand on the piles.

During the test conducted in June (summer), the soil pressure behind the abutment followed an approximately hyperbolic relationship that increased with displacement, with a degradation of the soil's modulus (earth pressure versus displacement). It was observed that the lateral earth pressure was higher at the obtuse corner than at the acute corner. As expected, the active state was reached during the first contraction cycle.

For the test conducted in December (winter), it was observed that the backfill soil was frozen and a gap formed behind the abutment. During expansion, the lateral earth pressure demonstrated an approximately linear response, and the earth pressure at the acute corner was slightly higher than at the obtuse corner. During contraction, earth pressures were close to zero due to the gap.

4.2 Small Scale (Laboratory) Tests

Small scale tests were performed to provide an improved understanding of backfill behavior under low frequency cyclic loading and to provide a reference for the verification and calibration of the constitutive model. Details of the small scale tests and findings are provided in Appendix C.

A testing apparatus was designed with a moving plate to simulate abutment movement and a fixed frame that represented the boundary conditions ("far field"). The moving plate of the apparatus was designed such that it could represent a wall at different angles with the soil. Different textures of the moving plate allowed for experimentation with smooth and rough surfaces. The dimensions of the apparatus were selected such that boundary effects were minimized. Selection was achieved through numerical simulations of the apparatus interacting with granular soils. The selected dimensions were 1.0 ft wide and 1.5 ft high with sample height of 1.0 ft. The total length of the apparatus was 3 ft, with sample lengths of 3.0 ft, 2.0 ft, and 1.27 ft for wall angles 0°, 45°, and 60°, respectively.

The apparatus was instrumented with a 2,000 lb load cell to measure the external force applied at the moving plate. Horizontal displacements of the moving plate representing the wall were recorded using two Linear Position Transducers (LPT). Vertical deformations of the sand were recorded using 3D camera system, utilizing digital image correlation (DIC).

The sand used for testing, known commercially as 430 Wedron Uniform Silica Sand, had a gradation curve close to Standard Ottawa Sand. Laboratory tests were conducted to determine the maximum and minimum void ratios and the internal friction angle (from a direct shear test) for the 430 Wedron Sand. It was found that the maximum and minimum void ratios were 0.770 and 0.496, respectively. The internal friction angle ranged from 31° and 37° for relative densities ranging from 20% to 80%, respectively. The compaction effort for the sand was calibrated against the number of drops of a specific weight from a given height. It was found that placing the sand in three layers and compacting each layer with a 4 lb dropped from a 4 in. height will resulted in a relative density of about 33%. The force required to overcome friction between the apparatus components was estimated, and the DIC was calibrated before each test.

A total of fifteen tests (15) were conducted by applying displacements to the moving plate/wall. Ten (10) tests were completed with full cycles, and five (5) tests were completed with half cycles. The tests with full cycles were performed with three wall angles (0°, 45°, and 60°), with both rough and smooth surfaces, totaling six (6) tests. In addition, two full cycle tests with 0° and 45° angles using smooth wall were conducted twice to check repeatability. These eight (8) tests were conducted with a displacement amplitude of ±0.1 in. starting with passive loading (pushing the wall toward the soil) for a total of 10 cycles. The remaining two full cycle tests were conducted as follows: one with an amplitude of ±0.2 in, starting with a passive loading for a total of 10 cycles, and the other test with an amplitude of ±0.1 in., starting with an active loading for a total of 10 cycles. Five half cycle tests were conducted for walls with 0° and 45° angles; four of which with a 0.1 in. amplitude (starting from zero to −0.1 in., i.e., active loading, and back to zero) for rough and smooth surfaces and the fifth test with a 0.2 in. amplitude (starting from zero to −0.2 in. and back to zero) using a 0° smooth wall. Plots of force as a function of displacement, normalized volumetric change as a function of displacement, lateral earth pressure coefficient as a function of cycle number, and three-dimensional settlement/heave were prepared.

The results showed an increase of the lateral earth pressure coefficient up to the fifth cycle (in tests with 0.1 in. amplitude) followed by either a constant or a slight reduction in the lateral earth pressure coefficient. The results also showed that the active state was reached during the first unloading. Based on the vertical displacements recorded next to the wall, a non-uniform pressure distribution behind angled walls was observed. The tests with skewed walls showed a lower lateral earth pressure than the wall with no skew. The heave magnitude was significantly larger in front of the skewed wall when compared with the zero degree (0°) wall (about 4 times larger) at most of the wall length. It should be noted, however, that for skewed wall and at the obtuse corner, the heave dropped to very small magnitude, suggesting a non-uniform pressure distribution behind skewed wall.

4.3 Development of Soil Constitutive Model

The soil's constitutive model used in this study was adopted from that of Jung (2009). The model was modified to capture the behavior of the foundation and backfill soils obtained from laboratory, large-scale tests, and monitoring of actual bridges. The details of the constitutive model development and implementation are provided in Appendix D.

The soil model was an elastoplastic model with a hyperbolic stress-strain relation. The original model captured the different initial slopes for unloading and reloading, the dependency of the small-strain shear modulus on confinement, and the stiffness degradation with strain. It included the Drucker-Prager yield function with a non-associated flow rule where plastic strains were calculated from a plastic potential function. The new model extends the original formulation to three dimensions (3D), includes rotation of the backbone curve upon unloading/reloading to account for the escalation of earth pressure with cycles of loading, and captures the observed quasi-linear response of the soil during reloading, as observed in the laboratory tests. The model was coded in Fortran 77 and then implemented in Abaqus© Explicit and Abaqus© Standard through VUMAT and UMAT subroutines, respectively. The attractive feature of the model is its simplicity and the small number of required parameters: twelve (12), where only five (5) are considered fitting parameters.

4.4 Verification and Calibration of Soil Constitutive Model

The ultimate objective of the model was acceptable calculation of the long term performance of IAB by capturing the behavior of the foundation and backfill soils. To accomplish this objective, an extensive validation of the model was conducted, which included comparisons between model predictions and results from laboratory tests found in the literature, laboratory tests completed in this investigation described in Section 4.2, tests on the ¼ scale bridge described in Section 4.1, and data from a full-scale instrumented bridge in Indiana (US 231 over the AEP Railroad Spur). The wide range of scales simulated provided confidence in the model's ability to capture behavior over a wide range of stress levels and soil types. Details of the constitutive model verification and calibration are provided in Appendix E.

Model validation was conducted using laboratory tests obtained from the literature. One such test was dynamic triaxial tests on sand with $e_o = 0.71$, $\sigma_c' = 3 kg/cm^2$ (Yu, 2007). The simulation was run with displacement control (as the actual test), with strains ranging from −0.6% to +0.7% (+ve represents loading). The model parameters were estimated from empirical correlations and the fitting parameters were calibrated such that a reasonable match was achieved between the simulation and experimental results. Abaqus© Explicit with subroutine VUMAT was used. The model showed acceptable capabilities. An additional validation was conducted using the results from a dynamic direct simple shear test conducted on sand ($e_o = 0.83$, $\sigma_c' = 1 kg/cm^2$), using the data from Pradhan,Tatsuoka, and Sato (1989). The simulation was run using displacement control (as the actual test), with strains ranging from −1.0% to +1.0%. The model parameters were estimated from empirical correlations, and the fitting parameters were calibrated to match the laboratory results. In this simulation, Abaqus© Standard with subroutine UMAT was used. The model showed acceptable capabilities and successful capturing of stress escalation through the rotation of the backbone curve.

The model predictions were also checked against the laboratory experiments conducted as part of this investigation and discussed in Section 4.2. Four tests were simulated: two with zero (0°) and two with forty-five (45°) degree wall angles, each with a smooth and rough wall. The simulations were performed with Abaqus© Standard with subroutine UMAT. The exact dimensions of the physical model were used in the simulations, and the contacts and boundaries were selected to reflect what was believed to exist in the physical model. The displacement time history was applied in a similar manner as in the test. Material models were chosen as linear elastic for the apparatus and the elastoplastic model developed in this study was used for the soils. The soil model parameters were taken either from measurements (such as ϕ) or estimated from measured parameters (such as G_{max}). The nonphysical parameters were calibrated against the test results to achieve an acceptable match with the experiments. The predictions from the simulations were all considered acceptable. Small differences between the model and the experiments were observed during the last cycle (10th cycle) for the cases with rough surfaces, for both 0° and 45° walls, and for the 45° wall with a smooth surface, where the simulation showed a stiffer response. This behavior was attributed to the accumulation of plastic strains, which caused a large rotation of the backbone curve.

The model was also validated with comparisons to the field tests. More specifically, with the simulation of the response obtained from a laterally loaded pile test and with the ¼ scale bridge. All simulations were completed using Abaqus© Standard with subroutine UMAT and with displacement control analysis. For the pile, the model used the exact dimensions of the pile, and the far field was assumed to be at approximately five times the pile diameter. The contacts and boundaries were selected to reflect what was believed to exist in the large scale test. The displacement history applied at the top of the pile mimicked the displacement time history of the test. Material models were linear elastic for the pile and the elastoplastic model for the foundation soils. Empirical correlations were used to estimate the physical parameters, and the nonphysical parameters were calibrated with the pile test. The simulations were successful in capturing the pile's deformed shape and inflection point.

For the ¼ scale bridge test, both the experiments with no backfill and with backfill (summer test) were simulated using Abaqus© Standard with subroutine UMAT and with displacement control. Exact dimensions and configuration of the ¼ scale bridge were used in the model. Foundation and backfill soils were extended in the horizontal directions (longitudinal and transverse) to minimize the effect of boundaries; contacts and boundaries were selected to reflect what was believed to exist in the large-scale test. Displacement history applied at the gap in the middle of the bridge was the same as that applied during the large-scale test. Material models were linear elastic for the deck, piles, girders, and abutment walls and elastoplastic for the foundation and backfill soils. Model parameters used for the foundation soils were the same as those used for the laterally loaded pile simulation. The model physical parameters for the backfill soil were estimated from empirical correlations and from a best-fit of the measured lateral earth pressures. Results from the tests with no backfill indicated that the simulation was capable of capturing the rigid body response of the bridge deck and the deformation of the pile-soil system. For the test with backfill, the results showed good agreement in earth pressures from the test and numerical simulation; the model was capable to capture key observations such as a higher lateral earth pressure at the obtuse corner, lateral earth pressure escalation during two successive cycles with the same amplitude, and the soil yielding during active loading.

Finally, a full scale instrumented bridge (US 231 over the AEP Railroad Spur) was simulated using Abaqus© Standard utilizing the UMAT subroutine, with a fully coupled thermal-displacement analysis with soil-structure interaction. The dimensions of the model were exactly the same as those of the full scale bridge, and model parameters for the foundation soil were the same as those used for the laterally loaded pile test. The nonphysical model parameters for the backfill soils were slightly modified from what was used in the ¼ scale bridge test to reach a better fit with the recorded soil pressures. The thermal time history applied to the bridge deck and girders includes temperature time history identical to that recorded during the monitoring period and equivalent temperature time history that will generate the anticipated shrinkage strains of the bridge superstructure. The simulation successfully captured the response of the backfill soils and showed acceptable results for the lateral earth pressures recorded. The model also captured the escalation of earth pressures with the number of cycles, distribution of lateral earth pressure along the wall (i.e., highest at the obtuse corner and lowest at the centerline of the abutment), and yielding of the soil during active loading. In addition, the model captured reasonably the displacements of the acute and obtuse corners.

4.5 Parametric Study

The objective of the parametric study was to identify the effect of various parameters on the long term performance of integral abutment bridges. Details of the parametric study are provided in Appendix F.

The selected parameters for the study were based on geometry parameters (bridge length, bridge skew angle, thickness of the abutment wall, and existence of wing walls), mechanical in nature (stiffness of the foundation soil), or other factors (shrinkage and sequence of loading). A total of twenty cases were analyzed to cover all cases. Table 4.1 presents the analyzed cases.

All cases were modeled with Abaqus© Standard with a fully coupled thermal-displacement analysis with soil-structure interaction. Contacts and constraints between structural elements and soil or at the boundaries were applied in the model to replicate what was believed to exist in an actual bridge. The bridge abutment walls and piles were modeled as linear elastic. The superstructure was modeled as a coupled thermal-mechanical elastic material. The foundation and the backfill soils were represented as elastoplastic materials using the soil's constitutive model developed in this study. The temperature time history input (bridge deck and girders) consisted of 10 uniform cycles with amplitude $\pm 50^\circ$F and period of 1 year, as shown on Figure 4.1. It should be noted that for the cases of shrinkage starting with active loading (Case 10 and Cases 15 through 18), shrinkage was simulated as a decrease of temperature. Therefore, the thermal time history incorporated temperatures associated with shrinkage strains along with the regular thermal expansion/contraction time history. The adopted shrinkage strain time history and the resulting thermal loading time history are presented in Figures 4.2 and 4.3, respectively. Two more cases were analyzed (Cases 19 and 20) with shrinkage strains and thermal loading temperatures oscillating from 0°F to -75°F, the resulting thermal loading time history are presented in Figure 4.4.

Case 3 was considered the base case. Therefore, the case was analyzed in detail and used as a basis of comparison with the other cases. The model captured well the anticipated features of the rigid body response of the base case in terms of the displacement demand on

TABLE 4.1
Analyzed Cases

Case	L (ft)	Skew (°)	Foundation Stiffness[1]	Wall (ft)	Wing Wall[2]	Shrinkage[3]	Starting Load[4]	Notes
1	200	60	Medium	3	No	No	Passive	±50°F
2	500	60	Medium	3	No	No	Passive	±50°F
3*	1000	60	Medium	3	No	No	Passive	±50°F
4	1000	30	Medium	3	No	No	Passive	±50°F
5	1000	45	Medium	3	No	No	Passive	±50°F
6	1500	60	Medium	3	No	No	Passive	±50°F
7	1000	60	Soft	3	No	No	Passive	±50°F
8	1000	60	Stiff	3	No	No	Passive	±50°F
9	1000	60	Medium	3	Yes	No	Passive	±50°F
10	1000	60	Medium	3	No	Yes	Active	±50°F
11	200	60	Soft	3	No	No	Passive	±50°F
12	200	60	Stiff	3	No	No	Passive	±50°F
13	1000	60	Medium	2	No	No	Passive	±50°F
14	1000	60	Medium	4	No	No	Passive	±50°F
15	200	60	Medium	3	No	Yes	Active	±50°F
16	500	60	Medium	3	No	Yes	Active	±50°F
17	1000	30	Medium	3	No	Yes	Active	±50°F
18	1000	45	Medium	3	No	Yes	Active	±50°F
19	1000	60	Medium	3	No	Yes	Active	0 to -75°F
20	500	60	Medium	3	No	Yes	Active	0 to -75°F

*Base case.

[1] Foundation stiffness refers to the small strain shear modulus of the foundation soils.

[2] Wing wall refers to whether abutment wing walls were included in the model.

[3] Shrinkage refer whether shrinkage deformation of the bridge deck with time was included in the analysis.

[4] "Passive" indicates that the first loading cycle is expansive (the backfill soil is loaded), while "Active" means that the first loading cycle is contractive (the backfill soil is unloaded).

piles, such as larger displacements on the piles at the acute corners. The earth pressure was highest at the obtuse corner and smallest at the abutment centerline, which was in agreement with both laboratory and field tests. In addition, an increase of the lateral earth pressure was observed during the first five cycles, followed by a steady state response which is again in agreement with test results. It was also found that lateral earth pressures were almost uniform along the abutment wall, with localized peaks at the acute and obtuse corners higher at the obtuse than at the acute, which agree with test observations. The lateral earth pressure coefficient was between 1.2 and 2.0, except at the corners. The stiffness of the foundation soils was found to be significant in increasing the displacement demand on piles, particularly for long bridges (≥1000 ft), but had only a small effect on pressures behind the abutment. The parametric study also showed that the presence of the wing walls, while increasing constraint in the backfill and thus increasing earth pressures, had no significant effect on the displacement demand of the piles.

From analysis of the results of the parametric study, it was concluded that the length of an integral abutment bridge could go up to a 500 ft with a maximum skew of 60°, with shrinkage and the loading sequence started with

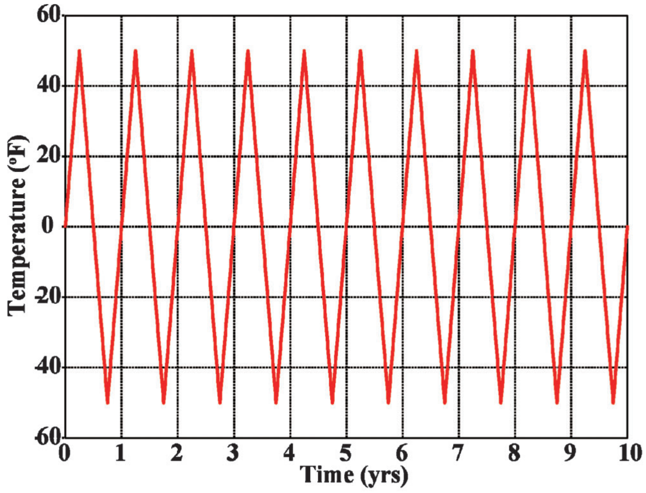

Figure 4.1 Thermal loading time history.

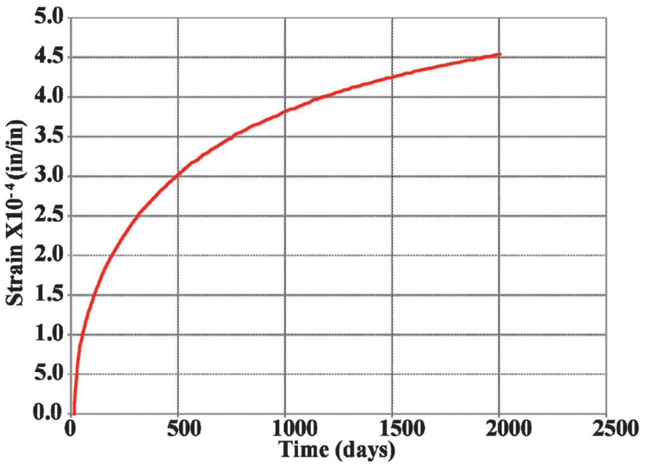

Figure 4.2 Shrinkage strains.

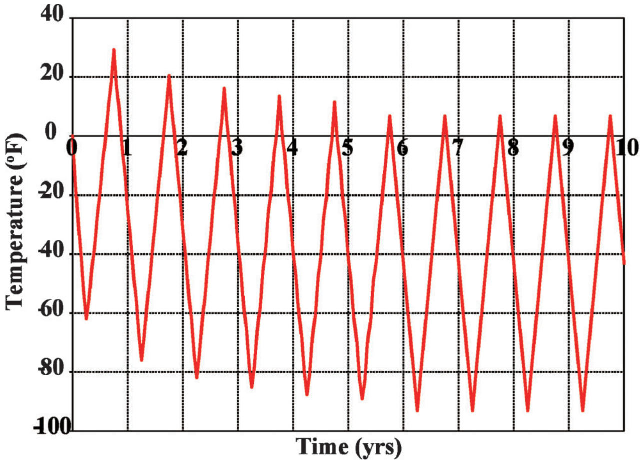

Figure 4.3 Thermal load time history to include shrinkage with initial contraction.

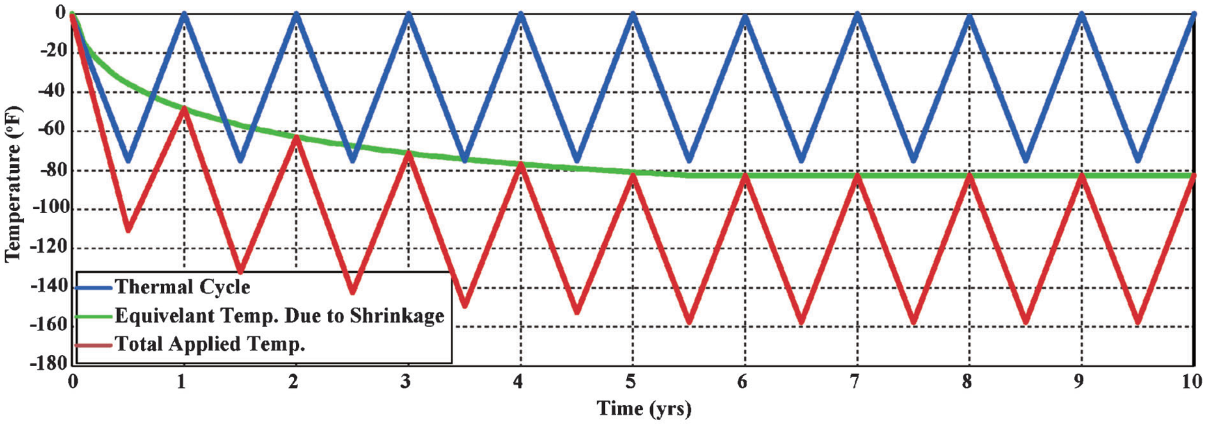

Figure 4.4 Thermal load time history to include shrinkage with thermal oscillation from 0°F to −75°F.

contraction. For models considering concrete shrinkage and loading starting from contraction induced larger displacement demands on the piles were observed than for cases without shrinkage and loading starting with expansion. Regardless and for lengths up to 500 ft and 60° skew, the larger displacement demands at the pile-abutment connection were still below the threshold limit of 2.0 in. as adopted from Frosch, Chovichien, Durbin, and Fedroff (2006) and Frosch (personal communication, 2013), as shown in Figure 4.5.

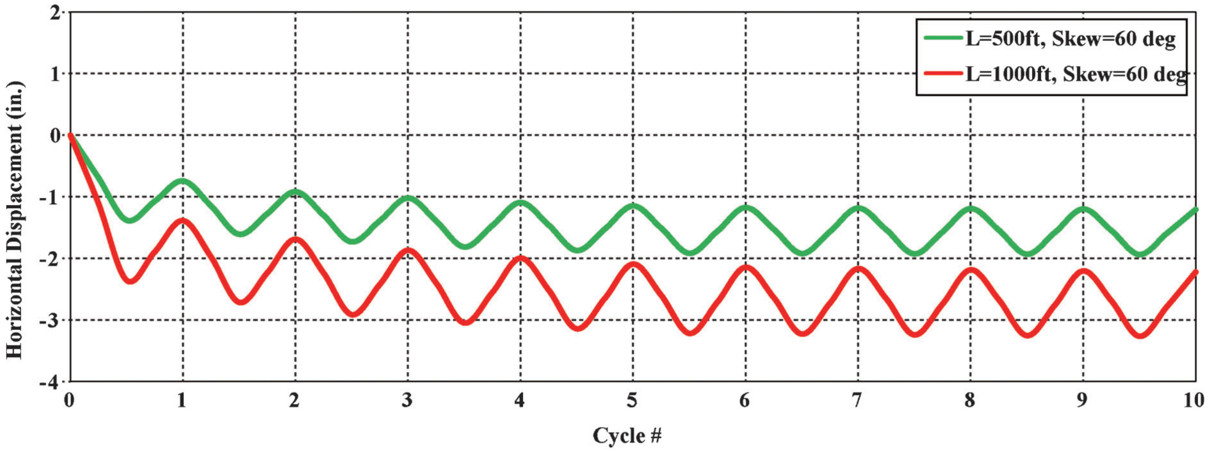

a- Acute Corner

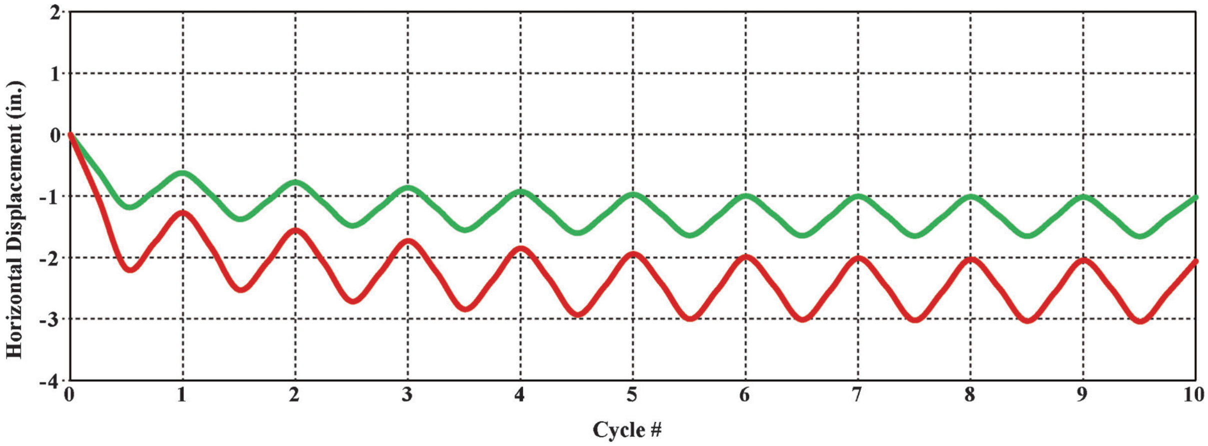

b- Obtuse Corner

Figure 4.5 Displacement at top of the pile as a function of the number of cycles.

5. CONCLUSIONS

Rigid body response of the bridge superstructure due to cycles of thermal loading dictates the response of the backfill soil, pressures on the abutments, and displacement demands on the piles. The skew angle of the bridge along with the restraints imposed by backfill and foundation piles results in longitudinal and transverse displacements and in rotations of the bridge deck in response to the thermal loading. Larger displacements are observed at the acute corner during both expansion and contraction of the bridge superstructure. This results in a rotation of the bridge deck toward the obtuse corner during expansion and toward the acute corner during contraction. The response of the abutment walls is complex as it includes bi-axial bending (in the horizontal and vertical directions) and torsion. The earth pressure behind the abutment wall follows a hyperbolic relationship during expansion, with increasing pressure with increased expansion, up to approximately the 5th cycle, after which the pressure and overall response of the bridge, stabilizes. It is also observed that the earth pressure is the highest at the obtuse corner and the lowest at the centerline of the abutment. At steady state, and based on the numerical modeling, only about 3% of the wall is subjected to a lateral earth pressure coefficient larger than 3 and most of the wall is subjected to lateral earth pressure coefficients ranging from 1.2 to 2.0. An active state of stress was reached in the backfill during the first contraction cycle. Interaction between the bridge deck, abutment wall, and backfill soil results in a displacement demand on the piles that is the largest at the acute corner. The fixity point of the piles is at relatively shallow depth compared to the total pile length (at about 25 ft for the 1000 ft bridge).

It is established that the constitutive model developed for this study showed acceptable performance under various stress levels and length scales. The model is capable of capturing the increase of earth pressure with expansion cycles through rotation of the backbone curve. The model is also able to capture the distribution of the earth pressure behind the abutment wall and yielding of the soil during active loading. Furthermore, the model performance is found acceptable in capturing the pile-soil system response in terms of deformation and location of the point of fixity. In some instances, where the model predicts large accumulation of plastic strains, predictions show a slightly stiffer response due to the larger rotation of the backbone curve. This behavior, however, was only observed after a number of cycles (10^{th} cycle) which may not have an effect on the overall predictive capabilities of the model, considering that steady state is usually reached between the 5^{th} and 7^{th} cycles (Frosch & Lovell, 2011).

Based on the lateral earth pressure distribution on the abutment wall and the lateral earth pressure coefficient acting on most of the wall length, it can be argued that the lateral earth pressure behind the abutment wall is not a contributing factor for the long term performance of the integral abutment bridges. Therefore, design of integral abutment bridges is limited solely by the lateral capacity of the pile-abutment connection. The horizontal displacement that induced buckling for a 10-in concrete filled tube pile (CFT) was 2.0 in (Frosch et al., 2006). This similar maximum limit was also considered by Frosch and Lovell (2011). Therefore, maximum displacement considered in this research is 2.0 in.

Although shrinkage and first loading in contraction has significant adverse effects on the displacement demands on piles, the parametric study showed that the displacement demands at the pile-abutment connection are still below the adopted threshold of 2 in. for a 500 ft bridge with a 60° skew. For a 1000 ft bridge with a 60° skew, displacements greater than 2 in. are developed and reached 3 in. To achieve these larger displacements, confining reinforcement as recommend by Frosch et al. (2009) is required. The effect of foundation stiffness on the IAB performance is not significant, except for long bridges (>1000 ft) on soft foundation soils. The effect of the wing wall and the thickness of the abutment wall on pile displacement demand are not significant.

6. IMPLEMENTATION RECOMMENDATIONS

This study was a continuation of research conducted at Purdue University on integral abutment bridges (Frosch et al. (2006, 2009), Frosch and Lovell (2011)). This research supports the conclusions provided by Frosch and Lovell (2011) and agrees with the recommendations already provided in the INDOT bridge design manual. This research indicates that it may be possible to increase the maximum bridge lengths for skew angles greater than 30°. For soft to very soft foundation soils and for long bridges (>1000 ft), bridge-specific analyses should be conducted utilizing soil-structure interaction.

7. FUTURE RESEARCH

While the work completed addresses a wide range of geometries, loading, and soil conditions, there are a number of aspects that still need further work.

1. It is recommended to conduct additional analyses using the same techniques and material models used in this study but with different piles (e.g., HP) only shells were considered here. In addition, studying different pile orientations is recommended. Furthermore, the piles' depth is additional parameters that could be studied.
2. The models used in the simulations could be used as part of a seismic study using Abaqus© Explicit with VUMAT. This study is to be conducted in three dimensions, to inspect the various modes of vibrations and the intermediate piers should be modeled as they may have an effect on the mode of vibration.
3. Additional validation and calibration of the constitutive model should be performed using field data of full size instrumented bridges in states other than Indiana to cover different type of foundations soils.
4. The use of a nonlinear constitutive model for concrete that also has the capabilities of including shrinkage may improve understanding of the long term performance of integral abutment bridges. The nonlinear stress strain relation will allow changes in the concrete elastic modulus, which is more realistic. In addition, stress relief by crack formation may have a significant effect on the rigid body movement of the bridge superstructure and may provide additional insights.

REFERENCES

Frosch, R. J., Chovichien, V., Durbin, K., & Fedroff, D. (2006). *Jointless and smoother bridges: Behavior and design of piles* (Joint Transportation Research Program Publication No. FHWA/IN/JTRP-2004/24). West Lafayette, IN: Purdue University. http://dx.doi.org/10.5703/1288284313379

Frosch, R. J., Kreger, M. E., & Talbott, A. M. (2009). *Earthquake resistance of integral abutment bridges* (Joint Transportation Research Program Publication No. FHWA/IN/JTRP-2008/11). West Lafayette, IN: Purdue University. http://dx.doi.org/10.5703/1288284313448

Frosch, R. J., & Lovell, M. D. (2011). *Long-term behavior of integral abutment bridges* (Joint Transportation Research Program Publication No. FHWA/IN/JTRP-2011/16). West Lafayette, IN: Purdue University. http://dx.doi.org/10.5703/1288284314640

Jung, C. (2009). *Seismic loading on earth retaining structures* (Unpublished doctoral dissertation). West Lafayette, IN: Purdue University.

Pradhan, T. B., Tatsuoka, F., & Sato, Y. (1989). Experimental stress-dilatancy relations of sand subjected to cyclic loading. *Soils and Foundations*, *29*(1), 45–64.

Wasserman, E. P., & Walker, J. J. (1996). Integral abutments for steel bridges. In *Highway structures design handbook: Vol II* (ch. 5). Chicago, IL: National Steel Bridge Alliance.

Yu, H., Khong, C., & Wang, J. (2007). A unified plasticity model for cyclic behavior of clay and sand. *Mechanics Research Communications*, *34*, 97–114.

APPENDICES

APPENDIX A. LITERATURE REVIEW

A.1 INTRODUCTION

The limitations imposed on the maximum skew angle and length of integral abutment bridges had been based on experience. Various studies were conducted to understand the behavior of Integral abutment bridges. The objective of the studies was to provide realistic bounds on the geometry of Integral abutment bridges. The objective was accomplished through different approaches such as instrumentation and monitoring of full-scale bridges, large laboratory scale testing, and numerical modeling.

A comparative survey was conducted in North America on the design and construction practices of Integral abutment bridges and showed that design practices varied for IAB's between different states in the US and provenances in Canada (Kunin & Alampalli, 1999). The differences in practice were mostly on how the earth pressure was calculated, how the limits for thermal movements were determined and the design philosophy of piles (Kunin & Alampalli, 1999).

In their state of the art paper, Arockiasamy, Butrieng, and Sivakumar (2004) identified issues affecting the integral abutment bridges design, namely: creep, thermal gradient, differential settlement and differential deflection, pavement relief pressure, and soil-pile interaction. Shrinkage (creep) causes additional stresses in the deck. However, since the shrinkage is directional and results in a net inward movements (shortening of the bridge), which will result in a smaller displacement during the expansion cycle, leading to smaller earth pressure. In addition, and due to shrinkage the thermal changes are offset toward the contraction phase of the thermal cycles resulting in a non-uniform cycles. Any differential settlement or piers settlement results in bending moments in the deck. In addition, lateral movement of the piles results in reduction of the pile's axial load capacity. The developed soil pressure behind the abutment is highly dependent on the longitudinal movement of the bridge deck. Also, the state-of-the art paper documented that the effect of the wing wall was dependent on the wing wall shape. The paper listed three types of wing walls that are common in integral abutment bridges; parallel, flared and U-type. It should be noted, however, that the existence of wing walls, and if they are structurally separated from the abutment, did not have any effect on the displacement from thermal loading. In addition, the authors stated that orientation of wing wall, which are integrated with the abutment, has an effect on the magnitude of developed earth pressure behind the abutment, for example the U-shape wall results in higher earth pressure when compared with transverse wing walls.

This research is a continuation of a previous study by Frosch and Lovell (2011), with a focus on the geotechnical aspects of the integral abutment bridges design practice. A summary of the work by Frosch and Lovell (2011) is presented in Section A.2. In Section A.3, a summary of the studies completed on earth pressure development behind IAB is included. Section A.4 presents findings on the displacement demands on piles. Section A.5 contains a discussion of the literature reviewed.

A.2 FROSCH AND LOVELL (2011)

The study by Frosch and Lovell was a continuation of a comprehensive effort carried out at Purdue University to better understand the long term behavior of integral abutment bridges (Durbin, 2001; Frosch, Chovichien, Durbin, & Fedroff, 2006; Frosch, Kreger, & Talbott, 2009). The study analyzed the data from three instrumented bridges across Indiana and data from a ¼ scale bridge test; it also included a parametric study through numerical simulations. The instrumented bridges were INDOT Bridge#I-65-176-5543C (Southbound I-65 over SR 25), INDOT Bridge#18-27-4518D (SR 18 over the Mississinewa River), and INDOT Bridge#231-74-2699 (US 231 over AEP Railway Spur).

The I-65 southbound bridge was a special case because it was a rehabilitated bridge. The entire superstructure was replaced after an impact in year 2000. The bridge had two equal spans of 76 ft (total length 152 ft) with 25° skew angle. The 8-in bridge deck was supported by seven (7) W36 × 150 steel girders. Each of the abutments was supported by ten piles, approximately 42 ft deep; four of them were concrete filled tube (CFT) with14.5-in diameter and six HP 12 × 53 steel piles oriented along their strong axis. The bridge was instrumented in the summer of 2000. Table A.1 summarizes the instrumentation used in the bridge.

The temperature recorded during the monitoring period (about 9.5 years) ranged from 107°F to −12°F, with 90° and 10°F as the average summer and winter temperatures, respectively. The cell pressure placed at 57 inches below the original ground surface showed an increase in pressure from 1000 psf in 2001 to 1700 psf in 2006. The cell pressure 10.5 inches below the original ground surface had lower earth pressures, with values of 1250 psf at the end of the first year, 1500 psf at the end of the second year, and then dropped to 1000 psf between the third and sixth years (i.e., between 2003 and 2006). The researchers calculated the theoretical passive and active earth pressures based on Rankine theory and found that the earth pressures measured were smaller than the theoretical passive or active pressures. They attributed the pressures lower than active to the formation of a gap between the backfill soil and the abutment, while the smaller passive earth pressures were attributed to the backfill soil not reaching its passive state.

The SR 18 bridge was a five span bridge (2 spans each 62 ft long and 3spans 81 ft long) with a total length of 367 ft with an 8° skew angle. The 8-in bridge deck was supported by five (5) 60-in prestressed concrete bulb tee girders. Each of the abutments was supported by five 14-in diameter concrete filled tube (CFT) piles, approximately 20.8 ft deep. The bridge was instrumented in the summer of 2003. Table A.2 summarizes the instrumentation used in the bridge.

The tiltmeter data was discarded because there were problems with the collected data (showing unexplained shifts in the readings), indicating malfunction of the tiltmeters. The temperature recorded during the monitoring period (from summer 2003

TABLE A.1
I-69 Bridge Instrumentation

Instrumentation	Location
Two potentiometers	Longitudinal direction at the centerline of the abutment close to the original ground surface Transverse direction at the obtuse corner of the abutment close to the original ground surface
Two pressure cells	Close to the obtuse corner @10.5 in below original ground surface Close to the obtuse corner @57 in below the original ground surface
Eighteen strain gages	Four gages at the HP pile close to the center of the abutment Four gages at the HP pile close to the obtuse corner of the abutment Five gages between the girders and the abutment at the center of the abutment Five gages between the girders and the abutment at the obtuse corner of the abutment

TABLE A.2
SR 18 Bridge Instrumentation

Instrumentation	Location
Three convergence meters	Longitudinal direction at the centerline of the 1st abutment at 15-in from the original ground surface Longitudinal direction at the centerline of the 2nd abutment at 15-in from the original ground surface Longitudinal direction at 31 in. from the obtuse corner of the 2nd abutment at 15 in. from the original ground surface
Two pressure cells	At 31 in. from the obtuse corner and 18 in. from the original ground surface (2nd abutment) At 277 in. from the obtuse corner (centerline) and at 18 in. from the original ground surface (2nd abutment)
Thirty-five strain gages	Three gages at the top of the convergence meter reference piles (far field for the convergence meter) Six gages in the three piles closer to the obtuse corner of the abutment (at the pile abutment connection); two of the piles were in the 1st abutment and one pile in the 2nd abutment (only longitudinal direction) Four gages in the two piles near the acute corner of the abutment (at the pile abutment connection); one pile at each abutment (only longitudinal direction) Four gages at the two piles near the centerline at the pile-abutment connection (recording deformation in the longitudinal direction) Eighteen gages with depth on one pile. Three gages at each depth (two directions; longitudinal and transverse) Depth interval between gages location is 48in interval with depth starting at the pile-abutment
Two tiltmeters	One tiltmeter at the centerline of each abutment

till 2009) ranged from 96°F to −11°F, with 90° and 20°F as the average summer and winter temperatures, respectively.

The convergence meter data showed a net inward movement of about 0.9-in over a six year period. On average the abutments had a net inward movement of 0.4-in during the first year, 0.6-in during the second year, 0.7-in during the third year, 0.8-in during the fourth and fifth years, and 0.9-in during the sixth year.

The recorded earth pressures showed an increase in the first three years, between 2003 and 2006, from 1000 psf to 2000 psf, then reached a steady state for the next three years with some softening. The earth pressures close to the obtuse corner (see Table A.2 for location) and centerline were similar (both escalated to reach 2000 psf during the third year), except that during the fourth year, the pressure at the obtuse corner was higher than at the centerline of the centerline (the earth pressure at the obtuse corner remained at 2000 psf, while at the centerline the earth pressure was about 1500 psf). The researchers calculated the theoretical passive and active earth pressures based on Rankine theory. They found that the earth pressures measured were smaller than the theoretical passive and active pressures. As with the previous bridge, the pressure lower than active was attributed to the formation of a gap between the backfill soil and the abutment wall, while the lower passive earth pressure was believed to be indicative of the backfill soil not reaching the passive state.

The deflected shapes of the piles were calculated during the first and last years and the results showed that the maximum deflection (0.9 in) occurred at the top of the piles. The data showed that fixity was only achieved at the bottom of the pile, at about 20 ft below the ground surface.

The US 231 bridge was a three span bridge (two spans 69.5 ft long each and one span 82 ft long) with a total length of 221ft and 33.8° skew angle. The 8-in bridge deck was supported by seven (7) prestressed, concrete type III, I beam girders. Each of the abutments was supported by seven 14-in diameter concrete filled tube (CFT) piles, approximately 81-ft deep. The bridge was instrumented in the fall of 2006. The two abutments had the same instrumentation. Table A.3 summarizes the instrumentation used in the bridge.

During the monitoring period there was a problem with the tiltmeter data and the strain gages and their data were discarded. Also in a number of occasions data was lost from the instruments due to power outages and surges.

The temperature recorded during the monitoring period (summer 2006 t0 2010) ranged from 100°F to 9°F, with 100°F and 20°F as the average summer and winter temperatures, respectively.

The convergence meter data showed a net inward movement over three and half years of monitoring (about 0.7-in at the acute corner). The inward movement was the highest at the acute corner and the lowest at the obtuse corner. On average, the abutment movements at the acute corner recorded a net inward movement of 0.4-in during the first year, and 0.1-in per year in the subsequent years. At the obtuse corner, the net inward movement was about 0.2-in during the first year and 0.05-in per year in the subsequent years.

The earth pressures increased in the first three years, between 2006 and 2009, from 250 psf to 1500 psf at the obtuse corner. The pressure was the highest close to the obtuse corner (reached 1500 psf in 2009) and lowest at the centerline (reached 1250 psf in 2009), with intermediate pressure at the acute corner (reached 1350 psf in 2009). The measured earth pressures were smaller than the active pressure, which was attributed to the formation of a gap between the backfill soils and the abutment wall. The recorded earth pressure close to the obtuse corner was close to the theoretical passive earth pressure with $K_p=3$.

TABLE A.3
US 231 Bridge Instrumentation at Each of the Abutments

Instrumentation	Location
Five convergence meters	Three along the longitudinal direction at the obtuse and acute corners and at the centerline of the abutment, placed 22 in below the original ground surface Two along the transverse direction at the obtuse and acute corners of the abutment, placed 22 in below the original ground surface
Three pressure cells	One pressure cell close to the obtuse corner, one close to the acute corner and one at the abutment centerline, at 22 in below the original ground surface
One strain gage	One gage at the top of the convergence meter reference piles, which was installed relatively at a far distance from the bridge, where movement is not anticipated
One tiltmeter	One tiltmeter at the centerline

Finite element models were run using SAP2000. The elements used in the models were frame and shell elements. The shell elements were employed for the abutment wall and for the deck, while frame elements were used for the girders and piles. A transformed steel section was used for the piles to model the composite section of the pile (steel and concrete). The transformed steel section has the same flexibility (EI) as the composite section.

The interaction between soil and pile or abutment was modeled using linear springs. The piles' spring constants were estimated based on Griemann et al. (1987) for clayey soils and granular soils. Springs were attached to the piles in two perpendicular directions to capture 3D effects. Rankine and log-spiral passive earth pressure theories were used to estimate the stiffness of the backfill, which was then modeled using one equivalent spring.

The seasonal temperature variations were converted into strains which were then applied to the bridge superstructure. In addition, strains due to shrinkage were estimated based on the CEB MC90 model and were added to the strains obtained from the seasonal temperature.

A total of six cases were analyzed for each bridge, SR 18 or US 231. Each of the analyzed cases relied on different assumptions regarding the inclusion or not of the backfill, adding or ignoring shrinkage, or considering the pile resistance with depth. The following list contains the analyzed cases along with the associated assumptions:

Case 1: Only strains from seasonal temperature (deck and girders) were considered. Pile springs were included but the backfill resistance was ignored.

Case 2: Strains from seasonal temperature and shrinkage were included for both the deck and the girders. Pile springs were included but the backfill resistance was ignored.

Case 3: Strains from seasonal temperature (deck and girders) and shrinkage (deck only) were included. Pile springs were included but the backfill resistance was ignored.

Case 4: Strains from seasonal temperature (deck and girders) and shrinkage (deck only) were included. Pile springs were included and the backfill resistance was modeled using spring constants based on Rankine theory.

Case 5: Strains from seasonal temperature (deck and girders) and shrinkage (deck only) were included. Pile springs were included and the backfill resistance was modeled using spring constants based on the log spiral theory.

Case 6: Strains from seasonal temperature (deck and girders) and shrinkage (deck only) were included. Pile springs were not included and the backfill resistance was modeled using spring constants based on the log spiral theory.

The results from each case were compared with the field data. It was found that, for the SR 18 bridge, Case 6 provided the closest match to the recorded convergence meter data. For US 231, however, none of the cases investigated provided a good match with the recorded field data. An additional case (Case 7) was added that included strains from seasonal temperature (deck and girders) and shrinkage (deck only), with pile springs only in the upper 20 ft and backfill resistance ignored. The results from Case 7 matched the recorded convergence meter in the longitudinal direction.

Based on the model calibration and verification, a parametric study was conducted to investigate the effect of length and skew angle on the piles' demand. It was concluded that up to a 30° skew angle, the bridge could have a maximum length of 500 ft with no damage to pile at the pile-abutment connection and 1100 ft with allowable damage to pile at the pile-abutment connection (only with HP section piles). For skew angles between 30° and 60° the length was reduced to 300 ft for no damage and 1000 ft with allowable damage (HP sections only).

The results from the field monitoring, the parametric study and analytical studies were used to provide a relation for calculating the displacement demands on piles. Frosch and Lovell (2011) suggested the following relationships:

For $0 \leq \theta \leq 30^\circ$

$$\Delta = \left\{ \begin{array}{ll} \sqrt{\left(F(\varepsilon_{\Delta T} + \varepsilon_s) + \frac{L}{2} + 0.006\theta \right)^2 + (0.01\theta)^2} & 0 \leq \theta \leq 30 \\ \sqrt{\left(F(\varepsilon_{\Delta T} + \varepsilon_s) \frac{L}{2} + .011\theta - 0.16 \right)^2 + (0.03\theta - 0.6)^2} & 30 \leq \theta \leq 60 \end{array} \right\} \tag{A.1}$$

Where,
Δ is the total demand deflection, in,
F is the restraint reduction factor (0.6),
$\varepsilon_{\Delta T}$ is strain due to temperature differential, in/in,
ε_s is the shrinkage strain, in/in (500με)
L is the bridge length, and
θ is the skew angle.

A.3 EARTH PRESSURE DEVELOPMENT BEHIND ABUTMENT WALLS OF IAB

The backfill soil pressure increase with successive cycles of expansion, the effect of skew on the magnitude and distribution of earth pressure on the abutment walls of integral abutment bridges, and the number of cycles required to achieve a constant earth pressure (steady state) had been studied by several researchers. Each of the studies focused on one or more of the issues on earth pressure development behind integral abutment walls; for example effect of skew angle on the magnitude and distribution of the developed earth pressure was studies by Sandford and Elgaaly (1994), Hassiotis and Xiong (2007), and Frosch and Lovell (2011). The issue of earth pressure escalation with thermal loading cycles of the bridge superstructure and the number of cycles to reach steady state were studied by Hassiotis and Xiong (2007), Frosch and Lovell (2011), Ng, Springman, and Norrish (1998), Tsang, England, and Dunstan (2002), and Xu, Clayton, and Bloodworth (2007). In addition, the approach followed by researchers varied between analysis of monitoring data from instrumented full scale bridges, to laboratory and element scales tests. Examples on using data from instrumented bridges include Sandford and Elgaaly (1994), Bonczar, Civjan, Breña, and DeJong (2005), Frosch, Wenning, and Chovichien (2005), Civjan, Bonczar, Breña, DeJong, and Crovo (2007), Hassiotis and Xiong (2007), and Frosch and Lovell (2011). Example on studies that used laboratory and element scale tests include Ng et al. (1998), Tsang et al. (2002), Cosgrove and Lehane (2003), Clayton, Xu, and Bloodworth (2006), and Xu et al. (2007). In Sections A.3.1 and A.3.2 summary of some of the conducted studies to address the above mentioned issues with earth pressure development behind integral wall.

A.3.1 Earth Pressure from Full Scale Instrumented Bridges

In general, earth pressure cells were installed behind the abutment walls to record backfill pressures with thermal loading cycles. Then the recorded earth pressures were correlated with other instrumentation data, such as bridge superstructure movement induced by thermal expansion or contraction. In some instances, the earth pressure cells installation was not successful (e.g., Bonczar et al. (2005)). The following sections provide a summary of a couple of studies using full scale instrumented bridges; the first study is by Sandford and Elgaaly (1994) is summarized in section A.3.1.1 and the other study by Hassiotis and Xiong (2007) in section A.3.1.2.

A.3.1.1 Sandford and Elgaaly (1994)

In 1994, Sandford and Elgaaly conducted a study to identify the earth pressure distribution along the abutment wall behind a skewed abutment. In their study, a 20° skewed bridge with steel girders supporting the bridge deck (The Fork Bridge in western Maine) was instrumented. The bridge was supported by shallow foundations. The bridge was 50.3 m long and 11.48 m wide. The depth of the abutment was 7.2 m. Sixteen pressure cells were installed on both abutments (eight earth pressure cells at each abutment). Four earth pressure cells were installed on each side of the abutment center line (at 3 m from the centerline) at different depths. The depth interval at which the earth pressure cells were installed ranged from 1.5 m to 2 m. The monitoring period was over two years. The main conclusions from the analysis of the instrumentation data are during expansion, the bridge movement is restrained by the backfill. The magnitude of earth pressure depends on the superstructure movement due to cycles of thermal loading, which is a function of the bridge length. The maximum earth pressure occurred at the girder level, then decreased with depth due to the movement restrains imposed by the foundation. Even though, the bridge was supported on shallow foundations the researchers made a note that the movement restrains at the foundation level varied with the foundation type. The highest earth pressure was observed at the pressure cells close to the obtuse corner. It was recommended to use the full passive earth pressure at the obtuse corner and the active pressure at the acute corner as the design soil pressures acting on the abutment wall.

A.3.1.2 Hassiotis and Xiong (2007)

Hassiotis and Xiong (2007) instrumented the Scotch Road Bridge in Trenton, NJ. This is an integral abutment bridge, 300 ft long, over I-95. The bridge deck was supported on 10 steel girders. Each abutment (11 ft deep) was supported by 19 HP14 × 102 steel piles. The bridge had a skew angle of 15°. Eight earth pressure cells were installed behind the abutment; two of them at about 11.3 ft from the acute corner, two at about 45.4 ft from the acute corner, and four more at about 28.3 ft from the obtuse corner. The monitoring period was from April 2003 to June 2006.

Hassiotis and Xiong (2007) suggested that that the lateral earth pressure coefficient increased with displacement until it peaked, and then it would continue with a small decrease. They suggested that after the mobilization of the peak internal friction angle, and with more displacement, the internal friction angle would start approaching the critical friction angle. They attributed the escalation of the lateral earth pressure to the densification of the backfill resulting from the formation of an active wedge during contraction. Based on the recorded earth pressures, during expansion, it was found that at a depth of 1 ft from the top of the abutment, and close to the acute corner (depth=1 ft), the lateral earth pressure coefficient increased from about 1.6 to 4.5 during the first three years, and then it decreased to about 4.2 during the fourth year. Close to the centerline (depth=1 ft), the lateral earth pressure coefficient increased from 1.5 to 4.2 during the first three years, and then decreased to about 4 during the fourth year. At a depth of about 10.3 ft from the top of the abutment, and close to the acute corner (depth=10 ft), the lateral earth pressure coefficient increased from 2.6 to about 5.5 during the monitoring period with no decrease of the lateral earth pressure during the fourth year. Close to the centerline (depth=1 ft), the earth pressure increased from about 2.3 to 4 during the first 3 years then decreased to about 3.5 during the fourth year. The main conclusion from the study was that the lateral earth pressure behind the abutment increased during the first three years, then reached a somewhat steady state after that. The increase of earth pressure was attributed to densification of the backfill after each contraction. The maximum developed lateral earth pressure coefficient was a function of the bridge length.

A.3.2 Earth Pressure From Laboratory Scale Tests

The advantages of laboratory scale tests over full scale tests are the control of the test's initial conditions and easier control of instrumentation. However, the boundaries of the testing apparatus may not reflect the far field conditions present in the field. In the following sections, summary of tests conducted on various scales will be presented. Section A.3.2.1 presents a summary of the tests that were conducted by Ng et al. (1998) using centrifuge apparatus. Section A.3.2.2 presents the summary of the tests conducted by Tsang et al. (2002), which consisted of a physical model that simulates the rotational movement of an abutment wall. Tests on element scale were conducted by Xu et al. (2007) and are presented in Section A.3.2.3.

A.3.2.1 Ng et al. (1998)

The researchers in this study conducted a series of centrifuge experiments to simulate a granular backfill response to cyclic loading due to thermal loading of the bridge deck. The Cambridge centrifuge was used by the researchers; the dimensions of the outside box of the centrifuge were 677 mm long and 535 mm tall. The abutment wall simulated in the centrifuge test was a spread-based abutment. The prototype simulated a 2.5 m high granular soil supported by 1 m thick spread base. The soil for the backfill and foundation was granular with minimum and maximum void ratios 0.613 and 1.014, respectively. A layer of sand was attached (by adhesive) to the wall to produce a friction between the wall and the soil that equaled the internal friction angle of the sand, thus minimizing the boundary effect.

An actuator was used to applied displacement to the wall. The actuator was capable of providing +/−6.0 to +/−60 mm displacement to the prototype. The initial stresses in the system were generated using an acceleration of 60 g.

The instrumentation was designed to capture the behavior of the structural elements and the soil. The force on the prototype wall and the bending moment on the prototype wall were recorded and calculated using a load cell and strain gages distributed on the wall. The wall movement was recorded using Linear Variable Differential Transducers (LVDTs). The surface deformations of the soil were also recorded using LVDTs. The deformation of the backfill was monitored through imaging.

Displacement amplitudes for serviceability, ultimate and extreme conditions were defined as +/−12 mm, +/−30 mm (with a deck rotation of +/−0.29°), and +/−60 mm (with a deck rotation of +/−0.58°), respectively. The tests were designed to capture the response of the bridge during its presumed lifetime of 120 years, as such each tests was run with run with 120 cycles. In addition, the tests were designed to include loose and dense fine dry sand as a backfill soil. As such, two tests were conducted with relative densities of 14% and 75%. Two tests were conducted for each of the displacement amplitudes; one with dense sand and the other with loose sand.

The recorded wall movement was decomposed into translational and rotational, and deflection caused by bending of the wall. When dense sand was used as backfill, the settlement was 420 mm adjacent to the wall and increasing up to 660 mm at a distance of 900 mm from the wall, then decreasing to 300 mm at a distance of 4500 mm from the wall; then tapering to the ground surface at about 5100 mm from the wall (zero settlement). Beyond the point of zero settlement, some heave was observed at about 8100 mm from the wall. With loose sand, a settlement of 720 mm was observed next to the wall, steadily decreasing to zero (no settlement) up to a distance of 9000 mm from the wall.

It was found that the lateral earth pressure coefficient measured behind the wall changed with depth, amplitude, and relative density, as follows: in terms of depth, it was observed that for both the loose and dense sand, the earth pressure coefficient was higher at a depth of 0.3 H than at 0.6 H, the lower earth pressure at 0.6 H is due to higher movement restriction from the backfill with depth. In terms of applied displacement amplitude, it was found that the passive earth pressure coefficient increased with the number of cycles, but reached a steady value after 20 cycles for the dense sand, and between 15 and 50 cycles for the loose sand, for all displacement amplitudes. For the cases with dense sand, the passive lateral earth pressure coefficient increased to about 1.3, 2.3, and 3.7 for the serviceability, ultimate and extreme conditions, respectively in the first 20 cycles, then approached the steady state. For the cases with loose sand, the passive lateral earth pressure increased to 1.5, 2.4, and about 4 for the serviceability, ultimate and extreme conditions, respectively, then approached steady state. In all tests, the active earth pressure coefficient was reached during the first cycles.

A.3.2.2 Tsang et al. (2002)

Tsang et al. (2002) used a testing apparatus to simulate rotational movement of an abutment wall. The apparatus consists of two major components; the hanger frame (outer frame), and the moving wall (inner frame). The wall height and width were 600 mm and 300 mm, respectively. The length of the outer frame was 1850 mm. The wall rotates about its base (around a hinge), the axis of rotation is at 50 mm from the bottom of the wall. The rotation was achieved by imposing a horizontal displacement at top of the wall. The tested backfill consisted of sand (no properties were reported for the sand). The sand specimen dimensions were 1140 mm long, 300 mm wide and 570 mm high. Two LVDTs were used to record the horizontal displacements at the top and bottom of the wall. Nine pressure transducers were used to record the earth pressure imposed by the soil to the wall; six were installed along the center of the wall at 75 mm depth intervals, two at 40 mm from the side at 150 mm and 375 mm from the top of the specimen, and one installed at 55 mm from the centerline at a depth of 375 mm. The tests consisted of applying displacement cycles to the top of the wall, allowing it to rotate about its base. Eleven tests were conducted varying the rotation amplitudes and the initial wall position, seven tests started with the wall at inclined position and four tests started with the wall at vertical position. In Tsang el al. (2002), only the results from one test were reported.

A test on sand with 300 cycles with +/−0.13% rotation was performed (equivalent to about +/−74 mm displacement of top of the wall). The results showed that the maximum passive earth pressure (about 4.5) occurred at the center of the wall and it was achieved after 200 cycles.

A.3.2.3 Xu et al. (2007)

A triaxial apparatus was modified to apply a controlled local cyclic radial strain to a soil specimen under a constant vertical stress (Cycles of loading/unloading in the radial direction). The purpose of the cyclic radial strain was to mimic the strain caused in the backfill due to abutment movement. The tested soils consisted of coarse granular soils and manufactured granular soils (glass ballotini). The coarse granular soil was Leighton Buzzard Fraction B Sand, with specific gravity 2.65 and maximum and minimum void ratios 0.768 and 0.510, respectively. The glass ballotini was made by smooth glass particles. The physical properties of the glass particles were G_s=2.5, e_{max}=0.674; specimens with e_{min}=0.515 were tested to investigate the effect of particle roughness. The specimens had a length to diameter ratio of 2:1, with a length of 200 mm. The instrumentation consisted of the internal load cell and submersible LVDTs to measure the axial and radial strains.

The test were conducted by first consolidating the samples under Ko condition (representing the state of stress at 4 m below the ground surface), then applying cyclic radial strains under drained conditions such that the specimen was subjected to loading in triaxial extension and unloading in triaxial compression. The amplitude of the radial strain was selected to represent the thermal loading on a 60 m bridge deck.

The results for the loose sand very dense sand, and the glass ballotini are presented in Table A.4, which summarizes the initial relative density, at rest earth pressure coefficient, initial void ratio, amplitude of applied cycles, no of cycles, maximum and minimum lateral earth pressure coefficient achieved during the tests, and the final relative density (at the end of the test).

In addition, it was observed that the drained tangent horizontal Young's modulus (varies with strain level) showed an increase with the number of cycles (more significant in the first 50 cycles) at the same strain level for the cases with loose and dense sand. The increase in stiffness at the same strain level was larger for the loose sand than for the dense sand.

For example, during the increase in radial strain (bridge expansion), in the case of loose sand, the tangent Young's modulus (at strain level=0.005%) increased from about 220 MPa to 340 MPa during the first 50 cycles. In the case of dense sand, tangent Young's modulus (at strain level=0.005%) increased from 680 MPa to 710 MPa during the first 50 cycles.

On the other hand, and during the decrease in radial strain (bridge contraction), the increase in tangent Young's modulus was less significant for both the loose and dense sand cases (for the case of loose sand the tangent Young's modulus at 0.005% strain level increased from about 185 MPa to 210 MPa during the first 50 cycles). For the case with Glass Ballotini there was no observed increase in stiffness with number of cycles.

The tangent Young's modulus response with strain level during the same cycle followed the typical hyperbolic response during the increase in radial strain and for all the soils tested. During the decrease in radial strain, the hyperbolic response was only observed in the tests with loose sand.

This increase in the tangent Young's modulus with number of cycles for the case of dense sand was attributed to the interlocking between the sand particles. In the case of loose sand, the increase the tangent Young's modulus with number of cycles was attributed to densification (contractive behavior) and interlocking of particles.

The effect of the interlocking between sand particles was investigated by testing the Glass Ballotini. The results showed that due to the lack of particle interlocking, the tangent stiffness was independent on the number of cycles.

Based on the observations from the tests conducted, it was recommended to use the full passive lateral earth pressure behind integral abutment walls. In addition, it was recommended to use dense sand as a backfill soil instead of loose sand that will exhibit contractive behavior, resulting in settlement.

A.4 PILES CAPACITY AND PERFORMANCE UNDER CYCLIC LOADING

The concerning issues for piles supporting integral abutments are the lateral displacement capacity before buckling while maintaining the axial load capacity, the piles orientation for noncircular piles (along weak or strong axis), depth of inflection point of the deformed shape of the piles, the effect of soil type and stiffness on the pile performance, and the effect of superstructure

TABLE A.4
Results of the Testing Program

Material	Dr (%)	K_o	e_o	Cycles Ampl. (%)	No. of Cycles	K_{max}	K_{min}	Dr (%) (Final)
Loose sand	18	0.5	0.72	0.05	120	1.7	0.2	31
				0.1	170	2.3	0.1	43
				0.25	60	2.8	0.1	48
Very dense sand	92	0.3	0.53	0.05	52	2.4	0.25	92
				0.1	250	4.8	0.2	90
Glass ballotini	76	0.5	0.55	0.05	15	1.4	0.35	

concrete shrinkage on the displacement demands of the piles. Dicleli and Albhaisi (2003) and Frosch et al. (2006) studied the displacement capacity against buckling. Frosch et al. (2006) studied the deterioration of the pile abutment connection and loss of capacity to withstand axial loads. The pile orientation of non-circular cross sections was studied by Dicleli and Albhaisi (2003) and Frosch et al. (2006). The depth of inflection point of the deformed shape and the effect of soil type and stiffness was studied by Frosch et al. (2006) and Arockiasamy et al. (2004). The effect of concrete shrinkage of the bridge superstructure was studied by Frosch and Lovell (2011). Other factors such as the depth of water table, the effect of predrilled holes were studied by Arockiasamy et al. (2004). Comparisons between simplified methods implemented in software such as LPILE and more complicated finite element analysis such as Abaqus were conducted by Khodair and Hassiotis (2005). To address the concerns with the performance of piles supporting integral abutments were addressed by researches either by combination of instrumentation data, large scale testing, analytical studies and parametric analysis, such as Dicleli and Albhaisi (2003), Frosch et al. (2006), and Frosch and Lovell (2011). Other studies just included numerical modeling and parametric studies such as Arockiasamy et al. (2004) and Khodair and Hassiotis (2005). In the numerical studies very general recommendations were given as guidelines for design and analysis of piles supporting integral abutments. Summaries of the studies conducted by Dicleli and Albhaisi (2003), Frosch et al. (2006), Arockiasamy et al. (2004) and Khodair and Hassiotis (2005) are presented in Sections A.4.1 through A.4.4.

A.4.1 Dicleli and Albhaisi (2003)

The purpose of Dicleli and Albhaisi (2003) study was to develop equations to estimate the lateral displacement capacity of steel H-Piles, which was then used to estimate the allowable maximum length of concrete and steel integral abutment bridges. In the study, the main issue was whether the slenderness ratio of H-piles allowed for plastic deformation before local buckling. If plastic deformations are allowed then larger lateral displacement capacity could be used for the piles when compared to the allowable lateral displacement capacity for piles without allowing plastic deformations. Two H-piles that satisfied the slenderness ratio, and thus allowed plastic strains before local buckling (HP250 × 85 and HP310 × 125), were selected for the parametric study. The study explored the effect of foundation soil stiffness, the effect of pile size and orientation and the connection between the pile and abutment.

The soil-pile interaction was examined by approximating the nonlinear relationship (hyperbolic) between lateral load (p) and lateral displacement (y) (p-y curve) with an elastic perfectly plastic relationship between p and y. The elastic modulus of the elastic perfectly p-y curve was selected as the secant modulus (at 50% strain) for clays and the initial modulus for sand. In the p-y approximation used in the study, plastic strains occur when the lateral load (p) reaches the ultimate soil resistance. The ultimate soil resistance was given as a function of the undrained shear strength for clays and as a function of active and at rest earth pressure, friction angle, unit weight, depth and surcharge loads for granular soils, as recommended by Haliburton (1971). The pile-soil system was modeled using the commercial finite element software SAP2000. The pile length was about 30 times the pile width. The soil was modeled using truss elements and the pile was modeled using beam elements. The selected parameters for cohesive (undrained shear strength and 50% strain) and granular soils (subgrade reaction constant, unit weight, and friction angle) presented in Table A.5.

The parametric study showed that for both granular and cohesive soils, the displacement capacity of H-piles decreased as the stiffness of the soil increased. For piles driven in sand the displacement capacity in loose sand was on average about 2.5 times the displacement capacity estimated in dense sands. In addition, it was found that the displacement capacity increased by increasing the pile's size. It was also found that a pinned connection between the pile and abutment would significantly enhance the pile's lateral displacement capacity by an approximately a factor of 3 to 4.

Based on the parametric analysis, the maximum length for concrete bridges in moderate climate (20°C variation in temperature) ranged between 320 m and 180 m for HP310 × 125 and HP200 × 63 piles, respectively. The maximum lengths were 265 m and 150 m for HP310 × 125 and HP200 × 63 piles, respectively, in cold weather (33°C variation in temperature).

A.4.2 Frosch et al. (2006)

Frosch et al. (2006) investigated the performance, in terms of buckling resistance, of integral abutment piles under lateral displacement by analyzing data from instrumented bridges, an experimental program, and a parametric study. Data was obtained from the following three instrumented bridges in Indiana: the SR 249 over US 12 bridge, the I-65 over SR 25 bridge, and the SR 18 over Mississinewa River. The analysis of the monitoring data was conducted using the commercially available software LPILE and SAP2000. However, due to insufficient deformation data recorded with pile depth at the SR 249 and I-65 bridges, the comparison between the analysis and the field data was done only for the SR 18 bridge.

The experimental testing program was conducted on steel H-Piles and concrete filled tube (CFT) piles. The piles' length was selected as 5 ft, based on their inflection point, as determined from a series of analysis using the L-Pile software. The purpose of the experimental program was to investigate pile behavior under lateral displacement. The setup of the experiments was based on the assumption that the pile supporting the bridge abutment behaves as a cantilever beam subjected to axial and lateral loads. The piles were tested as horizontal cantilevers (i.e., the axial load was in the horizontal direction and the lateral load in the vertical direction), the soil was ignored in the test setup. A total of nine (9) piles were tested; six (6) HP piles and three (3) concrete filled steel tube (CFT) piles. Tests on HP piles were done on (4) HP8 × 36,

TABLE A.5
Parameters for Cohesive and Granular Soils Used in Dicleli and Albhaisi (2003)

Soil	Cu (kPa)	ε_{50}	Subgrade constant, k (KN/m^3)	Unit Weight (KN/m^3)	ϕ (°)
Soft clay	20	0.02		NA	
Medium clay	40	0.01			
Medium-stiff clay	80	0.0065			
Stiff Clay	120	0.005			
Loose sand	NA		2000	16	30
Medium sand			6000	18	35
Medium-Dense sand			8000	19	37.5
Dense sand			12000	20	40

one (1) HP10 × 42, and one (1) HP12 × 53. Two of the HP8 × 36 piles were tested along their weak axis, one at 9 ksi of axial stress and the other at 18 ksi. One HP8 × 36 was tested along its strong axis at 9 ksi of axial stress, and one HP8 × 36 was tested at an angle of 45° from the web axis at 9 ksi of axial stress. Two of the CFT piles had 8 in. in diameter and one was 10 in. in diameter. One of the 8 in. CFT piles was tested at 9 ksi and the other at 18 ksi. The 10 in. CFT pile was tested at 9 ksi. It should be noted that in all the tests, no soil was included.

In each of the tests, the axial load was applied first, and then cyclic lateral displacements were applied. The lateral and axial loads were monitored during the test; failure was defined as either a drop in the axial or lateral load. The cycling was done as follows: first a 0.25 in. amplitude for 5 cycles; second a 0.5 in. magnitude for 10 cycles; third a 0.75 in. magnitude for 25 cycles. At amplitudes larger than 0.75 in., the steps consisted of 50 cycles. It was observed that for the 8in.-CFT piles, the buckling occurred at a lateral displacement of 1.75 in. with a corresponding lateral load of 13 kips. While the 10 in.-ft piles, the buckling occurred at a lateral displacement of 2.0 in. with a corresponding lateral load of 23 kips.

The parametric study was conducted using the LPILE software; the variables considered were the magnitude of the lateral displacement, axial load, pile length, pile type, pile orientation and soil type.

The analysis for lateral capacity of the piles of the SR 18 Bridge consisted of modeling of the abutment piles with LPILE and SAP2000. The piles at the SR 18 bridge were concrete filled tubes (CFT) with 14 in. in diameter and 0.312 steel tube wall thickness. The piles were driven and had a length of 23.5 ft. The subsurface condition at the SR 18 bridge site consisted of silt. According to the Frosch et al. (2006), since there are not recommended values in the literature for spring constants for Silt, two cases were analyzed; the first case with spring stiffness representing cohesive subsurface condition of stiff clay and the second case with spring stiffness representing medium sand. The abutment piles were modeled using LPILE and SAP2000. The difference between the LPILE models and SAP200 models is that in the LPILE analysis nonlinear springs to model the soil-structure interaction were used, while in the SAP2000 model linear springs to model the soil-structure interaction were used based on the initial stiffness of the soil.

The boundary conditions in the models consisted of rollers at the top of the pile and a hinge at the bottom of the pile. The axial load applied on top of the pile was 80 kips, with a lateral displacement of 0.38 in., which was equivalent to temperature changes of 60°F. The nonlinear springs used in LPILE were based on the p-y curves. For the case of the soil consisting of stiff clay, The P value remains constant at displacements larger than ($8y_{50}$), where y_{50} corresponds to the displacement at half of the ultimate soil reaction. The relationship for the p-y curve up to the yielding load is given according to Matlock (1970) as:

$$p = 0.5\left(\frac{y}{y_{50}}\right)^{\frac{1}{3}} p_u \tag{A.2}$$

Where,
p_u is the ultimate soil resistance, and is given according to Griemann (1987) as:

$$p_u(z) = \left\{ \begin{matrix} \left[3 + \frac{\gamma}{c_u} z + \frac{0.5}{B} z\right] c_u B, if\ p_u(z) < 9 c_u B \\ 9 c_u B \end{matrix} \right\} \tag{A.3}$$

Where,
γ is the soil unit weight,
c_u is the undrained shear strength,
B is the pile width,
z is the depth.

For the sand case, with the LPILE analysis, the ultimate load was assumed to occur at a displacement of 3B/80. The p-y curve was given by the following expression according to Reese at al. (1974):

$$p = Cy^{1/n} \tag{A.4}$$

Where,

$$C = \frac{y_m}{y_m^{1/n}} \tag{A.5}$$

$$y_m = B/60 \tag{A.6}$$

B is the pile width.

The ultimate load, for static loading, was estimated based on the soil strength as:

$$p_u = A_s P_s \tag{A.7}$$

Where,
A_s is a function of depth, with a value of 2.7 at the ground surface, decreasing with depth to a value of 0.88 at depths larger than five times the pile width.

P_s is calculated to be the lower from the following two equations:

$$P_s = \gamma z \left[\frac{k_o z tan\varphi sin\beta}{\tan(\beta - \varphi) cosa} + \frac{tan\beta}{\tan(\beta - \varphi} (B + z tan\beta tan\alpha) \right.$$
$$\left. + k_o z tan\beta (tan\varphi sin\beta - tan\alpha) - k_A B \right] \tag{A.8}$$

Or:

$$P_s = k_A B \gamma z \left(tan^8 \beta - 1 \right) + k_o B \gamma z tan\varphi tan^4 \beta \tag{A.9}$$

Where,
φ *is the soil angle of friction*
$\alpha = 0.5\varphi$
$\beta = 45^\circ + 0.5\varphi$
$k_o = 0.4$ (coefficient of active eartjh pressure)
$k_A = tan^2(45^\circ - 0.5\varphi)$ (coefficient of active eartjh pressure)
γ *is the soil unit weight*
z is the depth below ground surface

The analysis showed that both LPILE and SAP2000 gave comparable results for the two soil profiles. However, when the deformation shapes obtained from the numerical analysis compared with the monitoring data, the analysis results showed a slight underestimation of the deflections of the pile with depth. The inflection point from both analyses was at about 5 ft below the ground surface, which was in general agreement with the monitoring data. The calculated moments from strain gages along the pile depth were about 50% lower than estimated LPILE and SAP2000 at the ground surface; this was attributed to possible softening of the soil and the pile-abutment connection due to the formation of cracks.

Additional analyses were conducted based on the monitoring data and the previously calibrated LPILE models to estimate the lateral displacement capacity of additional pile sizes that were used by INDOT. It was found that for 7.1 ft long CFT piles in medium sand with 14 in. diameter and 0.312 in. of tube wall thickness, the lateral displacement capacity was about 2.42 in. In a stiff clay profile, the lateral load capacity increased to about 2.9 in. for a pile length of 7.6 ft. For the same pile diameter and when the wall thickness decreased to 0.203 in., the lateral displacement capacity decreased to about 2.2 in. when the pile was on sand and to about 2.6 in. on clay.

Based on the analysis, it was concluded that an integral abutment bridge, either with concrete or steel superstructure, could be constructed with a length of up to 500 ft with a temperature range of 60°F between summer and winter.

A.4.3 Arockiasamy et al. (2004)

In their state-of-the art paper the authors stated that there was not a unified procedure for the design and construction of integral abutment bridges. A parametric study was conducted to identify the effect of pre-drilled holes, water table elevation, soil type, and pile orientation on the performance of the integral abutment piles under lateral loading. LPILE and FB-Pier were used for the parametric study. A total of eleven (11) cases were analyzed for the study. Based on the parametric analysis, it was found that the displacement of the piles in pre-drilled holes was smaller than without pre-drilled holes; there was a slight increase of the shear stresses at top of the pile for the case of pre-drilled holes. The piles with pre-drilled holes are more fixable; however, they require a longer pile to the point of fixity. The depth of the water table did not have any significant effect on the response of the piles. For driven piles, soil type had a significant effect on the performance of the loaded piles, given that piles in stiff soils developed higher moments when compared to piles driven in a multi-layer soil profile. Also, it was observed that the denser the foundation soil, the lower the moments developed. In addition, the authors recommended the use of the piles along their weak axis.

A.4.4 Khodair and Hassiotis (2005)

The authors used Abaqus to model pile-soil interaction in 3D. The model consisted of a single HP pile embedded in a sand layer connected to an abutment wall. A tie constraint was imposed between the pile and the abutment wall. The penalty friction algorithm was imposed to simulate friction between the pile and the sand. A single loading step consisting of a 0.023 m horizontal displacement was imposed to the top of the pile to simulate the expansion of a bridge induced by a change in temperature of 42°. The pile was modeled as elastic perfectly plastic and the soil was modeled as strain-hardening with the Mohr-Coulomb failure criterion. The parameters used in the model (soil friction angle, elastic modulus for soil and steel pile, and the yield stress of steel pile) are summarized in Table A.6.

The model was verified by results from two pile loading tests. In addition, the results from the Finite Element Model were compared with L-Pile results under the same imposed displacement and for the same input properties. The results showed a reasonable match between the L-Pile code and the finite element model. It was concluded that strain-hardening with the Mohr-Coulomb failure criterion was sufficient to capture the pile behavior under lateral loading.

A.5 DISCUSSION OF THE EARTH PRESSURE AND PILES PERFORMANCE FROM THE LITERATURE REVIEW

The literature review on observations and findings on the lateral earth pressure behind integral abutments yields somewhat different conclusions and recommendations. For example Sandford and Elgaaly (1994) recommended using for abutment design the full passive earth pressure behind the obtuse corner and full active pressure behind the acute corner. This recommendation was based entirely on earth pressures recorded behind a skewed bridge at the obtuse and acute corners, without considering the earth pressures at the centerline of the abutment. However, Hassiotis (2007) and Hassiotis and Xiong (2007) showed that high lateral earth pressures (higher than at the centerline of the abutment) were still anticipated at the acute corner but lower than what was observed at the obtuse corner of the abutment, which contradicts Sandford and Elgaaly (1994) recommendation of using active earth pressure behind the acute corner. The reason for such wide range of observations is the difficulty to control the boundary conditions of a monitored bridge (e.g., shallow versus deep foundations). For example, the restrained of the movement is larger when deep foundations are used which will results in lower earth pressure towards the bottom of the abutment, also the type of foundation has significant effect on the anticipated rotation of the bridge deck and abutment (in the horizontal plane), which will result in different displacements at the acute and obtuse corners. It is also difficult to control the type of foundation soils and the compaction of the backfill, which will have an effect on restraining the movement of the bridge deck and abutment resulting in different earth pressures.

TABLE A.6
Sand Parameters Used in the Finite Element Analysis by Khodair and Hassiotis (2005)

Material	$\phi(^\circ)$	E (KPa)	σ_y(KPa)
Loose sand	30	27000	NA
Dense sand	38	69000	NA
Steel pile	NA	2×10^8	344750
Concrete abutment	NA	2.86×10^7	NA

There are also contradictions in the number of cycles required to reach a constant lateral earth pressure. For example, Ng et al. (1998) used a centrifuge to simulate the abutment movements, and concluded that steady state was reached after 20 cycles for dense sand and after 50 cycles for loose sand. However, Xu et al. (2007) based triaxial tests on sand, concluded that reaching a constant earth pressure (i.e., steady state) depended on the displacement amplitude, and on the relative density of the sand. Further differences are found with the work of Ng et al. (1998) on sand, who concluded that at cyclic strain amplitude of 0.1%, the number of cycles to reach steady state was 170 for loose sand and 250 for very dense sand, which were needed to overcome the interlocking of particles and not only for soil densification. The differences between Ng et al. (1998) and Xu et al. (2007) could be attributed to the different scales of both tests and the level of confining stress. Xu et al. (2007) applied confining stress equivalent to what is expected at the mid height of an 8 m abutment wall, while Ng et al. (1998) used the centrifuge to initiate the state of stresses acting on the full height of an integral abutment, with monitoring locations in the upper and lower third of the abutment wall height, as such the monitoring locations were different. In addition, in Xu et al. (2007) study, the movement of an abutment wall was simulated in terms of radial strains, which indicates only translational movements. On the other hand Ng et al. (1998) study allowed for both translational and rotational movements, which will lead to a different earth pressure response.

However, all the studies showed that a passive lateral earth pressure coefficient between 3 and 5 could be reach at the obtuse corner of the abutment, however, the distribution of the earth pressure behind the abutment wall varied between different studies. In addition, it was agreed among all studies that earth pressure will reach steady states after specific number of cycles; the discrepancy was on the number of cycles to achieve the steady state. The effect of the initial relative density on the developed earth pressure was agreed on between different studies. The studies showed that loose backfill will require larger number of cycles to stabilize and it will stabilize at slightly higher lateral passive earth pressure coefficient (e.g., when compared with dense sand).

The objective of the work reviewed regarding the performance of integral abutment piles is to understand the behavior of the piles under low frequency large amplitude cyclic lateral displacement. As discussed in Section A.4, the issues that need to be addressed to evaluate the performance of integral abutment supporting piles are:

1. The lateral displacement capacity before buckling while maintaining the axial load capacity.
2. The piles orientation for noncircular piles (along weak or strong axis).

3. Depth of inflection point of the deformed shape of the piles.
4. The effect of soil type and stiffness on the pile performance.
5. The effect of superstructure concrete shrinkage on the displacement demands of the piles.

In general the studies followed two paths to address the above mentioned issues:

1. Establish displacement criteria, based on a combination of experimental and numerical studies, for acceptable pile performance in terms of withstanding buckling failure and deterioration of the pile-abutment connection and estimated based on such criteria the acceptable bridge length (Arsoy et al., 1999; Dicleli & Albhaisi, 2003; Frosch et al., 2006; Thomson, 1999).
2. Conduct numerical studies, without experimental verification/supporting data to establish general design guidelines (Arockiasamy et al., 2004; Khodair & Hassiotis, 2005; Ooi et al., 2010; Wood & Nash, 2000).

The first category includes those cases where tests were performed in the laboratory, full scale bridges were monitored and the data analyzed, and parametric studies were done using numerical models, calibrated using the laboratory and/or the field data. Results from these cases also provide discrepancies. For example, Dicleli and Albhaisi (2003) recommended maximum bridge lengths not to exceed 1000 ft, while Frosch et al. (2006) recommended a maximum bridge length of 500 ft, both for a temperature variation of about 68°F. The discrepancy is mainly due to the type and size of piles used in the analysis and on the assumption of the behavior of the springs used to represent soil behavior, and how the spring/soil stiffness was estimated.

The other category of numerical studies is only useful to understand the general behavior without significant addition to design guidelines or analyses methods. The lack of significant addition to the guidelines is due to the use of general parameters without supporting experimental program.

All of the reviewed studies on the integral abutment supporting piles performance agreed on the advantage of orienting the piles along their weak axis. In addition, the reviewed studies showed that the piles loaded laterally are capable of maintaining their axial load capacity until buckling, then a reduction in the axial load capacity is observed. The significance of softening of the soil (nonlinear behavior) close to the pile abutment connection and degradation of the stiffness of the pile abutment connection on the performance of integral abutment supporting piles was not studied sufficiently. Also, the depth of inflection point and the effect of soil type on inflection point location were not addressed sufficiently.

A.6 REFERENCES

Arockiasamy, M., Butrieng, N., & Sivakumar, M. (2004). State-of-the art of integral abutment bridge. *Journal of Bridge Engineering*, *9*(5), 497–506.

Arsoy, S., Barker, R. M., & Duncan, J. M. (1999). *The behavior of integral abutment bridges* (Publication No. FHWA/VTRC 00-CR3). Charlottesville, VA: Virgina Transportation Research Council.

Bonczar, C., Civjan, S., Breña, S., & DeJong, J. (2005). *Behavior of integral abutment bridges: Field data and computer model* (Massachusetts Transportation Research Program, SPRII.03.20). Boston, MA: Massachusetts Department of Transportation.

Civjan, S. A., Bonczar, C., Breña, S., F., DeJong, J., & Crovo, D. (2007). Integral abutment bridge behavior: Parametric analysis of a Massachusetts bridge. *Journal of Bridge Engineering*, *12*(1), 64–71.

Clayton, C. R. I., Xu, M., & Bloodworth, A. (2006). A laboratory study of the development of earth pressure behind integral bride abutments. *Géotechnique*, *56*(8), 561–571.

Cosgrove, E. F., & Lehane, B. M. (2003). Cyclic loading of loose backfill placed adjacent to integral bridge abutment. *International Journal of Physical Modelling in Geotechnics*, *3*, 9–16.

Dicleli, M., & Albhaisi, S. (2004). Effect of cyclic thermal loading on the performance of steel H-piles in integral bridges with stub-abutments. *Journal of Constructional Steel Research*, *60*, 161–182.

Frosch, R. J., Albhaisi, S, Albhaisi, S & Lovell, M. D. (2011). *Long-term behavior of integral abutment bridges* (Joint Transportation Research Program Publication No. FHWA/IN/JTRP-2011/16). West Lafayette, IN: Purdue University. http://dx.doi.org/10.5703/12882843146

Frosch, R. J., Chovichien, V., Durbin, K., & Fedroff, D. (2006). *Jointless and smoother bridges: Behavior and design of piles* (Joint Transportation Research Program Publication No. FHWA/IN/JTRP-2004/24). West Lafayette, IN: Purdue University. http://dx.doi.org/10.5703/1288284313379

Frosch, R. J., Kreger, M. E., & Talbott, A. M. (2009). *Earthquake resistance of integral abutment bridges* (Joint Transportation Research Program Publication No. FHWA/IN/JTRP-2008/11). West Lafayette, IN: Purdue University. http://dx.doi.org/10.5703/1288284313448

Frosch, R., Wenning, M., & Chovichien, V. (2005). The in-service behavior of integral abutment bridges: Abutment-pile response. In *Proceedings of the 2005 FHWA Conference on Integral Abutment and Jointless Bridges* (pp. 30–40).

Hassiotis, S. (2007). Data gathering and design details of integral abutment bridge. In *18th Engineering Mechanics Division Conference (EMD2007),* Retrieved from http://www.utrc2.org/sites/default/files/pubs/journal-article-abutment-bridge_0.pdf

Hassiotis, S., & Xiong, K. (2007). *Deformation of cohesionless fill due to cyclic loading* (Stevens Institute of Technology Publication No. SPR ID# C-05-03). Hoboken, NJ: Federal Highway Administration, U.S. Department of Transportation, New York State Department of Transportation, University Transportation Research Center.

Khodair, Y. A., & Hassiotis, S. (2005). Analysis of soil–pile interaction in integral abutment. *Computers and Geotechnics*, *32*, 201–209.

Kunin, J., & Alampalli, S. (1999). *Integral abutment bridges: Current practice in the United States and Canada* (Special Report 132, Transportation Research and Development Bureau). Albany, NY: New York State Department of Transportation.

Ng, C. W. W., Springman, S. M., & Norrish, A. R. M. (1998). Centrifuge modelling of spread-base integral bridge abutments. *Journal of Geotechnical and Geoenvironmental Engineering*, *124*(5), 376–388.

Ooi, P. S. K., Lin, X., & Hamada, H. S. (2010). Numerical study of an integral abutment bridge supported on drilled shafts. *Journal of Bridge Engineering*, *15*(1), 19–31.

Sandford, T. C., & Elgaaly, M. (1994). Skew effects on backfill pressures at frame bridge abutments. *Transportation Research Record*, *1415*, 1–11.

Thomson, T. A. (1999). *Passive earth pressure behind integral bridge abutment* (Unpublished doctoral dissertation). Amherst: University of Massachusetts Amherst.

Tsang, N. C. M., England, G. L., & Dunstan, T. (2002). Soil/structure interaction of integral bridge with full height abutments. *Proceedings of the 15th ASCE Engineering Mechanics Conference*. New York, NY: Columbia University.

Wood, D. M., & Nash, D. (2000). Earth pressures on an integral bridge abutment: A numerical case study. *Journal of the Japanese Geotechnical Society of Soils and Foundations*, *40*(6), 23–38.

Xu, M., Clayton, C. R. I., & Bloodworth, A. G. (2007). The earth pressure behind full-height frame integral abutments supporting granular fill. *Canadian Geotechnical Journal*, *44*, 284–298.

APPENDIX B. FIELD TESTING

B.1 INTRODUCTION

This chapter presents and documents the results of a large scale test of an integral abutment bridge. The bridge was constructed at Bowen Laboratory at Purdue University. The purpose of the study was to evaluate the effect of a large skew angle on the bridge's movement generated by thermal expansion and contraction of the bridge's superstructure, and hence the effect of such movement on the demands on the piles supporting the abutment and on the lateral earth pressure of the backfill soils.

The large scale bridge was constructed and instrumented as part of a previous JTRP study (SPR-3223) by Frosch and Lovell (2011). The bridge dimensions and configuration was a quarter scale of the SR 18 bridge over the Mississinewa River, except for a higher skew angle. The bridge configuration was designed to allow displacement application at the middle of the bridge deck simulating expansion and contraction loading cycles. The bridge dimensions and piles configuration are presented in Section B.2.

Instrumentation was designed to capture the bridge's translational displacement and rotation by monitoring the longitudinal and transverse directions at each corner, the load associated with each cycle, the deflection shape of the piles, and the lateral earth pressure in the backfill (for cases where backfill included). The instrumentation is discussed in Section B.3.

Three tests were conducted for this study. The first test was conducted with no backfill soil behind the abutment walls while the other two tests were conducted with a granular backfill behind the walls during cold and hot weather to capture the effect of temperature on the backfill response. Details of the tests are included in Section B.4.

The test results illustrate the movement of the deck at each corner, the loading applied to generate the required displacement, the deformed shape of two piles, and the lateral soil pressures behind the integral bridge abutment. The results of the tests are presented for the case with no backfill and the two cases with backfill in Sections B.5, B.6 and B.7, respectively. The results are discussed in Section B.8, and the conclusions are presented in Section B.9.

B.2 BRIDGE GEOMETRY AND SUBSURFACE CONDITIONS

The bridge was designed as a quarter scale of the SR 18 bridge. The bridge is a single span bridge with a total length of 28′-4.5″. The bridge has a 4′-6″ gap in the center of the deck for displacement application. The bridge width is 12′-6″ and has a 45° skew. The bridge deck is supported on three 12 in. deep girders. The gap is bridged at the deck level through W14 × 68 steel beams. The bridge abutments are supported by five concrete filled steel shell piles (6 in. outer diameter with 0.25 in. thickness) at each abutment. The piles were driven into the ground and subsequently filled with concrete. Figure B.1 shows a schematic of the bridge and the bridge dimensions. Figure B.2 provides a detail of the steel beams that bridge the gap (transfer beams). The steel beams were coated with Teflon during construction of the bridge. After conducting the test with no backfill, high friction was observed at the transfer beams; as a result, additional Teflon sheets were installed at the beams to reduce friction for the other two tests. Figure B.3 illustrates the location of the piles in the abutments and includes their length.

There was no geotechnical investigation program conducted for the bridge site. Subsurface conditions were established at the site based on the borings that were drilled for the Bowen Laboratory in 2002 by Alt & Witzig Engineering, Inc (Borings B-4 and B-7). The subsurface conditions consist of an upper layer of medium dense to dense sand, down to an approximately depth of 20 ft. The blow counts are about 25 blows/ft. The sand layer is inter-bedded with silty clay and silt layers in Boring B-4. The sand layer is underlain by medium compact silt down to an approximate depth of 42 ft; the blow counts are of the order of 30 blows/ft. A very compact silt layer (blow counts larger than 50) was encountered below the medium compact silt down to the explored depth of 51 ft. The water table was encountered in Boring B-7 at a depth of about 9 ft.

B.3 BRIDGE INSTRUMENTATION

Instrumentation was installed to monitor displacements, applied pressure to the hydraulic actuators, pile deformation, lateral earth pressure on the abutments, and backfill settlements.

The displacements of bridge deck corners were recorded using strain gauge-based potentiometers (UniMeasure Model PA-10-DS and PA-25-DS). Four potentiometers were installed at the four outer corners to monitor the longitudinal and transverse displacements at the deck and as close as possible to the ground level. Transverse displacements at the west gap corners were monitored at the deck level. The applied displacement at the east and west gaps were monitored at the deck level with two potentiometers. The monitoring locations are shown in Figure B.4. It should be noted that the locations of the potentiometer shown on the figure are approximate.

Displacements were also monitored using conventional survey techniques by total station. The displacements of all corners were surveyed as Easting and Northing coordinates at the end of each displacement increment during the test with no backfill. For the other two tests only the initial and final coordinates of the corners were surveyed. The results showed good agreement with the potentiometers data. The survey was conducted by BCM 412 students (fall 2010) under the supervision of Professor Crawford Wesley of the Geomatics Engineering program at Purdue University.

The applied pressures to the hydraulic actuators used to induce opening or closing displacements to the gap were monitored by strain gauge-based pressure transducers (Omegadyne Inc. Model Number: PX409). Two pressure transducers were used at each hydraulic pump; one for the expansion phase and the other for the contraction phase.

The deformed shape of the piles was recorded by an accelerometer-based rope gauge (Microelectromechanical Systems, Measurand Model: SAAF). Four records of the deformed pile shape were recorded during each loading-unloading cycle. Figure B.5 shows the location of the monitored piles.

The lateral earth pressure behind the abutment walls was recorded by vibrating wire pressure cells (Geokon 4810 Model). The pressure cells were installed at the abutment wall against the backfill. The locations of the earth pressure cells are shown in Figure B.6.

B.4 TESTS DESCRIPTION

Three tests were completed. One without backfill on November 2, 2010 and the other two with a granular structural backfill behind the abutment walls on December 9, 2010 and June 8, 2011.

The backfill was placed in 18-in. layers and was compacted using a plate compactor. No field density tests were conducted during the fill placement. The backfill soils were classified according to Indiana Department of Transportation (INDOT) system as #4 Structure Backfill Sand. The grain size distribution was provided by the supplier (Vulcan Materials Company) and is presented in Figure B.7.

The backfill geometry was not surveyed; the initial measurements of the backfill geometry were measured with a measuring tape. The backfill width was on the order of 2.5 ft close to the bridge deck level then sloping at 2:1 to the existing grade. The geometry of the backfill is shown Figure B.8.

Each test consisted of applying a displacement at the gap and recording the displacements of the bridge corners, the pressure applied to the hydraulic actuators, and the deformation shapes of the piles. The displacement at the gap was applied in steps, each with a different maximum magnitude, and consisted of cycles of opening and closing, which mimic thermal expansion and contraction of the bridge superstructure.

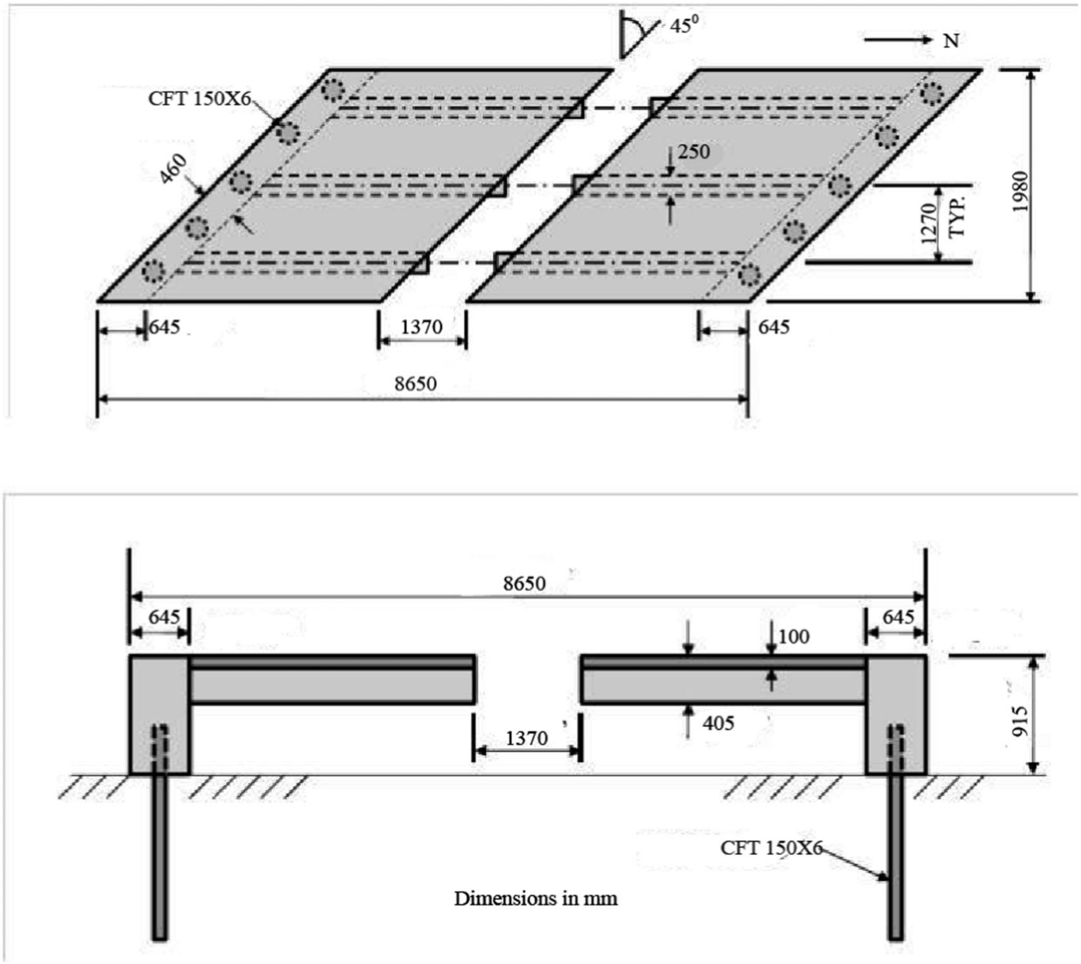

Figure B.1 Quarter scale bridge dimensions. (After Frosch and Lovell, 2011.)

Table B.1 shows the amplitude of each cycle.

During testing, displacements from all potentiometers were continuously recorded. Measurements such as the survey (for the test with no backfill only), deformed shape of the piles, and lateral earth pressures (when applicable) were taken at two instances during each cycle, (maximum amplitude and zero gap displacement).

The sign convention for displacements used throughout this report is positive for gap opening, inward longitudinal displacement at the corners, and counter clockwise for rotational movements. The test setup is shown in Figure B.9.

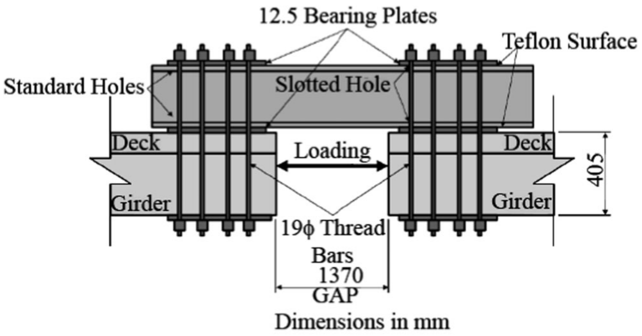

Figure B.2 Transfer beam configuration. (After Frosch and Lovell, 2011.)

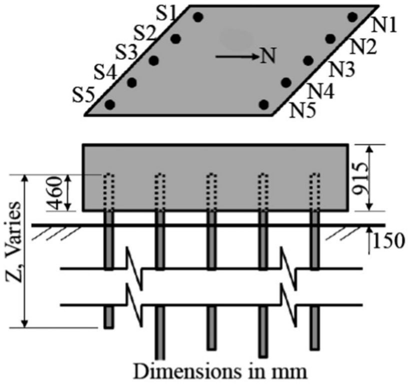

Figure B.3 Piles configuration and depth. (After Frosch and Lovell, 2011.)

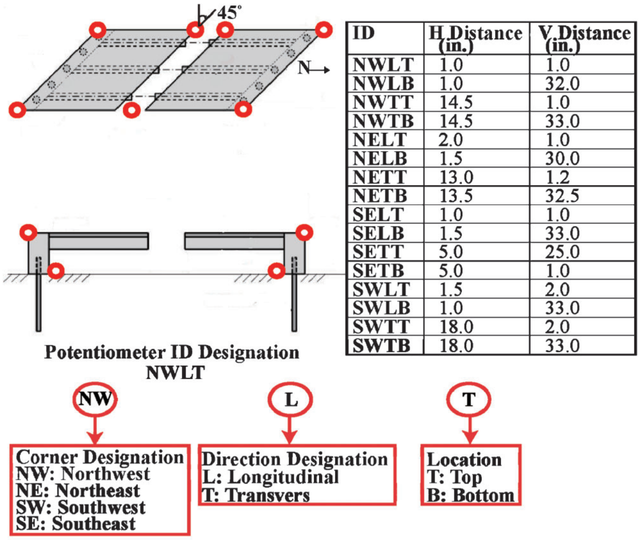

ID	H Distance (in.)	V Distance (in.)
NWLT	1.0	1.0
NWLB	1.0	32.0
NWTT	14.5	1.0
NWTB	14.5	33.0
NELT	2.0	1.0
NELB	1.5	30.0
NETT	13.0	1.2
NETB	13.5	32.5
SELT	1.0	1.0
SELB	1.5	33.0
SETT	5.0	25.0
SETB	5.0	1.0
SWLT	1.5	2.0
SWLB	1.0	33.0
SWTT	18.0	2.0
SWTB	18.0	33.0

Corner Designation
NW: Northwest
NE: Northeast
SW: Southwest
SE: Southeast

Direction Designation
L: Longitudinal
T: Transvers

Location
T: Top
B: Bottom

Figure B.4 Bridge displacement monitoring locations with potentiometers.

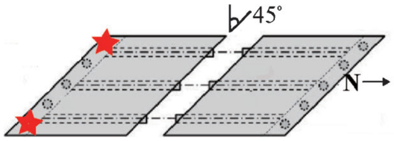

Figure B.5 Location of monitored piles.

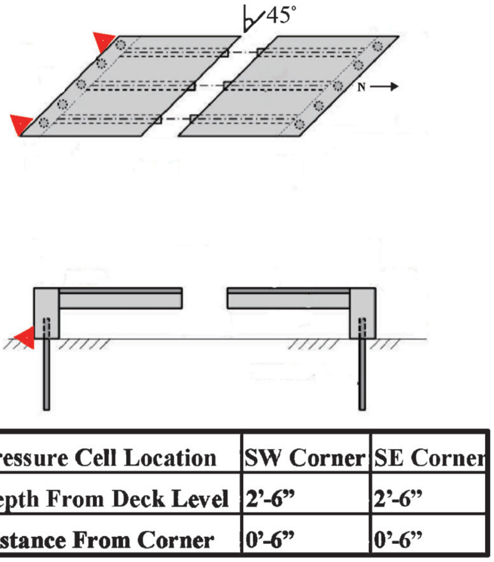

Pressure Cell Location	SW Corner	SE Corner
Depth From Deck Level	2’-6”	2’-6”
Distance From Corner	0’-6”	0’-6”

Figure B.6 Locations of the earth pressure cells.

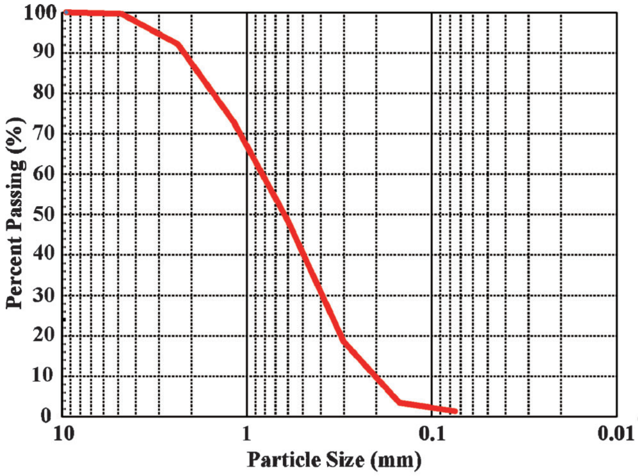

Figure B.7 Grain size distribution curve for the backfill soil (provided by Vulcan Materials Company).


a- North Side
b- South Side

Figure B.8 Photos of the backfill behind the abutments.

TABLE B.1
Amplitude of Each Displacement Cycle

No Backfill		With Backfill		With Backfill	
Cycle	Amplitude (in.)*	Cycle	Amplitude (in.)*	Cycle	Amplitude (in.)*
1	+/−0.25	1	+/−0.5	1	+/−0.5
2	+/−0.5	2	+/−1.0	2	+/−1.0
3	+/−0.75	3	+/−1.5	3	+/−1.5
4	+/−1.0	4	+/−2.0	4	+/−2.0
5	+/−1.5	5	+/−2.0	5	+/−2.0
6	+/−2.0			6	+/−2.5
7	+/−2.5			7	+3.0

*Displacement amplitude measured at the gap.

Figure B.9 Tests setup.

B.5 TEST RESULTS FOR THE BRIDGE WITH NO BACKFILL (TEST 1)

B.5.1 Rigid Body Movement

To examine the accuracy of the recorded data, displacements at each corner of the bridge deck were compared using measurements from the survey, potentiometers, and inclinometers. As mentioned in Section B.4, these are the measurements taken at the maximum gap amplitude and at the zero gap amplitude. Figure B.10 presents the comparisons.

It should be noted that the reported displacements from the survey were based on Northing and Easting measurements. However, the bridge is oriented approximately seven degrees (7°) from the true north. As such, the survey data was corrected to reflect the actual longitudinal and transverse displacement at each corner. It should be also noted that the monitoring locations at each corner for each of the measurement techniques were not identical (a maximum of 18 in. separated them; see the table in Figure B.4). Considering the applied displacement and the skew angle, the bridge undergoes rotational movement. Because the potentiometer and the survey monitoring locations are slightly different at each corner, the distance between the monitoring points and the axis of rotation are not the same. These differences result in a small deviation between the survey and potentiometer readings.

Even though there were slight differences, Figure B.10 indicates that the measurements from the three different sources were consistent. Because the data from the potentiometers is continuous, it is the standard measurement use to estimate longitudinal, transverse, and rotational movements of the bridge deck.

The hysteresis loops for the longitudinal movement from the potentiometers at the bridge deck versus the gap opening and closing are shown in Figure B.11. It is observed that the hysteresis is insignificant and the response is essentially linear.

The potentiometer displacements at the end of each cycle are plotted in Figure B.12 for each of the opposite corners for both the longitudinal and transverse directions. It was anticipated that the opposite corners will have the same displacement because of anti-symmetry. However, the plots for the longitudinal movements show an increasing difference in amplitude between opposite corners during the contraction phase. During the last test with backfill, hairline cracks were observed during the 2.5 in. contraction loading. The cracks extended from the bottom of the girders to the deck and were more obvious on the east side of the bridge. The cracks tended to close during the expansion cycle. The formation of these cracks is a possible explanation of the deviation of the measurements from symmetry.

To understand the bridge response, rigid body movement was estimated by utilizing three of the recoded potentio-

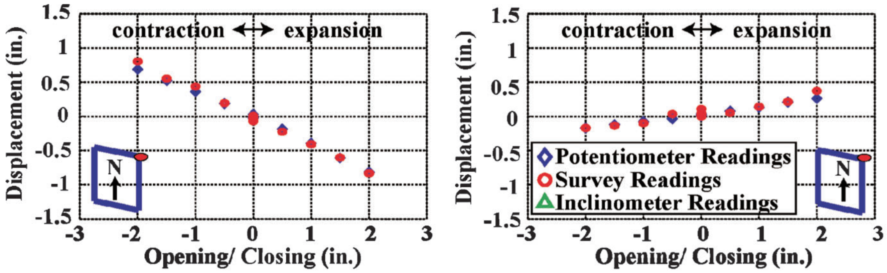

a- NE Corner (Long.)

b- NE Corner (Tran.)

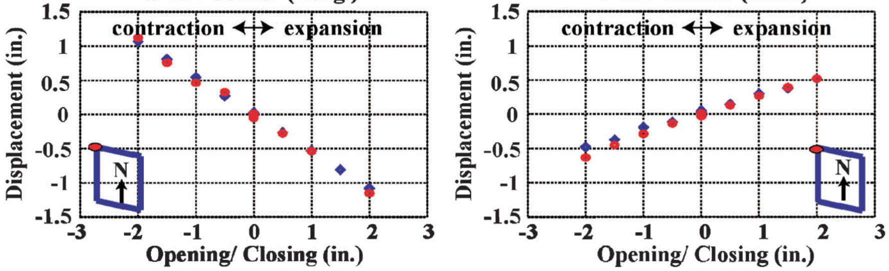

c- NW Corner (Long.)

d- NW Corner (Tran.)

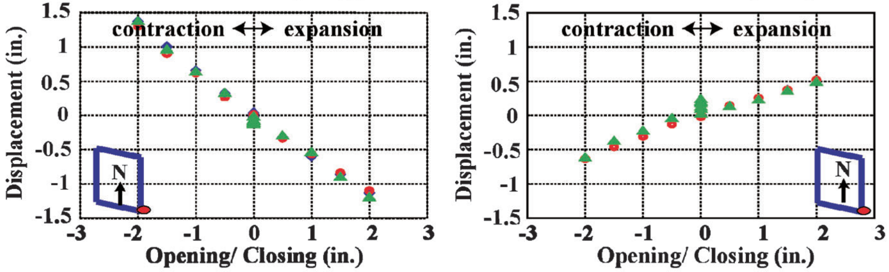

e- SE Corner (Long.)

f- SE Corner (Tran.)

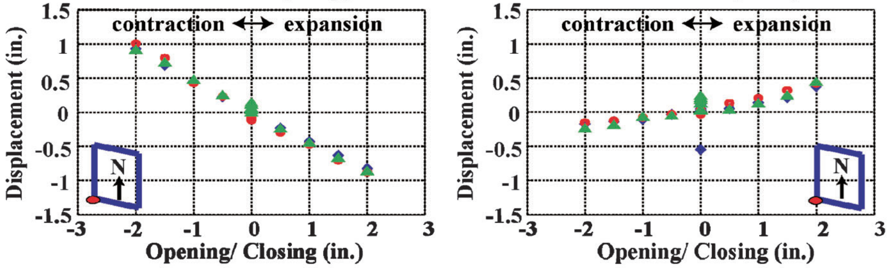

g- SW Corner (Long.)

h- SW Corner (Tran.)

Figure B.10 Comparison of displacements at the deck corners obtained from survey, potentiometers and inclinometers.

meter measurements. The rigid body movement refers to the longitudinal, transverse, and rotational responses of the center of the deck at the north and south halves of the bridge. Different monitoring point combinations were used, and the results of the estimates are shown in Figures B.13 and B.14 for the north and south sides, respectively.

It should be noted that the different symbols and colors in the plots represent different monitoring point combinations. In all cases, monitoring points at the deck level were used to estimate the rigid body movements. As one can see, the scatter of the transverse rigid body movements is larger than the longitudinal movements. This difference is attributed to the smaller transverse deformations; that is, small errors of small values result in relatively large scatter.

Average values of the estimated movement from different combinations were used to estimate the movement of each half of the bridge, and a polynomial curve was used to fit the data. The polynomial curve provided a better fit based on the tests with backfill, as will be discussed in the following sections. It should be noted that the magnitude of the rigid body movement is a function of the skew angle. Hence, the curve fitting equations are only valid for the bridge configuration tested. The average rigid body movements and the associated polynomial fit are shown in Figures B.15 and B.16 for the north and south sides, respectively.

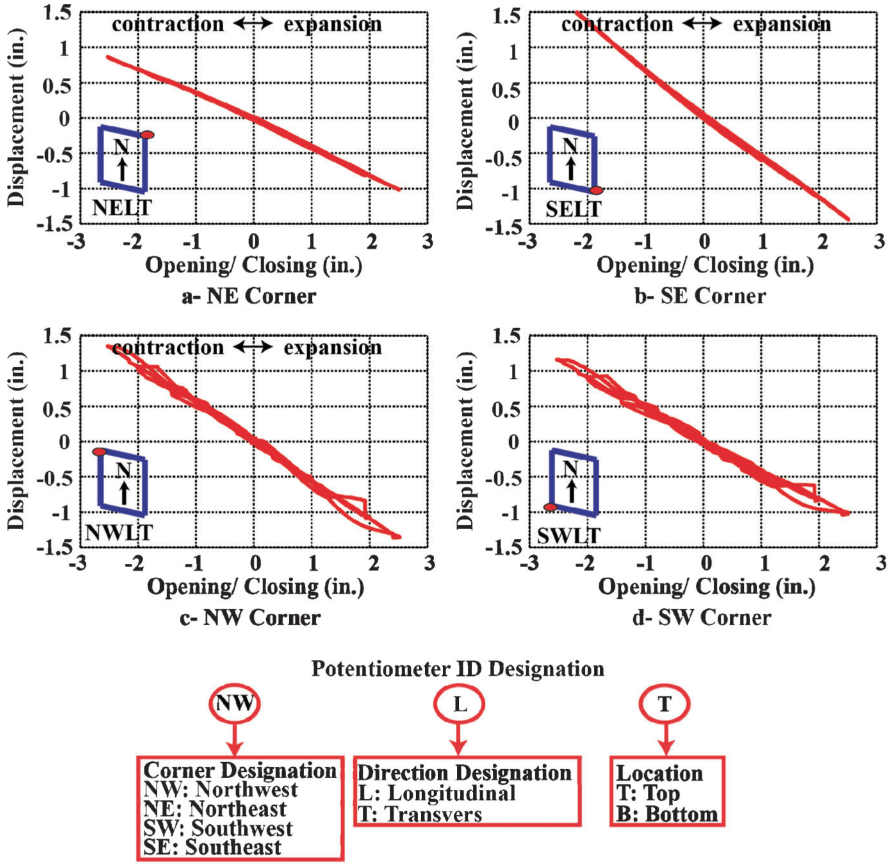

Figure B.11 Hysteresis plots of longitudinal movement at the bridge deck.

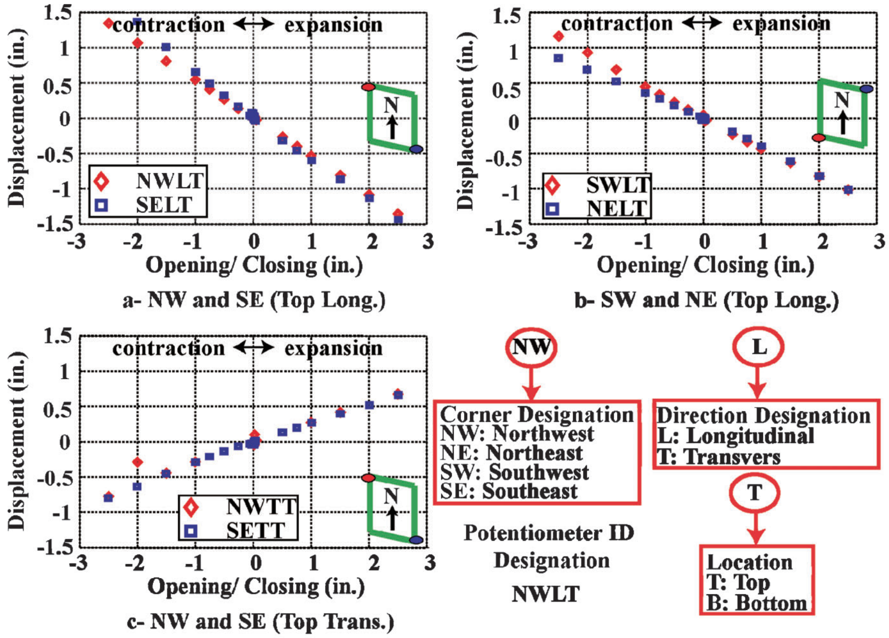

Figure B.12 Comparison of the potentiometer measurements at opposite corners.

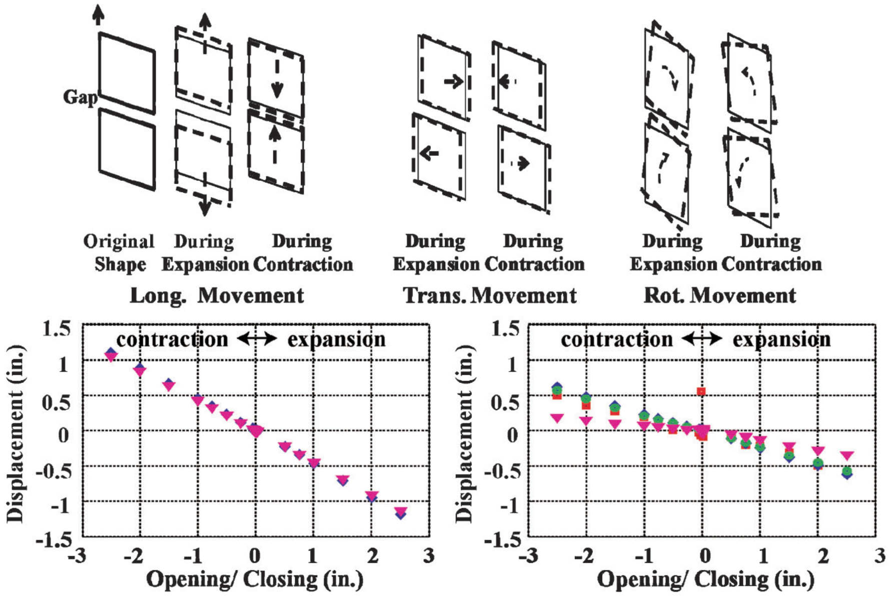

a- Longitudinal Movement

b- Transverse Movement

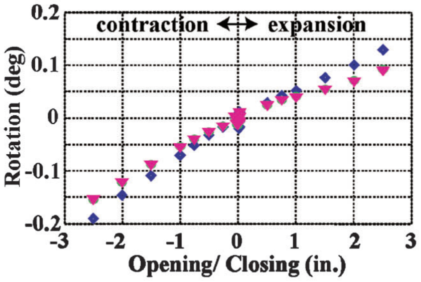

c- Rotational Movement

Figure B.13 Rigid body movements of the north side.

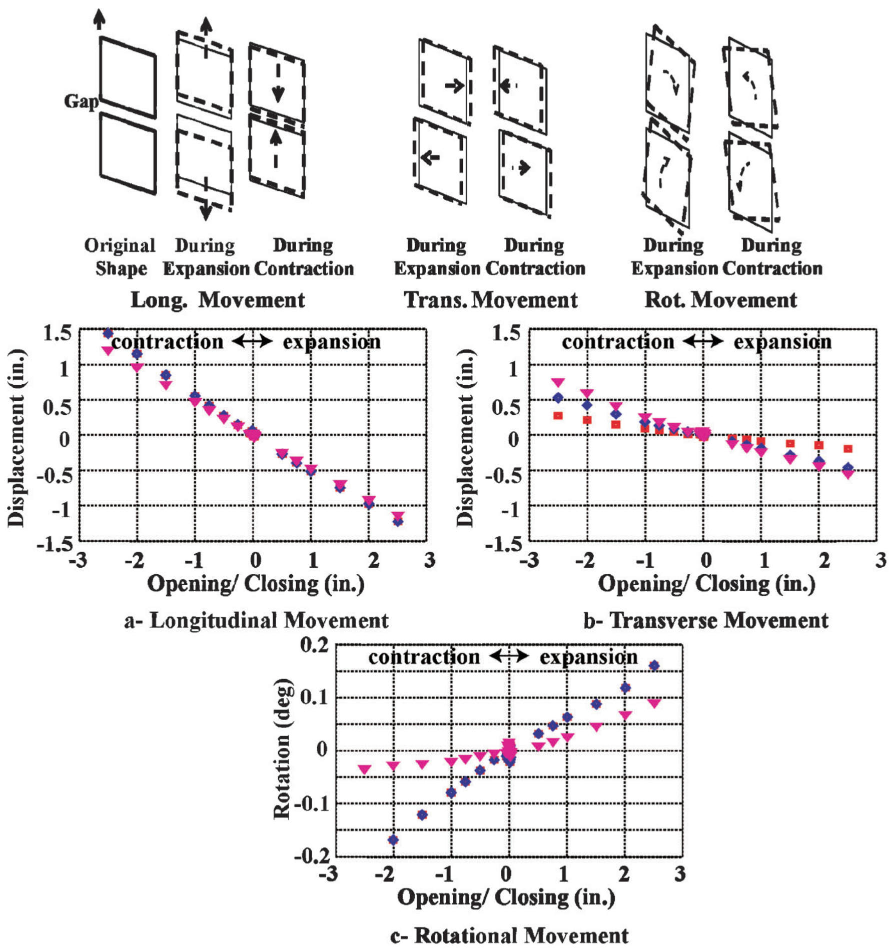

a- Longitudinal Movement

b- Transverse Movement

c- Rotational Movement

Figure B.14 Rigid body movements of the south side.

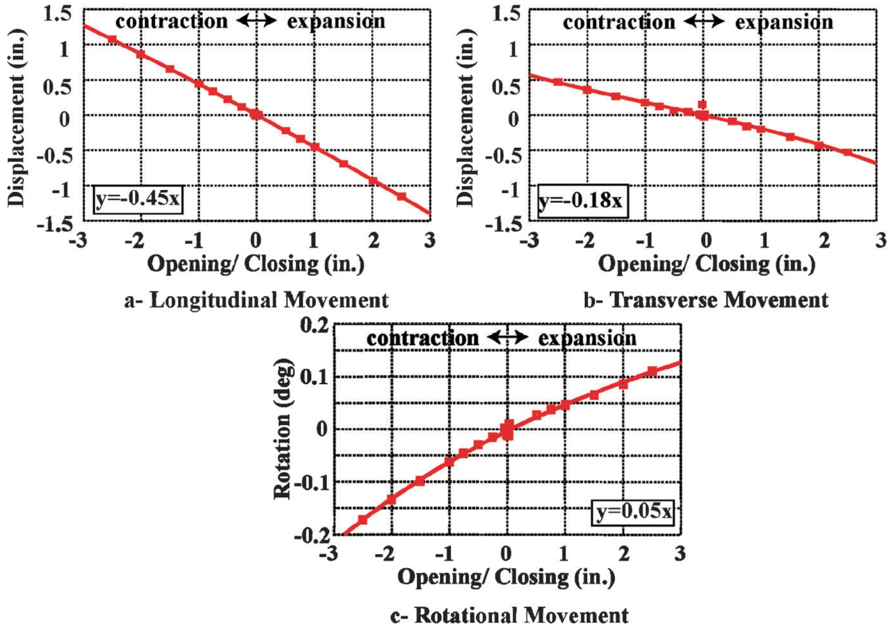

a- Longitudinal Movement

b- Transverse Movement

c- Rotational Movement

Figure B.15 Average rigid body movement of the north side.

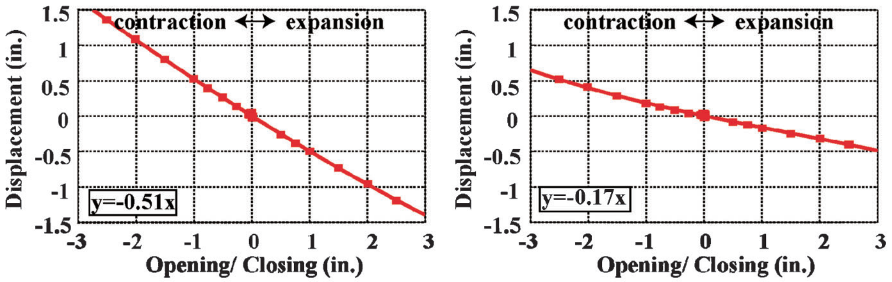

a- Longitudinal Movement b- Transverse Movement

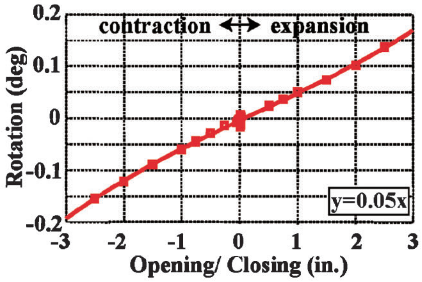

c- Rotational Movement

Figure B.16 Average rigid body movement of the south side.

B.5.2 Piles Deformation

Pile deformations were recorded at the maximum amplitude of each cycle. Figure B.17 shows the longitudinal and transverse deformations of the two piles for the 2.5 in. cycle. The longitudinal deformations of the piles at the depth of the potentiometers agree well with the potentiometer readings, as shown in Figure B.10.

The inflection point of the piles is at about 5–6 ft below the ground surface. The pile on the acute corner showed larger movements than on the obtuse corner, which agrees with the observations from Figure B.12. It is interesting to note that the displacements at the top of the wall did not go back to zero after the gap displacement went back to zero. This finding is in agreement with observation from the potentiometers and can be attributed to the formation of cracks in the girders.

B.5.3 Pressure of Hydraulic Jacks

Due to unknown friction between the transfer beam and the plate on the deck, the hydraulic pressures applied to the actuators do not represent the actual loads imposed to the deck. Figure B.18, which gives the pressures with the gap opening or closing, provides a qualitative representation of the loading process and bridge response.

Four plots are provided; two for the east side and two for the west side. Each side presents two plots of the pressures recorded during expansion and contraction. The pressures from the 2 in. cycle are plotted in green to facilitate discussion. The beginning of the expansion phase starts with the pressure release after the contraction phase of the previous cycle. For example, the east side contraction for the 2 in. cycles starts from a gap closing of about -1.2 in. (which is the irrecoverable displacement after the release of

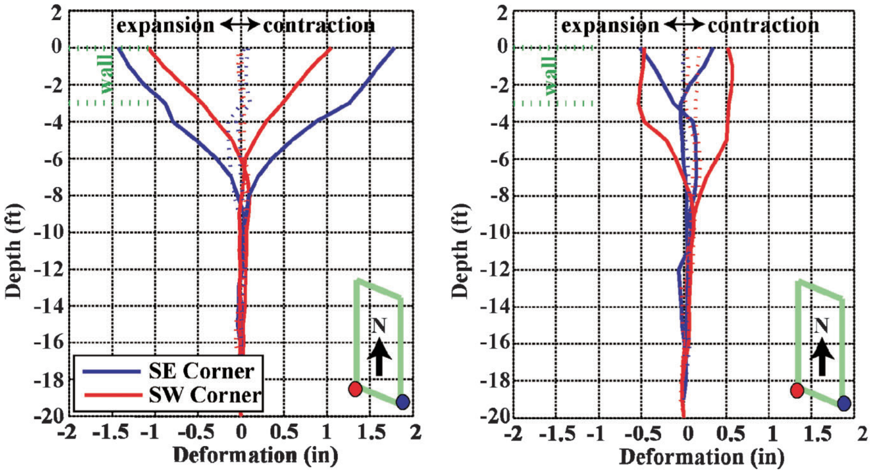

a- Longitudinal Direction-2in. Cycle b- Transverse Direction-2in. Cycle

Figure B.17 Longitudinal and transverse deformations of west and east piles at the south abutment.

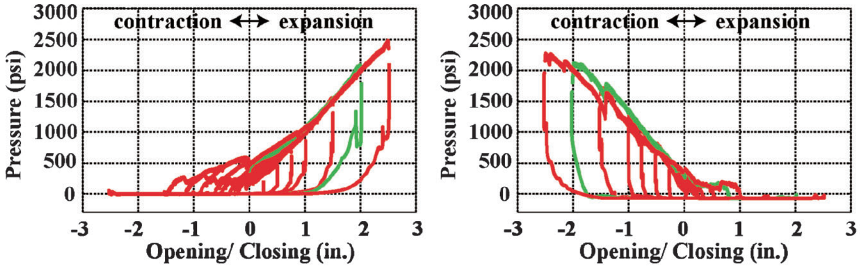

a- East Side, P-Expand

b- East Side, P-Contract

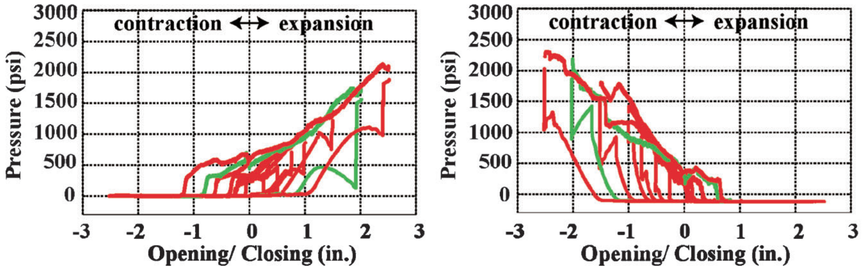

c- West Side, P-Expand

d- West Side, P-Contract

Figure B.18 Pressure hysteresis recorded at the hydraulic jacks pressure sensors.

the pressure from the previous cycle (1.5 in.). As the expansion displacement was applied, the gap passes through the zero gap displacement. After the zero gap reading and as expansion continued, the pressure increases at a steeper rate. Upon reaching the 2 in. expansion, the pressure is released as shown in the expansion plot; a very steep drop in the pressure is recorded with irrecoverable displacement of about 1 in.; then the contraction phase starts with the plot on the right hand side. The contraction phase then begins with the same process.

Upon pressure release, the gap did not go back to zero. This behavior is an indication of plasticity of the soil and piles. In addition, friction between the transfer beams and the deck also limit rebound. It is also observed after the expansion and contraction cycles and after releasing the pressure, the gap at the west side closed more than the gap at the east side. This difference in behavior can be contributed to the formation of the cracks that were observed in the last test, as the cracks were more significant at the east side than at the west side.

B.6 TEST RESULTS FOR THE BRIDGE WITH BACKFILL (TEST 2: WINTER)

B.6.1 Rigid Body Movement

To examine the accuracy of the recorded data, the displacements at each corner of the bridge deck were compared using readings from potentiometers and inclinometers. Figure B.19 presents the comparisons.

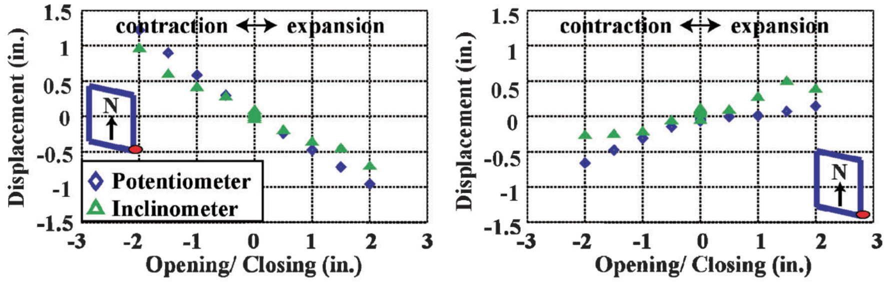

a- SE Corner Longitudinal Movement

b- SE Corner Transverse Movement

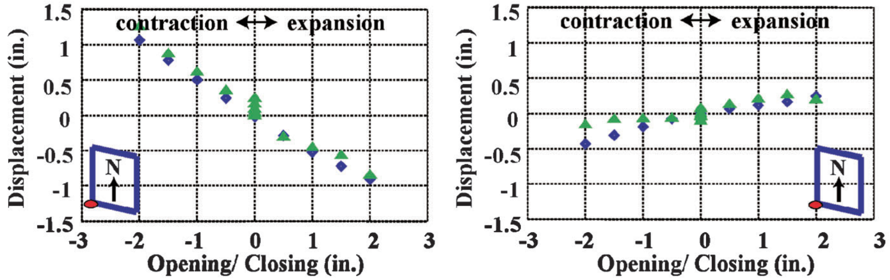

c- SW Corner Longitudinal Movement

d- SW Corner Transverse Movement

Figure B.19 Comparison of displacements at the deck corners obtained from potentiometers and inclinometers.

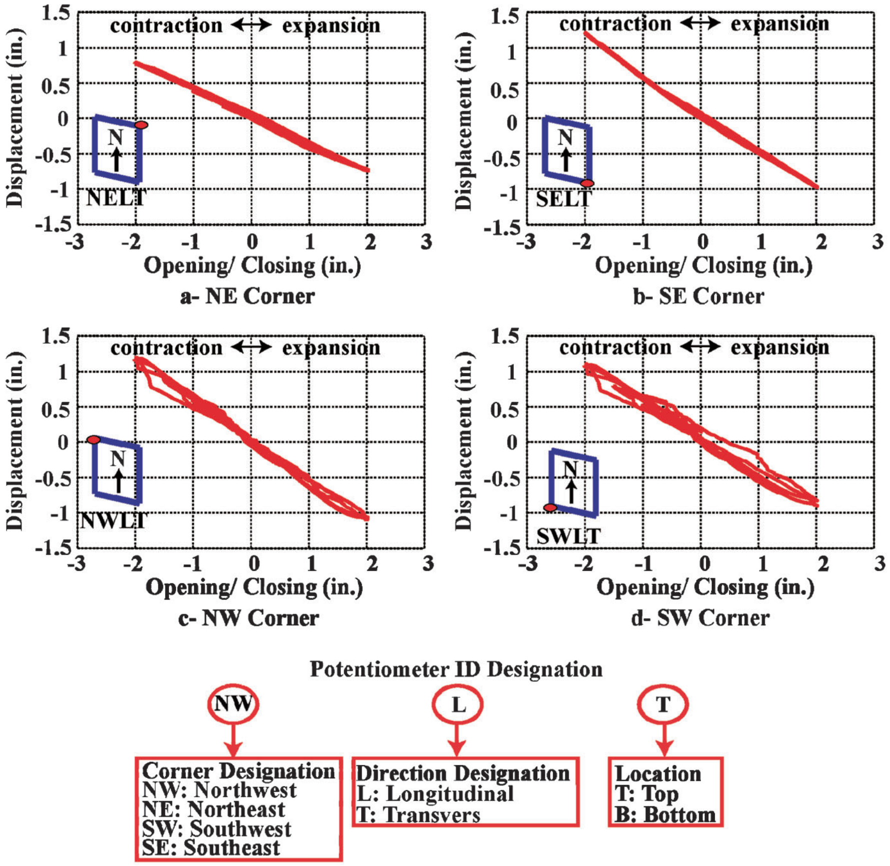

Figure B.20 Hysteresis plots of longitudinal movement at the bridge deck.

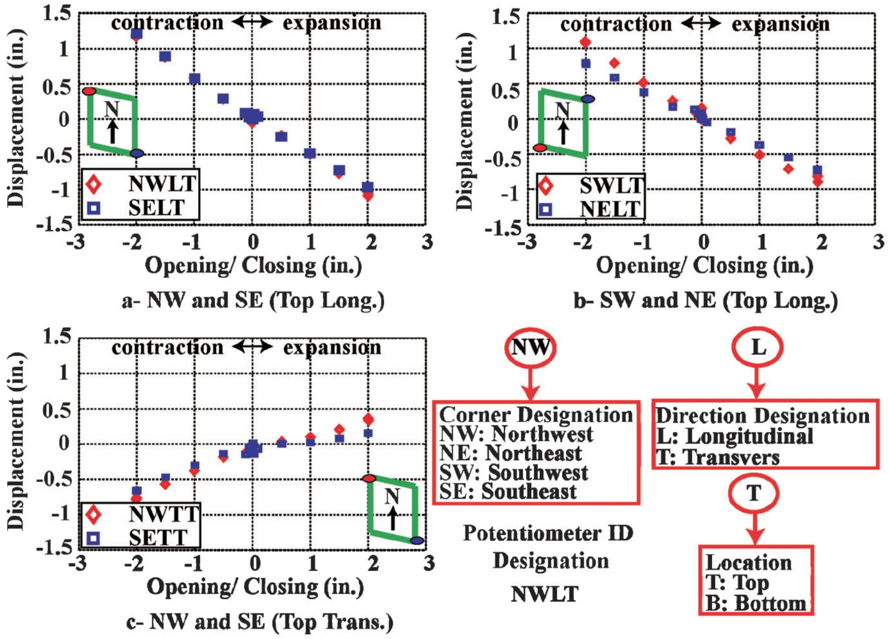

Figure B.21 Comparison of potentiometer measurements at opposite corners.

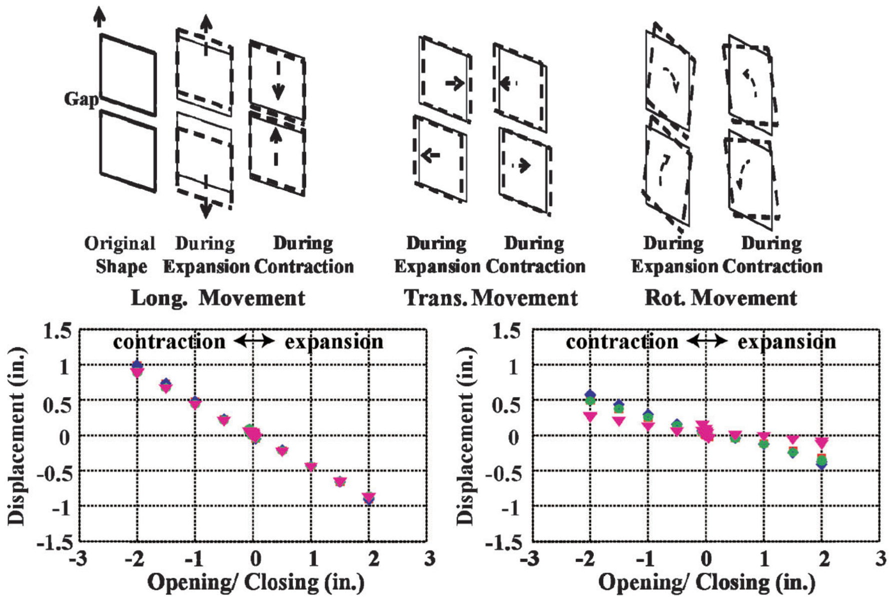

a- Longitudinal Movement

b- Transverse Movement

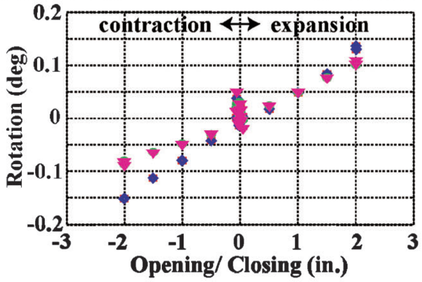

c- Rotational Movement

Figure B.22 North side rigid body movement.

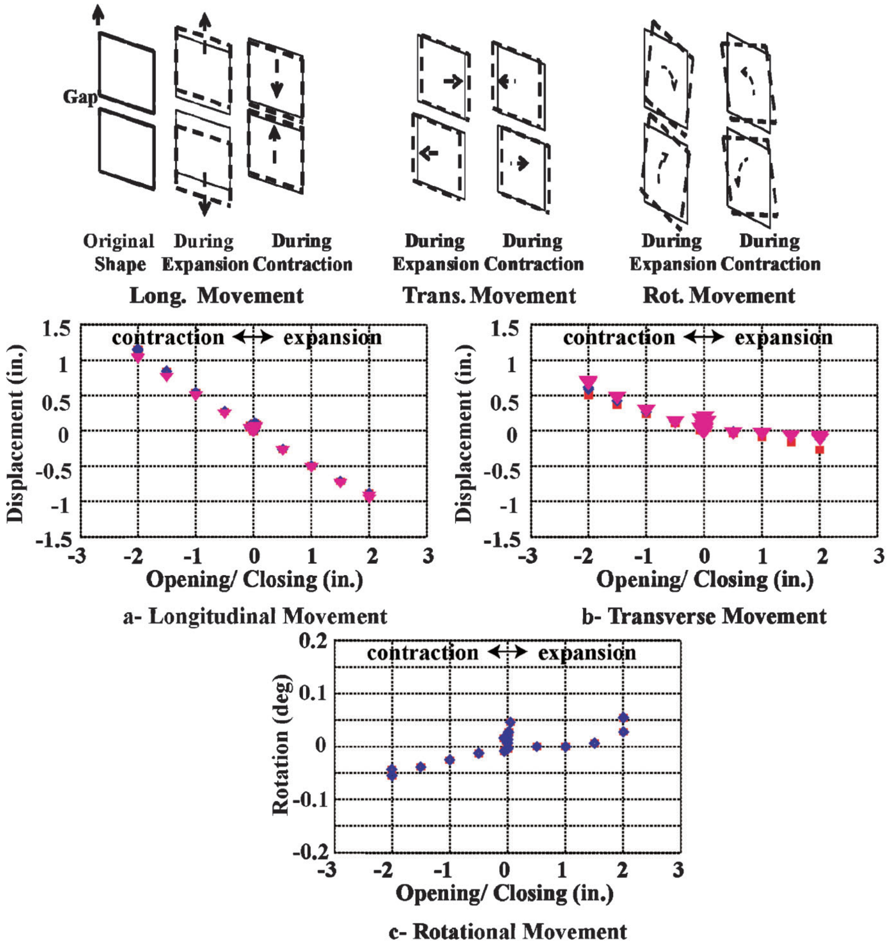

a- Longitudinal Movement

b- Transverse Movement

c- Rotational Movement

Figure B.23 South side rigid body movement.

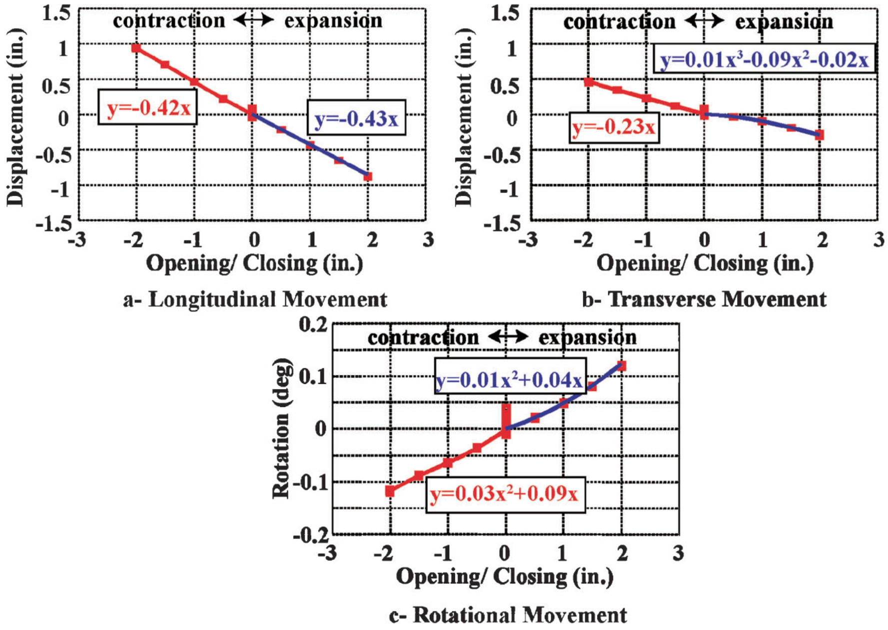

a- Longitudinal Movement

b- Transverse Movement

c- Rotational Movement

Figure B.24 Average rigid body movement of the north side.

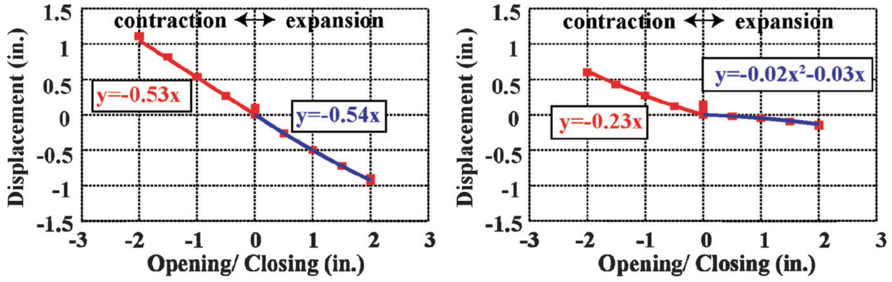

a- Longitudinal Movement

b- Transverse Movement

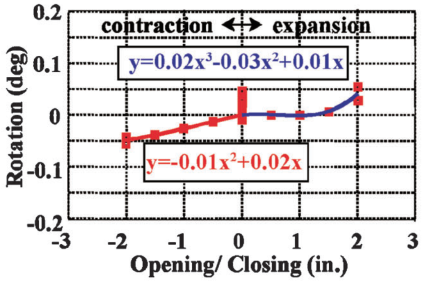

c- Rotational Movement

Figure B.25 Average rigid body movement of the south side.

As shown, the measurements from the two different sources were relatively consistent. The small deviation between the inclinometers and potentiometer readings is due to the rotation of the deck that occurred during the cycles. It should be also noted that the monitoring locations at each corner for each of the measurement techniques were not identical. A few inches separated them.

Considering the reliability of the potentiometers data, this measurement is used for all analyses.

The hysteresis loops for the longitudinal movement measured by the potentiometers at the bridge deck versus the gap opening and closing are shown in Figure B.20.

As observed, hysteresis is more significant in this test in comparison to the test with no backfill (Test 1).

The potentiometer displacements at the end of each cycle are plotted in Figure B.21 for opposite corners, for both the longitudinal and transverse directions. A small difference between opposite corners is observed. This difference is more obvious for the contraction half of the cycle at larger amplitudes. The formation of the crack, as discussed earlier, is a possible explanation of the deviation in the measurements.

To understand the bridge response, the rigid body movement of the bridge was estimated by using three of the potentiometer measurements. Rigid body movement refers to the longitudinal, transverse, and rotational response of the center of the north and south decks of the bridge. Different monitoring point combinations were used; the results of the estimates are shown in Figures B.22 and B.23 for the north and south sides, respectively.

Average values of the estimated movement were used to estimate the movement of each half of the bridge. A polynomial curve was then selected to fit the data. For this test with backfill different fits were used for contraction and expansion. The average rigid body movements and the associated polynomial fit are shown in Figures B.24 and B.25 for the north and south sides, respectively.

B.6.2 Piles Deformation

Pile deformations were recorded at the maximum amplitude in each cycle. The longitudinal deformations of the piles at the depth of the potentiometers relatively agree well with the potentiometer readings, as shown in Figure B.19. Figure B.26 shows the longitudinal and transverse deformations of the two piles for the 2.0 in. amplitude cycle.

The inflection point of the piles is at about 5–6 ft below the ground surface. The observations made in Section B.5 about the pile performance apply to this test as well.

B.6.3 Pressure of Hydraulic Jacks

Figure B.27 presents the pressure of hydraulic actuators as a function of the gap opening/closing. The same observations about the non-recoverable gap displacements that were made in the SectionB.5 for Test 1 are also applicable to this test.

B.6.4 Lateral Earth Pressure

Earth pressure at the bottom of the wall was measured at the end of each cycle at the southwest and southeast corners. The lateral earth pressure coefficients were also estimated. The lateral earth pressure and the earth pressure coefficients are shown on Figure B.28.

It should be noted that the backfill soil mass was frozen and a gap formed between the wall and the soil during bridge contraction. Therefore, zero (0) earth pressure was recorded during the contraction phase. For expansion, the earth pressure coefficients increased as the amplitude of the cycles increased. It was observed that the lateral soil pressure was approximately the same at both the east and west sides. The 2 in. cycle was repeated twice (first 2 in. cycle and second 2 in. cycle) to investigate the effect of repeated cycles with the same amplitude on the lateral soil pressure. It was observed that the lateral soil pressure increased in the second 2 in. cycle relative to the first 2 in. cycle. An 15% and 19% increase was observed for the east and west sides, respectively.

The measured pressure data was fitted using a hyperbolic curve as shown in Figure B.29. The choice of hyperbolic fitting is common for the soil stress-strain relationships.

B.6.5 Settlement Plates

Five settlement plates were installed in the backfill to monitor soil settlement during testing. The settlement plates consisted of

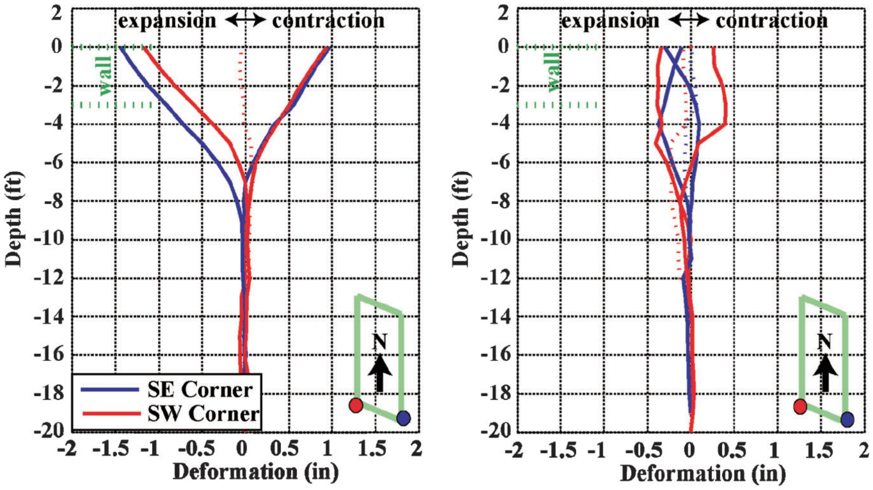

a- Longitudinal Direction-2in. Cycle b- Transverse Direction-2in. Cycle

Figure B.26 Longitudinal and transverse deformations of west and east piles at the south abutment.

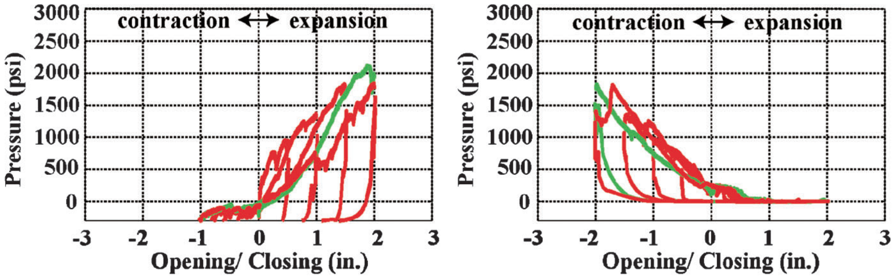

a- East Side, P-Expand b- East Side, P-Contract

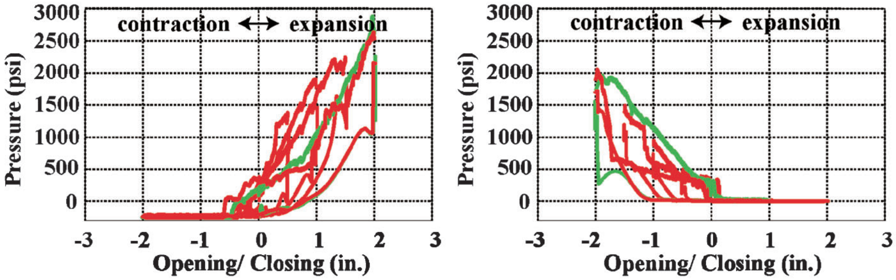

c- West Side, P-Expand d- West Side, P-Contract

Figure B.27 Pressure hysteresis recorded at the hydraulic jacks pressure sensors.

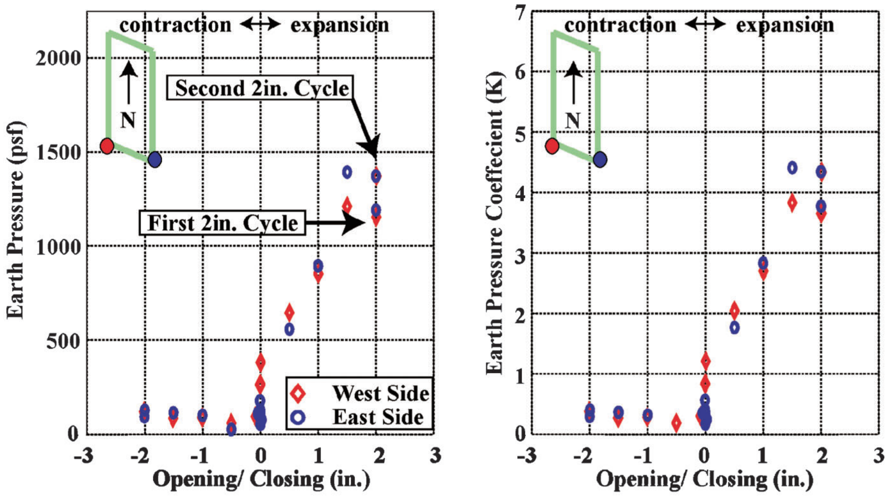

a- Horizontal Earth Pressure

b- Earth Pressure Coeffeceint

Figure B.28 Lateral earth pressure and earth pressure coefficients.

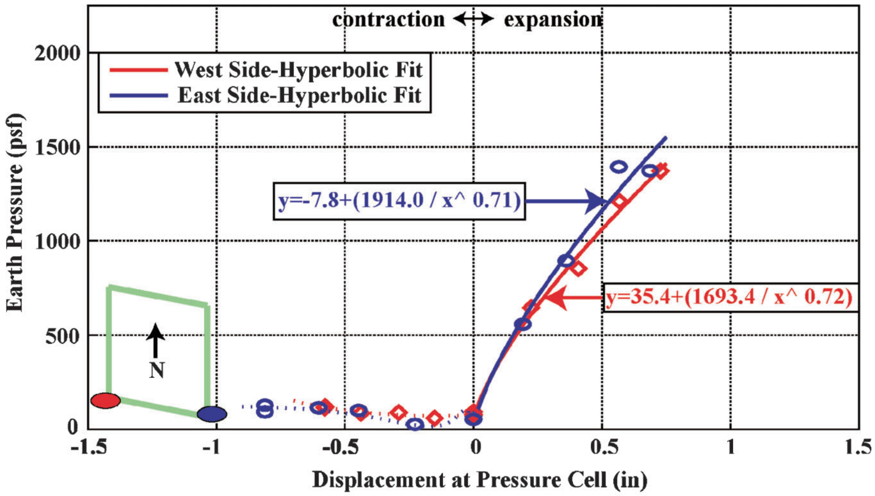

Figure B.29 Lateral earth pressure and hyperbolic fitting.

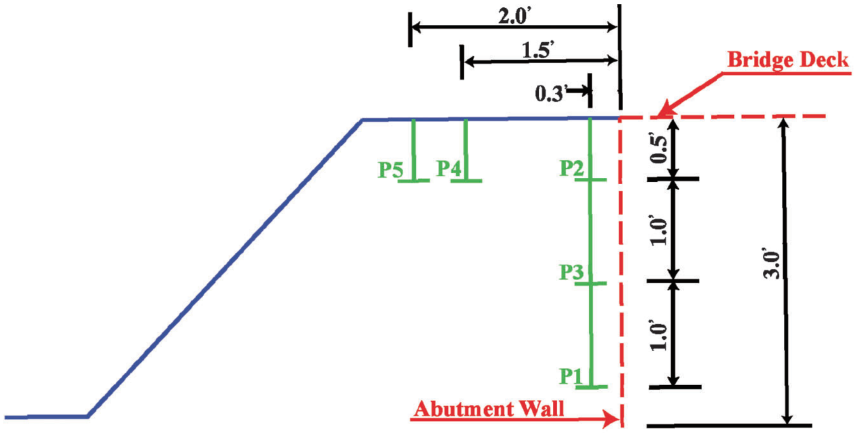

	Cycle Amplitude									
Point ID	0.5	-0.5	1	-1	1.5	-1.5	2	-2	2	-2
P1	-0.012	0.036	0.048	0.12	0.108	0.276	0.168	0.42	0.324	0.54
P2	-0.012	-0.036	-0.012	0.096	0.036	0.384	0.24	1.212	0.984	1.908
P3	0.012	-0.06	-0.024	0	0	0.288	0.144	1.008	0.828	1.716
P4	0.06	-0.012	-0.108	-0.024	-0.168	-0.036	-0.24	-0.06	-0.372	-0.156
P5	0.06	-0.024	-0.108	-0.024	-0.168	-0.048	-0.264	-0.096	-0.396	-0.192

Figure B.30 Recorded settlement (in inches) in the backfill (positive is settlement).

steel plates connected to a steel rod that extended above the backfill surface.

The location of settlement plates and the recorded settlements are shown in Figure B.30.

The settlement plates were surveyed at the end of each loading phase. It is observed that the settlement points far from the wall (at 1.5 and 2.0 ft) did not record any settlement. However, the settlement plates next to the wall showed settlement during the contraction phase and a small amount of heave during the expansion phase.

B.7 TEST RESULTS FOR THE BRIDGE WITH BACKFILL (TEST 3: SUMMER)

B.7.1 Rigid Body Movement

The hysteresis loops for the longitudinal movement of the bridge deck are computed from potentiometers measurements and presented in Figure B.31.

As observed, the hysteresis is more significant in this test than for the test with no backfill (Test 1), which is shown in Figure B.11.

Figure B.32 presents the longitudinal and transverse displacements of the bridge measured at opposite corners. The small differences observed during the contraction cycles may be explained by the presence of the crack in the deck. While deviations during the expansion cycles may be attributed to differences in backfill stiffness between the north and south sides. Overall, the responses are quite similar.

The average rigid body movements are shown in Figures B.33 and B.34 for the north and south sides, respectively.

Average values of the estimated movement were used to estimate the movement of each half of the bridge. A polynomial curve was then selected to fit the data. For this test with backfill different fits were used for contraction and expansion. The average rigid body movements and the associated polynomial fit are shown in Figures B.35 and B.36 for the north and south sides, respectively.

B.7.2 Piles Deformation

The pile deformations were recorded at maximum amplitude of each cycle. Figure B.37 shows the longitudinal and transverse deformations of the two piles for the 2.0-inch cycle.

The inflection point of the piles is at about 5–6 ft below the ground surface. The observations made in Section B.5 about pile performance apply to this test as well.

B.7.3 Pressure of Hydraulic Jacks

Figure B.38 presents pressure applied the hydraulic actuators as a function of the gap opening/closing. The same observations regarding the non-recoverable gap displacements that were made in Section B.5 for Test 1 are also applicable to this test.

B.7.4 Lateral Earth Pressure

The earth pressure at the bottom of the wall was measured at the end of each cycle at the southwest and southeast corners. The lateral earth pressure coefficients were also estimated. The lateral earth pressure and the earth pressure coefficients are shown on Figure B.39.

The lateral earth pressure coefficients increased as the amplitude of the cycles increased up to the 2 in. cycle. Displacement beyond this level resulted in a reduction in the lateral earth pressure coefficient. The lateral soil pressure observed at the obtuse corner was larger than at acute corner. The 2 in. cycle was repeated twice (first 2 in. cycle and second 2 in. cycle) to investigate the effect of repeated cycles with the same amplitude on the lateral soil pressure. It was observed that the lateral soil pressure increased in the second 2 in. cycle relative to the first 2 in. cycle. An 8.8% and 12% increase was observed for the east and west sides, respectively.

The measured pressure data was fitted using a hyperbolic curve as shown in Figure B.40. The choice of hyperbolic fitting is common for the soil stress-strain relationships.

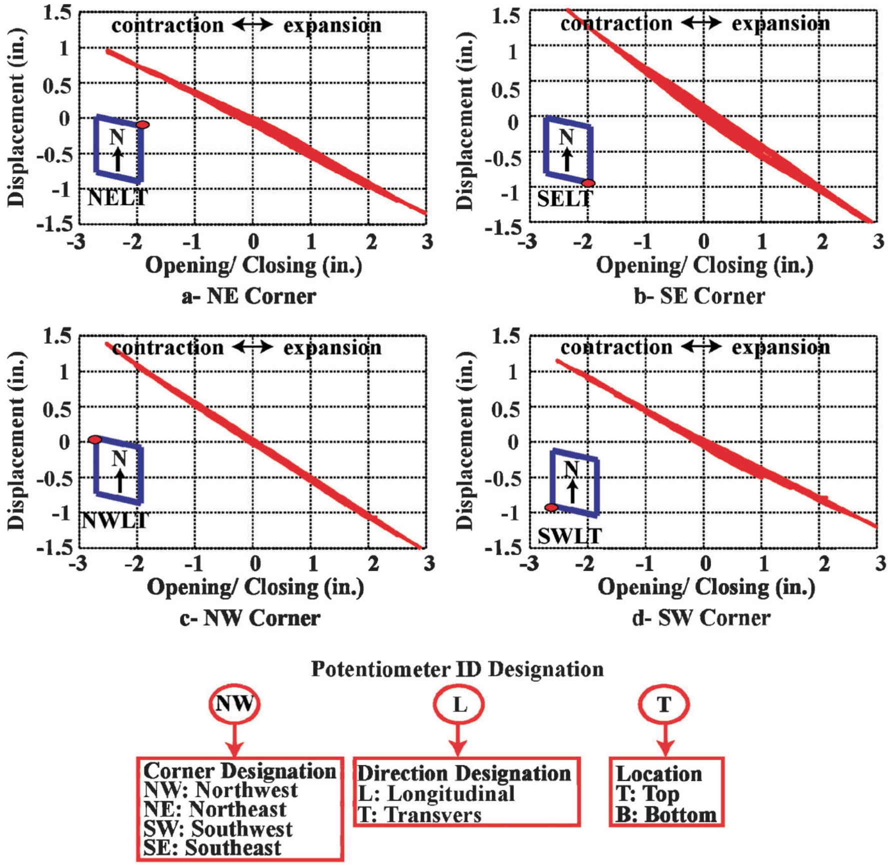

Figure B.31 Hysteresis plots of longitudinal movement at the bridge deck.

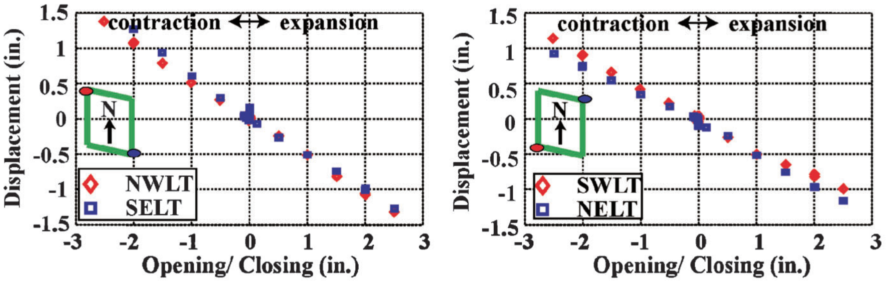

a- NW and SE (Top Long.)

b- SW and NE (Top Long.)

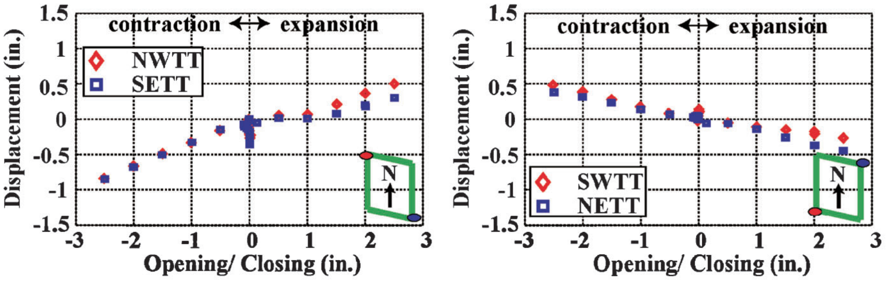

c- NW and SE (Top Trans.)

d- SW and NE (Top Trans.)

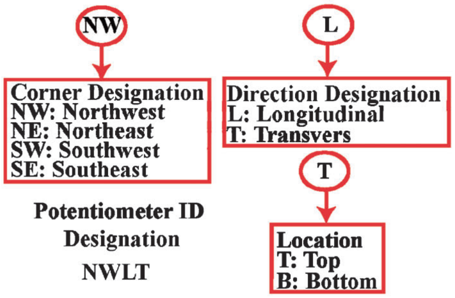

Figure B.32 Comparison of potentiometer measurements at opposite corners.

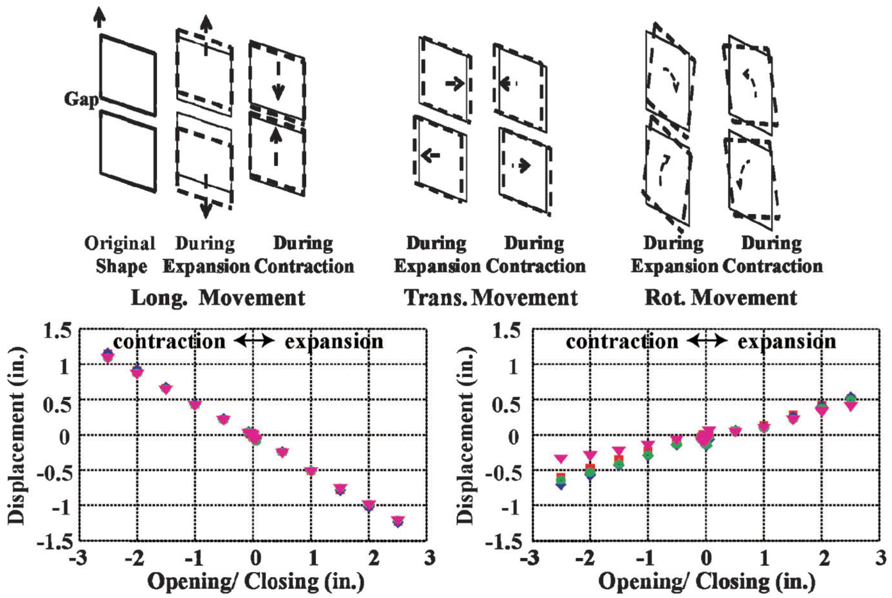

a- Longitudinal Movement

b- Transverse Movement

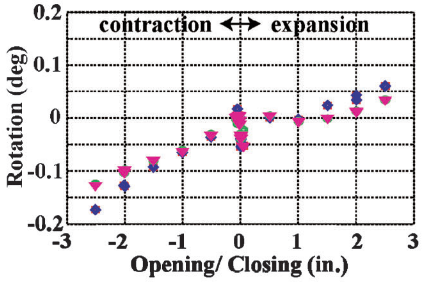

c- Rotational Movement

Figure B.33 Rigid body movement of the north side.

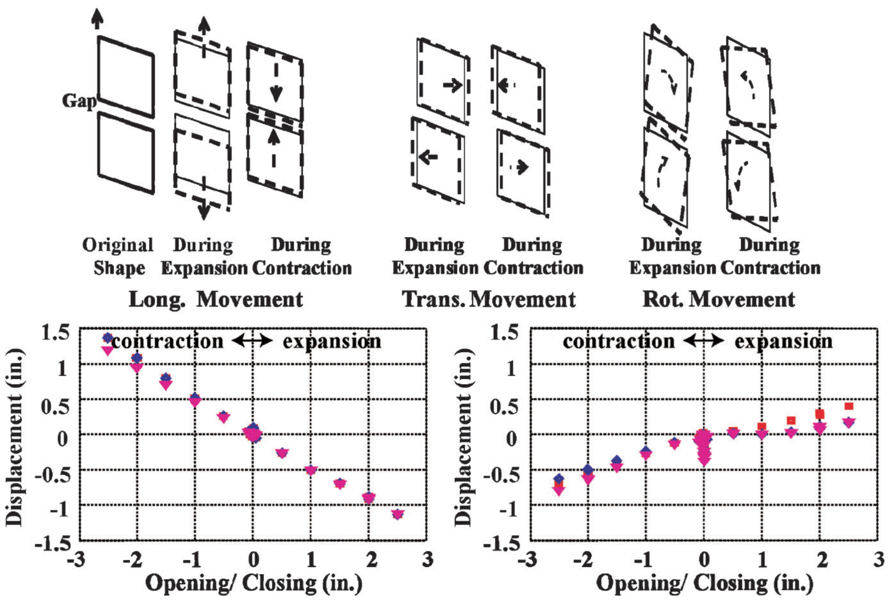

a- Longitudinal Movement

b- Transverse Movement

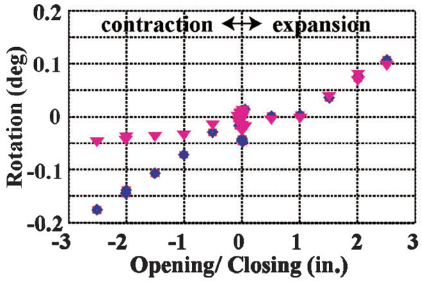

c- Rotational Movement

Figure B.34 Rigid body movement of the south side.

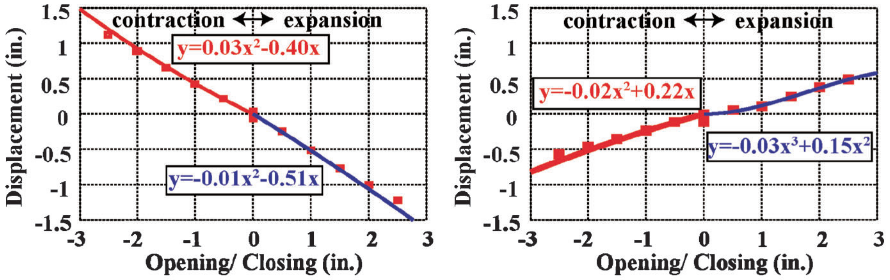

a- Longitudinal Movement

b- Transverse Movement

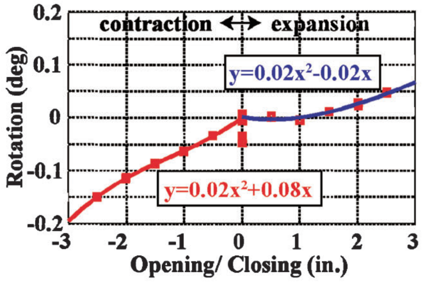

c- Rotational Movement

Figure B.35 Average rigid body movement of the north side.

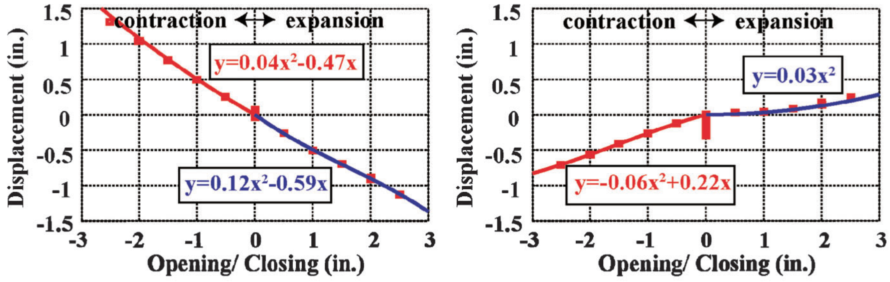

a- Longitudinal Movement **b- Transverse Movement**

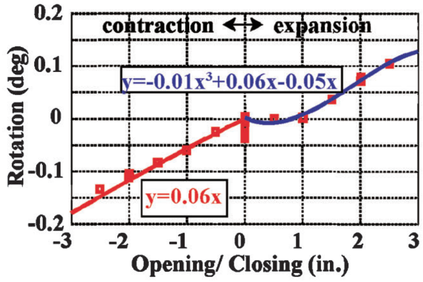

c- Rotational Movement

Figure B.36 Average rigid body movement of the south side.

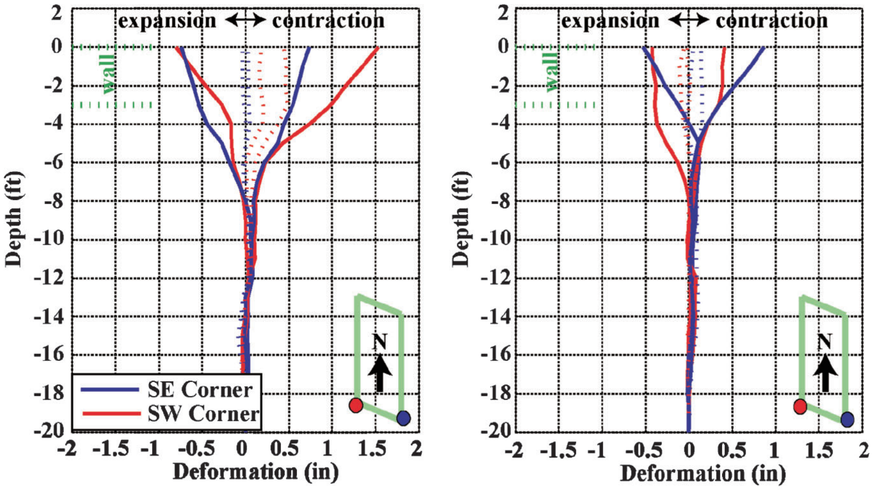

a- Longitudinal Direction-2in. Cycle **b- Transverse Direction-2in. Cycle**

Figure B.37 Longitudinal and transverse deformations of west and east piles at the south abutment.

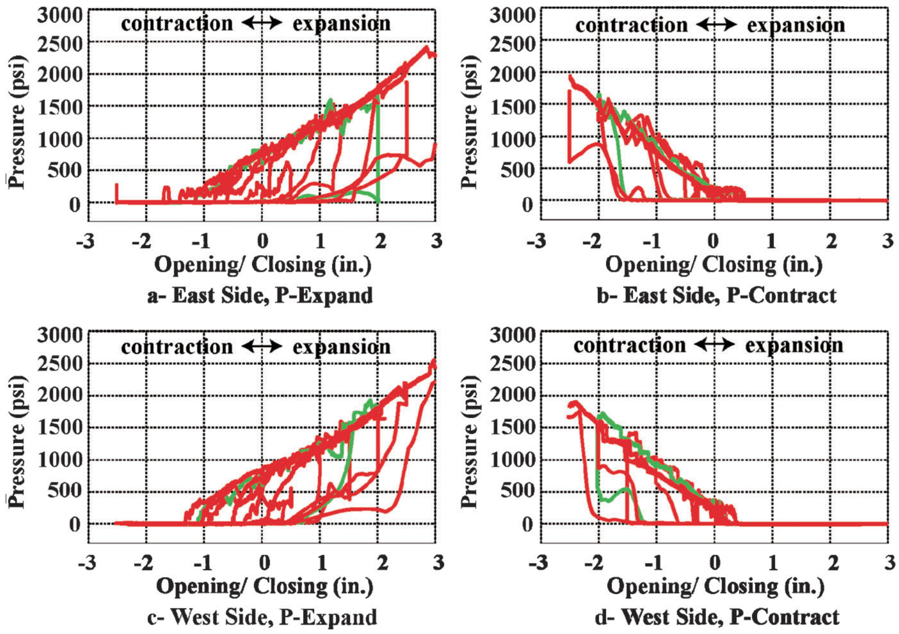

a- East Side, P-Expand

b- East Side, P-Contract

c- West Side, P-Expand

d- West Side, P-Contract

Figure B.38 Pressure hysteresis recorded at the hydraulic jacks pressure sensors.

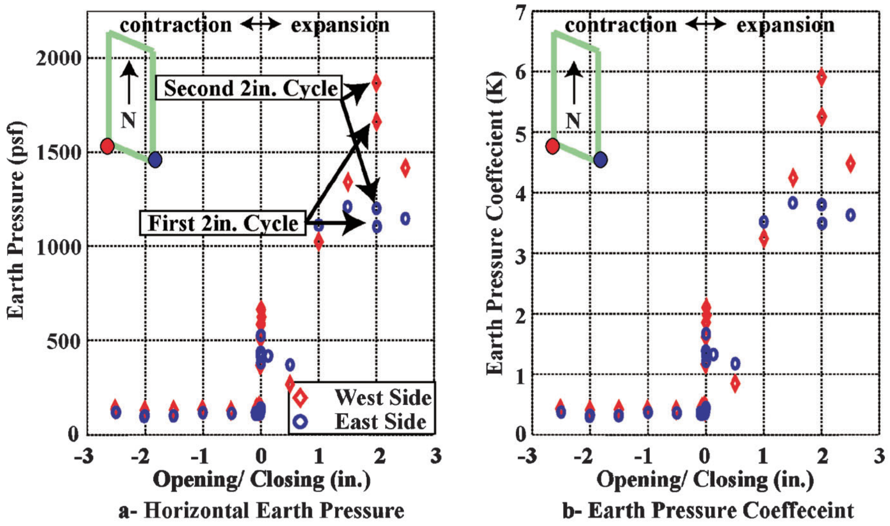

a- Horizontal Earth Pressure

b- Earth Pressure Coeffeceint

Figure B.39 Lateral earth pressure and earth pressure coefficients.

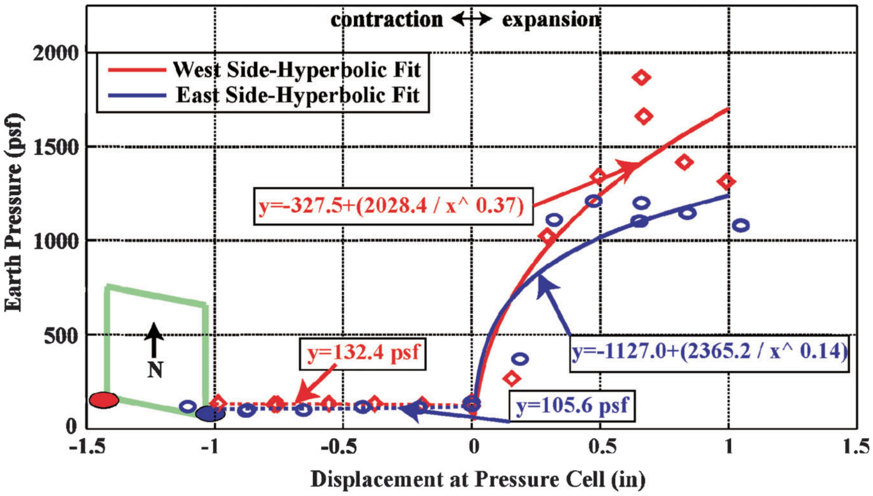

Figure B.40 Lateral earth pressure and hyperbolic fitting.

B.8 DISCUSSION OF THE RESULTS

B.8.1 Rigid Body Response

In general, for a zero skew angle, any applied longitudinal displacement at the deck will result only in longitudinal displacements of the bridge abutments. The magnitude of the longitudinal displacements at the abutments will be half the applied displacement at the deck, given that symmetrical boundary conditions exist at the abutments. However, when a skew angle is introduced, the resulting displacement at the abutments will consist of longitudinal, transverse and rotational movements as a result of the loss of symmetry due to the skew. The magnitude of each of the movements is dependent on the skew angle and boundary conditions at the abutments.

To understand the resulting movements from the tested bridge (45° skew) and the effect of the boundary conditions, three types of plots were prepared:

1. The end of cycle displacement at each corner versus the gap opening or closing,
2. The hysteresis plots at each corner from all the cycles versus the gap opening or closing,
3. The equivalent bridge deck rigid body movement.

The end of cycles longitudinal displacement plots were compared for the acute (NW, SE) and obtuse (NE, SW) corners of the bridge for all the three tests, as shown on Figures B.41 and B.42.

In general, the responses are similar for all cases. It is also seen that the acute corners displaced more than the obtuse corners. In all cases, the sum of the displacements of each deck was equal to the total displacement applied at the gap, with the exception of large amplitude cycles during contraction, which is thought to be caused by the formation of cracks, as discussed in Section B.7.

The hysteresis plots, Figures B.43 and B.44, show the displacements at the corners for all the cycles.

It can be noted that the cycles during the expansion stage demonstrate a more pronounced hysteresis behavior during the tests with backfill than with no backfill. However, during the contraction cycles, hysteresis is less obvious. For the test with no backfill, the rigid body response in the longitudinal direction is mainly controlled by the response of the bridge structure, which is expected to be primarily elastic (no hysteresis). On the other hand, during the June test (Test 3: Summer), as the bridge expands, the backfill is subjected to passive loading, which means that the abutment wall is pushing the soil. As a result, the rigid body response in the longitudinal direction is controlled by the backfill

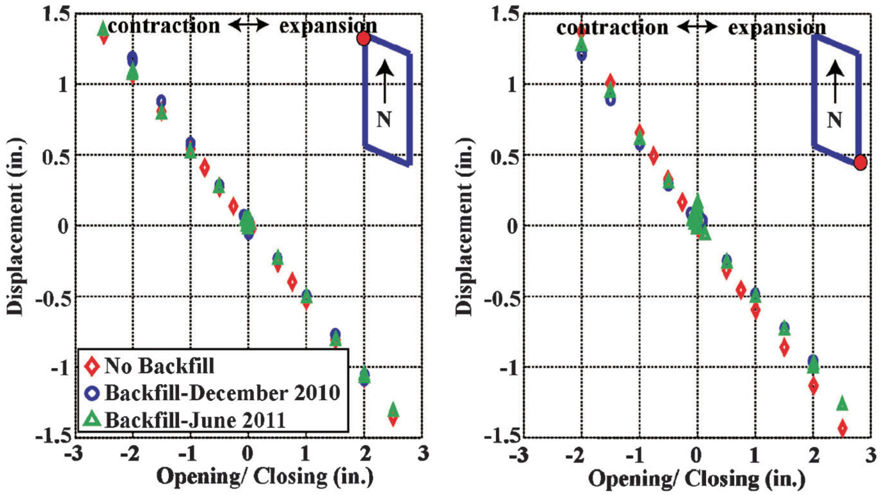

a- Northwest Corner

b- Southeast Corner

Figure B.41 End of cycles' longitudinal displacements at acute corners.

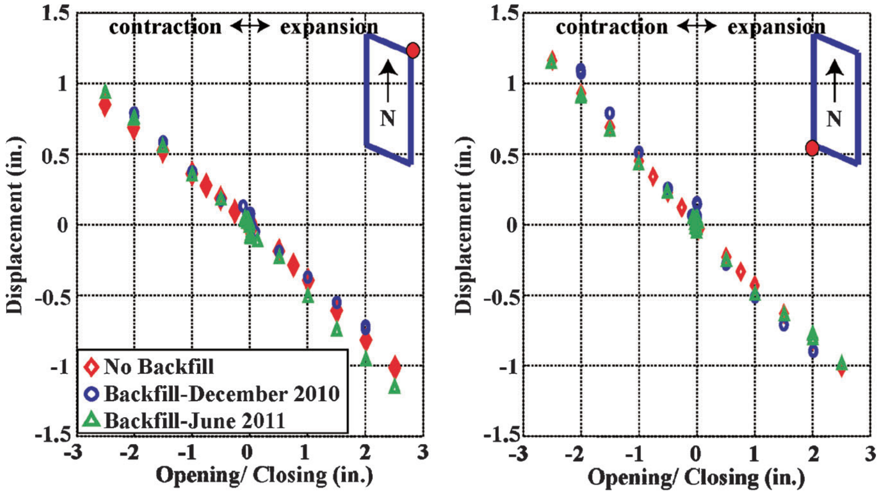

a- Northeast Corner

b- Southwest Corner

Figure B.42 End of cycles' longitudinal displacements at obtuse corners.

response, which is expected to be elastoplastic and thus results in hysteretic response. During bridge contraction, the backfill is subjected to active loading (wall moves away from the soil). Therefore, the rigid body response in the longitudinal direction is controlled by the response of the bridge structure, which results in a small hysteresis response. In addition, due to the observed behavior of the backfill during the December 2010 test (Test 2: Winter), where the soil was frozen and behaved somewhere between a rigid body and a granular soil, the hysteresis behavior is less obvious than in the test with backfill in June.

The observations regarding hysteresis are more obvious for the recoded transverse movements as shown in Figure B.45.

During the expansion phase, the response deviates from linear for the tests with backfill (Figure B.45(a)). This deviation is attributed to the hysteretic behavior of the soil behind the wall when subjected to cycles of loading and to friction between the abutment and the backfill that leave lock-in shear stresses at the end of each loading cycle. For the test with no backfill, movement in the lateral direction is not restrained, which results in a response close to linear. For the December test, there is minimal hysteretic behavior during contraction, which is attributed to the formation of a gap between the soil and the wall, as explained before. Figures B.45(b) and B.45(c) provide a conceptual visualization of the interaction between the structure and the soil. During expansion, the bridge moves against the backfill resulting in a rotation in a clockwise direction, while during contraction the wall moves away from the backfill (detaches from the backfill in the December test) and rotates in a counter-clockwise direction. A soil element at the interface between the backfill and the abutment wall is subjected to shearing and thus would have an elastoplastic response that results in hysteretic nonlinear displacements of the abutment (Figure B.45(c)).

For the December test with backfill, the response at the acute corner can be represented by a bi-linear approximation; the interval for the first linear portion is from a gap opening of −2.0 in. to 0 and the second from 0 to +2.0 in. This behavior is explained using the schematic in Figure B.45(b). During expansion, the abutment wall moved against a frozen backfill soil (based on observations during the test), which was quite stiff. As shown in the schematic, the interpretation is that the interface behaved as rigid-plastic. This is supported by the observation that the rigid-body response of the bridge in the transverse direction was linear during the expansion phase, with a softer response than when there was no backfill. The response was also linear during the contraction phase similar to when there was no backfill. It is worth noting that some hysteretic behavior was observed in the

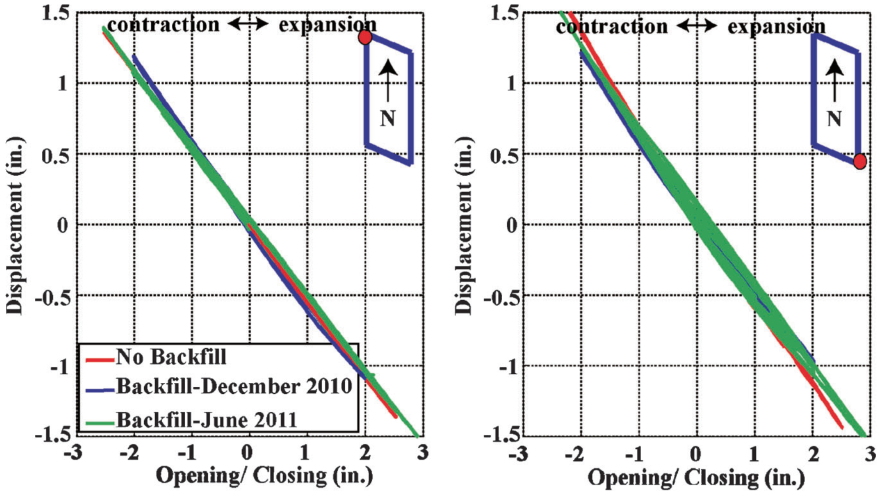

a- Northwest Corner

b- Southeast Corner

Figure B.43 Acute corners hysteresis of longitudinal displacements.

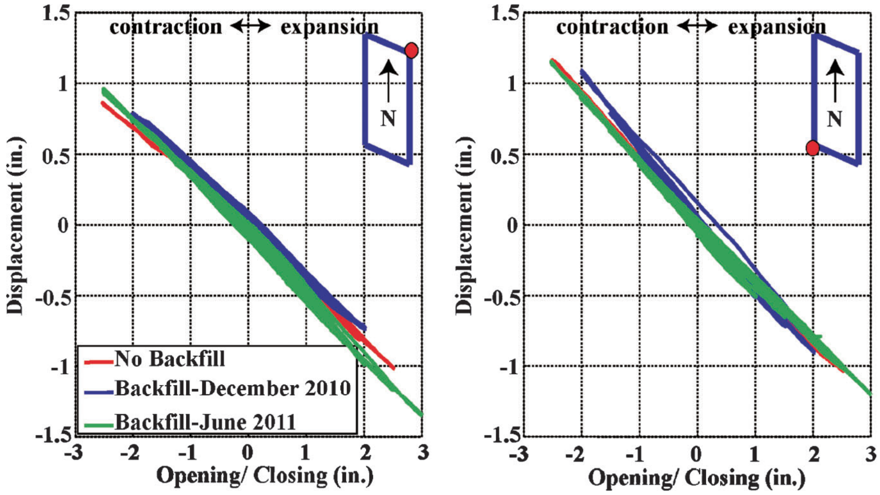

a- Northeast Corner

b- Southwest Corner

Figure B.44 Obtuse corners hysteresis of longitudinal displacements.

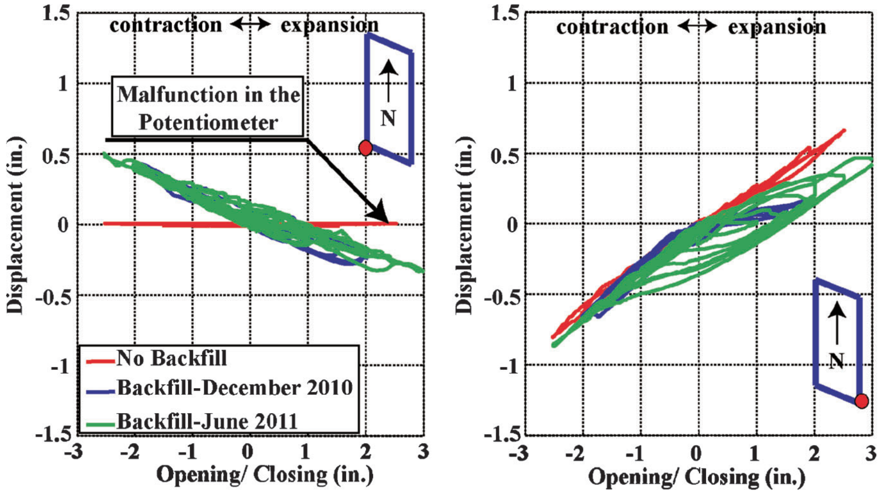

a- South Side Hysteresis of Transverse Displacements

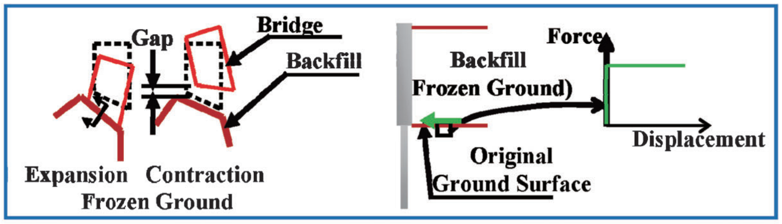

b- Schematic of Backfill Response Dec., 2010 Test

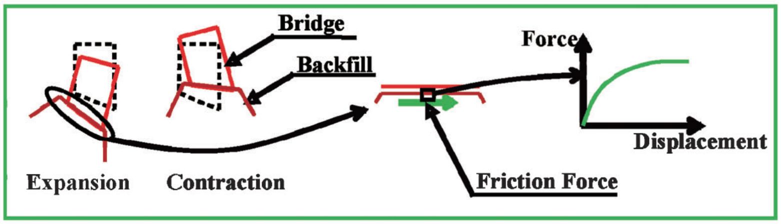

c- Schematic of Backfill Response June, 2011 Test

Figure B.45 Hysteresis of transverse movement and schematic of backfill response.

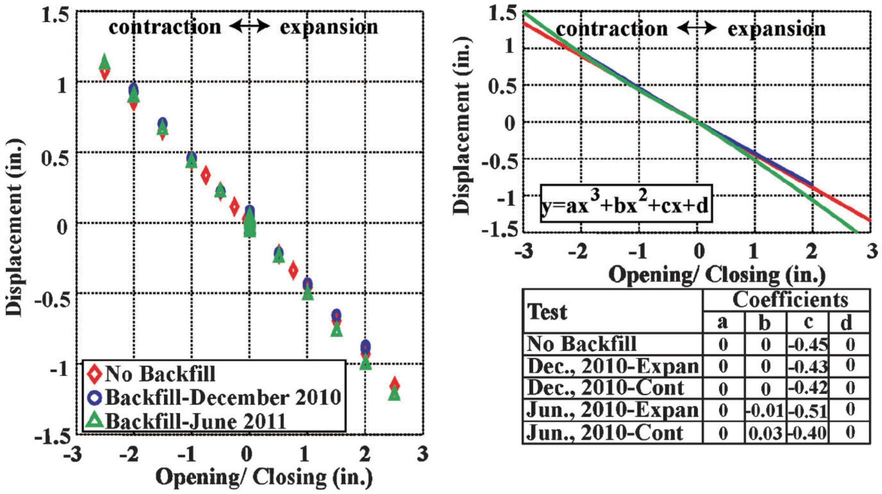

Test	Coefficients			
	a	b	c	d
No Backfill	0	0	-0.45	0
Dec., 2010-Expan	0	0	-0.43	0
Dec., 2010-Cont	0	0	-0.42	0
Jun., 2010-Expan	0	-0.01	-0.51	0
Jun., 2010-Cont	0	0.03	-0.40	0

a- North Side

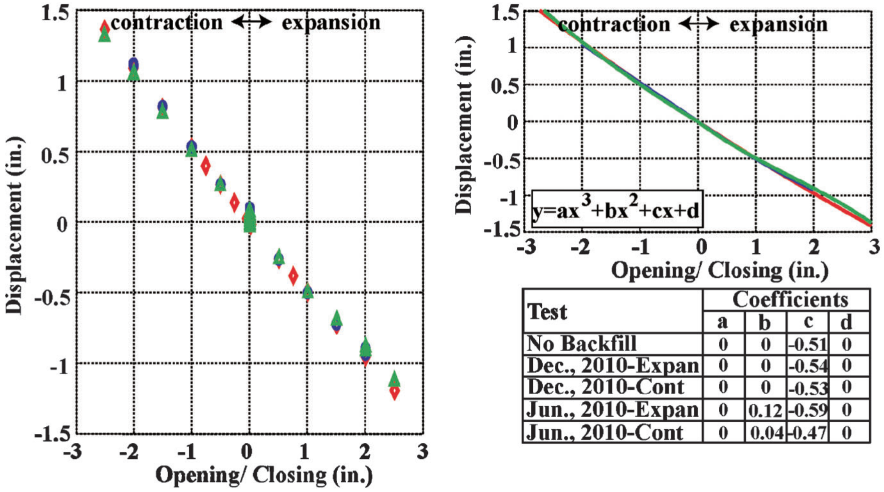

Test	Coefficients			
	a	b	c	d
No Backfill	0	0	-0.51	0
Dec., 2010-Expan	0	0	-0.54	0
Dec., 2010-Cont	0	0	-0.53	0
Jun., 2010-Expan	0	0.12	-0.59	0
Jun., 2010-Cont	0	0.04	-0.47	0

b- South Side

Figure B.46 Bridge deck rigid body longitudinal movement.

obtuse corner (significantly smaller hysteresis occurred in the acute corner) which is associated with a nonlinear response of the soil. The difference between the observed responses of the acute and obtuse corners is attributed to rotation during the expansion cycle. The rotation was observed in a clockwise direction, which suggests that the soil in the acute corner would deform more than in the obtuse corner.

Figures B.46(a) and B.46(b) show the estimated rigid body movement of the north and south sides of the bridge deck for each test.

During contraction, all the tests resulted in similar estimates of the longitudinal movement, except at larger amplitudes where the tests with backfill resulted in a larger displacement at the north side from the test with no backfill. This behavior is due to the formation of the cracks discussed earlier. During the expansion phase, results from the June test (Test 2: Summer) with backfill resulted in larger longitudinal movement at the north side and slightly smaller longitudinal movement at the south side from those with no backfill. These differences between the north and south sides can be attributed to difference in backfill stiffness. Overall, however, the differences are attributed to the added boundary conditions (backfill behind the abutments). Based on Figures B.46(a) and B.46(b) and depending on the boundary conditions (with backfill and with no backfill) the resulting rigid-body longitudinal movement ranged from 40% to 50% of the total displacement imposed at the gap. For example at the north side (Figure B.46(a)) and for a 2 in. total displacement imposed at the gap, the resulting rigid movement of the bridge's deck in the longitudinal direction ranged from 0.8 in. to 1.0 in. for the cases with backfill and with no backfill, respectively.

The effect of the backfill is better observed in the rigid body response in the transverse direction. This is due to the effect of friction between the soil and the abutment walls on the response, as shown in the schematics in Figure B.45(b) and B.45(c). As shown in Figure B.47, the relationship between the total displacement imposed at the gap and the resulting rigid body movement of the bridge deck in the transverse direction was primarily linear for the case of no backfill and nonlinear for the cases with backfill.

Figure B.47(b) shows nonlinear transverse displacements with the presence of backfill. It is interesting to note that the difference in transverse displacements between the tests with backfill and the test with no backfill increase up to a gap opening of 1.5 in., then the differences are approximately constant. This could be attributed to the mobilization of full friction between the backfill soil and the abutment walls. It is estimated that, for the case of no backfill, the transverse movement is about 18% of the imposed gap for both expansion and contraction. For the test with backfill the transverse movement is about 10% of the gap for expansion and 30% for contraction.

Figures B.48(a) and B.48(b) show the estimated rigid body rotational movement of the north and south sides of the bridge

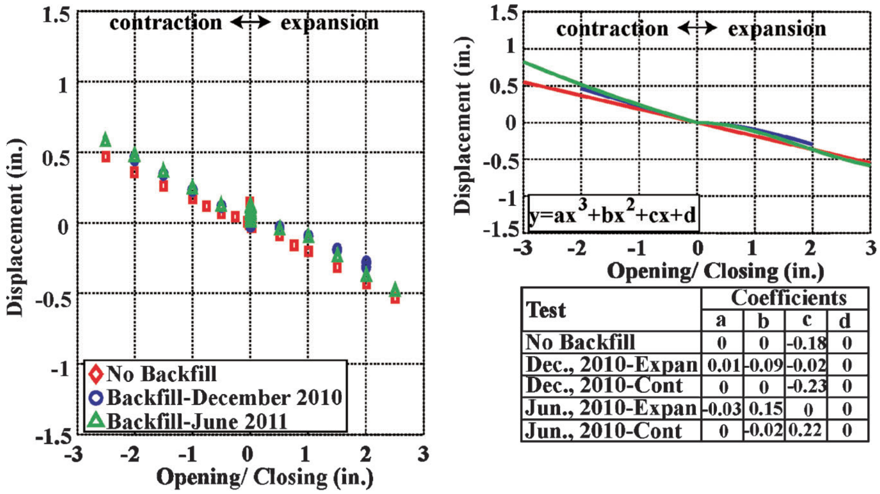

Test	Coefficients			
	a	b	c	d
No Backfill	0	0	-0.18	0
Dec., 2010-Expan	0.01	-0.09	-0.02	0
Dec., 2010-Cont	0	0	-0.23	0
Jun., 2010-Expan	-0.03	0.15	0	0
Jun., 2010-Cont	0	-0.02	0.22	0

a- North Side

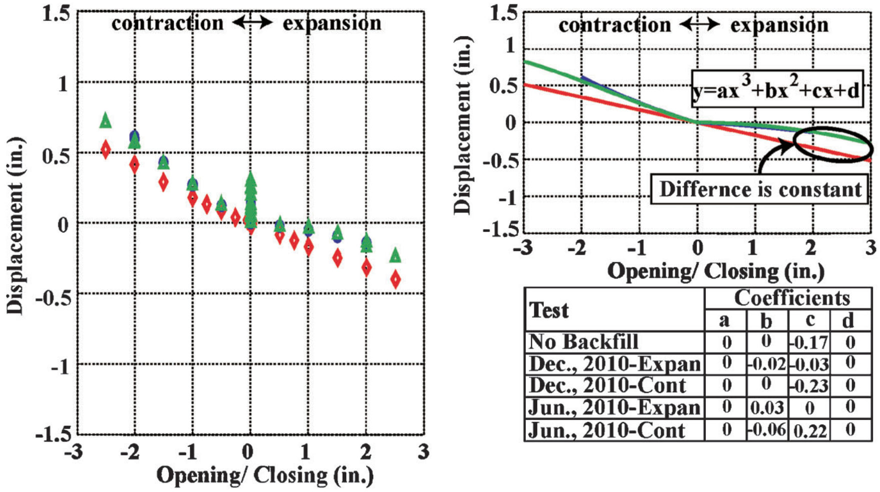

Test	Coefficients			
	a	b	c	d
No Backfill	0	0	-0.17	0
Dec., 2010-Expan	0	-0.02	-0.03	0
Dec., 2010-Cont	0	0	-0.23	0
Jun., 2010-Expan	0	0.03	0	0
Jun., 2010-Cont	0	-0.06	0.22	0

b- South Side

Figure B.47 Bridge deck rigid body transverse movement.

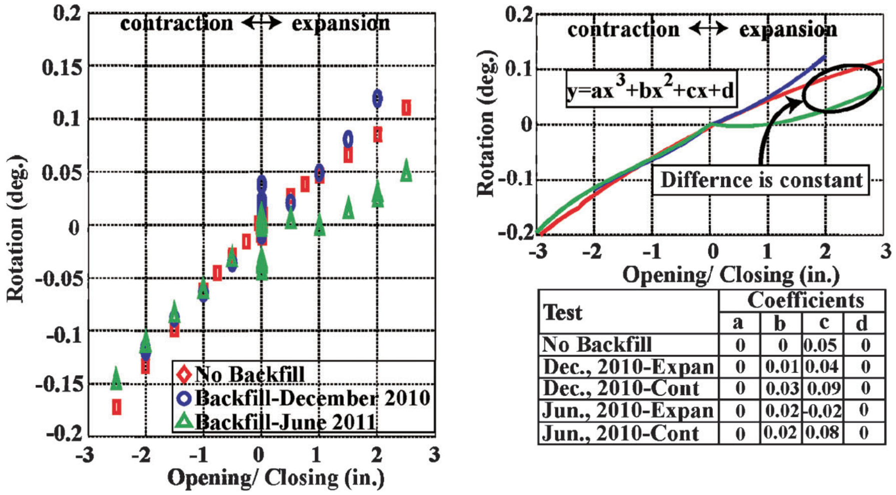

Test	Coefficients			
	a	b	c	d
No Backfill	0	0	0.05	0
Dec., 2010-Expan	0	0.01	0.04	0
Dec., 2010-Cont	0	0.03	0.09	0
Jun., 2010-Expan	0	0.02	-0.02	0
Jun., 2010-Cont	0	0.02	0.08	0

a- North Side

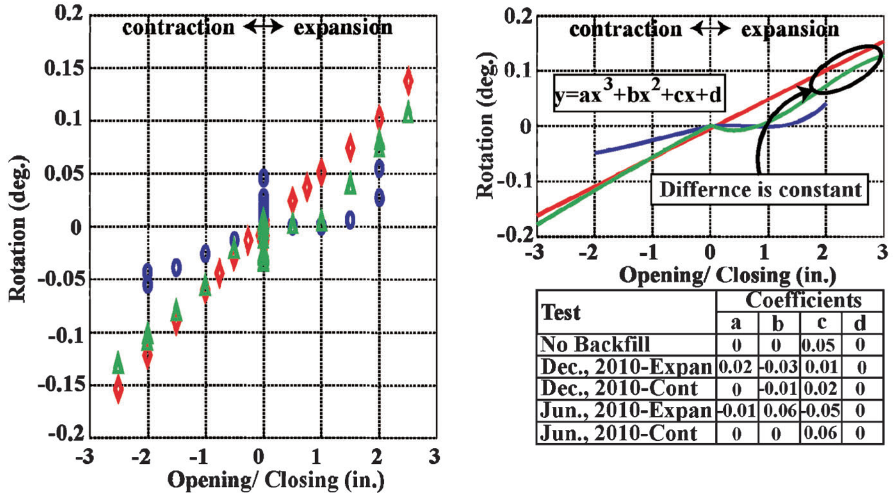

Test	Coefficients			
	a	b	c	d
No Backfill	0	0	0.05	0
Dec., 2010-Expan	0.02	-0.03	0.01	0
Dec., 2010-Cont	0	-0.01	0.02	0
Jun., 2010-Expan	-0.01	0.06	-0.05	0
Jun., 2010-Cont	0	0	0.06	0

b- South Side

Figure B.48 Bridge deck rigid body rotational movement.

deck for each test. It can be seem that the bridge deck rotated in a clockwise motion during expansion and counter-clockwise motion during contraction.

As shown, smaller rotations during expansion occurred for the case with backfill than for the case with no backfill. It should be noted that during expansion, for the case of backfill and at about a 1.5 in. gap opening, the rotational response tends to become parallel to the response of the case with no backfill. This observation supports the notion that the frictional limit between the backfill soil and the abutment wall was completely mobilized at an imposed total displacement at the gap between 1 in. and 1.5 in., as explained previously in the case of transverse movement.

During the contraction phase, the lateral earth pressure dropped rapidly to the active condition, as shown in Figures B.28 and B.39. Friction between two surfaces or frictional resistance of a granular material is dependent on the normal force acting on the two surfaces or at the contacts between particles. As such, when the lateral earth pressure dropped to its smallest value (active earth pressure), the normal force between the sand particles close to the wall or the normal force between the abutment wall and the backfill soil was reduced significantly resulting in reduced friction between the abutment wall and the soil. As established earlier, friction is a controlling factor for the difference in rotational response of the bridge deck between the case of no backfill and the case with backfill. It was anticipated that as the friction between the abutment wall and the soil is reduced, the rotational response of the bridge deck would converge to that of the bridge with no backfill. This is supported by the data plotted in Figure B.48 that shows a similar response of the cases with and without backfill during the contraction phase.

It is interesting to observe that the bridge deck rotation of the December 2010 test at the south side was less than the rotation for the June 2011 test. It is hypothesized that the differences are due to the frozen backfill during the test in December. Because the frozen backfill acts close to a rigid body, which means that the entire backfill "block" needs to rotate with the abutment wall, larger resistance to deck rotation is provided when compared with the June test. During contraction phase, however, the deck rotation of the December 2010 test at the south side was still less than the rotation of the June 2011 test. This observation can be attributed a small strain energy stored in the abutment wall-pile system during expansion. The release of this small energy during contraction caused smaller rotation during the contraction phase.

B.8.2 Pile Response

The longitudinal and transverse response of the piles at the southwest (SW) and southeast (SE) corners are compared in Figure B.49 at the end of the 2 in. displacement cycle.

As shown that the inflection point of the piles is at approximately 5 ft below the ground surface.

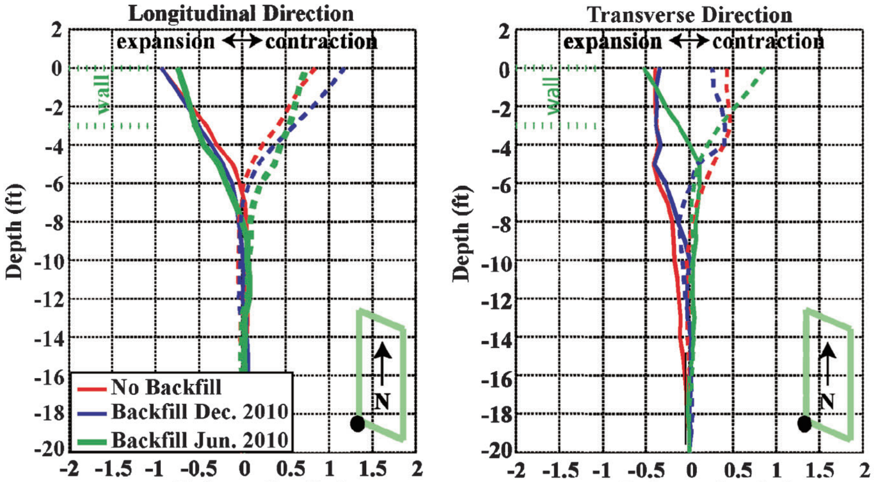

a- SW Corner (Obtuse)

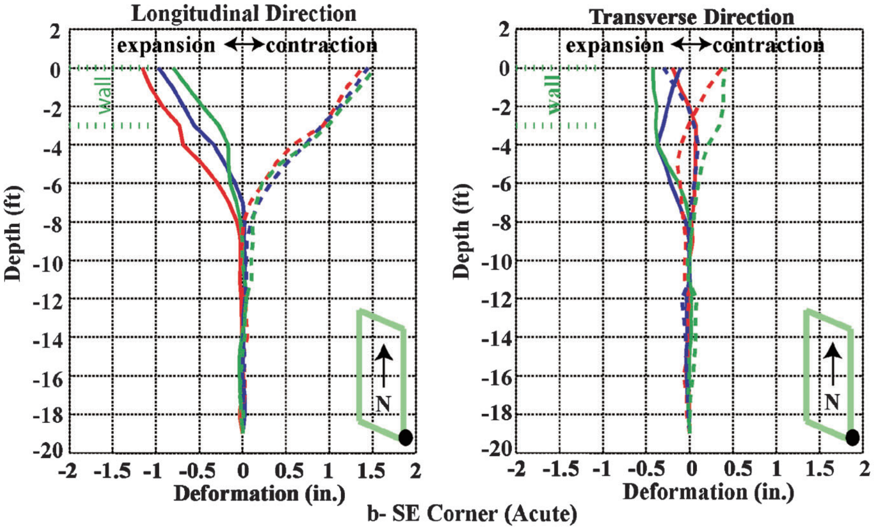

b- SE Corner (Acute)

Figure B.49 Piles response.

The abutment displacement is controlled by the type of foundation. An abutment supported on a shallow foundation moves under a rotational mode, while an abutment supported on a deep foundation moves under a translational and rotational mixed-mode (Thomson, 1999). Hence, it is interesting to investigate the effect of the abutment displacement mode on the deformation of the piles. Figure B.50 presents the southwest and southeast piles deformed shape in the longitudinal direction for the June 2011 test and for all cycles. A plot of the southeast and southwest corners longitudinal displacement at the top and bottom of the abutment is also shown, which reflects the rotational and translational components of the wall's displacement.

In Figure B.50(c), the red symbols represent the acute corner and the green symbols the obtuse corner; the triangles denote the top level and the squares the bottom level. It is clear that there is more rotation in the vertical direction at the acute corner. This behavior results in higher displacement demands on the pile at the acute corner and a steep slope of the pile's deformation shape near the ground surface. The pile at the obtuse corner, where less vertical rotation of the abutment was observed, showed uniform curvature down to the inflection point. Therefore, higher moments are anticipated at the acute corner just below the wall. In addition, the stiffer the pile was (higher EI) the higher the moment. As a result, the stiffer the pile, the more damage is anticipated at the location where the deformation gradient is the largest. This observation agrees with the conclusion by Frosch et al. (2006) who from an extensive experimental program on abutment-pile connections for H-steel piles and concrete filled tube piles (CFT) with different stiffness, found that pile deterioration was severe at the abutment-pile connection with a level of severity increasing with increasing pile stiffness.

Figure B.50 shows that at the acute corner, a higher displacement demand occurred during the contraction phase than during the expansion phase, while the opposite was true for the obtuse corner. The higher demand correlates with rigid body movements of the bridge. During contraction, the bridge moved away from the backfill soil and rotated counter-clock wise meaning that the acute corner had less constraint from the backfill soil resulting in larger deformation of the piles.

B.8.3 Pressure of Hydraulic Actuators

Two observations can be derived from the pressure applied to the hydraulic actuators. One of the observations is about the effect of the Teflon sheets that were added after the first test, and the other is about the formation of cracks at larger amplitudes. Figure B.51 plots the pressure at the end of each cycle versus the gap opening/closing. Figure B.52 displays the hysteresis of the pressure versus gap opening/closing.

During contraction, the pressures recorded for the tests with backfill, (after replacing the Teflon), were smaller than those

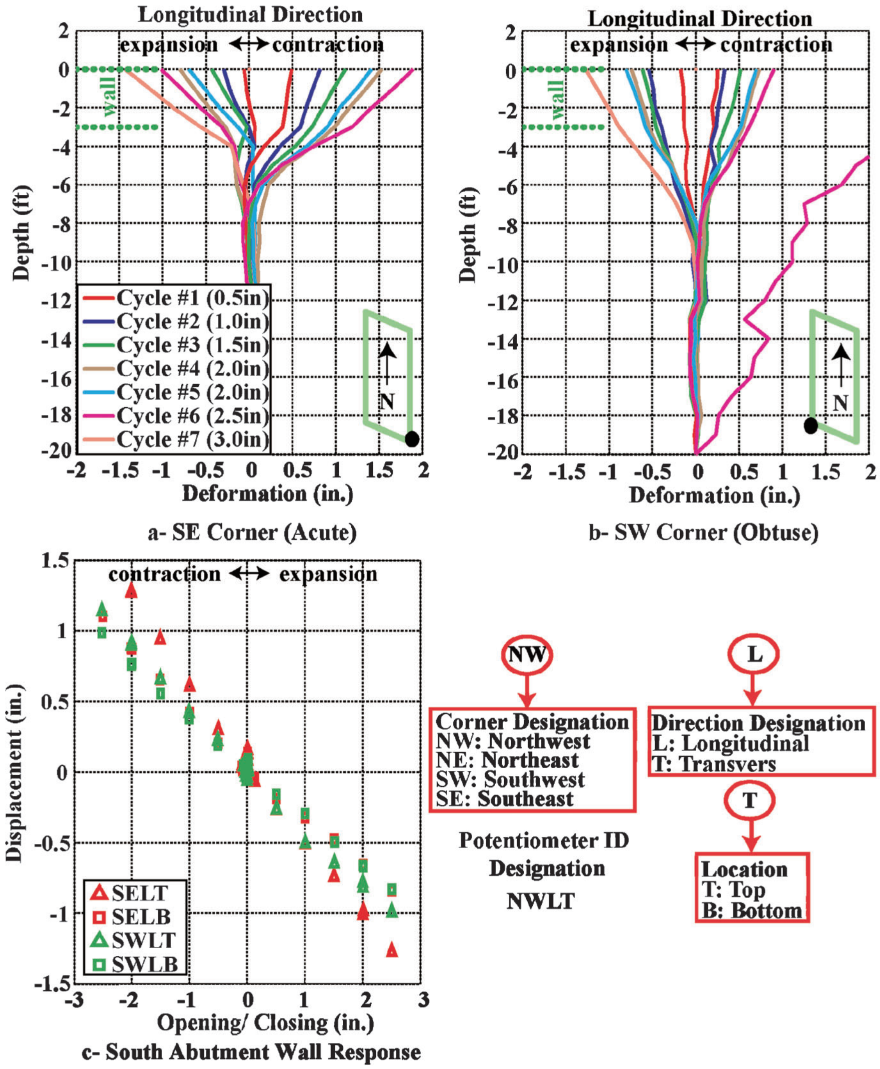

Figure B.50 Piles and abutment wall response at the south side.

recorded for the first test even though the displacement amplitudes were the same. Clearly, the tests with the backfill required higher pressures than without backfill, at least during the expansion phase. During expansion, the pressures for the test with backfill in June were either the same or slightly higher than the test without backfill. This behavior is thought to be due to the introduction of the Teflon sheets that reduced friction and compensated for the additional resistance from the backfill (note that for the December test the backfill was frozen and thus the resistance of the soil was larger).

Figure B.52 shows that after the contraction phase and after pressure release, very small displacements were recovered on the east side. For example, if the red curve at 2.5 in. amplitude is followed during the contraction phase at the east and west sides (Figure B.52(b) and B.52(d)), it can be observed that upon pressure release after contraction, the east side gap goes back to 2 in. while the west side goes back to approximately 1.5 in. This observation supports the earlier discussion on the observed cracks in the girders.

B.8.4 Lateral Earth Pressure Response

Lateral earth pressures were measured at the end of each loading sequence (four readings per cycle). Figure B.53 shows the lateral earth pressure versus displacement.

For the December test and during the expansion phase, Figure B.53 shows very small modulus degradation with displacement, as indicated by an approximately linear pressure with displacement. These observations are due to the frozen soil during the test in December. The approximately linear response of the pressures during expansion suggests an elastic response of the soil. The photos in Figure B.54 were taken during the contraction phase, where a relatively uniform gap can be seen (red arrows) after contraction, which suggests that the expansion phase was displacing a fairly rigid block of soil.

The June test showed significant modulus degradation (Figure B.53(b)). In addition, there were large differences between the pressures at the acute and obtuse corners during testing. During the expansion phase, the bridge structure rotated clockwise, which means the acute corner rotated toward the soil and the obtuse corner rotated away from the soil. Rotation toward the soil results in larger shear stresses at the acute corner when compared to the obtuse corner. This shear stress results in larger degradation of the soil stiffness at the acute corner and thus, for the same displacement, lower soil pressure will result at the acute corner. In addition, two successive cycles were conducted with the same amplitude (2 in.). A higher pressure was recorded during the second 2 in. cycle. This behavior can be explained by denser soil forming behind the wall due to the preceding contraction phase. The photos in Figure B.55 show that the backfill settled next to the wall when the wall moved away from the soil due to the

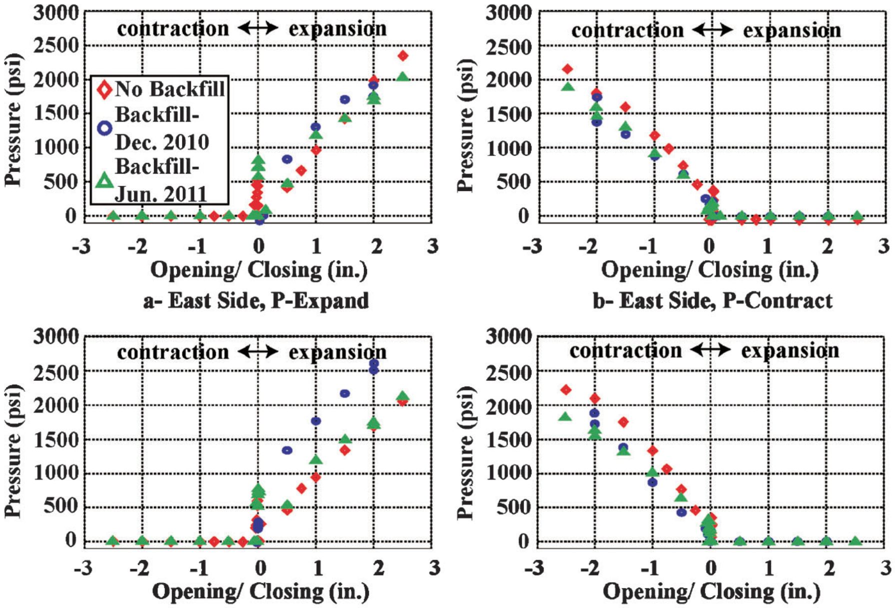

a- East Side, P-Expand
b- East Side, P-Contract
c- West Side, P-Expand
d- West Side, P-Contract

Figure B.51 Pressures at the hydraulic actuators.

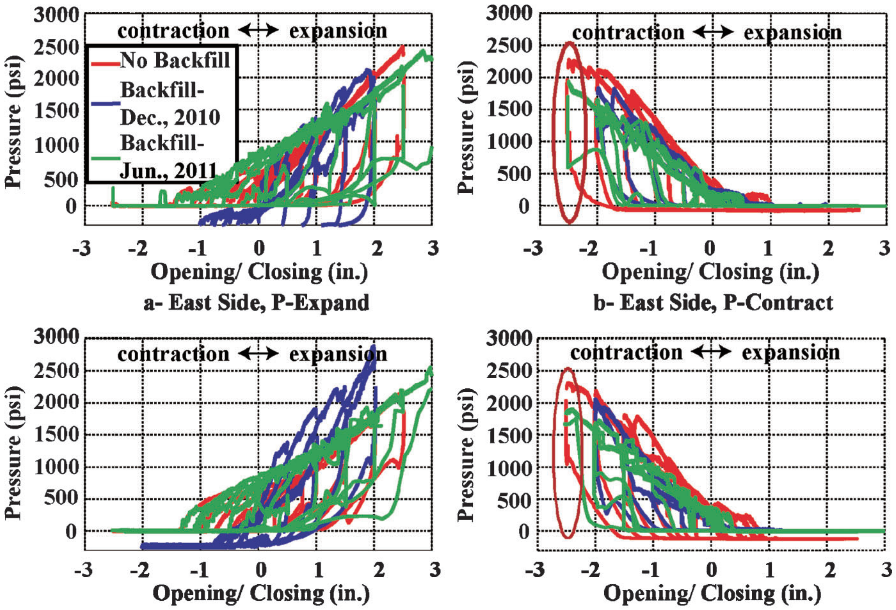

a- East Side, P-Expand
b- East Side, P-Contract
c- West Side, P-Expand
d- West Side, P-Contract

Figure B.52 Pressure hysteresis recorded at the hydraulic jacks pressure sensors.

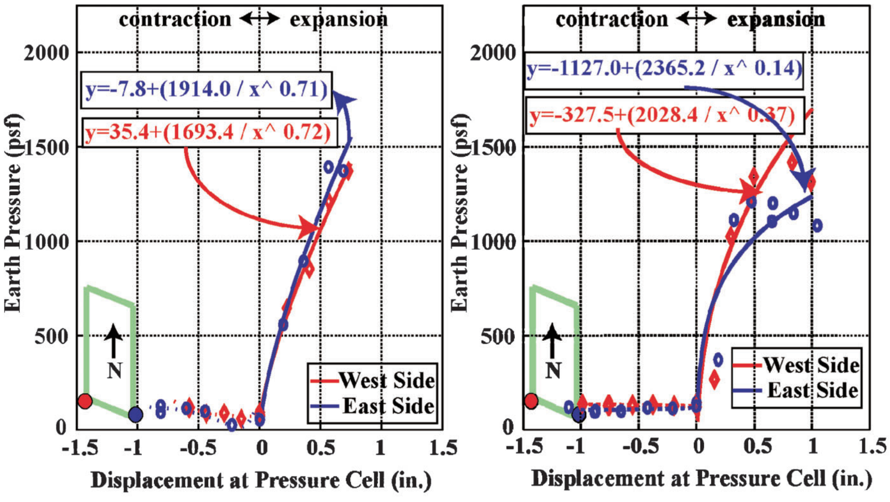

a-December, 2010 Test **b-June, 2011 Test**

Figure B.53 Lateral earth pressure versus displacement.

Figure B.54 Contraction phase in December test.

Figure B.55 Contraction and expansion phases in June test.

formation of the active wedge (red arrows). Once expansion starts, the same mass of soil (forming the active wedge) will be occupying less volume (denser state) resulting in a higher pressure. This observation was also made by several researchers (Thomson, 1999; Hassiotis & Xiong, 2007).

Figure B.56 replots the data shown in Figure B.53, but the responses from the two sides of the bridge are separated. Therefore, Figure B.56(a) plots earth pressures on the east side (acute angle) and Figure B.56(b) on the west side (obtuse angle).

As shown in Figure B.56 the freezing conditions during the December test changed the behavior of the backfill. Therefore, this test is not considered in evaluating the soil behavior for passive conditions and only the June test is considered. As explained earlier, the soil modulus on the acute side degraded faster than on the obtuse side due to bridge rotation during the expansion phase, resulting in higher pressures on the obtuse side. This agrees with the observation made by Sandford and Elgaaly (1994), which used data collected from an instrumented skewed steel bridge in Maine to recommend the use of full passive Rankine earth pressure at the obtuse corner and active Rankine earth pressure at the acute corner. In addition, at the west side, the lateral soil pressure decreased after the 2 in. cycle, which could be contributed to the mobilization of the full shear strength in the backfill soil during previous cycles. A similar observation was made by Hassiotis and Xiong (2007) who analyzed data collected from an instrumented bridge in Massachusetts and found that the lateral earth pressure coefficient would increase with displacement until it peaked, followed by a small decrease. They suggested that after the mobilization of the peak internal friction angle, and with more displacement, the internal friction angle would start approaching the critical friction angle. A lateral earth pressure coefficient of 6 (six) was observed followed by a softening of the behavior. Based on the work on this issue (Thomson, 1999) it is expected that the maximum lateral earth pressure coefficient should be a function of the initial relative density.

Figure B.56 also shows that during the contraction phase, the pressures were very small. The active pressure was mobilized during the first cycle (0.5 in. amplitude cycle). Therefore, pressures during subsequent contraction phases remained unchanged. The photos in Figure B.55 illustrated the active wedge (red arrow).

B.9 CONCLUSIONS

Based on the field tests and measurements, it can be concluded that:

1. Skew angles impose transverse and rotational movements to the deck, in addition to the longitudinal movements expected from expansion or contraction due to thermal effects.
2. The presence of backfill introduces friction between the soil and the abutment, which reduces the rotational and transverse movements during the expansion cycles.
3. Displacement demands on the piles are controlled by the rigid body movements of the bridge, namely longitudinal translational and rotational.
4. The orientation of the piles along the weak axis is beneficial in preventing high stress concentrations at the pile-wall connection (fixed connection).

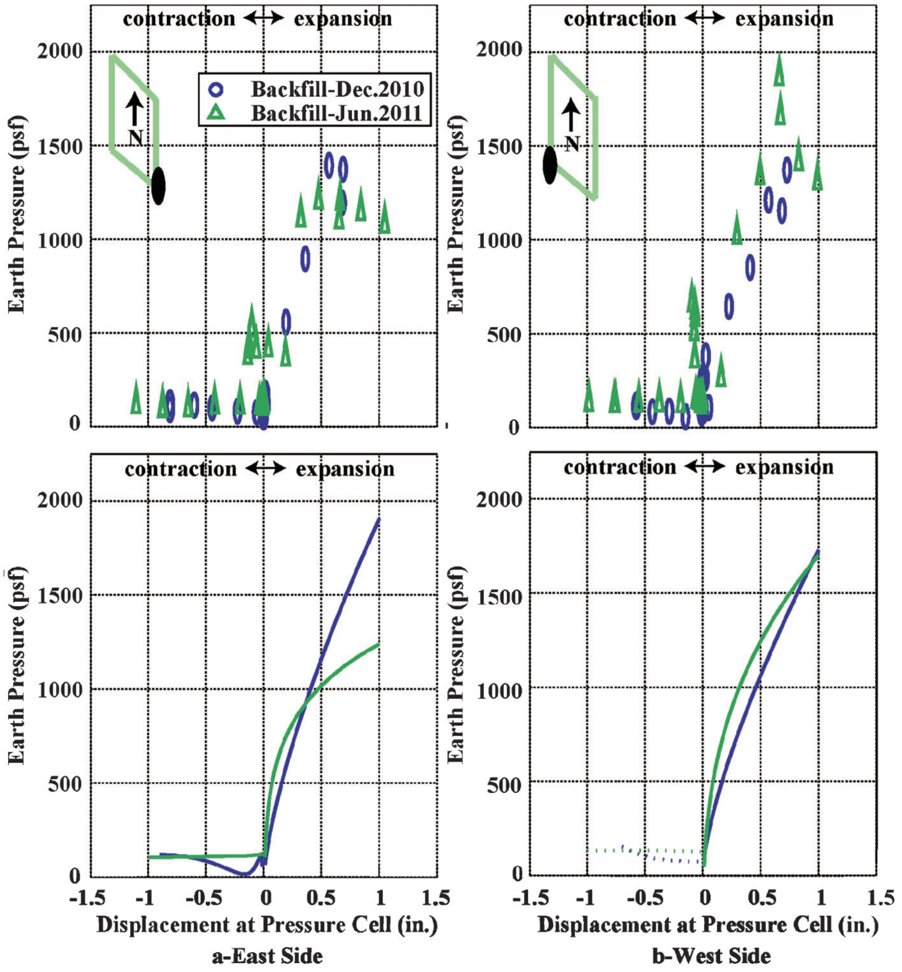

a-East Side

b-West Side

Figure B.56 Lateral earth pressure versus displacement.

5. During cold weather and if the soil is frozen, contraction may generate a “gap” at the soil-wall interface. This behavior was observed during the December (winter) test.
6. Settlement in the backfill at the abutment wall is an indication of the active wedge formation during the contraction phase. This behavior was observed during the June (summer) test.
7. Soil pressures at the obtuse corner of the abutment are larger than at the acute corner due to the larger degradation of the stiffness at the acute corner due to rigid body rotation during expansion.
8. Lateral earth pressure coefficients as high as six may be reached.

B.10 REFERENCES

Frosch, R. J., Chovichien, V., Durbin, K., & Fedroff, D. (2006). *Jointless and smoother bridges: Behavior and design of piles* (Joint Transportation Research Program Publication No. FHWA/IN/JTRP-2004/24). West Lafayette, IN: Purdue University. http://dx.doi.org/10.5703/1288284313379

Frosch, R. J., & Lovell, M. D. (2011). *Long-term behavior of integral abutment bridges* (Joint Transportation Research Program Publication No. FHWA/IN/JTRP-2011/16). West Lafayette, IN: Purdue University. http://dx.doi.org/10.5703/1288284314640

Hassiotis S., & Xiong, K. (2007). *Deformation of cohesionless fill due to cyclic loading* (SPR ID# C-05-03). Hoboken, NJ: Stevens Institute of Technology.

Sandford, T. C., & Elgaaly, M. (1994). Skew effects on backfill pressures at frame bridge abutments. *Transportation Research Record*, *1415*, 1–11.

Thomson, T. A. (1999). *Passive earth pressure behind integral bridge abutment* (Unpublished doctoral dissertation). Amherst: University of Massachusetts Amherst.

APPENDIX C. LABORATORY TESTING

C.1 INTRODUCTION

This chapter presents and documents the results of a small-scale test that simulates the movement of an abutment wall of an integral abutment bridge. The purpose of the tests is twofold. One, to understand the granular backfill behavior under low frequency cyclic movement of the abutment wall; and two, use the test results to calibrate the constitutive model.

A special apparatus was designed and built in the lab to conducts the tests. The apparatus consisted of a moving element to simulate the wall, and fixed elements for the boundary conditions. Uniform sand from Wedron, IL was used in all the tests. The apparatus was instrumented such that the applied horizontal displacements at the wall, the force imposed, and the displacement field of the sand was continuously recorded. A detailed description of the apparatus, instrumentation, sand characterization and test setup will be presented in Sections C.2, C.3, and C.4.

A total of fifteen (15) tests were conducted using the testing apparatus. The tests reflect different wall configurations (skew angle), wall conditions (smooth and rough), cycles' amplitude and loading pattern. The details of each test and the results will be presented in Section C.5.

The results from different tests will be compared and discussed in Section C.6. The key observations will be presented in Section C.7.

C.2 APPARATUS DESIGN AND INSTRUMENTATION

In order to simulate the movement of an integral abutment bridge wall under controlled boundary conditions, a special apparatus was designed. The apparatus consisted of moving elements to simulate the wall movement and fixed elements to simulate boundary conditions ("far field"). Figure C.1 shows a photo of the testing apparatus. In essence, the moving elements are the front, the sidewalls and the bottom plate. These three elements are rigidly connected and move together. As they move, they push the sand towards the end of the apparatus, where the fixed end is placed. This design avoids gaps or contacts near the wall that could affect the response of the soil close to the wall and places them at the far end. To further minimize friction between the sand and the walls, a sheet of Teflon was attached to the walls. The apparatus design facilitated changing the wall angle to investigate the effect of bridge skew angle on sand behavior. Furthermore, the apparatus allowed changes of the roughness of the wall to investigate the effects of rough and smooth surfaces.

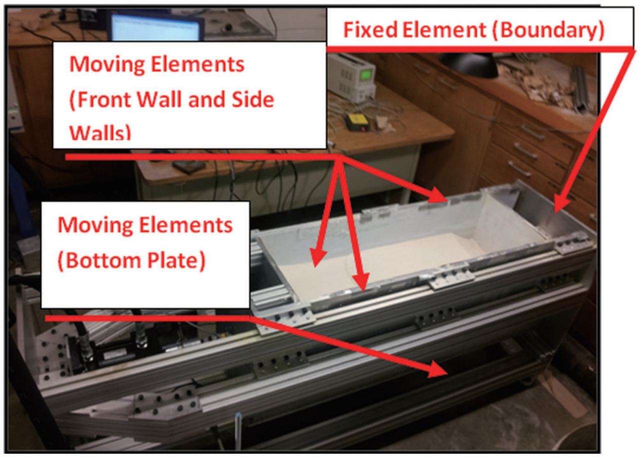

Figure C.1 Testing apparatus.

C.2.1 Geometry Selection

The apparatus dimensions were selected such that the boundaries would have minimum effect on the response of the sand that was used as backfill. The effects of the boundaries on the specimen were examined with the Finite Element model Abaqus explicit. The constitutive model developed for this study was used as a user-defined material. The model is three-dimensional, incorporates plasticity and obeys the Drucker-Prager yield criterion with unassociated flow rule. The constitutive model is based on a hyperbolic relationship between strains and stresses with different initial slopes for the unloading/reloading curves. A schematic of the stress-strain relationship used in the model is shown in Figure C.2. The model requires ten parameters, four of which are nonphysical. Detailed formulation of the constitutive model is presented in Chapter 5.

The purpose of the numerical model was to simulate a moving wall representing the abutment wall, the far field boundary simulated by the back plate, the soil represented as continuum, and side walls that are the lateral boundaries of the soil. The interaction between different elements of the apparatus and the soil was set to be rough, with a friction coefficient of 0.3 to account for any friction between the sidewalls and the soil. Since the problem of integral abutment bridges is driven by displacements, the numerical simulation was displacement controlled. The prescribed displacement was applied at the front wall as a function of time. The model elements and the dimensions of the simulated soil continuum are shown in Figure C.3. The figure depicts the front wall and the sidewalls that are rigidly connected and thus move together. However, it should be noted that this model was performed on an earlier version of the design, where the bottom plate was fixed to the back plate. As the front and sidewalls move, there is friction along the contacts between these elements and the back plate (top of Figure C.3 for contacts between sidewalls and bottom of Figure C.3 for contact with bottom plate).

The apparatus elements were simulated as steel with elastic properties, while the soil was modeled as elastoplastic using the user-defined constitutive model. The soil model parameters were selected based on model calibrations conducted for a Direct Simple Shear (DSS) test on sands published in the literature (Pradhan, Tatsuoka, & Sato, 1989). Details of different calibrations conducted for the model are presented in Chapter 6. The model parameters used for the simulations are presented in Table C.1.

The objective of the numerical simulations was to examine if the length and width of the soil sample was sufficient to avoid boundary effects caused by friction between the sand and the box, and between the moving and the fixed elements. Figure C.4 shows contour plots of horizontal displacements when a 0.2 in. displacement is imposed to the front wall. What can be seen in the figure are the displacements along a vertical section through the middle of the sand.

Based on Figure C.4, it can be observed that the displacement gradients are distributed along the sand with no steep gradient

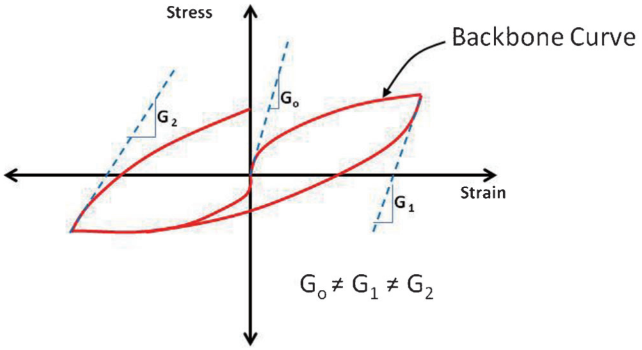

Figure C.2 Schematic of the stress-strain relationship used in the constitutive model.

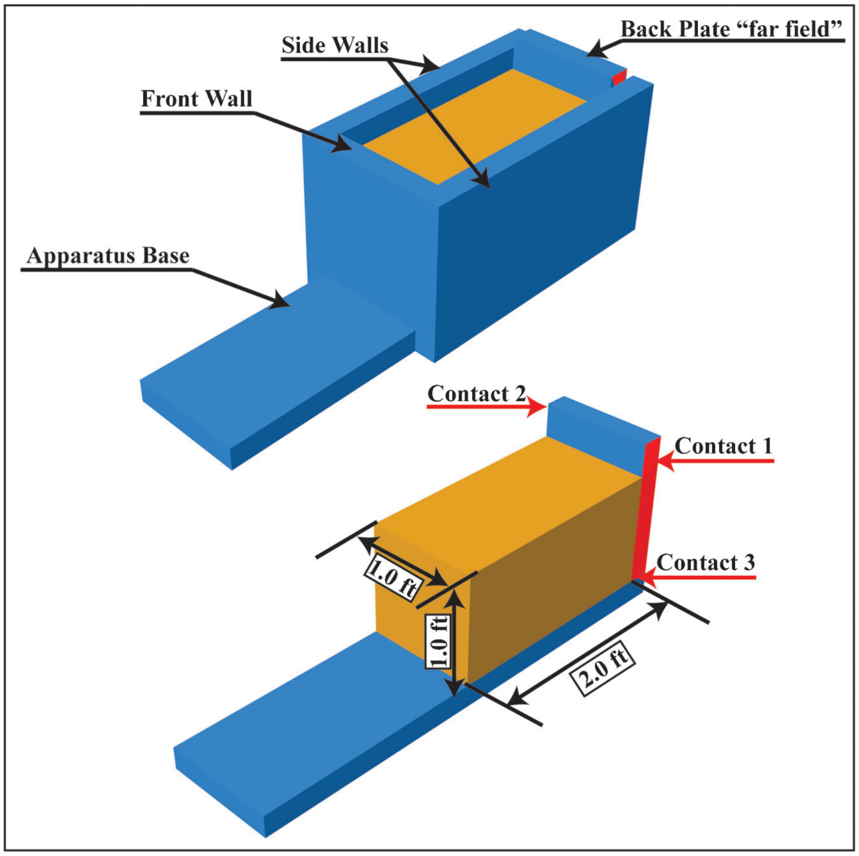

Figure C.3 Abaqus© model element and dimensions.

towards the back plate (imposed zero displacement boundary) and that the largest displacements occur within a volume of soil close to the wall, which is the area of interest. This observation suggested that the length was sufficient and the boundary at the back of the sand had minimum effect on the test.

To examine if the width of the sand was sufficient, the shear stress distribution across the soil was investigated. Figure C.5 shows contours of the shear stresses for a maximum wall displacement of 0.2 in.

The maximum shear stresses ranged from 40 psf to 190 psf and were obtained at the corners. This is expected because of the singularity that occurs at mathematical corners. Shear stresses were also found close to the walls because of the friction between the sand and the wall (as mentioned, a coefficient of friction of 0.3 was used for the simulations). What is important to note is that there is a large volume of soil around the center of the specimen where there are no significant shear stresses. Based on the finite element analysis results, it was decided that a sand specimen with dimensions 2 ft long × 1 ft wide × 1 ft tall would be sufficient to minimize boundaries effects. Note that a coefficient of friction of 0.3 was thought to be an unreachable upper bound since all the walls were coated with Teflon sheets to minimize friction with the sand.

After the dimensions selection, a few design iterations were made to explore different configurations for the new apparatus, to identify potential problems such as the possibility of looing sand through the contact areas between the moving and fixed elements, and possible friction forces between the apparatus elements. It was

TABLE C.1
Model Parameters Used in Abaqus© Simulation for the New Apparatus

Material	Steel	Soil
Model	Elastic	Elastoplastic
E (psf)	4.17e9	
G_o (psf)		4.5e5
υ	0.27	0.3
α (°)		43
κ (psf)		10
σ'_m(psf)		98
a		-0.7
b		0.1
n1		2
n2		1.8
ψ(°)		1.0

Where: E is the elastic modulus,
G_o is the reference small strain shear modulus,
υ is Poisson’s ratio,
α and κ are the Drucker-Prager material constants,
σ'_m is the reference effective mean stress,
a, b are fitting parameters for the degradation curve,
n1 and n2 are the parameters controlling the initial slope for the unloading/reloading curves,
and ψ is the dilation angle.

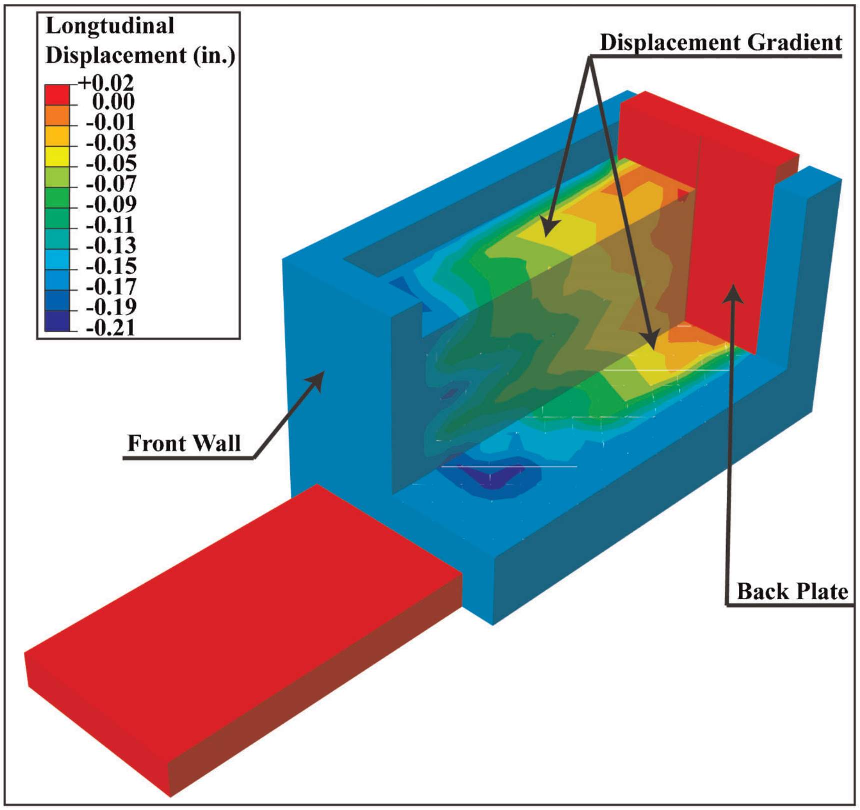

Figure C.4 Displacement gradients from the Abaqus© model of the proposed apparatus.

decided to minimize the number of contacts between the moving and fixed elements of the apparatus, and so the sidewalls, front wall and bottom wall were connected and designed as a rigid element, as shown in Figure C.3. The design was further modified to allow the installation of walls with three different angles (0°, 45°, and 60°). The design drawings are shown in Figure C.6.

Figure C.6 shows the four main components of the apparatus:

1. The outer frame, which provided the reaction required. The back plate and the hydraulic jack were attached to the outer frame with full fixity.
2. The inner frame, which contains the sand, consists of the front wall, the side walls and the apparatus base. The inner frame has one degree of freedom that allows only translational movement in the longitudinal direction. The other degrees of freedom were suppressed by the guiding steel angle that has Teflon parts to connect the inner frame with the rails on the outer frame; the detail of the angle is shown in Figure C.6.
3. The back plate. It is fixed to the outer frame and has three contacts with the inner frame; two with the sidewalls and one with the bottom plate.
4. The fourth element is the abutment wall. This element consists of a rigid steel plate that can have an angle of zero degrees (0°) (measured perpendicular to the direction of displacement), forty-five degrees (45°) or sixty degrees (60°), as shown in Figure C.6. All steel plates used in the apparatus were half inch (0.5″) thick.

In addition, Teflon sheets were used to cover the side walls, apparatus base, back wall and abutment wall (if a smooth wall is desired) to minimize friction between the walls and the sand. Also, aerosol Teflon was applied before each test on all contact surfaces, and also between the Teflon on the steel angle and the rail.

The parts of the apparatus were machined at the Purdue Physics machine shop and transported to the laboratory where they were assembled.

C.2.2 Instrumentation

The instrumentation of the test was designed to record the force applied, the horizontal displacement of the wall and the deformations of the sand surface. The force was recorded with a 2000-lb Geotac load cell and the displacement with a 3 in. Linear Position Transducer (LPT). The force and displacement transducers are shown in Figure C.7. Force and displacements were continuously recorded with a Geotac Test Data Acquisition System. The data acquisition system is shown in Figure C.8.

The three-dimensional displacements of the sand surface were obtained using a stereo vision-3D camera system. The images were captured by Vic-Snap software while the Digital Image Correlation (DIC) was performed using Vic-3D software by Correlated Solutions. The advantage of using the DIC is that it provides a continuous displacement field in space and a quasi-continuous displacement field in time (the interval between images was 1 sec.). The stereo vision-3D camera system is shown in Figure C.9.

C.3 SAND CHARACTERIZATION

430 Wedron uniform silica sand was used for all the tests. Since this sand is not a standard soil, a series of physical and mechanical tests was performed. The physical tests consisted of Particle Size Gradation and maximum and minimum densities. Since the tested sand was deemed similar to Ottawa Sand, the physical tests results were compared with published results for Ottawa sand. The mechanical tests included direct shear tests at various relative densities. All tests were performed in accordance with ASTM standards.

The results of the gradation tests using mechanical sieves are shown in Figure C.10.

The results for maximum and minimum densities are shown in Table C.2.

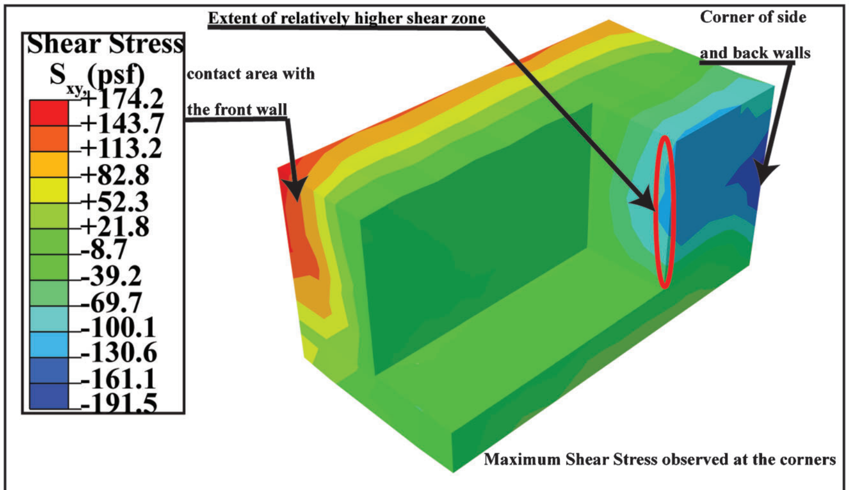

a- Shear Stress (XY Plane)

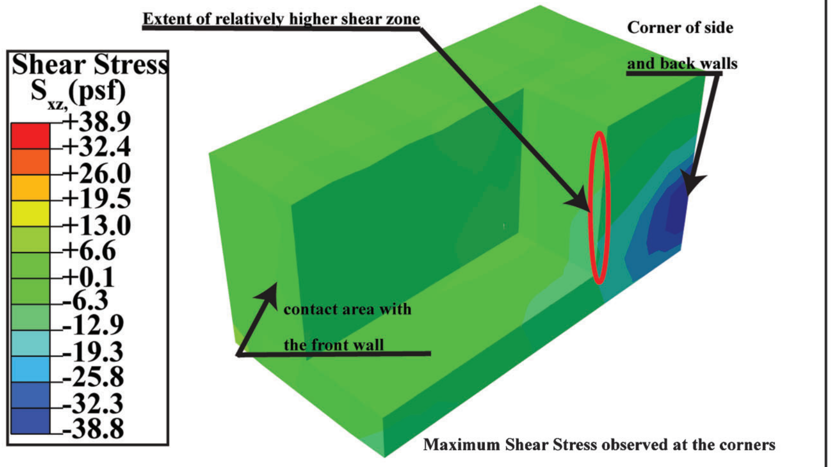

b- Shear Stress (XZ Plane)

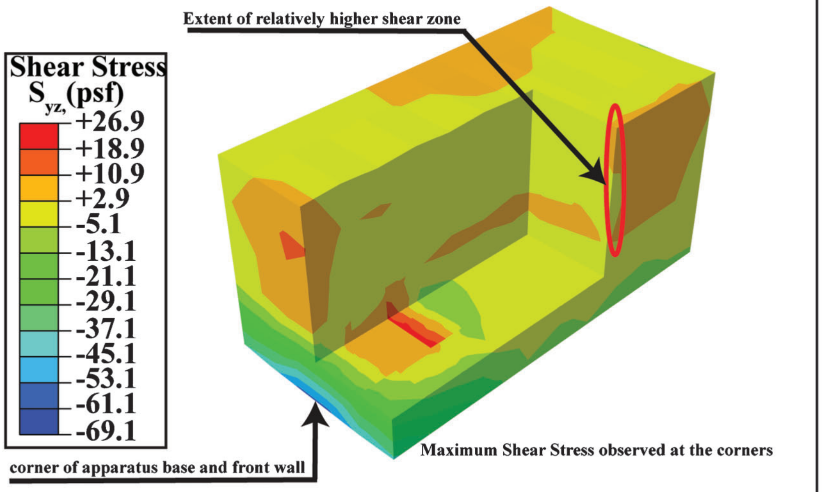

c- Shear Stress (YZ Plane)

Figure C.5 Shear stress (in psf) distribution in the sand specimen.

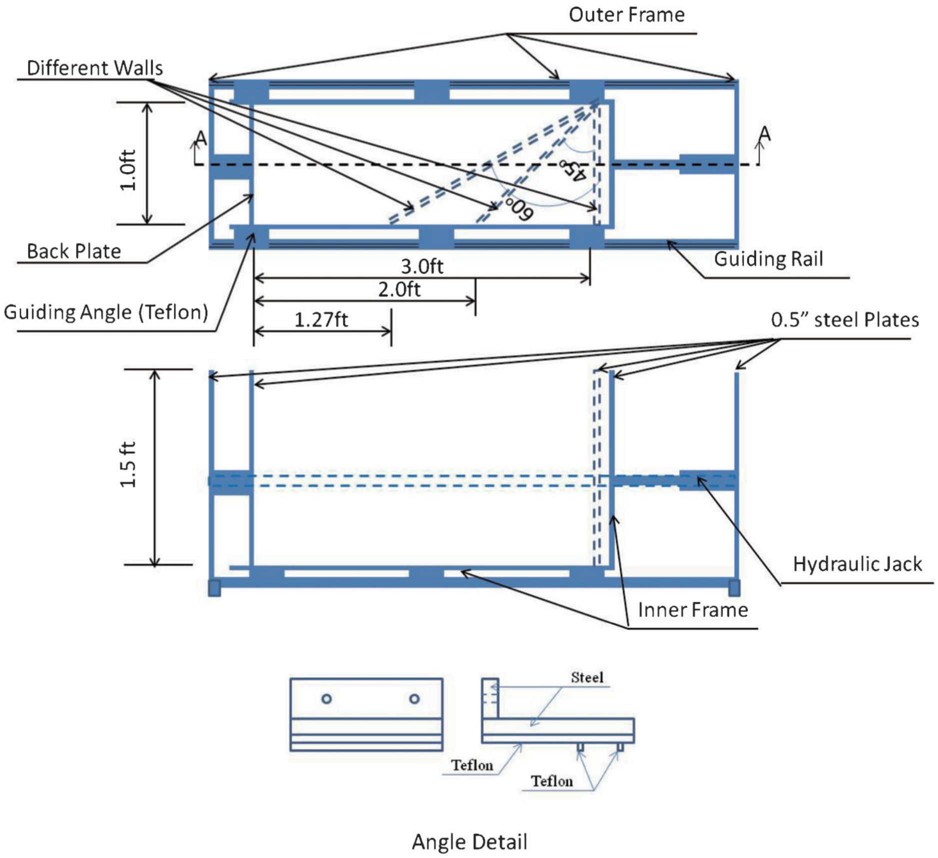

Figure C.6 Apparatus design.

The results of the direct shear box tests are shown in Figure C.11.

C.4 PRELIMINARY TESTS

A number of preliminary tests were conducted prior to the laboratory tests. The objectives were to evaluate the method for sand placement in the box, to estimate the friction that would be developed within the moving parts of the device, and finally to calibrate the 3D camera system. The following tasks were completed:

1. Compaction effort calibration, which was conducted prior to any testing.
2. A friction test before each test to record frictional forces as a function of displacement. The results from the friction tests were used to correct the measured forces.
3. Calibration of the Stereo Vision 3D Camera System before each test, to calibrate for distance from the specimen and distance between cameras.

The method of placement of the sand in the box was as follows: a layer of sand was placed first, about 4 in thick and compacted by

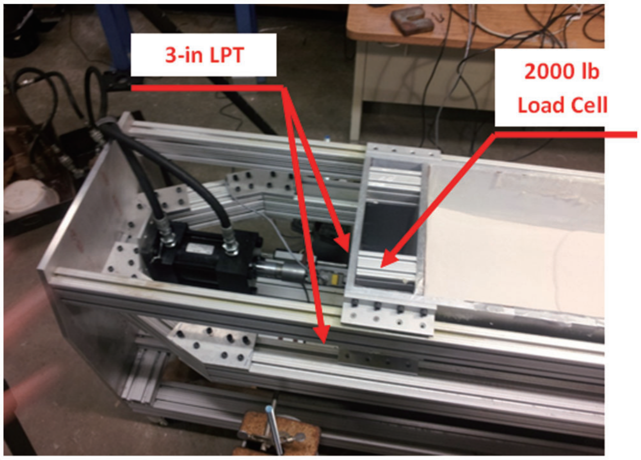

Figure C.7 Force and displacement sensors.

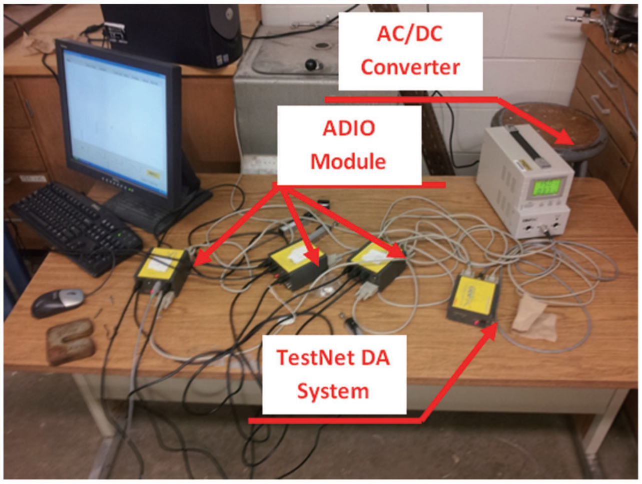

Figure C.8 Data acquisition system.

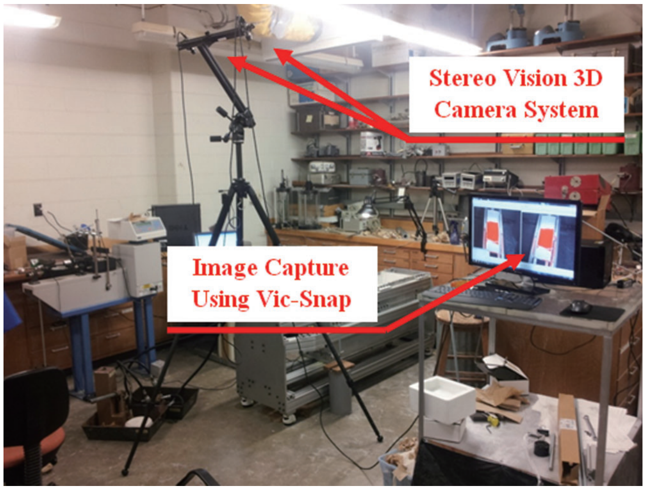

Figure C.9 Stereo vision-3D camera system.

repeatedly dropping a weight of about 4lb from a 4 in. height. A second layer was then placed and the compaction repeated. The process was followed until the full height of the sand was reached. Preliminary compaction tests were done to investigate the compaction effort that was needed and the uniformity achieved through the volume. To do this, ten (10) containers with a known volume were placed within the sub layers prior to compaction. After the entire specimen was compacted, the containers were retrieved and weighed. The maximum and minimum densities in Table C.2 were used to estimate the in-situ relative densities achieved. A number of the calibration tests were performed by changing the number of blows per sub layer. The results of the compaction tests are presented in Figure C.12. It should be noted that each test was repeated twice for repeatability; this resulted in a standard deviation of the relative densities from the ten containers of less than 3%.

Based on Figure C.12, it was decided to use 4 blows per sub layer as the compaction effort, which would result in a relative density of the order of 30%–35%. This represents the relative density of a soil next to the bridge abutment.

The friction developed within the equipment was measured by running a test with no sand, but with a weight inside the box close to that of the sand in a typical test. An example of a friction test is shown in Figure C.13. A friction test was always done before any of the regular tests.

TABLE C.2
Maximum and Minimum Densities for the 430 Wedron and Ottawa Sand

	430 Wedron Sand	Ottawa Sand*
Maximum density (pcf)	110.5	110
Minimum density (pcf)	93.1	92
e_{max}	0.77	
e_{min}	0.496	

*From Lambe and Whitman (1969).

The third type of preliminary tests consisted of the calibration of the Digital Imaging system. Calibration of the Stereo Vision 3D Camera System was performed using a standardized plate. The plate had circular dots with a fixed precise distance between them. After the cameras were placed in their location, and fixed in terms of distance from the specimen and distance and angle between the two cameras, images of the calibration plate were taken (20 to 25 images per calibration). The plate was moved to different locations on the apparatus and was rotated along three independent axes, as shown in Figure C.14. Given that the distance between the dots was known, the processing program was used to obtain calibration coefficients that would then be used to process the images of the sand surface obtained during the test. Figure C.14 shows an image from the calibration test.

C.5 TEST RESULTS

A total of fifteen (15) tests were conducted between May 16 and July 28, 2012. The tests reflect different skew angles (0°, 45°, and 60°), different wall condition (smooth and rough), different was displacement amplitudes (0.1 and 0.2 in.) and different displacement cycle configuration (full and half cycles). In all the tests the height of the sand was 12 in. It should be noted that tests 1 through 10 were conducted as full cycles tests. Tests 11 through 15 were only half cycles, starting with active loading, then loading back to zero displacement and then unloading. Tests 1 and 2 were repeatability tests. The purpose of the tests were to examine the response of the sand to displacement-controlled loading of 0.1 in. with a zero degree (0°) smooth wall and to check if the test setup would generate repeatable results. Tests 2, 3 and 4 had zero degree (0°) smooth walls. Test 3 was conducted to study the effect of amplitude on the observed behavior of sand since the amplitude used in test 3 was 0.2 in. Test 4 was used to study the effect of

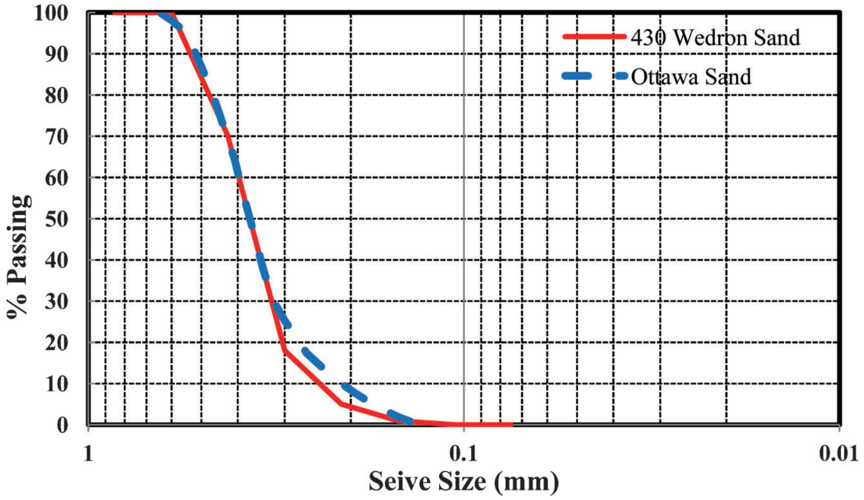

Figure C.10 Gradation curve for the 430 Wedron Sand.

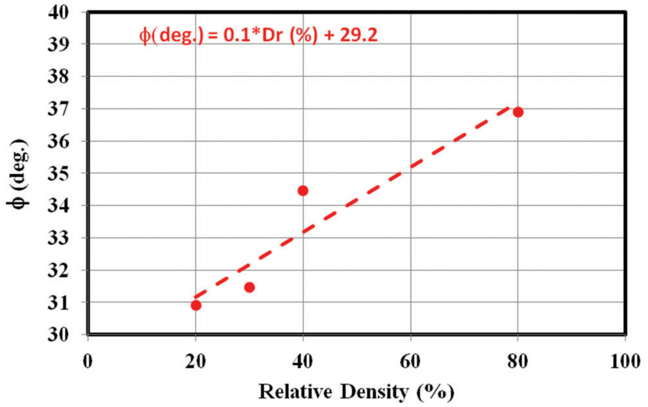

Figure C.11 Direct shear box tests for the 430 Wedron Sand.

Figure C.12 Compaction effort calibration for the 430 Wedron Sand.

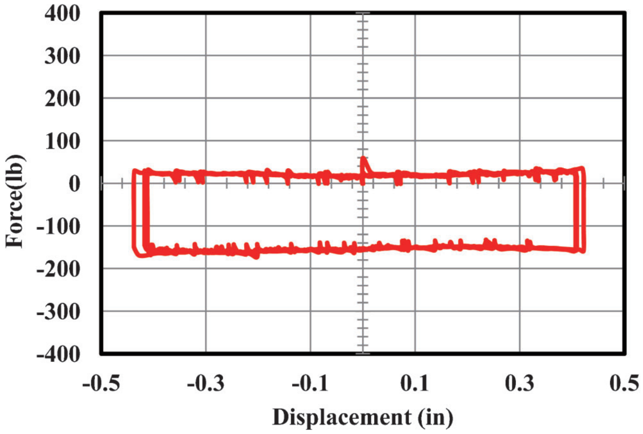

Figure C.13 Example of a friction test.

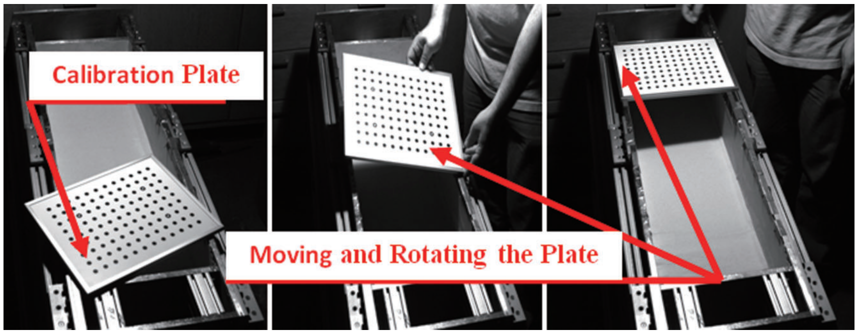

Figure C.14 Image from the calibration test.

loading sequence on the sand response; in this test a 0.1 in. displacement amplitude was applied to the same setup as tests 1, 2 and 3, but the initial cycle started at active loading (moving the wall away from the sand) instead of starting at passive loading (moving the wall towards the soil). Test 9 had similar setup, amplitude and loading sequence, as Test 1, but with a rough surface to study the effect of the wall friction on the sand response.

The effect of the wall's skew angle was examined in tests 6 and 7. Tests 6 and 7 had a smooth wall, displacement amplitude of 0.1 in. starting with passive loading, but the skew angles were sixty (60°) and forty-five (45°) degrees, respectively. In addition, wall roughness effect on the response of sand to 0.1 in. amplitude displacement was examined in tests 5 and 10 with skew angles of forty-five (45°) and sixty (60°) degrees, respectively. Tests 7 and 8 had a forty-five (45°) degree smooth wall and 0.1 in. displacement amplitude to investigate repeatability.

The half cycle tests (tests 11 through 15) were conducted to probe the sand response for loading starting from an active condition, but with a maximum displacement of zero during reloading. This was done to replicate the field cases where an integral abutment bridge would always go to a net active displacement at the end of the cycle (i.e., the displacement will not go back to zero at the end of the expansion phase). The zero degree (0°) wall configuration was examined with half cycles in tests 11, 14 and 15. Tests 14 had a smooth wall and 0.1 in. displacement amplitude, while Test 11 had a rough wall with 0.1 in. displacement amplitude and Test 15 had a smooth wall with 0.2 in. displacement amplitude. Two half cycle tests (Tests 12 and 13) were conducted on a wall with forty-five (45°) degrees and 0.1 in. displacement amplitude. The difference between the two tests is that Test 12 had a smooth wall and Test 13 a rough wall.

The rough surface was produced by attaching sand paper to the front wall; the sand paper was grit #36.

Table C.3 presents a summary of the tests.

For each of the tests, the following plots were made:

1. Force, after correction for friction, as a function of displacement.
2. Normalized volumetric changes measured at the sand surface, calculated from the Digital Image Correlation (DIC), as a function of displacement. The normalized volumetric change was obtained by calculating the volume (volume integration) of the deformed shape of the entire sand surface obtained from the DIC. The volume under the deformed shape was then subtracted from the initial volume and normalized with respect to the initial volume. A three-dimensional plot of the deformed shape of the sand surface was also made.
3. The ratio of the horizontal stress to the vertical stress as a function of the cycle number. Also, the ratio of the horizontal stress to the vertical stress versus the normalized plastic volumetric change. The plastic volumetric change is defined as the normalized volumetric change at zero displacement at the end of each cycle. Figure C.15 contains the plot for test #1, i.e., smooth wall at 0° with +/−0.1 in. amplitude. Results from all the tests are presented in Appendix C-1. A comparison between different tests and discussion of the results will be presented in Section C.6.

C.6 DISCUSSION OF THE RESULTS

This section includes a description of the results for the base case: smooth wall at 0° with displacement amplitude of +/−0.1 in. It also includes a comparison between two identical tests completed for the base case under identical conditions to evaluate test repeatability.

Test repeatability can be evaluated by comparing tests 1 and 2 and tests 7 and 8. Tests 1 and 2 are identical; both have a zero (0°) degree smooth wall with amplitude of +/−0.1 in. Tests 7 and 8 are also identical and both have a forty-five (45°) degree smooth wall with amplitude of +/−0.1 in. Figures C.16 through C.18 show the comparison for tests 1 and 2 in terms of force-displacement curves, coefficient of earth pressure and normalized volumetric changes.

Figures C.16 through C.18 show that the results from the two tests are comparable with each other, which ensures the repeatability of the results. Figures C.19 through C.21 show the comparison for tests 7 and 8. The same observation made for the 0° wall can now be made for the 45° wall, in the sense that the results are repeatable.

The results for the base case (i.e., smooth wall with zero (0°) degree and +/−0.1 in. amplitude (Test 2)) are presented in Figure C.22.

The force displacement plot in Figure C.22(a) indicates that there is an evolution of the force-displacement curves with cycles. As the number of cycles increases, the soil has a stiffer response, which results in a small upward rotation of the backbone curve. Such a stiffer response is observed up to cycle 5; afterwards the load-displacement curves are similar, but with a slight decrease of the force applied. With increasing number of cycles, a steady-state response is reached. This behavior was found in all the tests with the same amplitude regardless of the wall condition and skew angle. The increase of load up to the 5th cycle and the slight decrease are shown more clearly on the plot of the lateral earth pressure coefficient (k) as a function of the cycle number (Figure C.22(b)). The value of k increased from ~1.2 (this is the value of the force measured at the end of sand placement and compaction) to about 2.5 in. the first cycle, and then it monotonically increased with the cycles up to 3 in the 5th cycle;

TABLE C.3
Summary of the Tests

Test #	Ampl. (in)	Wall Angle (deg)	Wall Condition	Notes
1	+/−0.1	0	Smooth	Repeatability test
2	+/−0.1	0	Smooth	Repeatability test
3	+/−0.2	0	Smooth	
4	+/−0.1	0	Smooth	Starting with active
5	+/−0.1	45	Rough	
6	+/−0.1	60	Smooth	
7	+/−0.1	45	Smooth	Repeatability test
8	+/−0.1	45	Smooth	Repeatability test
9	+/−0.1	0	Rough	
10	+/−0.1	60	Rough	
11	0 to −0.1 to 0	0	Rough	Half cycle
12	0 to −0.1 to 0	45	Smooth	Half cycle
13	0 to −0.1 to 0	45	Rough	Half cycle
14	0 to −0.1 to 0	0	Smooth	Half cycle
15	0 to −0.2 to 0	0	Smooth	Half cycle

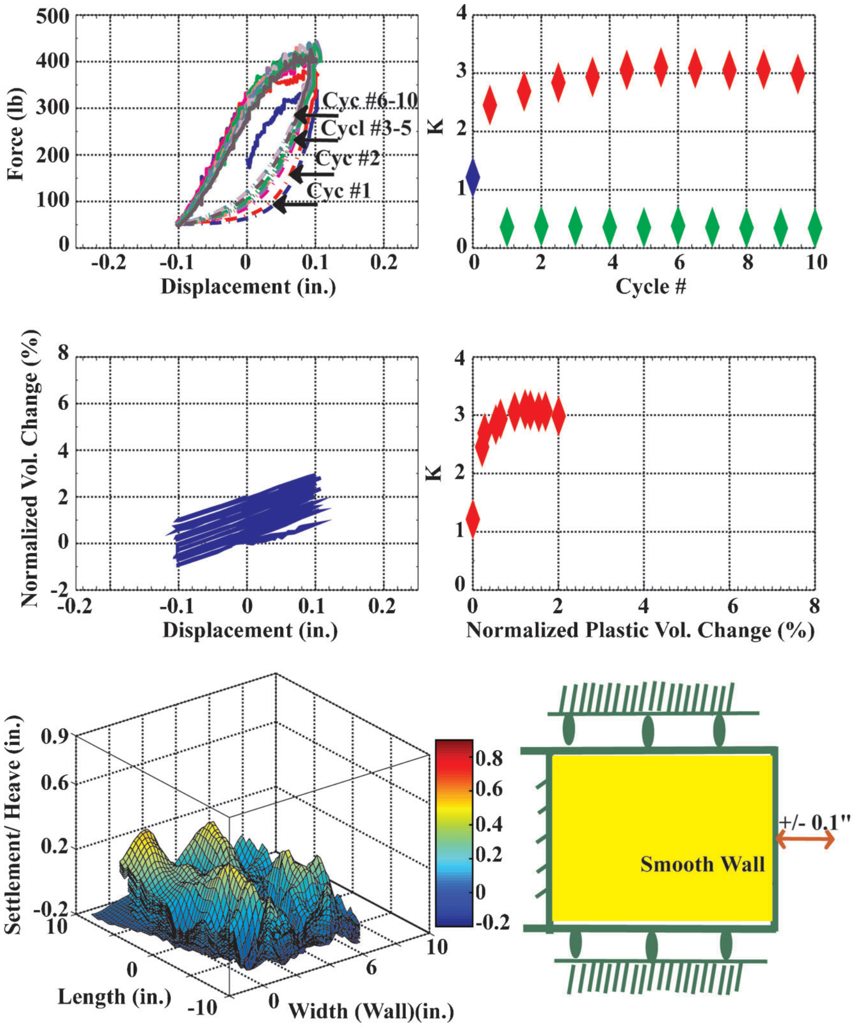

Figure C.15 Summary plot for Test #1.

then it decreased to a steady-state value of ~2.7. A similar observation was made by Hassiotis and Xiong (2007), who analyzed the data, collected from an instrumented bridge in Massachusetts and found that the lateral earth pressure coefficient increased with displacement until it peaked, and then it would go through a small decrease. Hassiotis and Xiong (2007) suggested that after the mobilization of the peak internal friction angle, and with more displacement, the sand internal friction angle would start approaching the critical internal friction angle. The value of k from the active condition remained constant at about 0.3 during the entire test. The increase of k during the passive loading cycle and subsequent stabilization after the 5th cycle could be attributed to the accumulation of plastic volumetric change in the sand. This is observed in Figure C.22(d), where at maximum k, the normalized plastic volumetric change was about 1.2% and less than 0.8% accumulated to the end of test. However, it should be noted that within the active wedge very small plastic deformations were observed after the 5th cycle, as shown in Figure C.22(g). The active wedge is about 6.5 in. from the wall (theoretical estimation is about 7 in.). After the 5th cycle, a plane of failure was developed, which resulted in the stabilization of k. The passive wedge is shown in Figure C.22(g) at about 13.5 in. from the wall (theoretical estimation is about 15.5 in.). While the displacement imposed during the forward motion was not enough to induce a failure plane (this occurred at cycle 5), the backward displacement (during the active loading phase of the cycle) was enough for yielding the sand during the 1st cycle; that is, enough to develop an active wedge.

It is interesting to point out that most of the volumetric change measured in the soil within the active wedge occurred during the first five cycles; see Figure C.22(g). The evolution of plastic strains with k shown in the Figure is representative of what was observed in all other tests. The plot of settlement/heave shows that at a given distance from the wall, large dilation was observed in the soil even after the 5th cycle. To understand the normalized volumetric change behavior, longitudinal and transverse vertical sections have been prepared. Normalized Vertical Deformations were calculated by normalizing the vertical deformation by the initial specimen thickness (12 in.) at each point within the processing area. Figure C.23 shows the Normalized Vertical Deformation and the longitudinal and horizontal displacements along three longitudinal sections: two close to the sidewalls and one through the center of the specimen.

Figure C.23 shows that at about 6.5 in. from the wall there is a sudden change in Normalized Vertical Deformation after the 5th cycle. This is in contrast to the gradual, steady increase observed from cycles 1 through 5. This is mainly due to the formation of the active and passive wedges within the specimen, as shown in Figure C.24.

It was mentioned earlier that yielding from active loading occurred during the 1st cycle, which means that an active wedge formed during the 1st cycle. The passive wedge however was not

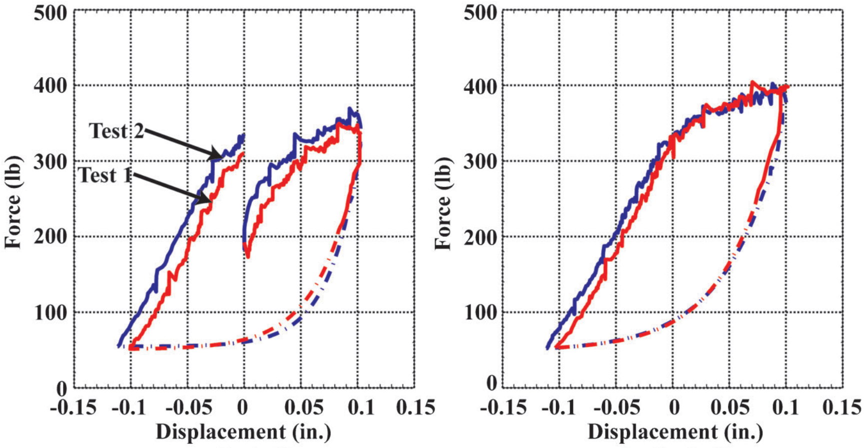

a- Cycle #1

b- Cycle #3

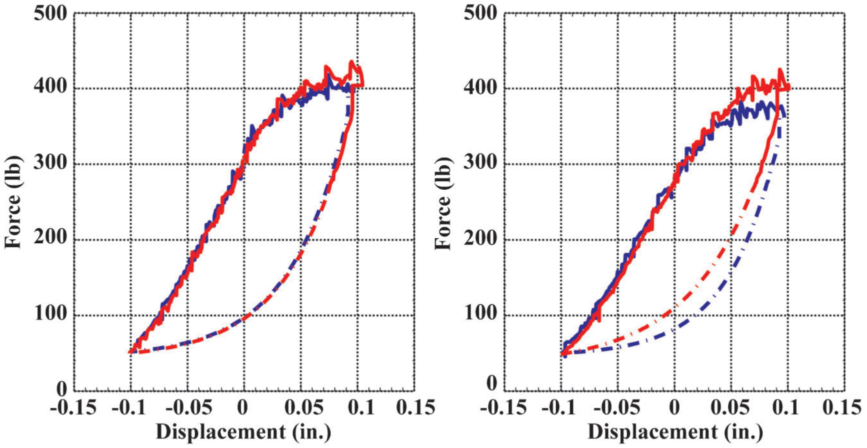

c- Cycle #5

d- Cycle #10

Figure C.16 Force versus displacement for Tests 1 and 2.

fully developed until the 5th cycle, as shown in Figure C.22(g). Hence, up to the 5th cycle deformation during passive loading did not occur along a specific failure surface but it was gradual and distributed across the entire sand volume. After the formation of the passive wedge, the vertical displacements showed a sudden change at the point where the active wedge daylights. The longitudinal horizontal displacements (Figure C.23) showed, after the 5th cycle, a change of sign during passive loading at the point where the active wedge daylights. This is interpreted as particles rolling back at this point due to the abrupt increase of the vertical deformation. In addition, it seems that after the formation of the active and passive wedges, the soil in the wedges is displacing as a rigid body along the failure plane. This can be observed in the plots of Figures C.23(d), C.23(e), and C.23(f).

Figure C.23 also shows that the Normalized Vertical Deformations along the three longitudinal sections have a different shape, especially where the active wedge is located. Two transverse sections, one at 3 inches from the wall and the other at 13 inches, are included in Figure C.25 to investigate this result.

The transverse section that is 13-in from the wall (Figure C.25(b)) shows that the difference in the Normalized Vertical Deformation between the ends of the section is not significant. In other words, the soil deformations are uniform across the section, and so the constrains that the lateral walls may place on the movement of the sand are negligible; thus, there are no frictional effects of consideration at the lateral wall-sand interfaces.

The section that is 6 in. from the front wall (the section starts 3 in. from the left side wall and ends 2 in. from the right side wall; Figure C.25(a)) shows that the strains are symmetrical with respect to the center of the wall. In addition, it appears that the distribution of the Normalized Vertical Deformation is mostly uniform up to the 3rd cycle. However, after the 3rd cycle, the distribution is not uniform as the vertical displacements increase more at the center than at the sides. This could be due to friction developing at the side walls (scratching the Teflon) or could be attributed to confinement. This can be clarified by inspection of Figure C.26.

By inspecting the distribution of the longitudinal displacement, when a +0.1″ is imposed to the wall, of the 2nd and 3rd cycles (Figure C.26(a) and C.26(b)), one can see that the gradient is uniform across the width, which could be also seen in Figures C.23(d), C.23(e), and C.23(f). However, at the 5th cycle, and at the marked location in Figure C.26(c), one can see that at the corners of the processed area the gradient of the longitudinal displacement is not uniform. There are larger displacement vectors. This effect is more pronounced in the plot for the 10th cycle (Figure C.26(d)). If this behavior was due to friction, the magnitude of the longitudinal displacement should be reversed, i.e., the displacement at the center should be larger than at the sides since friction will cause particles to resist movement. It is known that when confinement increases, dilatation decreases. As shown in Figure C.25(a), dilation at the center of the transverse section is larger than at the sides; this would possibly support the notion of larger confinement close to the corners. The confinement has also similar effects on the formation of the active wedge, as shown in the 10th cycle plot (Figure C.26(d)). The observed wedge from the image curves, as marked by the solid blue line; however, the anticipated wedge for a wall with zero skew is a

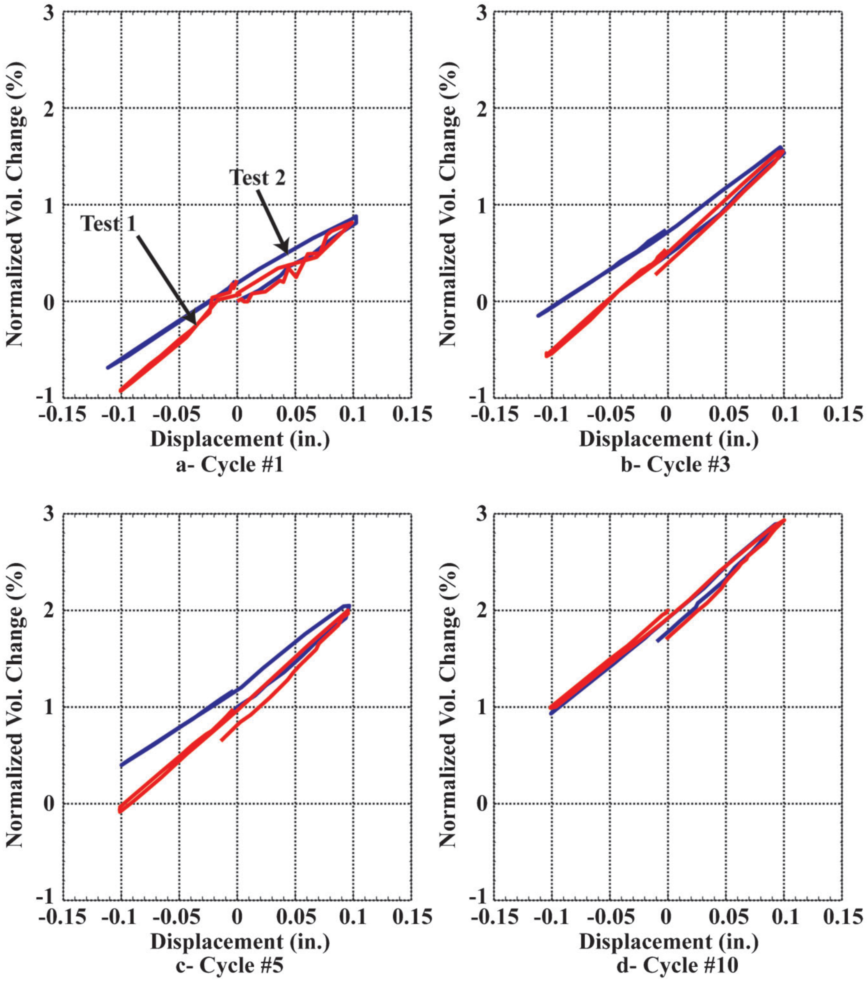

Figure C.17 Normalized volumetric change versus displacement for Tests 1 and 2.

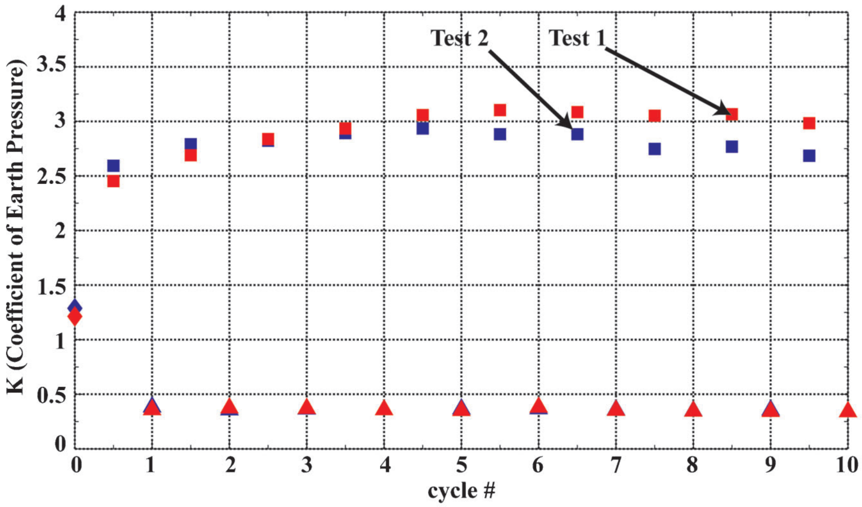

Figure C.18 Coefficient of earth pressure versus cycle number for Tests 1 and 2.

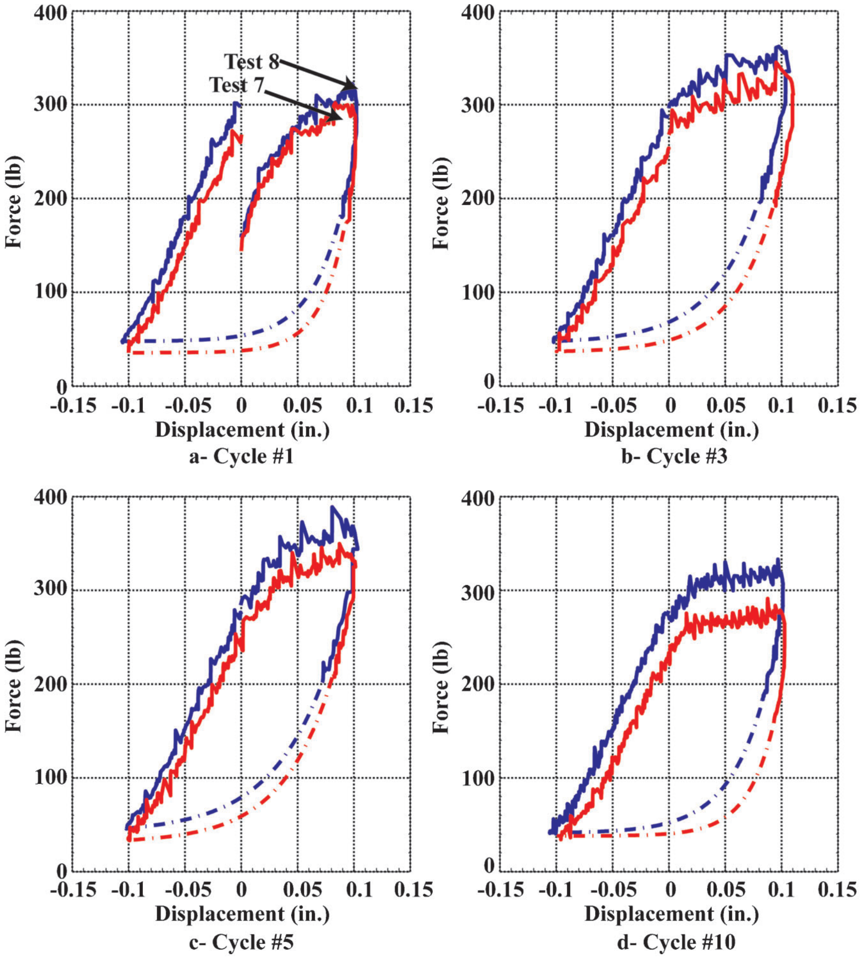

Figure C.19 Force versus displacement for Tests 7 and 8.

straight line (dotted blue). As the confinement gets larger the shear strength that is mobilized is higher (for a simple Mohr-Coulomb Material). The active wedge will form at the locations where the active shear strength is mobilized, which means that the active wedge will follow the locations of smaller shear strength, which will result in the shape shown in Figure C.26(d).

A set of plots was prepared to facilitate comparisons between different tests. The first plot (Figure C.27) summarizes the coefficient of lateral earth pressure as a function of the cycle number for all the tests (15 tests).

From Figure C.27, it can be observed that all the tests yielded during active loading during the first cycle, resulting in a relatively constant active earth pressure coefficient. However, the passive earth pressure coefficient changed with test configuration.

To investigate the effect of skew angle, tests with forty-five degrees (45°) and sixty degrees (60°) skew angles were conducted. The amplitude of the tests was +/−0.1 in. and the surfaces were smooth. The results from the tests are compared in Figures C.28 through C.31.

As with the zero degree (0°) wall test, the force-displacement plots in Figure C.28 show a marked nonlinear and hysteretic behavior, with response changing with the number of cycles. For the forty-five degrees (45°) wall, the response was stiffer with the number of cycles for the first five cycles, and then a softer response was observed, as shown in Figure C.28 (see also Figure C.30). During the test, the coefficient of earth pressure also evolved in the first 5 cycles (Figure C.30) where the earth pressure coefficient increased from 1.05 (initial stress in the soil after compaction) to 2.25 in the first cycle, peaking at 2.8 during the fifth cycle, and then softening gradually after the 5th cycle until it reached a value of 2.5 in. the 10th cycle. The normalized volumetric change (Figure C.29) showed dilation during passive loading and contraction during active loading. It is interesting to note that the total normalized volumetric change was 5%; dilation occurred gradually with cycles, with values of 1.8% during the first cycle, 2.8% at the end of the third cycle, 3.8% at the end of the sixth cycle, and finally 5% at the tenth cycle. It should be noted that the normalized vertical deformation was not uniform across the specimen. Figure C.30 shows the vertical deformations along a vertical plane parallel to the wall; for comparison, the vertical deformations obtained with the zero degree (0°) wall are also included in the figure. The vertical deformations were very small next to the obtuse corner and large next to the acute corner, with a very steep increase near the obtuse corner to the value observed at the acute corner. A comparison between the vertical deformations produced in the 0° and 45° walls (Figure C.30) clearly indicates that a skewed wall increases deformations, in this case by a factor of five.

The test with the sixty degrees (60°) showed a behavior similar to that observed for the forty-five degrees (45°) wall test. During the experiment, the coefficient of earth pressure changed in the first 5 cycles, increasing from 1.1 (initial stress in the soil after compaction) to 2.2 in. the first cycle and peaking at 2.7 during the fifth cycle; afterwards, a softening response occurred where the earth pressure coefficient dropped gradually until it reached a value of 2.3 in. the 9th and 10th cycles, as presented in Figure C.30. The normalized volumetric change showed dilation during the passive loading and contraction during the active loading, as shown in Figure C.29; it can be also observed that the normalized volumetric change was larger for the 60° wall

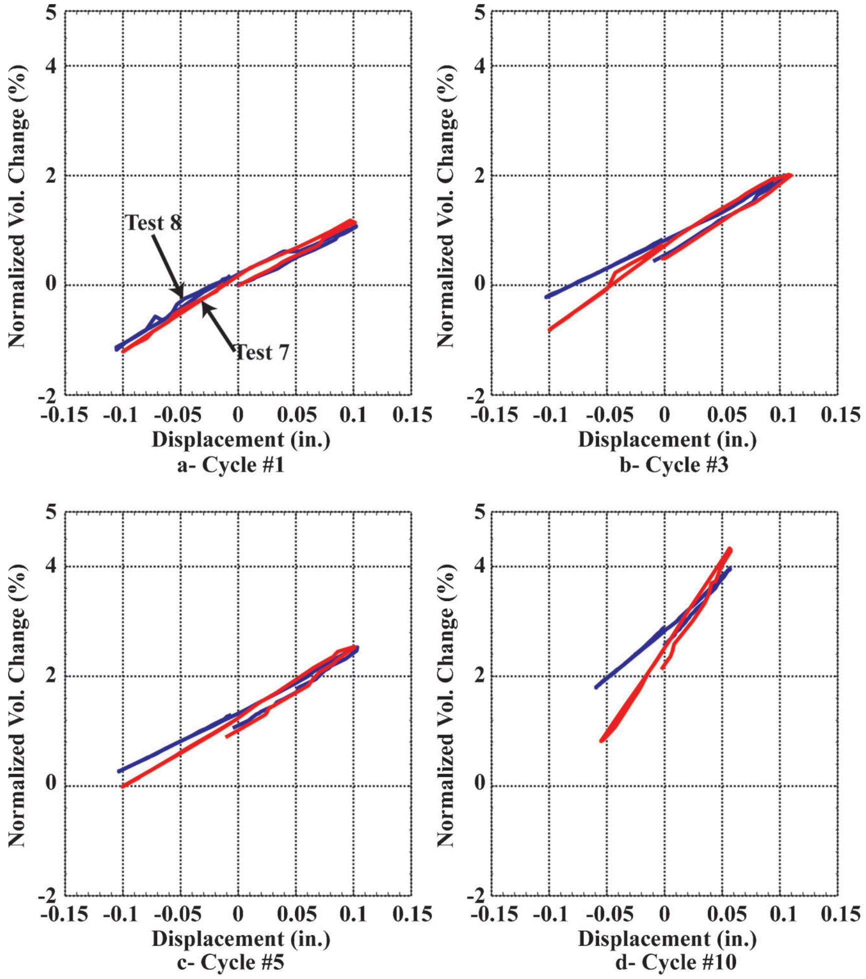

a- Cycle #1

b- Cycle #3

c- Cycle #5

d- Cycle #10

Figure C.20 Normalized volumetric change versus displacement for Tests 7 and 8.

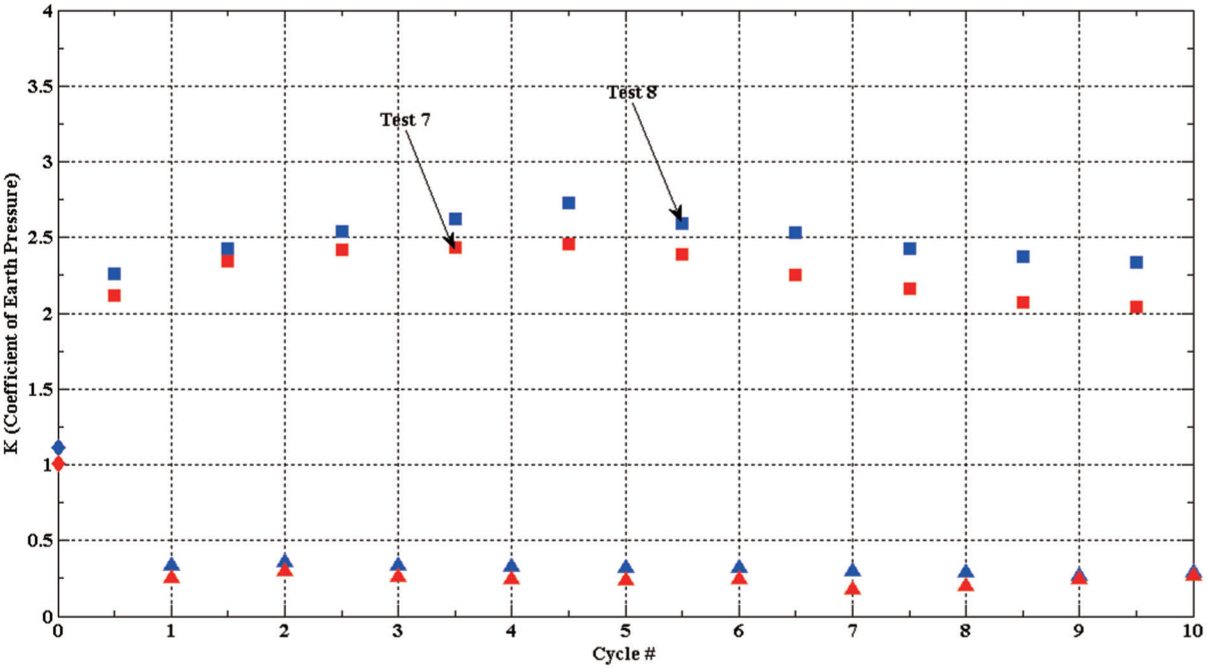

Figure C.21 Coefficient of earth pressure versus cycle number for Tests 7 and 8.

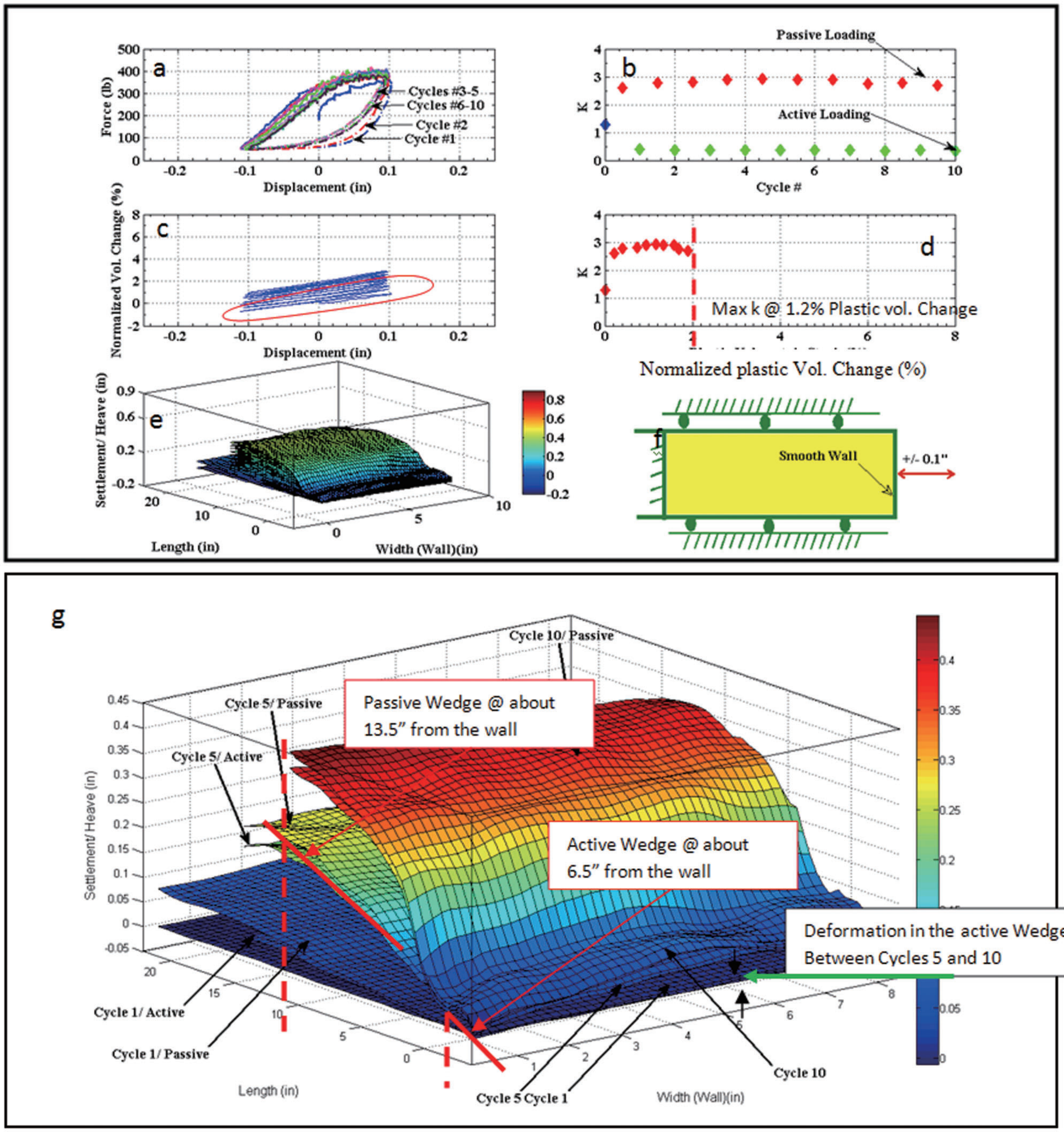

Figure C.22 Summary plot for Test #2.

when compared to the 45° wall. As shown in Figure C.29 dilation and contraction increased not only with the number of cycles, but also with the skew of the wall. As with the 45° wall, the Normalized Vertical Deformation was not uniform parallel to the wall. It had a very small vertical deformation just next to the obtuse corner, followed by a steep increase near the obtuse corner to values similar to those in the acute corner. This is shown in Figure C.32 that is a plot of the surface deformed shape for cycles 1, 5 and 10. It should be noted that for the case of the sixty degrees (60°) wall, the boundary at the back of the specimen was too close to the wall, in particular to the obtuse corner of the wall, and so the results may have been affected by the boundaries. This issue can be ascertained by inspection of Figure C.32, where the processing area is terminated at the acute corner, and so the validity of the data at this location is questionable and indicates that the corner was too close to the back boundary (<24 in.). Hence, the tests with sixty degrees (60°) may be questionable.

Figure C.28 shows that the force applied at the zero degree (0°) wall was higher than the force applied at the forty-five degree (45°) wall for the same displacement, i.e., a stiffer response was observed for the zero degree (0°) wall. Furthermore, it could be observed that at the 10th cycle, as indicated in the figure for the case of 45° skewed wall, the force dropped to a value close to that of the first cycle. The force drop (softening) for the two cases (0° and 45°) occurred after the 5th cycle; however, the softening with

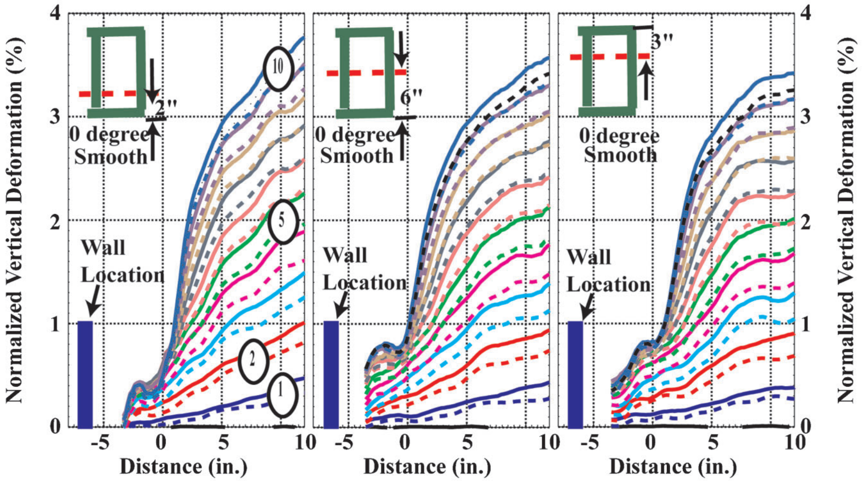

a- Section at 2in. from the left side wall-vertical deformation

b- Section at 6in. from the left side wall-vertical deformation

c- Section at 3in. from the right side wall-vertical deformation

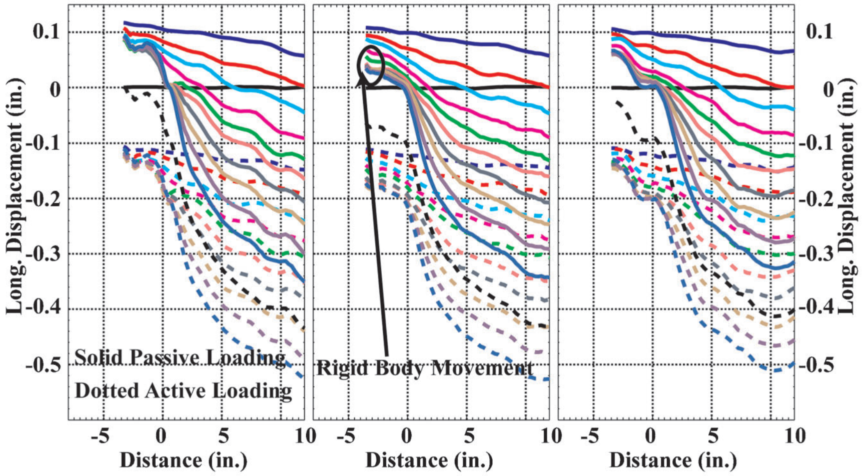

d- Section at 2in. from the left side wall-long. displacement

e- Section at 6in. from the left side wall-long. displacement

f- Section at 3in. from the right side wall-long. displacement

Figure C.23 Normalized Vertical Deformation and longitudinal horizontal displacements along longitudinal vertical sections.

the skewed wall was more significant. A similar observation can be made for the 60° wall, albeit qualitative since the values may be affected by the back boundary, as previously explained.

The observed softening response can be further explored by inspection of Figure C.30, which shows the coefficient of earth pressure as a function of the cycle number. The figure shows that the zero degree wall (0°) developed a higher earth pressure coefficient than the forty-five degrees wall (45°). This could be explained by the volume change associated with the forty-five degrees wall (45°). Figure C.29 plots the normalized volumetric change, which shows a higher dilation for the case of forty-five degree (45°) wall than the zero degrees (0°) wall. This result in a reduction of the relative density of the sand, and thus a reduction of the stiffness and internal friction angle that carries a reduction of the force required to impose a given displacement. Since the distribution of the vertical deformation behind the zero degrees wall (0°) is uniform, it is expected that the pressure from the soil to the wall is uniform. In contrast, the vertical deformations of the sand behind the skewed wall are not uniform and have the largest value at the acute corner; thus it is expected that the pressures on the wall will be the largest at the obtuse corner.

The effect of amplitude on the wall response was investigated by running additional tests where the imposed displacement was increased to 0.2 in. The tests were performed on the base case, i.e., smooth wall at zero degrees (0°). Figures C.33 through C.35 shows the results of the additional tests and provides a comparison with the base case.

Figures C.33 to C.35 indicate that the response of the wall shows similar trends even though the displacement amplitude was increased by a factor of 2. There however very important differences. First, a faster evolution/change of force with cycles. As shown in Figures C.33 and C.34, the force on the wall, for the 0.1 in. amplitude test, increased gradually from the first cycle until it peaked at cycle five. The increase was much faster for the 0.2 in. test, where the peak occurred at about cycle 2. The softening behavior was also more pronounced with the large amplitude test. The magnitude of the force, as expected, increased with the displacement. For the 0.1 in. test, the peak coefficient of horizontal pressure was about 2.5 while it was about 3.2 for the 0.2 in. test. In both cases, after the peak, the coefficient of earth pressure decreased with the number of cycles, with a much faster reduction with larger amplitude. A steady-state response was

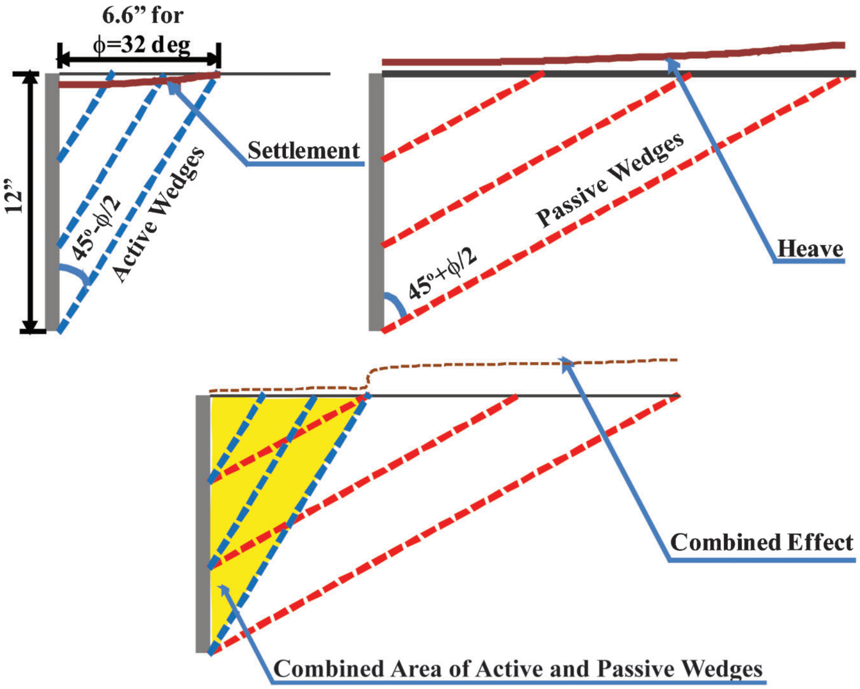

Figure C.24 Formation of active and passive wedges.

finally obtained with values of 2.0 after the 8th cycle for the base case and 2.4 after the 6th cycle for the new test. In both tests, the soil yielded during active loading. The normalized volumetric change showed dilation during the passive loading and contraction during the active loading, as shown in Figure C.35. The magnitude, as expected was larger with larger amplitude, increasing by about a factor of two with respect to the base case.

Figure C.35 shows the normalized volumetric change for the two tests. At the end of the active phase during the first 3 cycles, for the test with 0.2 in. amplitude, the net average change was settlement. The settlement amplitudes, for the 0.2 in. amplitude test, were almost twice those observed for the same number of cycles for the 0.1 in. amplitude test. This higher settlement suggests that the soil was denser before reloading, which explains the higher stiffness observed when compared to the 0.1 in. amplitude test. The softening after the 2nd cycle could be attributed to the mobilization of the full shear strength during the 2nd cycle, as reported by Hassiotis and Xiong (2007). With additional cycles, a steady state is reached.

The effect of the shape and amplitude of the displacement cycles was investigated by running additional tests where only half cycle of displacement was imposed. That is, each cycle started at zero displacement and the wall moved away from the soil, i.e., only the active phase of the loading was imposed. This was done to mimic what is expected to happen to bridges in the field, since they are built in the summer and thus they mainly experience contractive deformations due to the reduction of temperature in the winter. Two amplitudes were investigated:

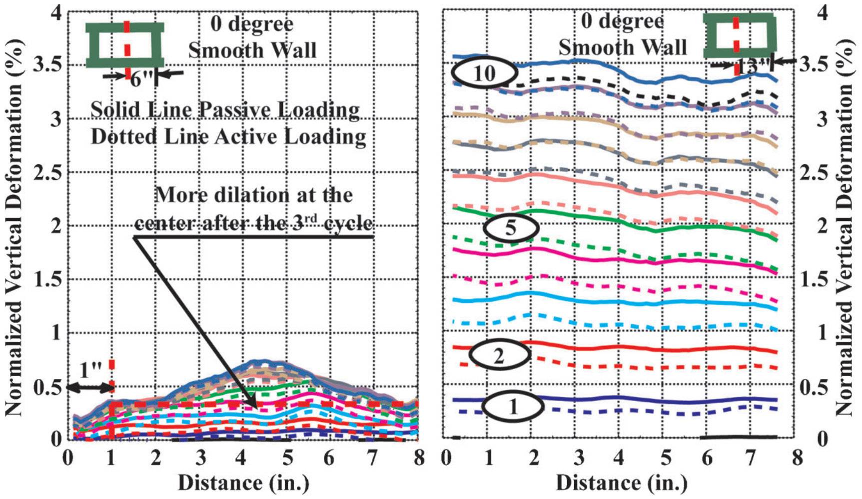

a- Section at 6in. From Wall

b- Section at 13in. From Wall

Figure C.25 Normalized Vertical Deformation along section in the transverse direction.

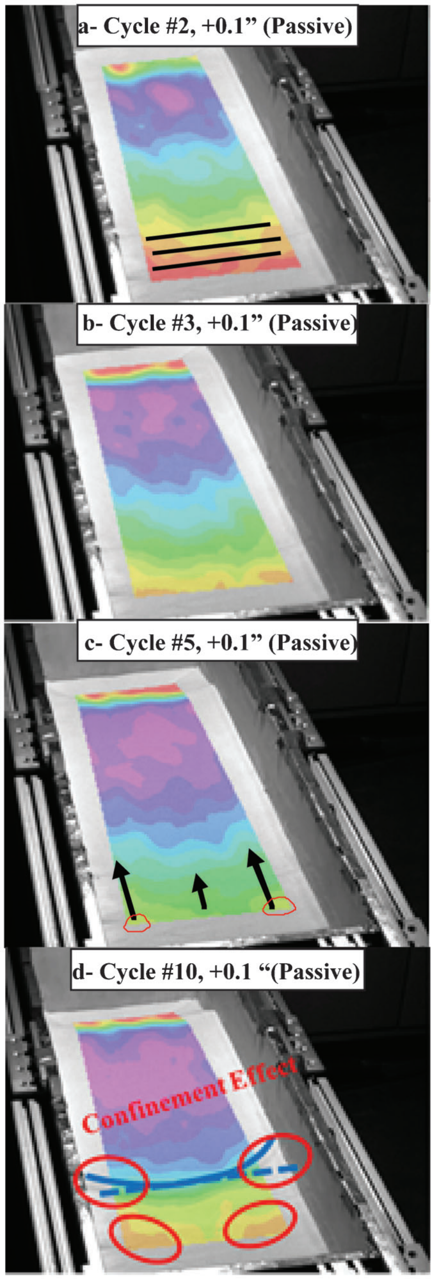

Figure C.26 Distribution of longitudinal displacement, (a) 2nd cycle, (b) 3rd cycle, (c) 5th cycle and (d) 10th cycle.

−0.1 and −0.2 in. All cases were performed with the base case (i.e., smooth wall at zero degrees (0°)). Figures C.36 through C.38 show the results of the additional tests and provide a comparison with the base case.

As seen in Figure C.36, all the tests showed a non-linear hysteretic behavior. The response was stiffer with number of cycles for the first eight cycles, and then softer for larger cycles (see also Figure C.37). During the tests, the coefficient of earth pressure evolved. For the -0.1 in. amplitude test, the pressures monotonically increased. They started at 1.5 (initial stress in the soil after compaction) and increased to 2.0 in the first cycle, peaked at 2.4 during the eighth cycle, and approached steady state in subsequent cycles, as presented in Figure C.37. The −0.2 in. displacement test showed a behavior more similar to those previously described, in that the coefficient of earth pressure increased from 1.25 (initial stress in the soil after compaction) to 2.3 in the first cycle and peaked at 2.45 during the third cycle, followed by softening until reaching a value 2.05 in the 7th cycle. As anticipated, in the base case (zero degree (0°) smooth wall and full cycles with 0.1″ amplitude), a larger earth pressure coefficient of 3 was observed at the 5th cycle (Figure C.34).

In both tests, the normalized volumetric change showed dilation during the passive loading and compression during the active loading, as shown in Figure C.38. As expected, dilation and contraction increased with amplitude.

Figures C.36 and C.37 indicate that the maximum force is almost the same in the two tests. For the case of −0.1 in. (half cycle), it took 8 cycles to reach the maximum force, while it took only three cycles for −0.2 in. (half cycle) case. However, both tests showed smaller force when compared to the base case (Figure C.33), which is expected due to larger passive displacement in the case of full cycle.

Figure C.38 shows the normalized volumetric change for the two tests. It can be seen that at the end of the active phase during the first 3 cycles, for the test with −0.2 in. amplitude, the net average change was settlement. The settlement amplitudes, for the −0.2 in. amplitude test, were almost twice those observed in the −0.1 in. amplitude test, for the same number of cycles. This higher settlement suggests that the soil was denser before reloading during the −0.2 in. amplitude test, which explains the higher stiffness observed.

The effect of loading sequence on wall response was investigated by running additional tests with a full loading cycle, but with the imposed displacement starting with active loading instead of passive loading. The tests were performed on the base case, i.e., smooth wall at zero degrees (0°). Figures C.39 through C.41 shows the results of the additional tests and provides a comparison with the base case.

The new test resulted in a response that was similar to that of the base case. The distinct feature of the test starting with active loading is that the earth pressure decreased first from the initial value (after compaction) to active earth pressure, as shown in Figure C.39. This resulted in larger contraction during the first few cycles, while the magnitude of dilation did not change much. With subsequent passive loading, the earth pressure coefficient increased but to a value smaller than what was observed in the base case.

The effect of wall friction (smooth versus rough) was examined for the zero degree (0°) wall and forty-five degree (45°) wall. In addition, effect of wall friction on tests with half cycles was examined for the zero degree (0°) wall and forty-five degree (45°) wall. The comparisons for the forty-five degree (45°) wall with full cycle are presented in Figures C.42 through C.44.

The two tests, as shown in Figures C.42 to C.44 show similar trends. The most important difference is that the rough wall developed less force than the smooth wall. In addition, the force peaked earlier (less number of cycles) in the rough wall (see Figure C.43). In both walls the earth pressure coefficient decreased after peaking to a value similar to that developed during the initial loading. Figure C.44 shows that at the obtuse corner of the smooth wall dilation was smaller than at the obtuse corner of the rough wall. A similar observation could be made for the acute corner. This is related to the additional shear stress that occurs at the contact between the sand and the rough wall that constrains the displacements of the soil and that ultimately result in smaller force.

The comparisons for the zero degree (0°) wall with full cycle are presented in Figures C.45 through C.47.

The zero degree (0°) smooth and rough walls show similar trends, as shown in Figures C.45. The most important difference is that the rough wall developed less force than the smooth wall. However, for both walls the force at the same cycle (see Figure C.46). In both walls the earth pressure coefficient decreased after peaking, however, for the case with the rough wall the reduction in earth pressure coefficient was more significant, where it approached steady state at the 8th cycle reaching an earth pressure coefficient less than what was developed in the first cycle. Figure C.47 shows that the two tests developed the same dilation magnitude; however, for the

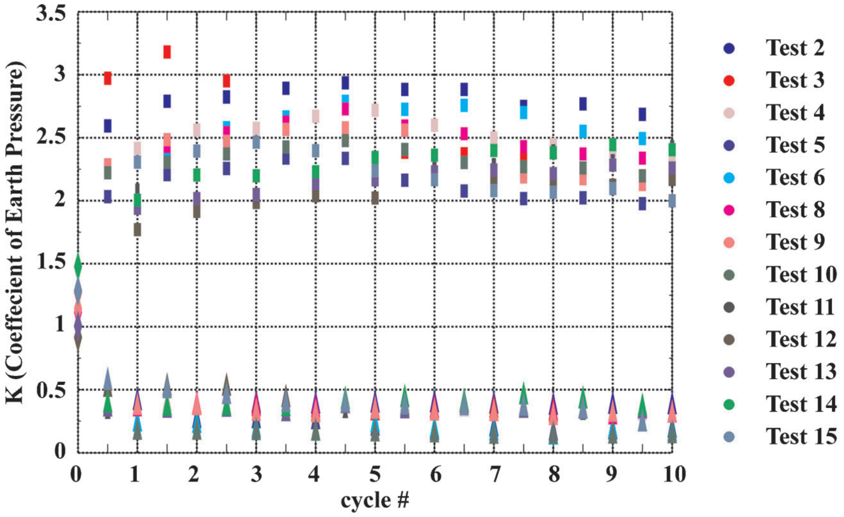

Test #	Ampl. (in)	Wall Angle (deg)	Wall Condition	Notes
1	+/-0.1	0	smooth	Repeatability Tests
2	+/-0.1	0	smooth	
3	+/-0.2	0	smooth	
4	+/-0.1	0	smooth	Starting with active
5	+/-0.1	45	rough	
6	+/-0.1	60	smooth	
7	+/-0.1	45	smooth	Repeatability Tests
8	+/-0.1	45	smooth	
9	+/-0.1	0	rough	
10	+/-0.1	60	rough	
11	0 to -0.1 to 0	0	rough	half Cycle
12	0 to -0.1 to 0	45	smooth	half Cycle
13	0 to -0.1 to 0	45	rough	half Cycle
14	0 to -0.1 to 0	0	smooth	half Cycle
15	0 to -0.2 to 0	0	smooth	half Cycle

Figure C.27 Coefficient of lateral earth pressure.

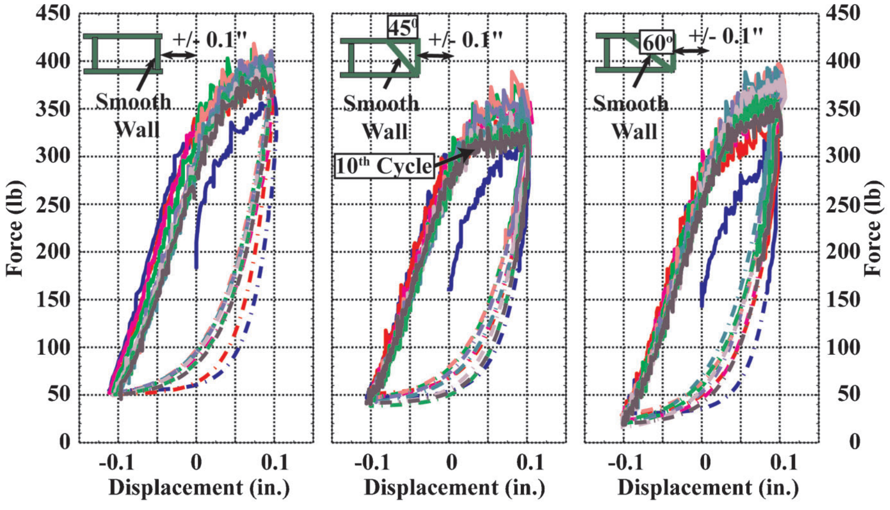

a- Zero degree (0°) b- Forty five degree (45°) c- Sixty degree (60°)

Figure C.28 Effect of skew angle on soil's response. Comparison between Tests 2, 6, and 8.

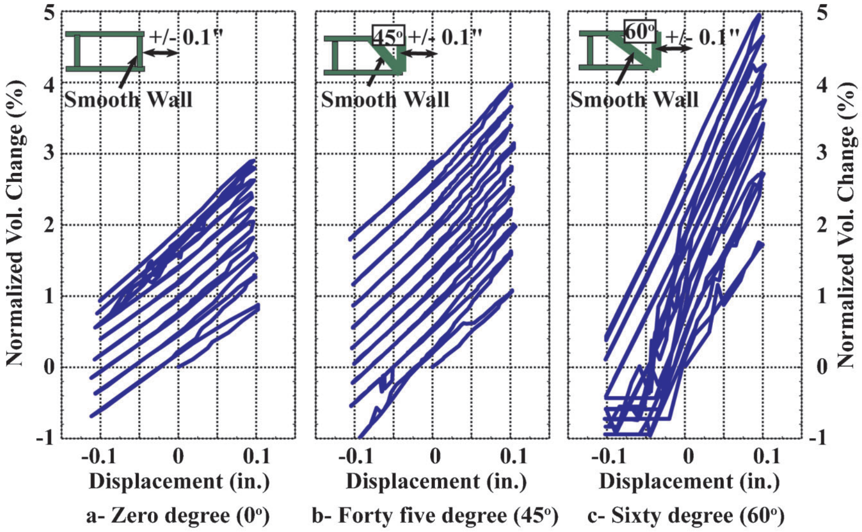

Figure C.29 Effect of skew angle on normalized volumetric change. Comparison between Tests 2, 6, and 8.

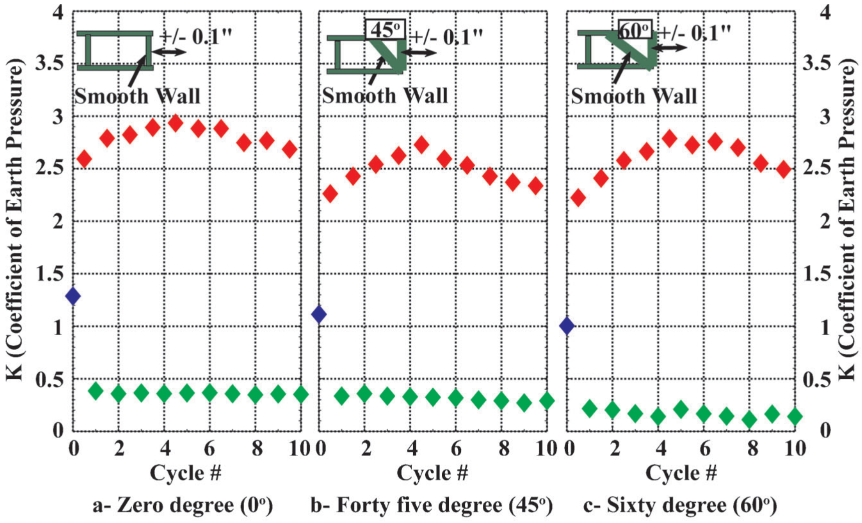

Figure C.30 Effect of skew angle on coefficient of earth pressure. Comparison between Tests 2, 6, and 8.

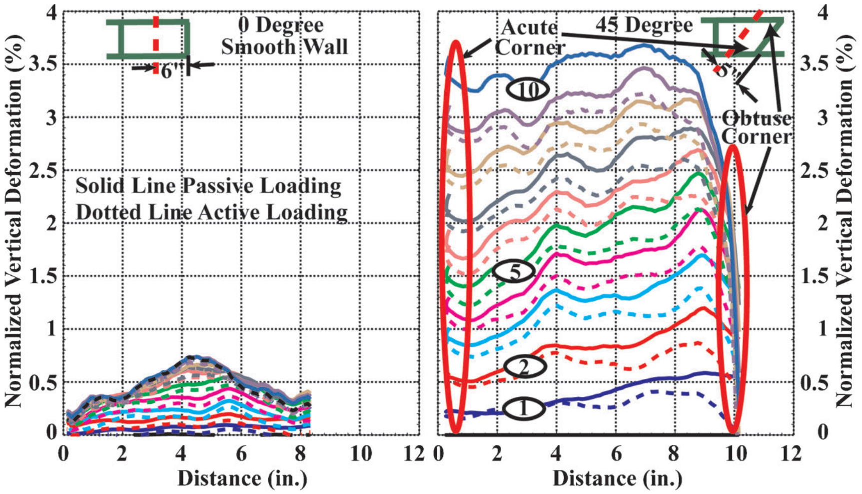

a- Zero degree (0°)

b- Forty five degree (45°)

Figure C.31 Effect of skew angle on Normalized Vertical Deformation along sections parallel to the face. Comparison between Tests 2 and 8.

smooth wall more settlement was observed at the end of active loading. This higher settlement suggests that the soil was denser before reloading in the case of smooth wall test, which explains the higher stiffness observed.

The effect of wall roughness was less significant for the half cycle cases comparisons for the zero degree (0°) wall and forty-five degree (45°) wall with half cycle are presented in Figures C.48 through C.49, respectively.

The four tests showed similar trend, however, unlike the tests with the full cycles, the effect of wall friction in reducing the applied force was not significant. This could be attributed to the smaller passive displacement imposed by the wall, where it was not

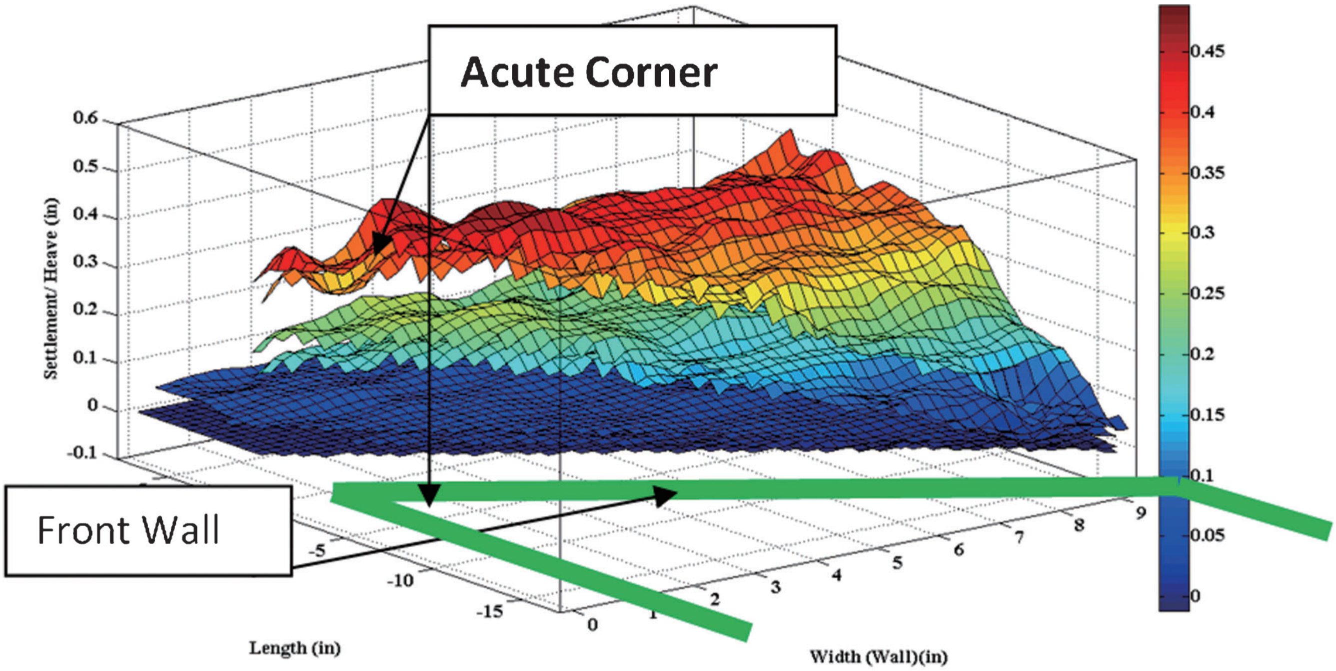

Figure C.32 Surface deformed shape for the sixty degree (60°) wall (Test 6).

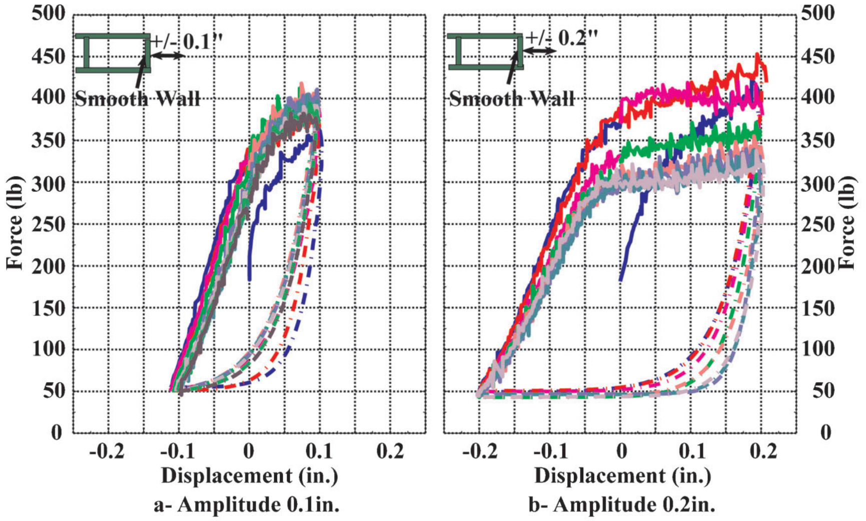

Figure C.33 Effect of amplitude on soil's response. Comparison between Tests 2 and 3.

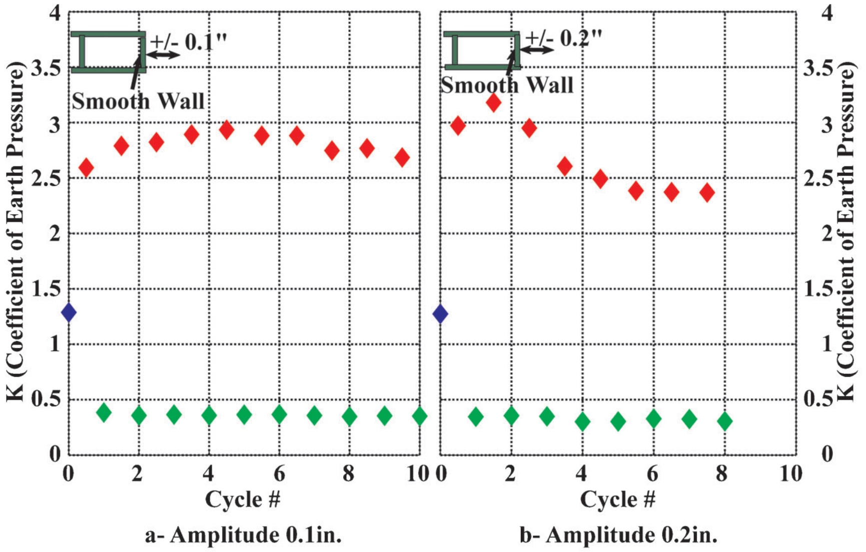

Figure C.34 Effect of amplitude on coefficient of earth pressure. Comparison between Tests 2 and 3.

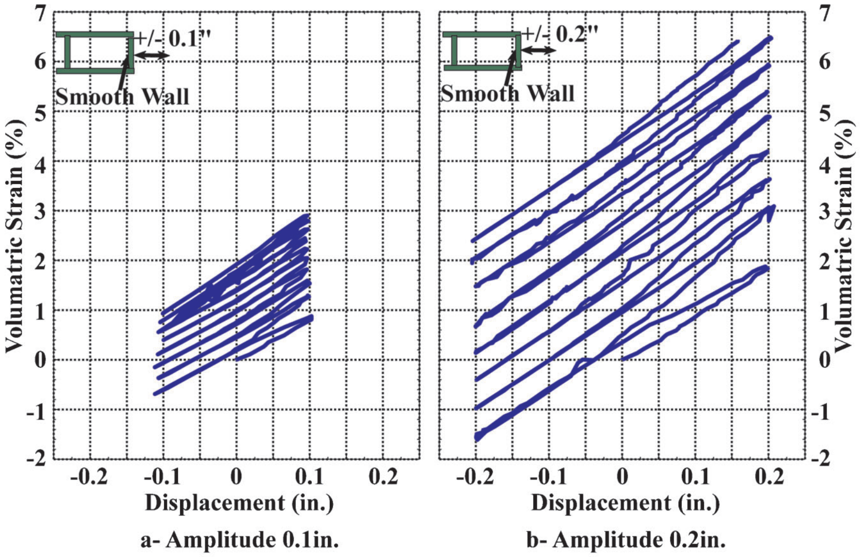

Figure C.35 Effect of skew angle on normalized volumetric change. Comparison between Tests 2 and 3.

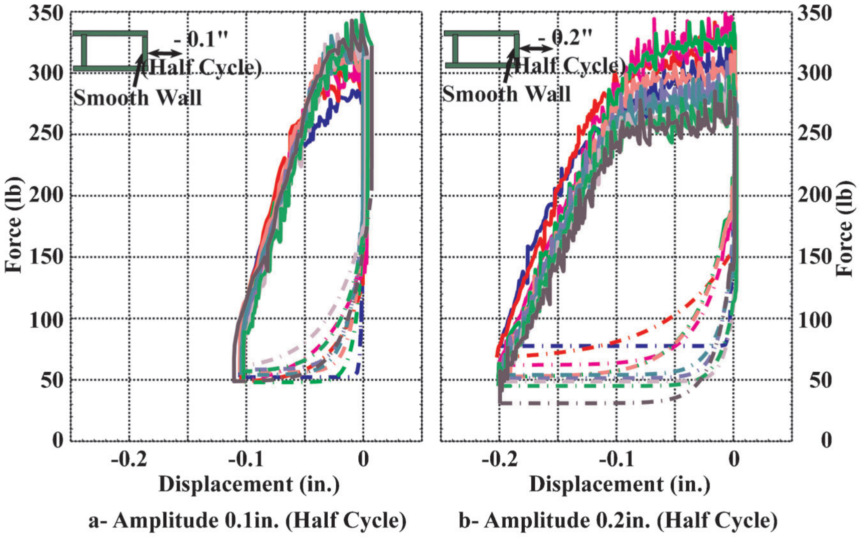

Figure C.36 Effect of amplitude on soil's response during half cycle tests. Comparison between Tests 14 and 15.

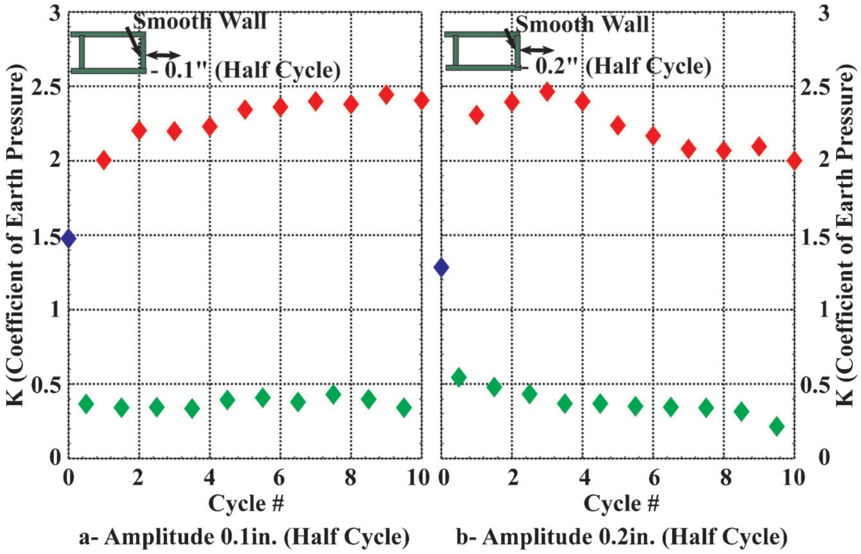

Figure C.37 Effect of amplitude on coefficient of earth pressure during half cycle tests. Comparison between Tests 14 and 15.

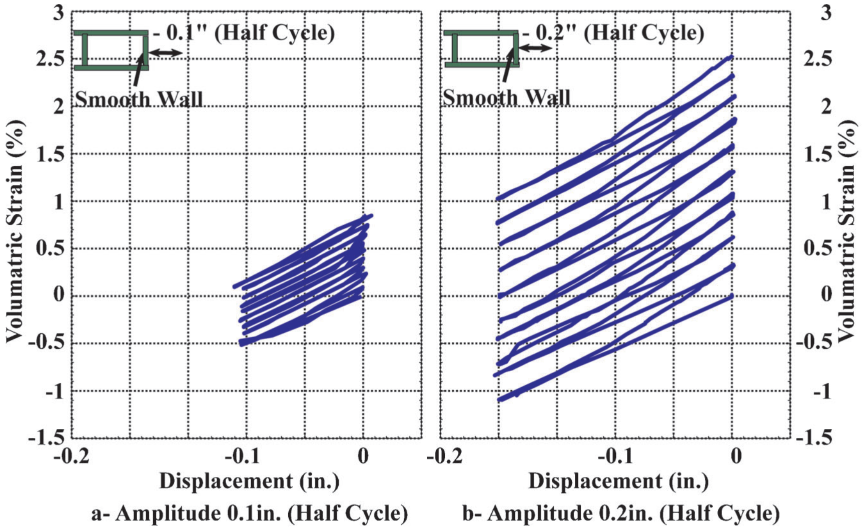

Figure C.38 Effect of amplitude on normalized volumetric change during half cycle tests. Comparison between Tests 14 and 15.

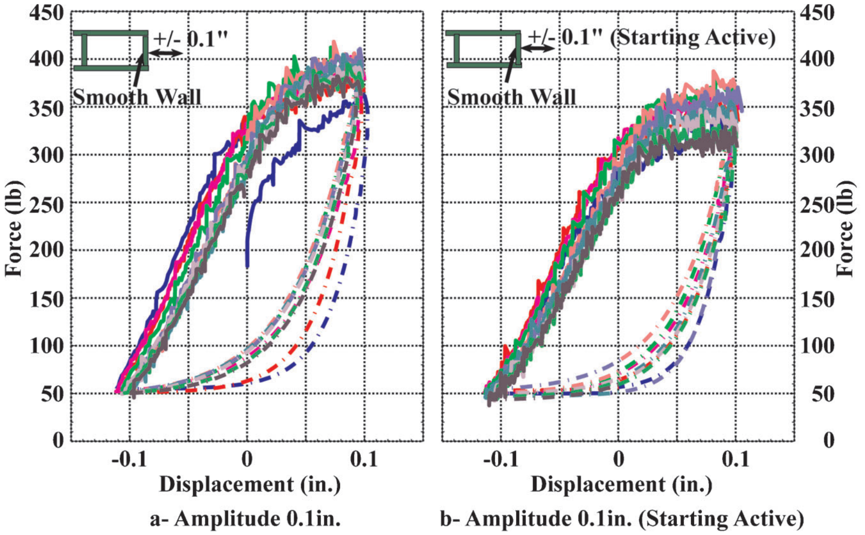

a- Amplitude 0.1in.

b- Amplitude 0.1in. (Starting Active)

Figure C.39 Effect of loading sequence on soil's response. Comparison between Tests 2 and 4.

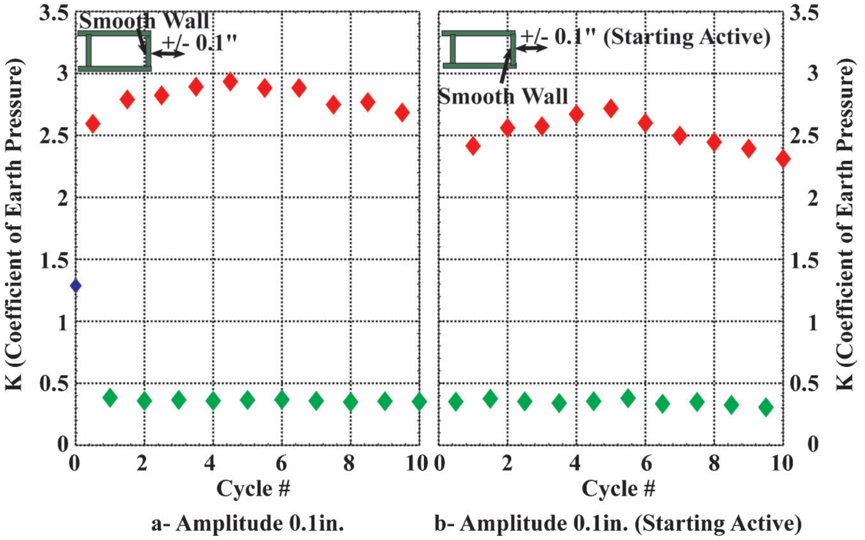

a- Amplitude 0.1in.

b- Amplitude 0.1in. (Starting Active)

Figure C.40 Effect of loading sequence on coefficient of earth pressure. Comparison between Tests 2 and 4.

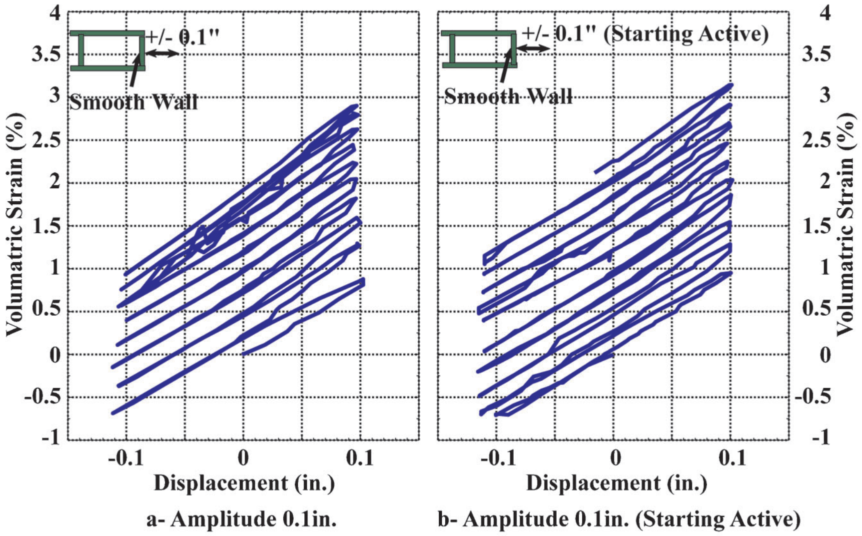

Figure C.41 Effect of loading sequence on normalized volumetric change. Comparison between Tests 2 and 4.

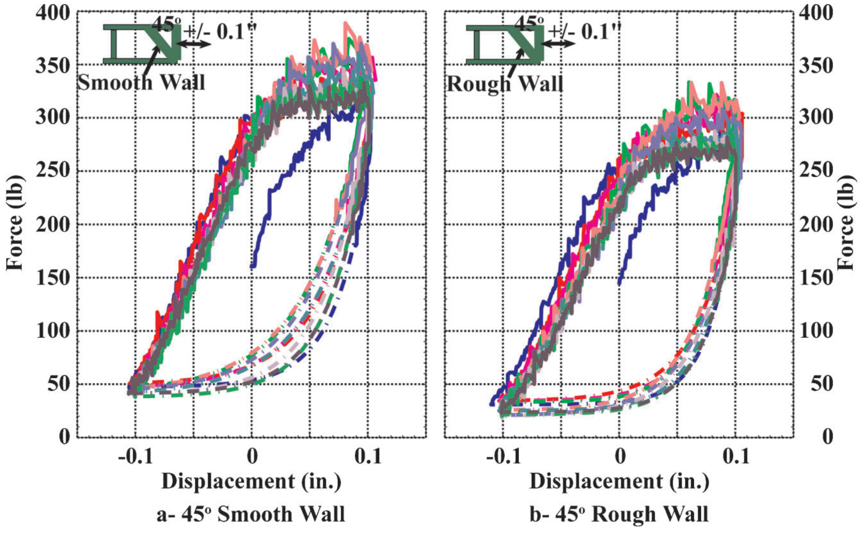

Figure C.42 Effect of rough skewed wall on soil's response. Comparison between Tests 5 and 8.

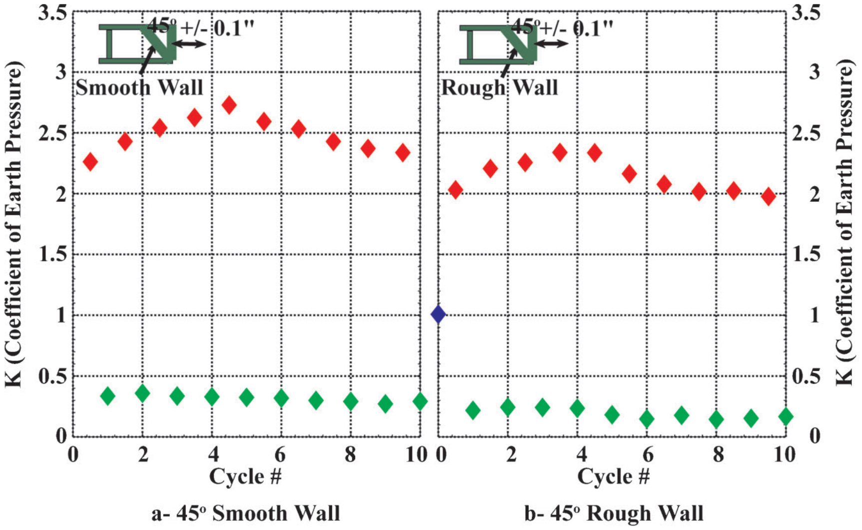

Figure C.43 Effect of rough skewed wall on coefficient of earth pressure. Comparison between Tests 5 and 8.

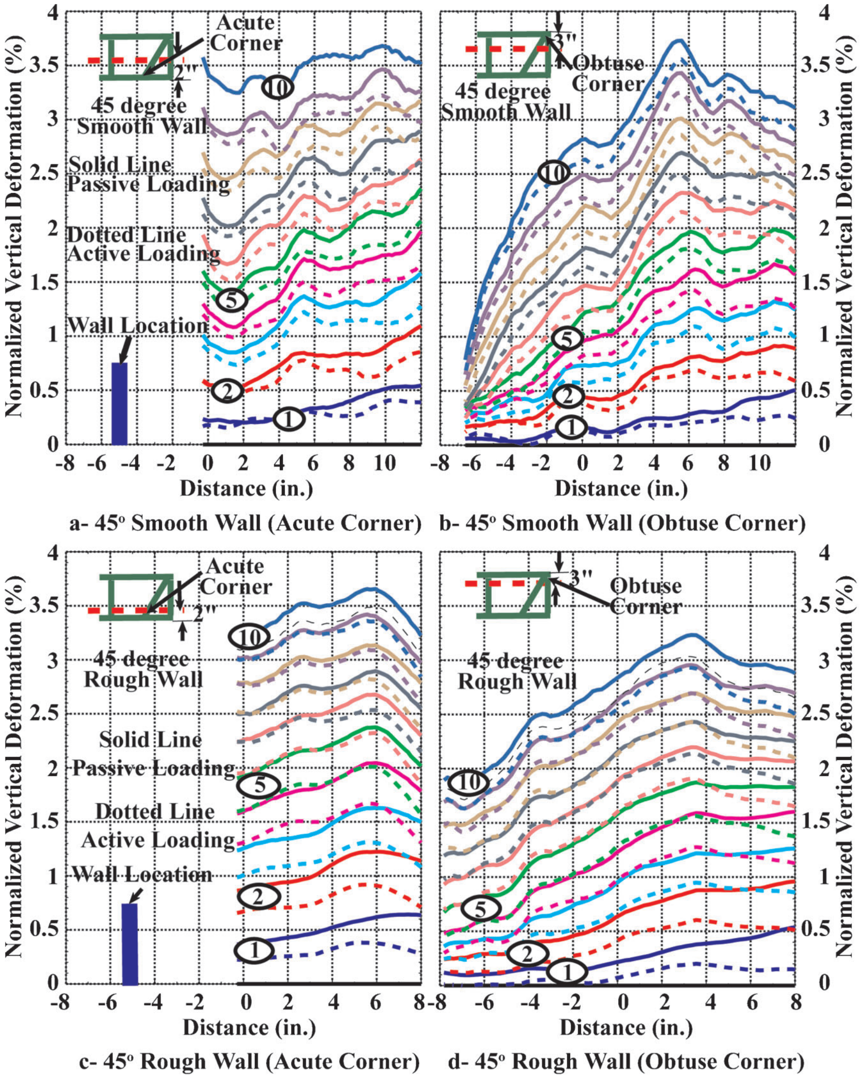

Figure C.44 Effect of rough skewed wall on Normalized Vertical Deformation along longitudinal sections. Comparison between Tests 5 and 8.

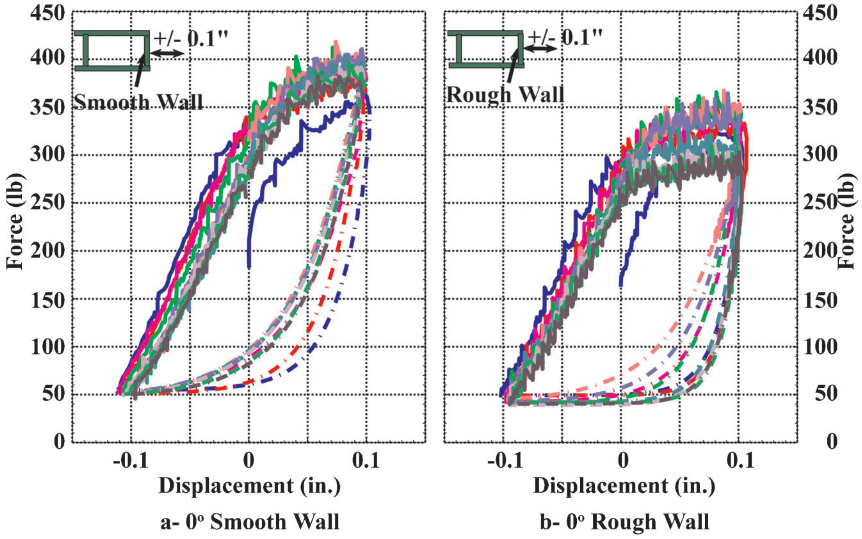

a- 0° Smooth Wall b- 0° Rough Wall

Figure C.45 Effect of rough wall on soil's response. Comparison between Tests 2 and 9.

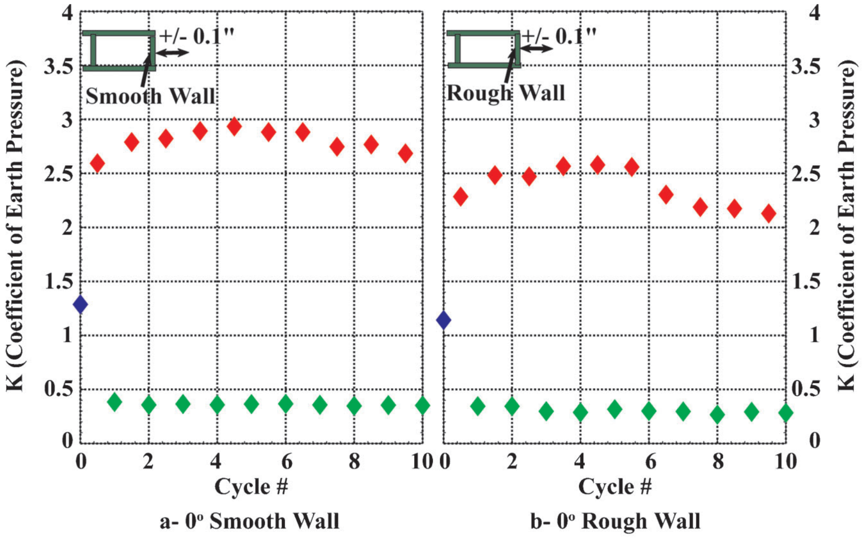

a- 0° Smooth Wall b- 0° Rough Wall

Figure C.46 Effect of rough wall on coefficient of earth pressure. Comparison between Tests 2 and 9.

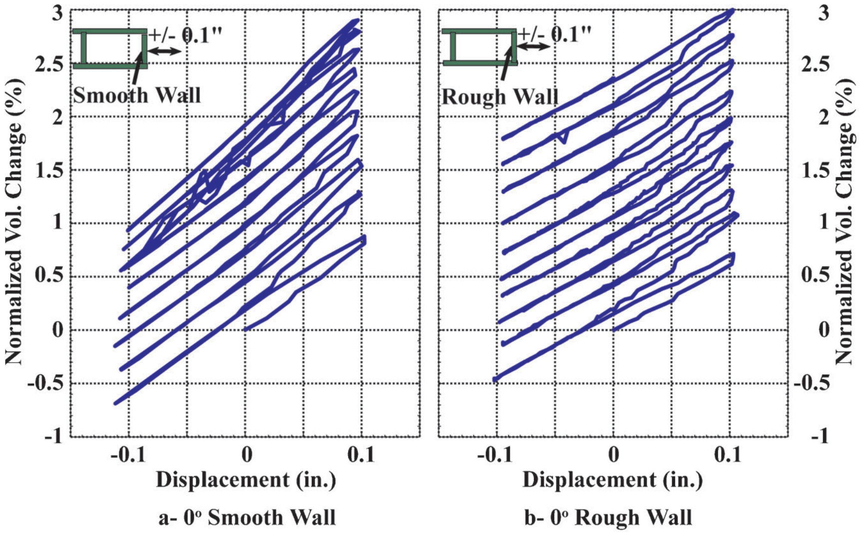

Figure C.47 Effect of rough wall on normalized volumetric change. Comparison between Tests 2 and 9.

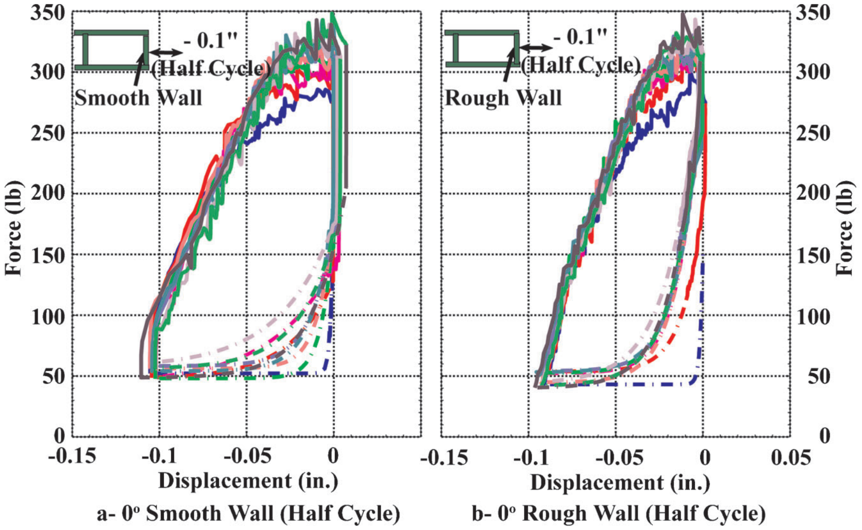

Figure C.48 Effect of rough wall on soil's response (half cycles). Comparison between Tests 11 and 14.

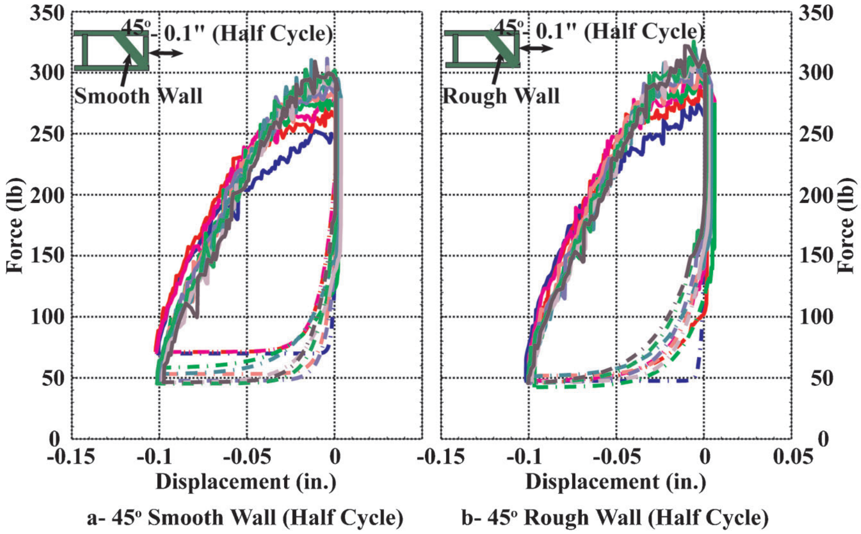

Figure C.49 Effect of skewed rough wall on soil's response (half cycles). Comparison between Tests 12 and 13.

enough to develop the friction at the interface between the soil and the rough wall. As such, there was not any significant constrains on the soil displacement next to the rough wall, and ultimately the rough wall behaved similar to the smooth wall.

C.7 KEY OBSERVATIONS

Based on the discussion in Section C.6, the following conclusions can be made:

1. The repeatability tests showed that the setup is capable of producing the same results in duplicate experiments.
2. In all the tests, the passive load increased with number of cycles to a peak and then showed a reduction until a steady-state value was reached.
3. For most of the tests the soil pressures decreased after the 5th cycle.
4. Development of active conditions occurred during the first cycle.
5. Development of passive loading was observed at about 1.2% plastic normalized volumetric change.
6. The tests with a skewed wall developed less soil pressure than the tests with a zero angle wall.
7. The tests with a rough surface developed less soil pressure than the tests with a smooth surface; this observation was less significant for the tests with half cycles.
8. The magnitude of volumetric change showed a direct relation with the development of soil pressure. As dilation increased, the force applied decreased.
9. Behind the obtuse corner, dilation was the smallest and increased toward the acute angle, which suggests a higher pressure behind the obtuse angle.

C.8 REFERENCES

Pradhan, T. B., Tatsuoka, F., & Sato, Y. (1989). Experimental stress-dilatancy relations of sand subjected to cyclic loading. *Soils and Foundations*, *29*(1), 45–64.

Hassiotis H., & Xiong, K. (2007). *Deformation of cohesionless fill due to cyclic loading* (SPR ID# C-05-03). Hoboken, NJ: Stevens Institute of Technology.

APPENDIX C-1

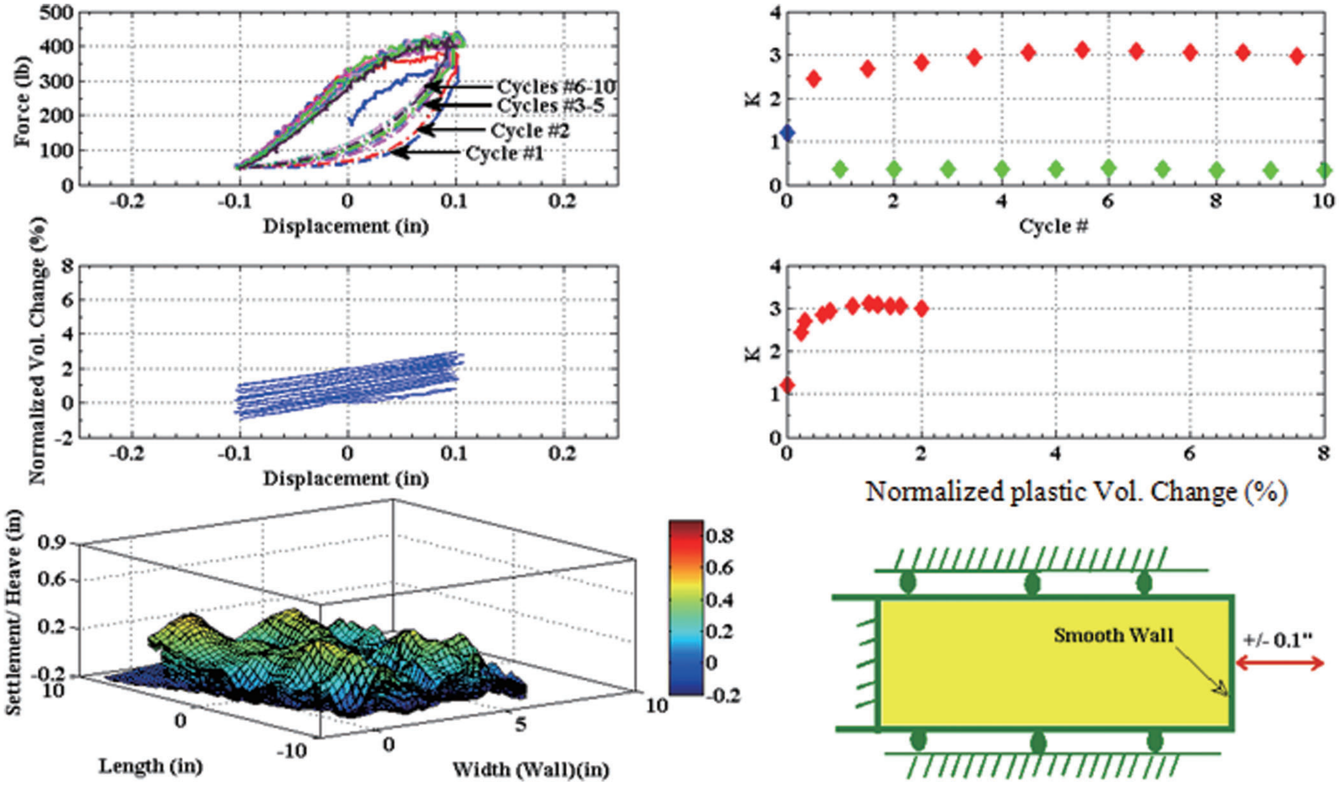

Figure C-1.1 Summary plot for Test #1.

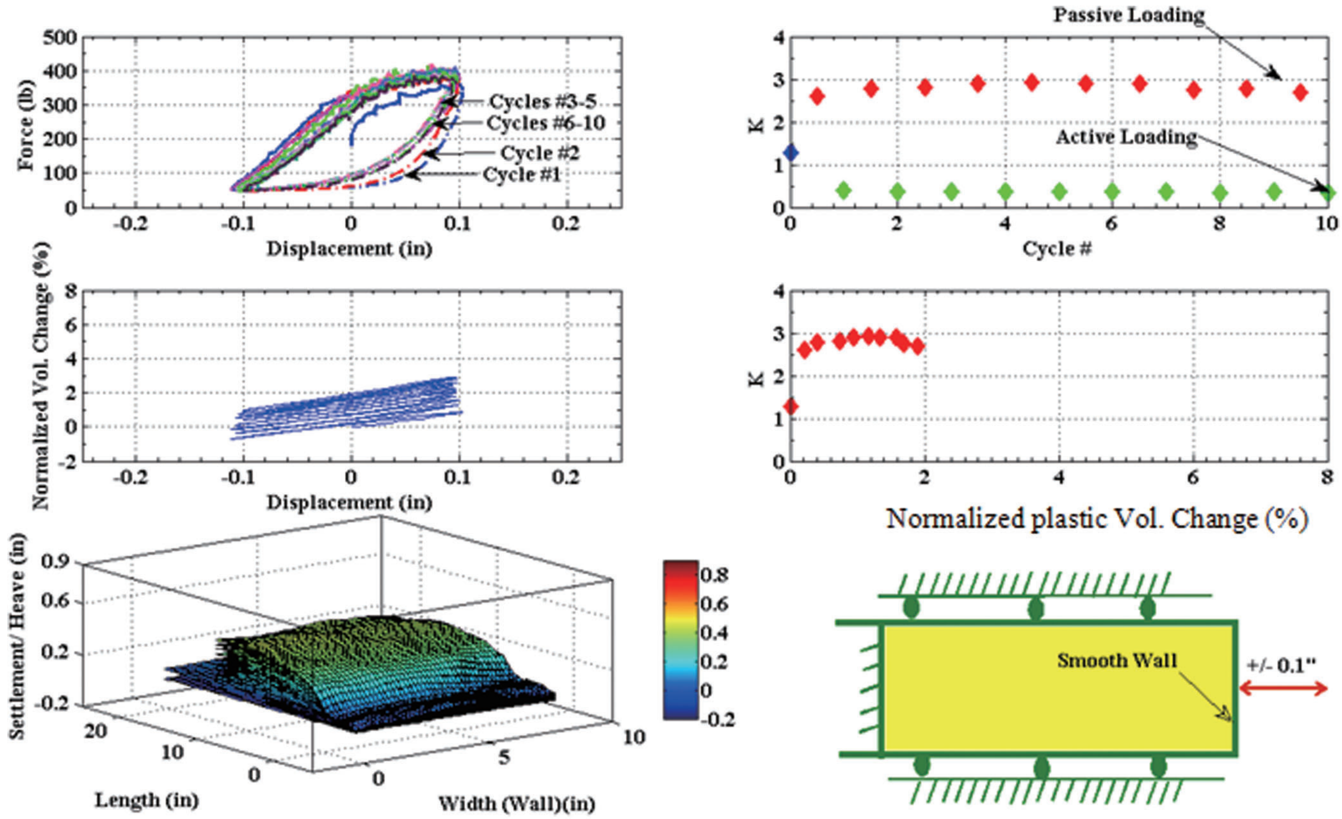

Figure C-1.2 Summary plot for Test #2.

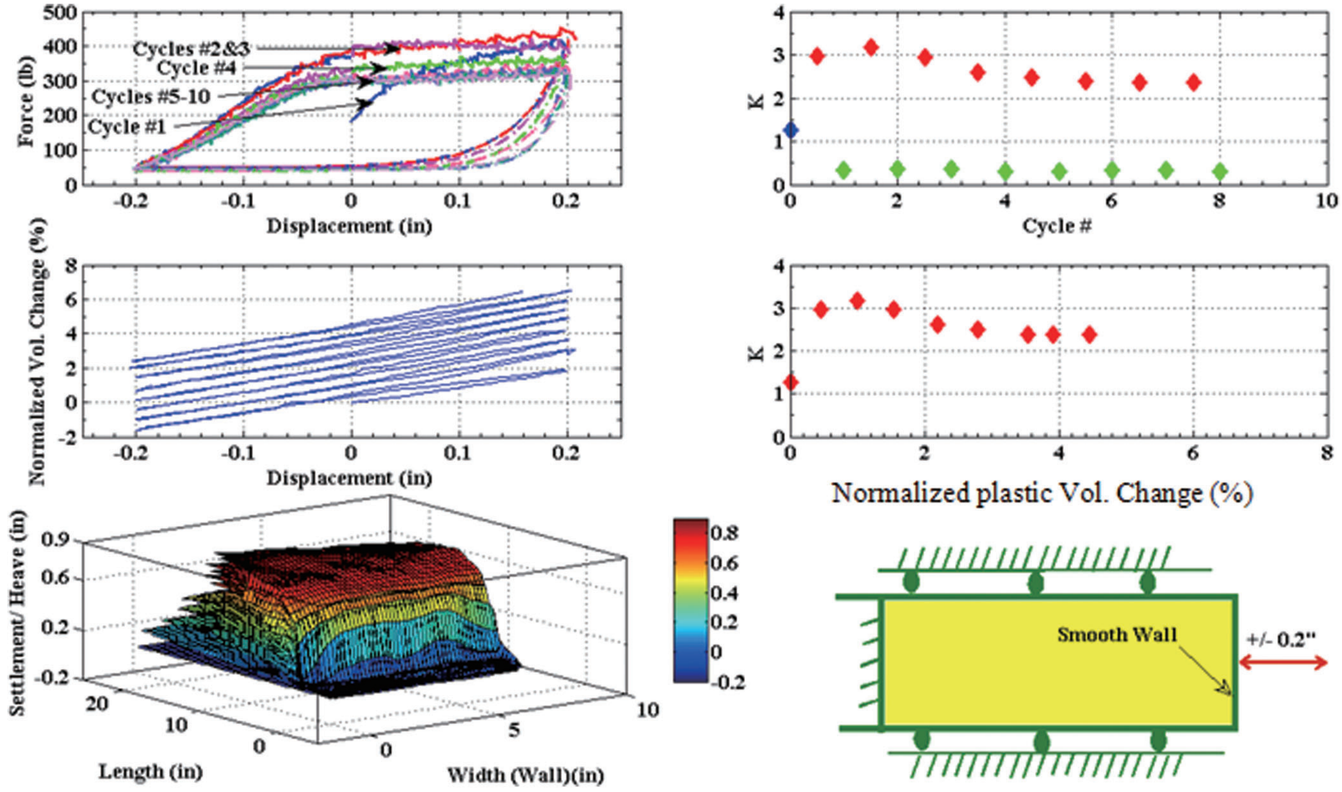

Figure C-1.3 Summary plot for Test #3.

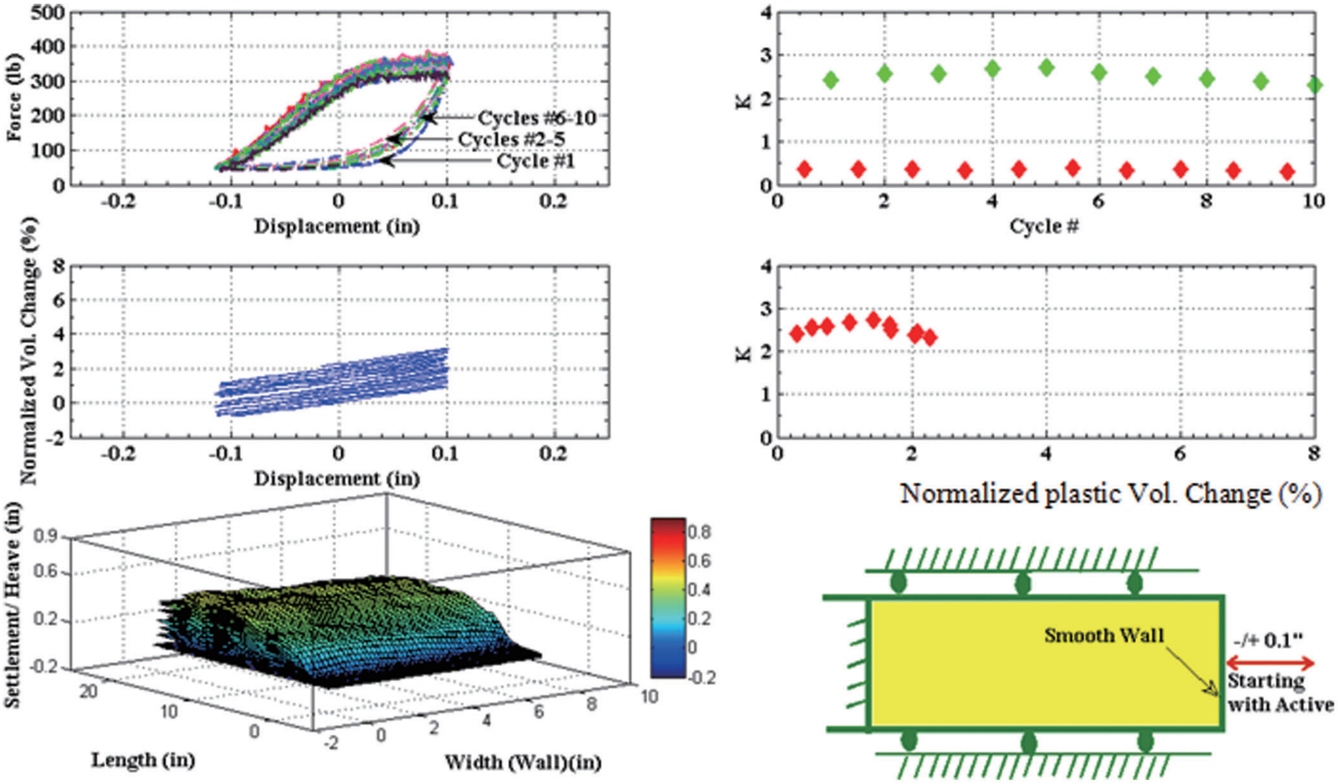

Figure C-1.4 Summary plot for Test #4.

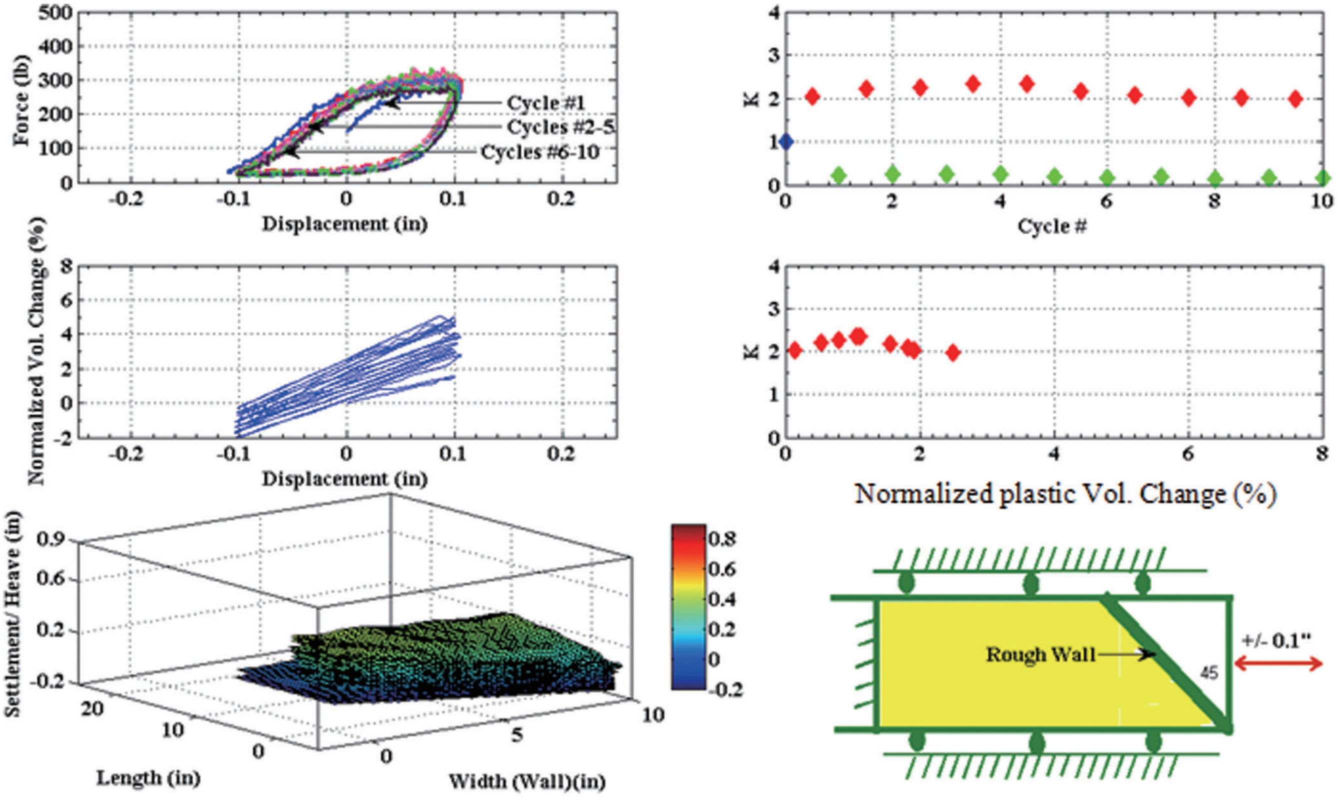

Figure C-1.5 Summary plot for Test #5.

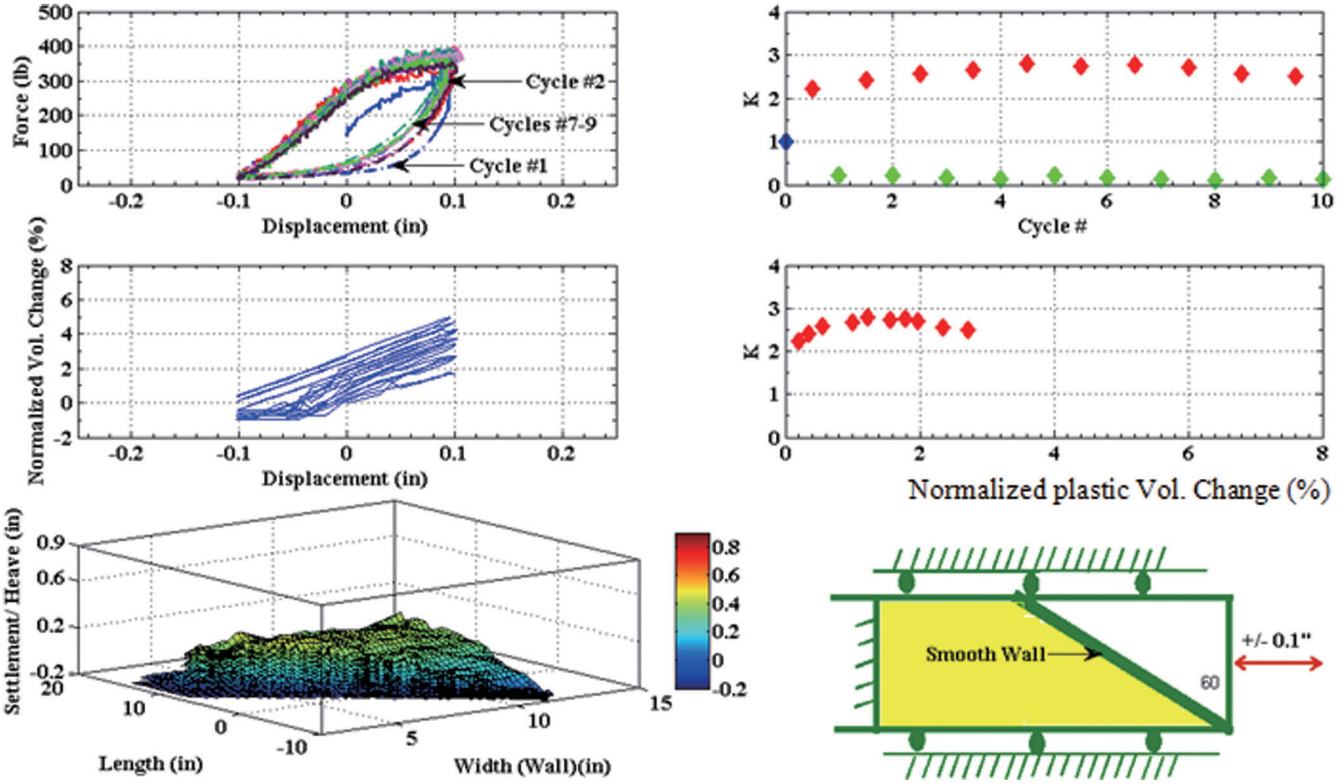

Figure C-1.6 Summary plot for Test #6.

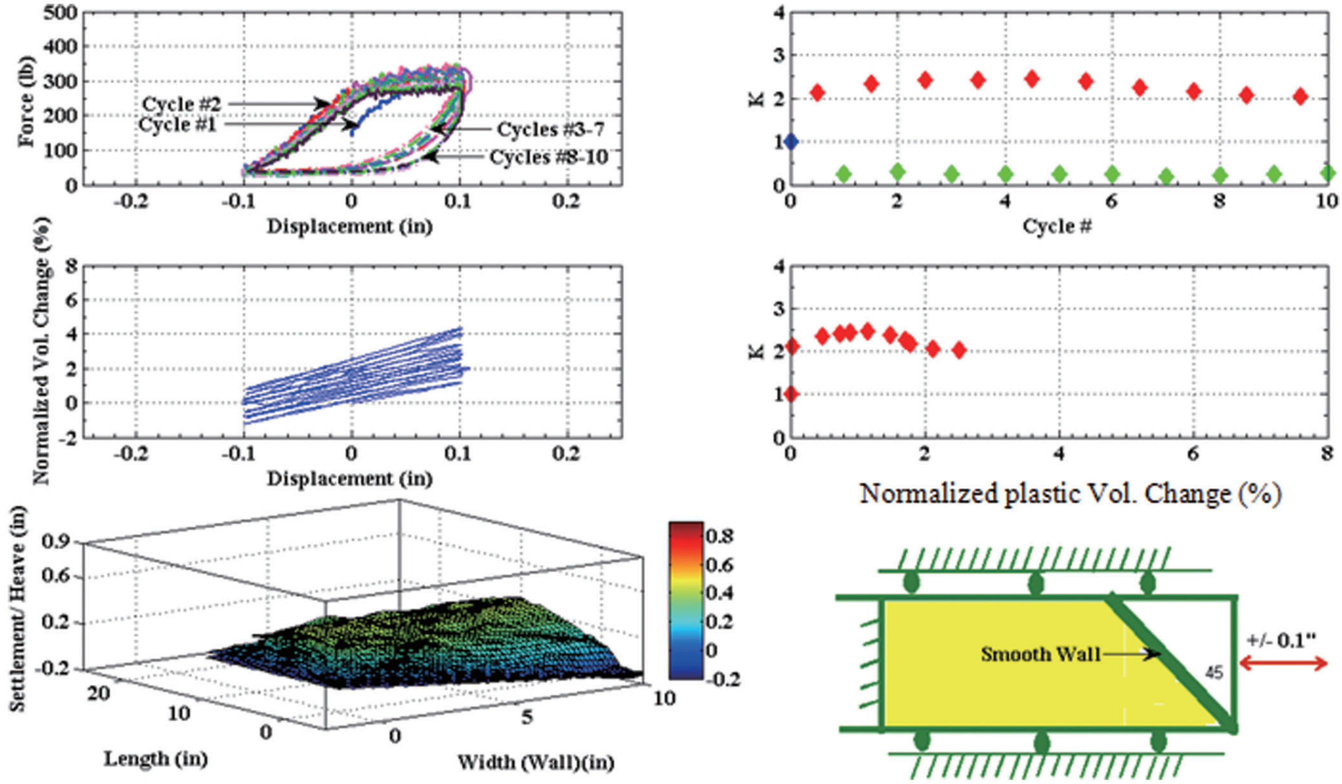

Figure C-1.7 Summary plot for Test #7.

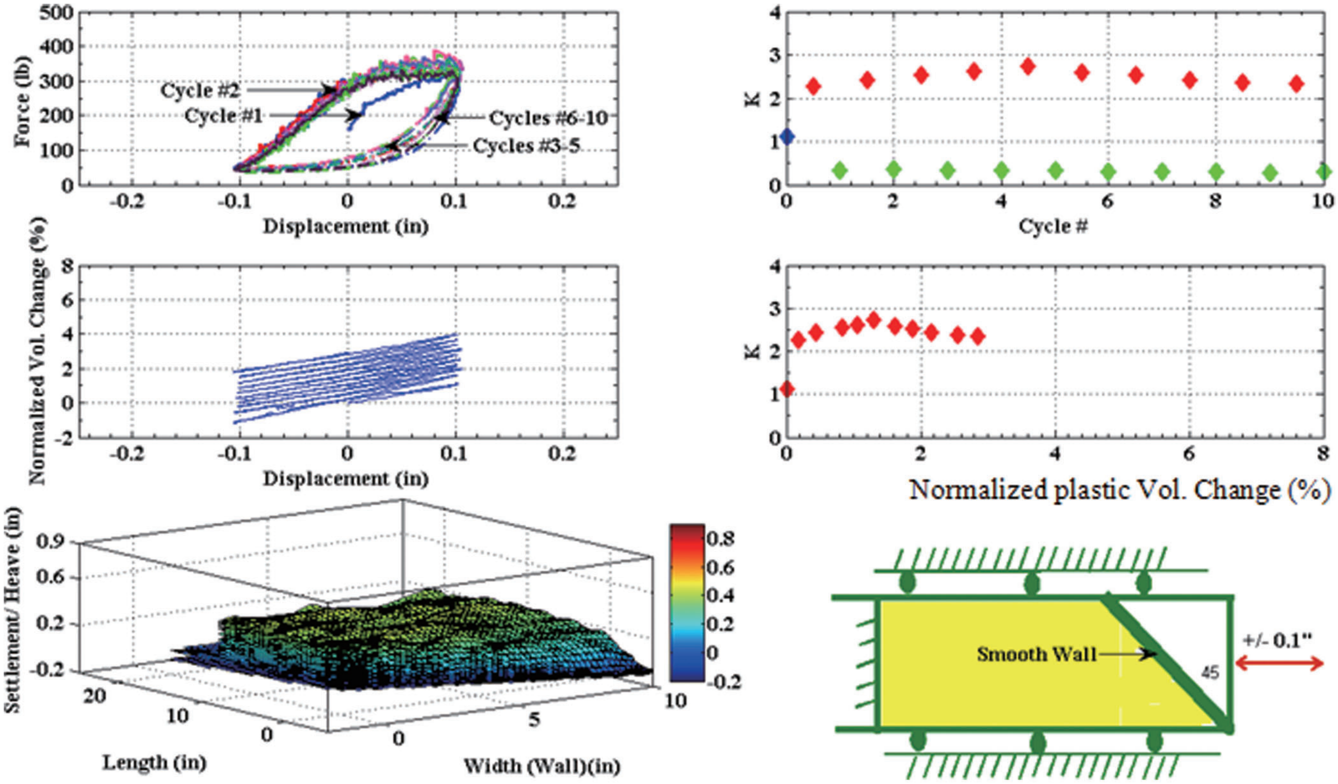

Figure C-1.8 Summary plot for Test #8.

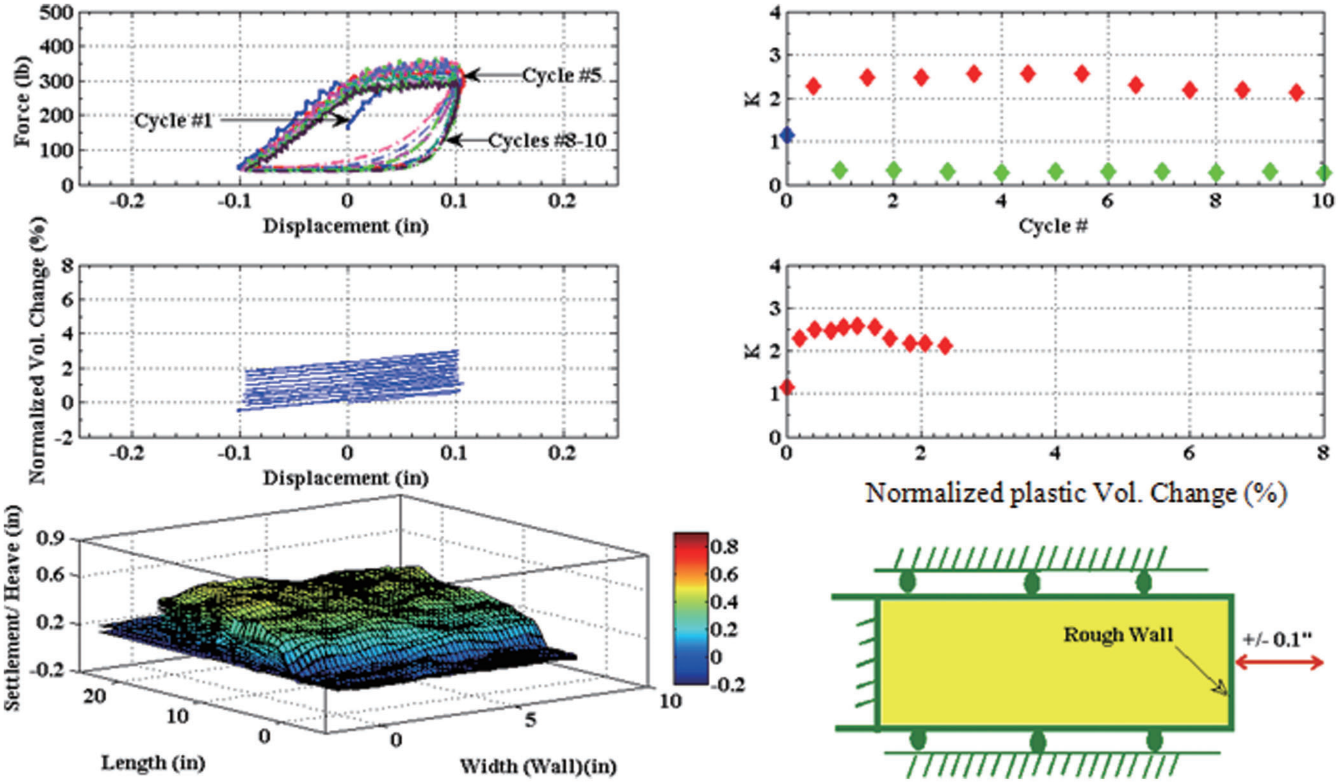

Figure C-1.9 Summary plot for Test #9.

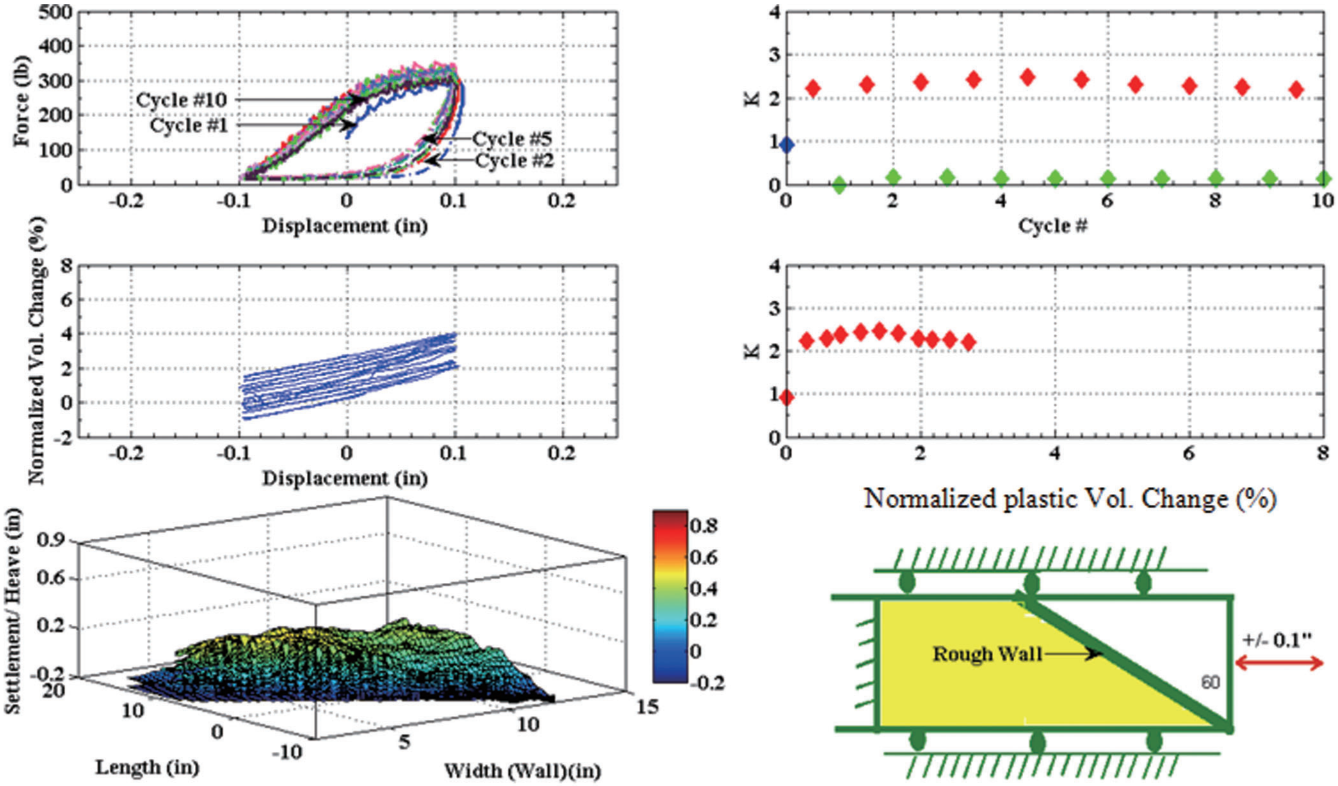

Figure C-1.10 Summary plot for Test #10.

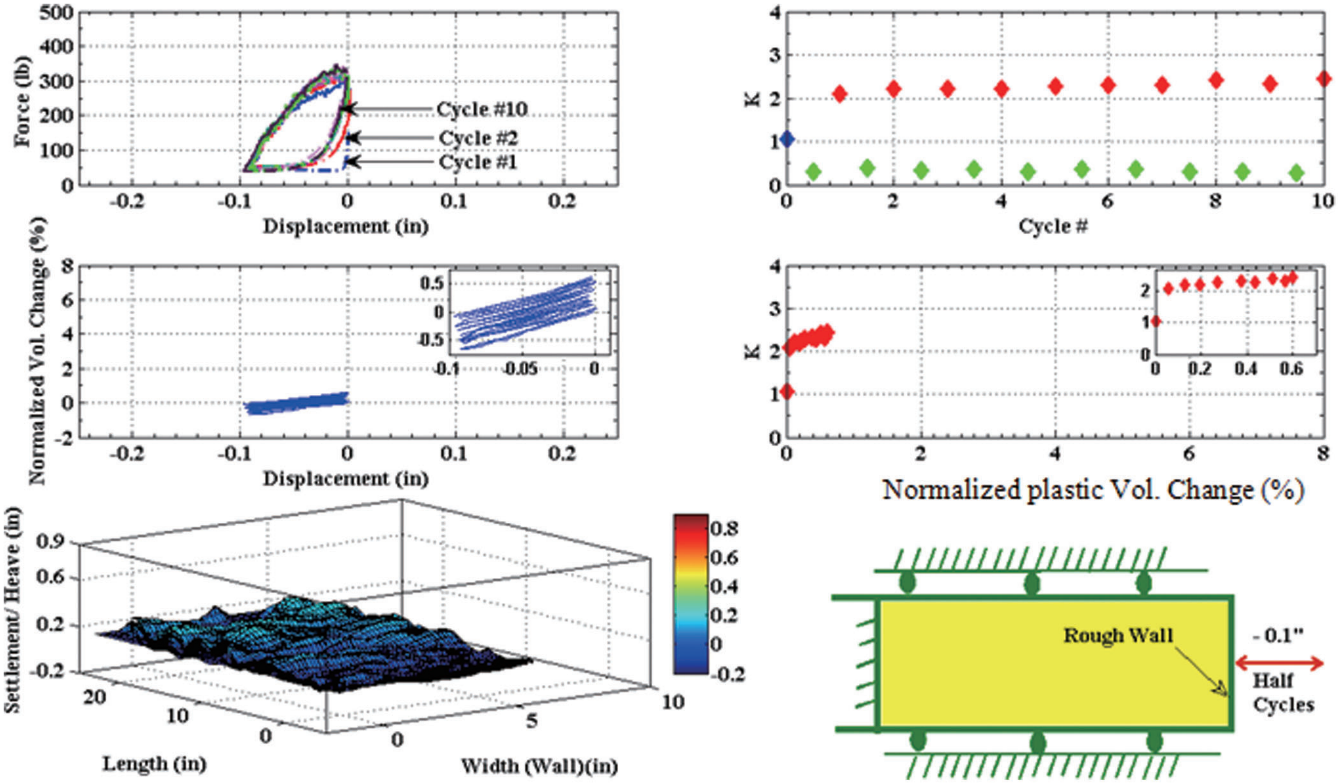

Figure C-1.11 Summary plot for Test #11.

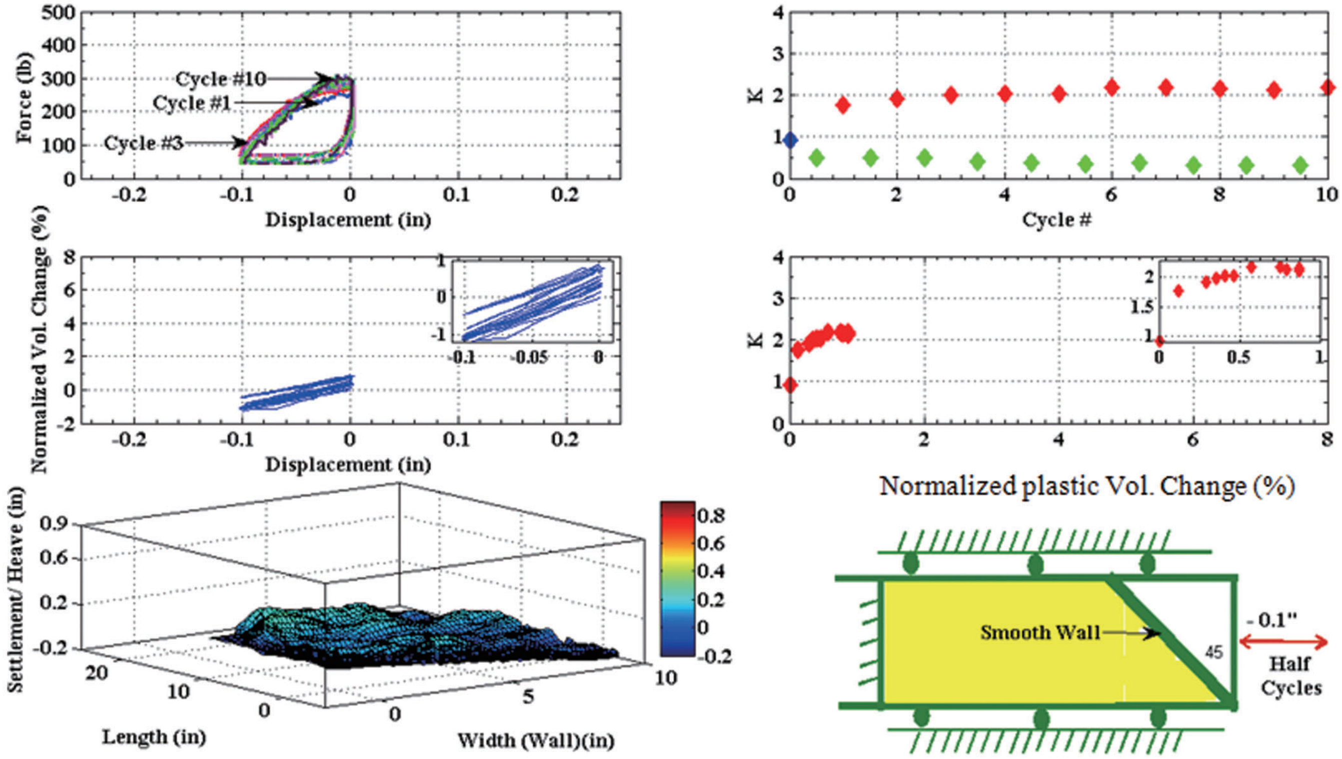

Figure C-1.12 Summary plot for Test #12.

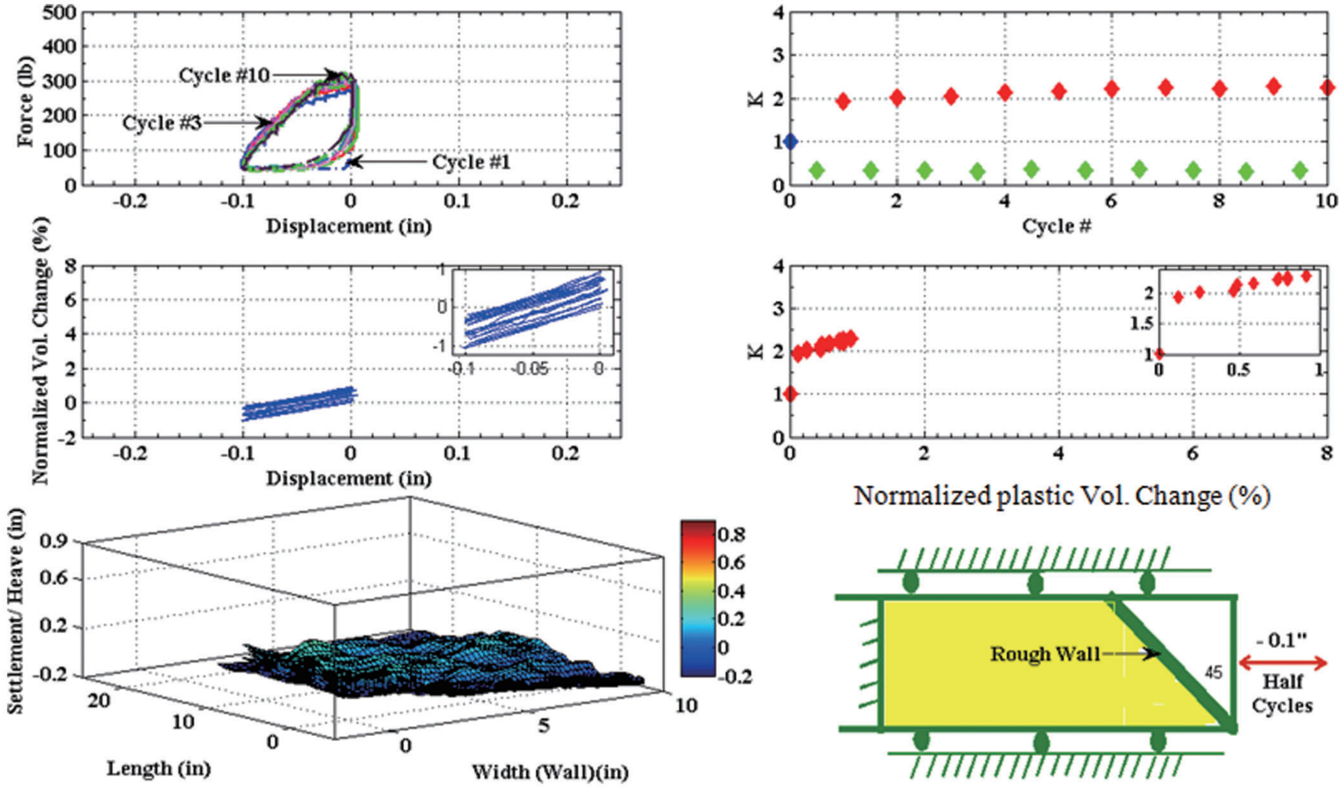

Figure C-1.13 Summary plot for Test #13.

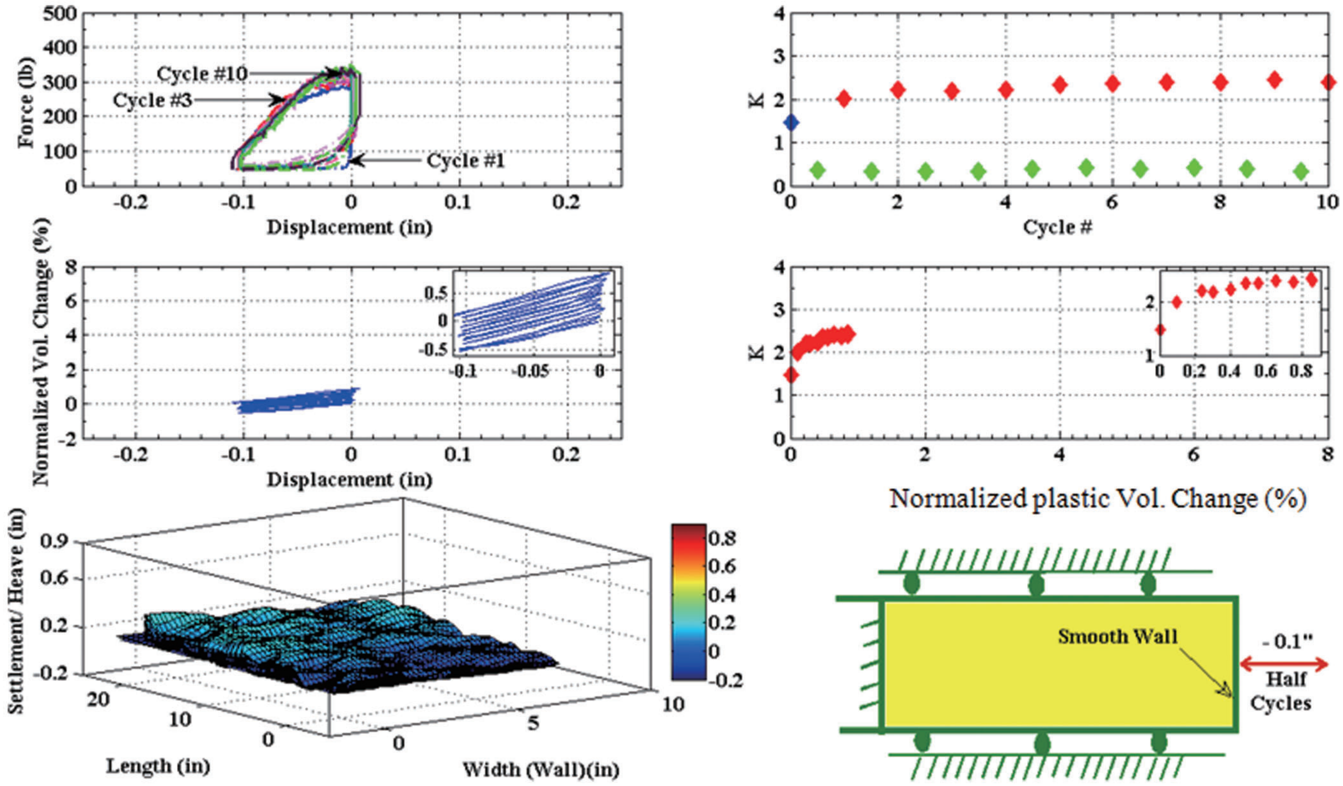

Figure C-1.14 Summary plot for Test #14.

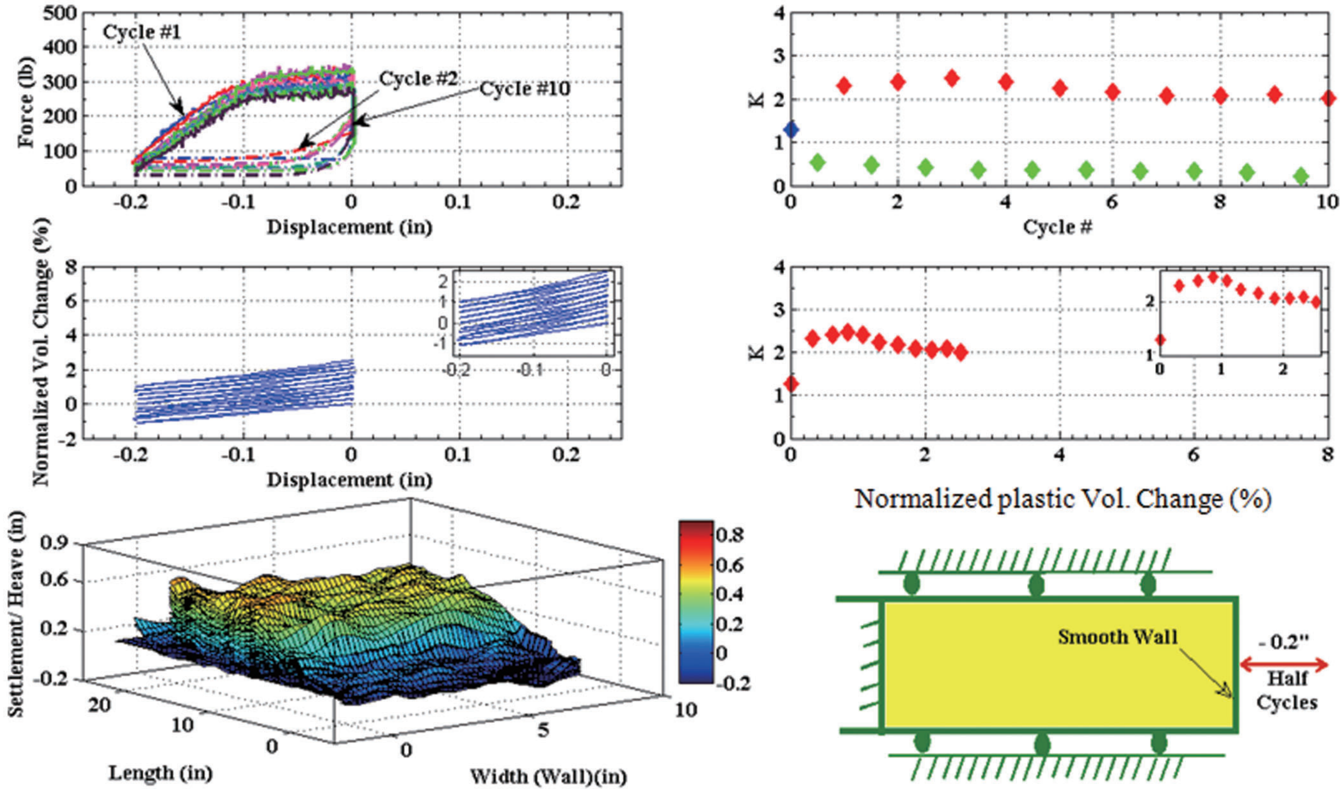

Figure C-1.15 Summary plot for Test #15.

APPENDIX D. SOIL'S CONSTITUTIVE MODEL

D.1 INTRODUCTION

This chapter presents the proposed soil's constitutive model for the numerical simulations of the integral abutment bridges. It is well known that attempts to simulate a general soil behavior for various loading mechanisms, different drainage conditions, and various grain sizes through critical state soil mechanics and general plasticity theory will result in a very complicated constitutive model with large number of parameters (Yu & Wang, 2007) (mostly nonphysical parameters). It was decided to implement a "simplified" soil model with minimum number of fitting parameters that suite the applications in the current study.

The proposed constitutive model is a modified version of what was proposed by Jung (2009). The modifications on the constitutive model were implemented based on the needs to capture the behavior of backfill and foundation soils of the integral abutment bridges. The integral abutment bridges behavior was explored through monitoring of instrumented bridges, large scale tests (Chapter 3), and laboratory scale tests (Chapter 4). The main modifications in the model were: the extension into a three-dimensional state of stresses, the rotation of the backbone curve to account for the escalation of the soil pressure with number of cycles, and the capture of the observed linear response at the beginning of reloading after the unloading phase.

The elastoplastic model and its implementation in Abaqus will be presented in sections D.2, and D.3, respectively.

D.2 THE ELASTOPLASTIC MODEL

Soils, in general, exhibit a highly nonlinear stress strain behavior at a relatively small strain. Ishihara (1982) defined thresholds between the elastic and the elastoplastic responses at shear strains of 10^{-05} ($\gamma = 10^{-05}$). From the elasticity theory with infinitesimal strains:

$$d\sigma_{ij} = C^{e}_{ijkl} d\varepsilon^{e}_{kl} \tag{D.1}$$

Where,

$d\sigma_{ij}$ the tensor of incremental stress,

$C^{e}_{ijkl}$the tensor of the elastic modulus,

$d\epsilon^{e}_{ij}$ the tensor of elastic strain.

The tensor of the elastic constants could be written as:

$$C^{e}_{ijkl} = \frac{E}{2(1+\mu)}\left(\delta_{il}\delta_{jk} + \delta_{ik}\delta_{jl}\right) + \frac{E\mu}{(1+\mu)(1-2\mu)}\delta_{ij}\delta_{kl} \tag{D.2}$$

$$K = \frac{E}{3(1-2\mu)}, G = \frac{E}{2(1+\mu)} \tag{D.3}$$

Where,

E the young's modulus,

μ the Poisson's ratio,

K the bulk modulus,

G the shear modulus.

If the elastic modulus tensor is independent on the strain amplitude and rate and direction of loading, the above constitutive relationships will capture the behavior of a linear elastic material.

However, during the elastoplastic response, the modulus tensor changes with the strain increment and plastic strains will evolve. Hence, the total strain increment is equal the summation of the elastic strain increment and the plastic strain increment as follows:

$$\dot{\epsilon}^{total}_{ij} = \dot{\epsilon}^{e}_{ij} + \dot{\epsilon}^{p}_{ij} \tag{D.4}$$

Where,

$d\epsilon^{total}_{ij}$ the tensor of incremental total strain,

$d\epsilon^{e}_{ij}$ the tensor of elastic strain,

$d\epsilon^{p}_{ij}$ the tensor of plastic strain.

D.2.1 Monotonic Loading

The degradation of the modulus during loading of a granular soil is a function of strain amplitude, mean stress, void ratio, and some other factors such as cementation (Hardin & Drnevich, 1972a). A modified hyperbolic stress-strain relation with a steeper than hyperbolic stress-strain curve at small strains is a better fit for actual soil behavior (Hardin & Drnevich, 1972b). Figure D.1 shows a schematic of a modified hyperbolic stress-strain relationship and the associated modulus degradation curve.

Jung (2009) presented the relation for the modified hyperbolic relation based on Hardin and Drnevich (1972b) as follows:

$$G = \frac{d\tau}{d\gamma} = G_o \frac{1}{(1+\gamma_h)^2} \tag{D.5}$$

Defining γ_h as:

$$\gamma_h = \frac{\gamma}{\gamma_r}\left[1 + aexp\left(-b\left({}^{\gamma}\!/_{\gamma_r}\right)\right)\right] \tag{D.6}$$

Defining γ_r as:

$$\gamma_r = \frac{\tau_f}{G_0} \tag{D.7}$$

Where,

G_0 the small strain shear modulus,

γ the shear strain,

γ_r the reference shear strain,

a, b fitting parameters,

τ_f the shear stress at failure.

The small strain shear modulus for granular soils and its dependency on the mean effective stress can be estimated based on the empirical correlations provided by Hardin (1978) as follows:

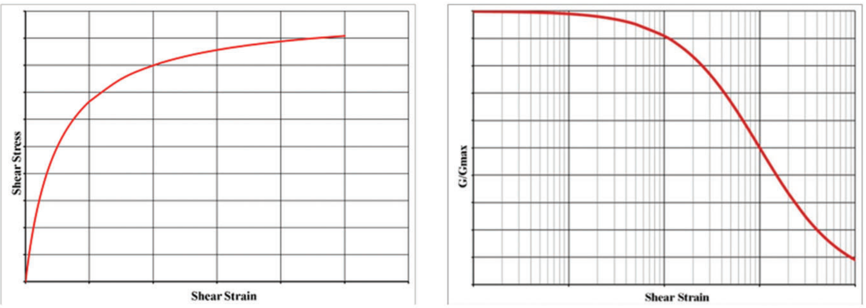

(a) Hyperbolic stress-strain curve (b) Modulus degradation curve

Figure D.1 Schematic of a modified hyperbolic stress-strain relationship and associated modulus degradation curve.

$$G_o^{ref} = 625 \frac{1}{0.3 + 0.7e^2} \sqrt{P_a \sigma'_{m,ref}} \qquad \text{(D.8)}$$

$$G_o = G_o^{ref} \left(\frac{\sigma_m}{\sigma_m^{ref}} \right)^{0.5} \qquad \text{(D.9)}$$

Where,
e the void ratio,
P_a the atmospheric pressure,
$\sigma'_m$the mean effective stress,
G_o^{ref} the reference small strain shear modulus,
σ_m^{ref} the reference effective mean stress.

D.2.2 Cyclic Loading

The unloading and reloading stress-strain relationships for soils follow "rules." The rules control the initial stiffness and the modulus degradation during the unloading/reloading phases. The original Masing's rules, as reported in Tatsuoka et al. (2003), call for a symmetrical backbone curve and the initial stiffness upon unloading/reloading to be equal to the initial stiffness of the backbone curve. Furthermore, the degradation relationships for the unloading/reloading curves are the same as the backbone curve. Figure D.2 shows a schematic explaining Masing's rules.

Based on the schematic in Figure D.2, it is obvious that for there will be no increase in the stress with number of cycles at the same strain amplitude. This is attributed to the use of the same small strain shear modulus for initial loading, unloading, and reloading (G_o). Hence, Masing's rules require some modifications to capture the observed behavior of granular soils under cyclic loading. An example of the observed cyclic response of dry granular soils is presented in the current study (Chapter 4) and can be found in the literature (Masuda, Tatsuoka, Yamada, & Sato, 1999).

The modifications on Masing's rules are geared toward capturing the observed behavior from certain loading paths such as plane strain versus triaxial loading/unloading (Tatsuoka, Masuda, Siddiquee, & Koseki, 2003; Jung, 2009). Jung (2009) proposed different modulus degradation relationships for the initial loading (backbone curve), unloading, and reloading, as follows:

$$G = G_o \frac{1}{\left(1 + \frac{1}{n} \left| \Gamma - \Gamma_{rev} \right| \right)^2} \qquad \text{(D.10)}$$

$$\Gamma = \frac{\gamma_{oct}}{\gamma_{oct,r}} \left[1 + aexp\left(-b\left({}^{\gamma_{oct}}\!/_{\gamma_{oct,r}} \right) \right) \right] \qquad \text{(D.11)}$$

$$\Gamma_{\text{rev}} = \frac{\gamma_{oct,rev}}{\gamma_{oct,r}} \left[1 + aexp\left(-b\left({}^{\gamma_{oct\ rev}}\!/_{\gamma_{oct,r}} \right) \right) \right] \qquad \text{(D.12)}$$

$$\gamma_{oct} = \frac{2}{3} \left[(\epsilon_{11} - \epsilon_{22})^2 + (\epsilon_{22} - \epsilon_{33})^2 + (\epsilon_{33} - \epsilon_{11})^2 + 6\left(\epsilon_{12}^2 + \epsilon_{23}^2 + \epsilon_{31}^2\right) \right]^{0.5} \qquad \text{(D.13)}$$

$$n = \left\{ \begin{matrix} n_1, & unloading \\ n_2, & reloading \end{matrix} \right\} \qquad \text{(D.14)}$$

Where,
n is a constant.
$\gamma_{oct,rev}$ is the octahedral shear strain at reversal point.
$\gamma_{oct,r}$ is the reference octahedral shear strain as determined from the octahedral shear stress at failure and the initial shear modulus.

Based on the above formulation, the initial shear modulus is determined based on the effective mean stress and the degradation of the unloading/reloading curve is different from the backbone curve. This modification will result in an unsymmetrical backbone curve and unloading/reloading curves. Figure D.3 presents a schematic of the response based on the modifications provided by Jung (2009). It should be noted that the escalation of stresses occurs only during the first cycle after the initial backbone curve. The subsequent cycles will be relatively similar to the first unloading/reloading. The similarity in subsequent cycles resulted from the use of relatively similar unloading/reloading initial shear modulus (as shown in Figure D.3). However, it should be noted that any changes of the initial modulus between subsequent cycles in Jung's 2009 model are due to the update of the effective confining pressure (equation D.9).

In this study, two modifications, other than extending the model to the three-dimensional stress space, were implemented on the model developed by Jung (2009): shifting of the backbone curve and capture the soil's behavior during reloading.

The shifting of the backbone curve along the horizontal axis was implemented to capture the escalation of stresses with the number of cycles. The shifting was achieved by utilizing the incremental plastic strain at the reversal point. This concept of the shifting of the backbone curve as a function of the plastic strain was used by Tatsuoka et al. (2003). In the current study the function used to determine the shifting magnitude was developed based on the tests presented in Chapter 4. Furthermore, different

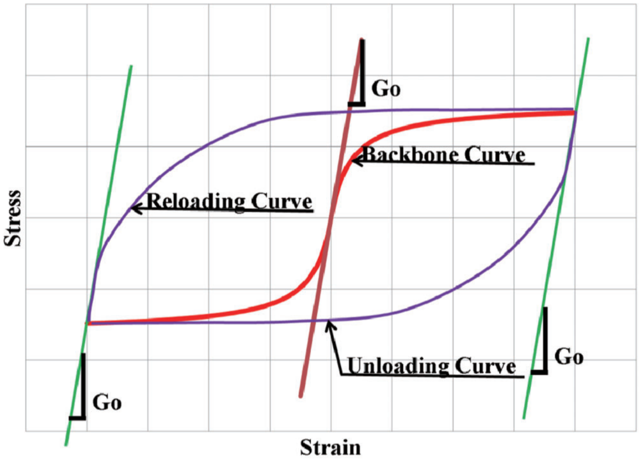

Figure D.2 Schematic of a full loading cycle with Masing's rules.

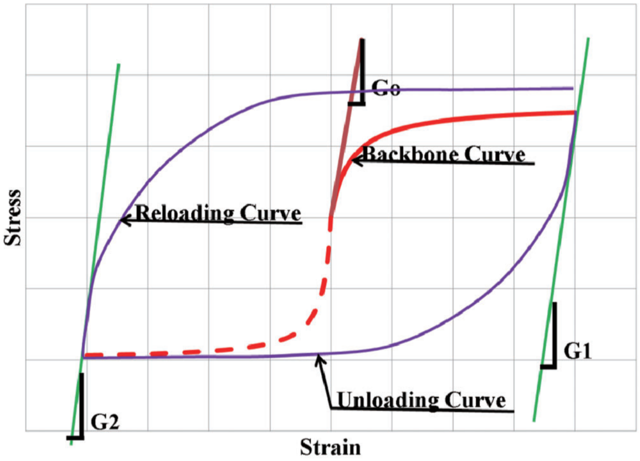

Figure D.3 Schematic of a full loading cycle based on Jung (2009).

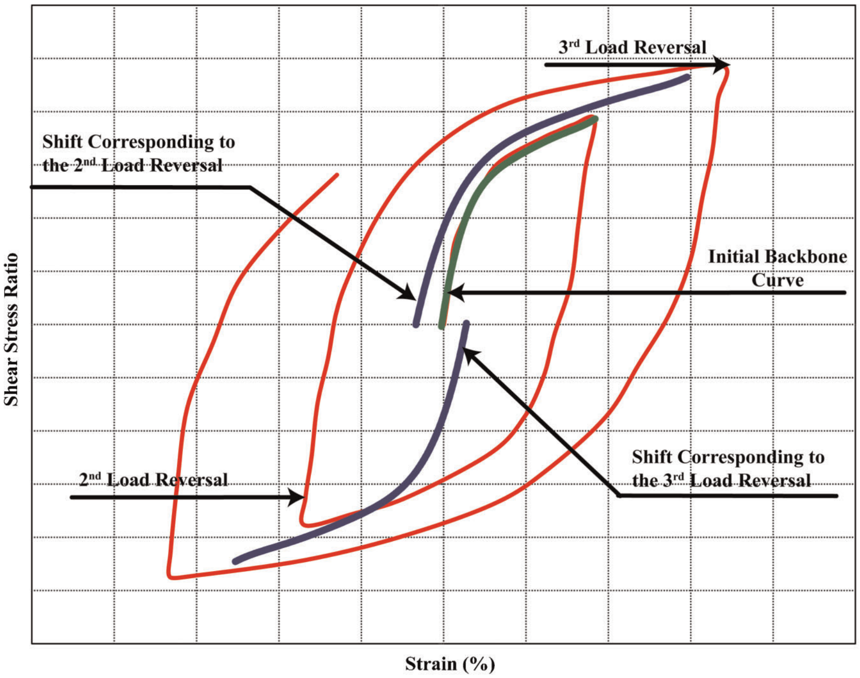

Figure D.4 Shifting of the backbone curve.

shifting functions were used during unloading and reloading. The shifting concept is illustrated in Figure D.4 using actual Cyclic Direct Simple Shear laboratory test results (Pradhan, Tatsuoka, & Sato, 1989).

It is noted from Figure D.4 that the shifting happens after reversal. The shifting magnitude is a function of the plastic strain increment ($\varepsilon_p^{'}$) and the number of cycles. The shifting direction is in the positive direction for the reloading and in the negative direction for the unloading. As one can see in equations D.11 and D.12, the degradation of the shear modulus curve is a function of the octahedral shear strain (equation D.13). The following equations illustrate how the shifting is achieved at load reversal. A load reversal is identified when the multiplication of any subsequent octahedral shear strain increment is less than zero (i.e., $\gamma_{oct,r}^{'}\gamma_{oct,r+1}^{'} < 0$). Once this is done, it is determined whether it is unloading or reloading reversal to apply the right shift. This is done as follows:

$$\gamma_{oct@load\ reversal} = \left\{ \begin{array}{cc} 0, & No\ Shifting \\ 0 + f\left(\varepsilon_p^{'}, N\right), & unloading \\ 0 - f\left(\varepsilon_p^{'}, N\right), & reloading \end{array} \right\} \quad \text{(D.15)}$$

Where,
$\varepsilon_p^{'}$ the plastic strain increment,
N the number of cycles.

The second modification of Jung's 2009 model was done to capture the soil's behavior upon reloading, as observed from the tests discussed on Chapter 4 and from the results from plane strain tests presented by Masuda et al. (1999). Figure D.5 shows one of the test results from Chapter 4 of this study with the observed response upon reloading.

Figure D.5 shows that upon reloading the response is close to linear up to zero displacement and then the stress-strain curve follows a hyperbolic curve. This behavior was also observed in the plane strain tests reported by Masuda et al. (1999) and in the tests conducted as part of this study (Chapter 4). It follows that such response should be expected from cyclic loading on a retaining wall. For triaxial and direct simple shear tests, only the hyperbolic (or close to hyperbolic) response was observed upon reloading (i.e., without the linear option); see Pradhan et al. (1989). It was found that the linear portion of the unloading curve has an approximately constant slope. The constant slope is a fraction of the initial small strain shear modulus (G$_o$). The following equations present the relationships used upon reloading:

$$G = \left\{ \begin{array}{ll} G_o \dfrac{1}{\left(1 + \dfrac{1}{n}\left|\Gamma - \Gamma_{rev}\right|\right)^2} & Without\ initial\ linear\ response \\ {}^{G_o}\!/_{C1} & With\ initial\ linear\ response,\ \varepsilon < 0 \\ G_o \dfrac{1}{\left(1 + \dfrac{1}{n}\left|\Gamma - \Gamma_{rev}\right|\right)^2} & With\ initial\ linear\ response\ \varepsilon > 0 \end{array} \right\} \quad \text{(D.16)}$$

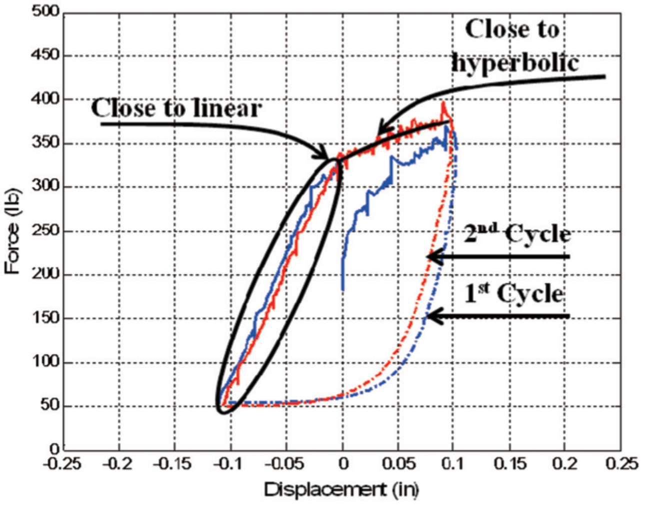

Figure D.5 Linear and hyperbolic response upon reloading.

Where,
C1 is a constant.

G_o, Γ, and Γ_{rev} as calculated by equations (D.9), (D.11), and (D.12), respectively.

The new constitutive model allows the user to choose between the two observed behaviors.

D.2.3 Yield Criteria and Plastic Strains

The yield criteria used in the model is the Drucker-Prager (D-P) with unassociated flow rule (as reported by Jung (2009)). The yield surface of the D-P is considered suitable for granular soils. The function for the yield surface is given in terms of the first stress invariant (I_1) and the second deviatoric stress invariant (J_2) as follows:

$$F=\sqrt{3J_2}-\frac{1}{3}I_1 tan\alpha-\kappa=0 \qquad (D.17)$$

$$I_1=\sigma_{kk} \qquad (D.18)$$

$$J_2=\frac{1}{2}S_{ij}S_{ij} \qquad (D.19)$$

$$S_{ij}=\sigma_{ij}-\frac{1}{3}\sigma_{kk}\delta_{ij} \qquad (D.20)$$

Where,
α is a function of the soil's friction angle (ϕ) and dilation angle (ψ),
κ is a function of cohesion,
S_{ij} is the deviatoric stress tensor.

Jung (2009) suggested the use of the following plastic potential function:

$$Q=\sqrt{J_2}+\frac{1}{3}I_1 tan\psi \qquad (D.21)$$

The plastic strain increment is calculated as a function of the equivalent plastic strain increment ($d\bar{\varepsilon}^{pl}$) and the plastic potential function (Q) as follows:

$$d\varepsilon_{ij}^{pl}=d\bar{\varepsilon}^{pl}\frac{dQ}{dS_{ij}} \qquad (D.22)$$

$$d\varepsilon_{ij}^{pl}=d\bar{\varepsilon}^{pl}\left(\frac{\sqrt{3}}{2}\frac{1}{\sqrt{J_2}}S_{ij}+\frac{1}{3}tan\psi\delta_{ij}\right) \qquad (D.23)$$

The incremental plastic strain ($d\bar{\varepsilon}^{pl}$) is given as follows:

$$d\bar{\varepsilon}^{pl}=\left\{\begin{array}{ll} 0 & No\ yield \\ d\varepsilon_{11}^{pl}(Axial\ Loading) & other\ wise \\ \frac{d\gamma_{12}^{pl}}{\sqrt{3}}(Shear\ Laoding) & \end{array}\right\} \qquad (D.24)$$

D.3 MODEL IMPLEMENTATION

The model was coded in a Fortran 77 programming language to be used as a user defined material subroutine for Abaqus© Standard (UMAT) and for Abaqus© Explicit (VUMAT). Since the thermal cyclic loading on Integral Abutment Bridges is a low frequency cyclic loading, the use of Abaqus Standard is considered appropriate.

One of the objectives of the research was to keep the model simple while capturing fundamental soil behavior. The model has twelve input parameters; they are as follows:

1. Reference small strain shear modulus
2. Reference effective mean stress
3. Poisson's ratio at small strains
4. Drucker-Prager friction angle
5. Drucker-Prager cohesion
6. Modulus degradation constant (a) for all cycles including the backbone curve
7. Modulus degradation constant (b) for all cycles including the backbone curve
8. Modulus degradation constant (n1) for unloading curves
9. Modulus degradation constant (n2) for reloading curves
10. Constant for the linear portion of the reloading curves (c1)
11. Static time, time before the first load reversal
12. Dilation angle

It could be observed that seven (7) of the above parameters are considered physical parameters and the other five (5) could be considered as fitting parameters. The flow chart of the model implementation is presented in Figure D.6. The Fortran 77 code is attached as Appendix D-1.

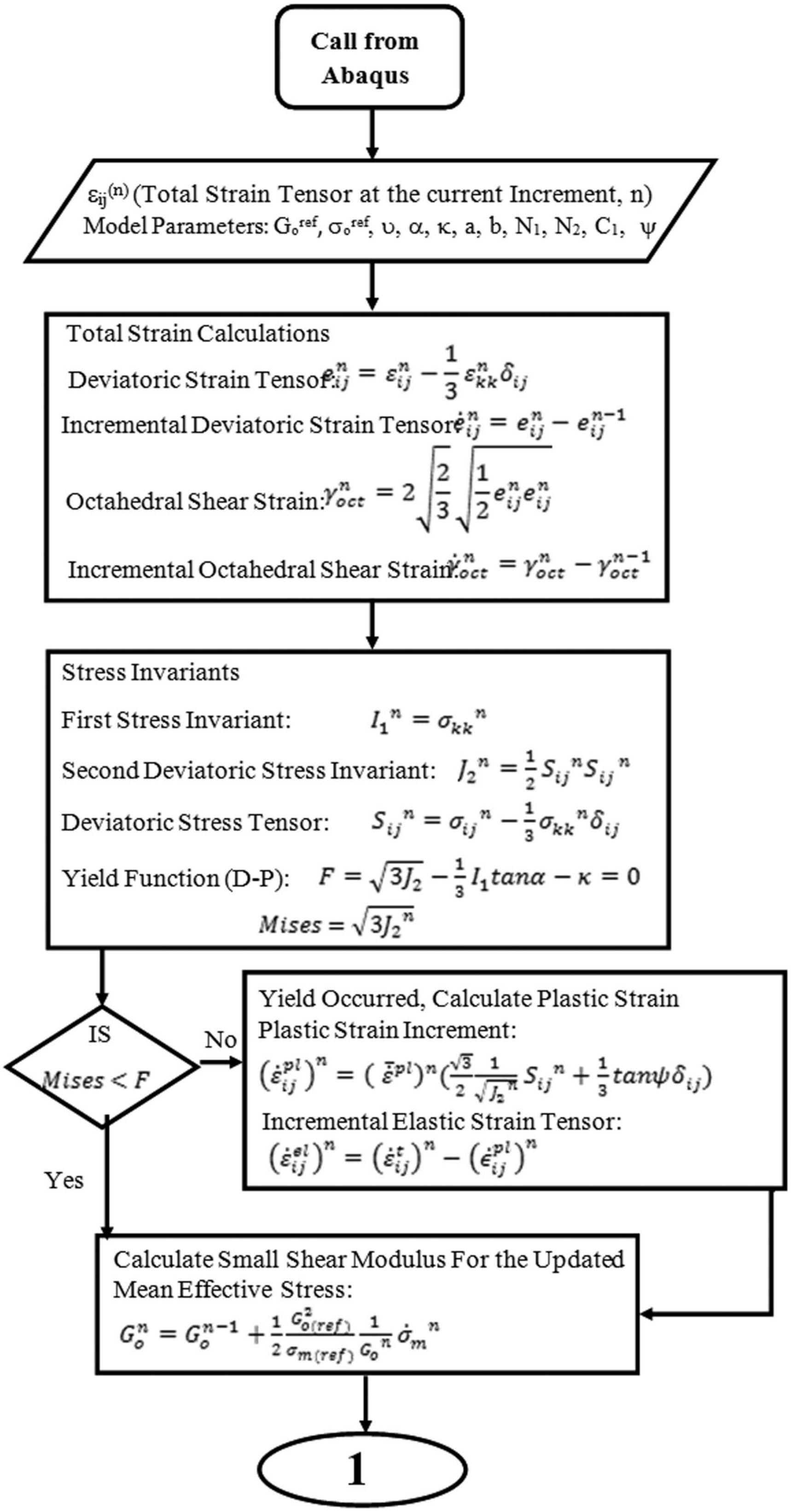

Figure D.6 Flow chart for model implementation in Abaqus© Standard.

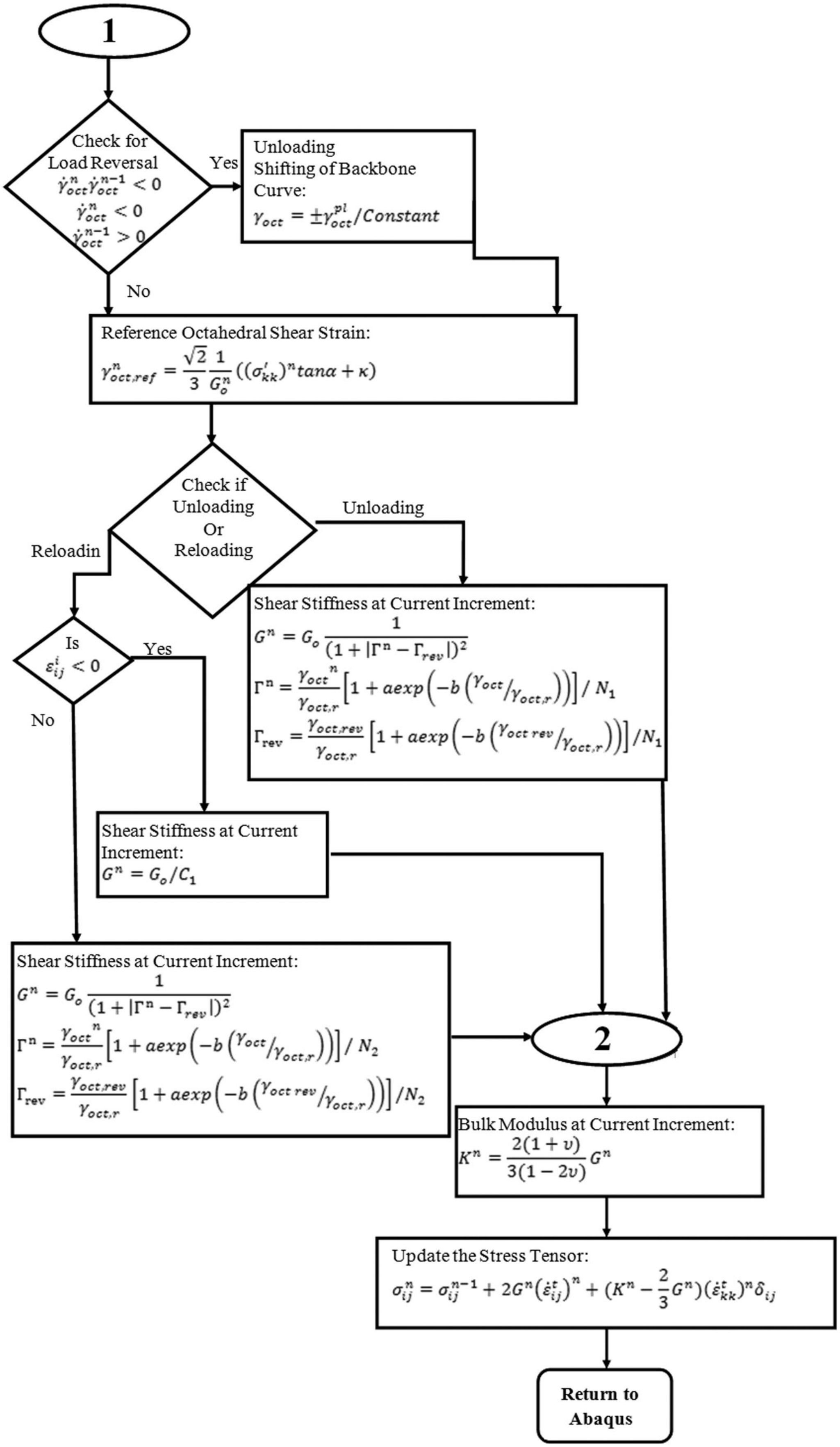

Figure D.6 Continued.

D.4 REFERENCES

Hardin, B. O., & Drnevich, V. P. (1972a). Shear modulus and damping in soils: Measurement and parameter effects. *Journal of the Soil Mechanics and Foundation Division*, *98*(6), 603–624.

Hardin, B. O., & Drnevich, V. P. (1972b). Shear modulus and damping in soils: Design equations and curves. *Journal of the Soil Mechanics and Foundation Division*, *98*(7), 667–692.

Hardin, B. O. (1978). The nature of stress-strain behavior for soils. In *Earthquake Engineering and Soil Dynamics—Proceedings of the ASCE Geotechnical Engineering Division Specialty Conference* (pp. 3–90), June 19–21, 1978, Pasadena, CA.

Ishihara, K. (1982). Evolution of soil properties for use in earthquake response analysis. *Proceedings of the International Symposium of Numerical Models in Geomechanics*, Zurich, 237–259.

Jung, C. (2009). *Seismic loading on earth retaining structures* (Unpublished doctoral thesis). West Lafayette, IN: Purdue University.

Masuda, T., Tatsuoka, F., Yamada, S., & Sato, T. (1999). Stress-strain behavior of sand in plane strain compression, extension and cyclic loading tests. *Soils and Foundations*, *39*, 31–45.

Pradhan, T. B., Tatsuoka, F., & Sato, Y. (1989). Experimental stress-dilatancy relations of sand subjected to cyclic loading. *Soils and Foundations*, *29*(1), 45–64.

Tatsuoka, F., Masuda, T., Siddiquee, M. S., & Koseki, J. (2003). Modeling the stress-strain relations of sand in cyclic plane strain loading. *Journal of Geotechnical and Geoenvironmental Engineering*, *129*, 450–467.

Yu, H., Khong, C., & Wang, J. (2007). A unified plasticity model for cyclic behavior of clay and sand. *Mechanics Research Communications*, *34*, 97–114.

APPENDIX D-1

```
      SUBROUTINE UMAT(STRESS,STATEV,DDSDDE,SSE,SPD,SCD,
     1 RPL,DDSDDT,DRPLDE,DRPLDT,STRAN,DSTRAN,
     2 TIME,DTIME,TEMP,DTEMP,PREDEF,DPRED,MATERL,NDI,NSHR,NTENS,
     3 NSTATV,PROPS,NPROPS,COORDS,DROT,PNEWDT,CELENT,
     4 DFGRD0,DFGRD1,NOEL,NPT,KSLAY,KSPT,KSTEP,KINC)
C
      INCLUDE 'ABA_PARAM.INC'
C
      CHARACTER*80 MATERL
       DOUBLE PRECISION STRESS(NTENS),STATEV(NSTATV),
     1 DDSDDE(NTENS,NTENS),DDSDDT(NTENS),DRPLDE(NTENS),
     2 STRAN(NTENS),DSTRAN(NTENS),TIME(2),PREDEF(1),DPRED(1),
     3 PROPS(NPROPS),COORDS(3),DROT(3,3),
     4 DFGRD0(3,3),DFGRD1(3,3)
C
      DIMENSION EELAS(NTENS),EPLAS(NTENS),FLOW(NTENS)
        DOUBLE PRECISION gzeroref, meanpref, nuzero, alpha, kappa, a, b
        DOUBLE PRECISION none, ntwo, threshold, statictime, psi
        DOUBLE PRECISION gzero, gmin, G, K,Ione, rtJtwo, Mises, F
        DOUBLE PRECISION dgamma, gammay, gamratio, s11, s22, s33, s12
        DOUBLE PRECISION dmeanp, tauoctmax, sqrtJ2e, yield
        DOUBLE PRECISION depl11, depl22, depl33, depl12, depl23, depl31
        DOUBLE PRECISION deel11, deel22, deel33, deel12, deel23, deel31
        DOUBLE PRECISION depleq, epleq, depleq23
        DOUBLE PRECISION depleq1, depleq2, depleq3, depleq12, depleq31
        integer s, sg, loadtype, option
C
C -----------------------------------------------------------

C -----------------------------------------------------------

C -----------------------------------------------------------
C

C
C  INPUT MATERIAL PROPERITIES
C
         gzeroref=props(1)
         meanpref=props(2)
         nuzero=props(3)
         alpha=props(4)
         kappa=props(5)
         a=props(6)
         b=props(7)
         none=props(8)
         ntwo=props(9)
         option=props(10)
         statictime=props(11)
         psi=props(12)

      IF(nuzero.GT.0.4999.AND.nuzero.LT.0.5001) nuzero=0.499
```

```
      K=(2.d0*gzeroref*(1.d0+nuzero))/(3.d0*(1.d0-2.d0*nuzero))

C
C     ELASTIC STIFFNESS
C
      DO 20 K1=1,NTENS
        DO 10 K2=1,NTENS
           DDSDDE(K2,K1)=0.0
 10     CONTINUE
 20   CONTINUE
C
      DO 40 K1=1,NDI
        DO 30 K2=1,NDI
           DDSDDE(K2,K1)=k-(2.d0*gzeroref/3.d0)
 30     CONTINUE
        DDSDDE(K1,K1)=k+(2.d0*gzeroref/3.d0)
 40   CONTINUE
      DO 50 K1=NDI+1,NTENS
        DDSDDE(K1,K1)=2.d0*gzeroref
 50   CONTINUE
C  Writing Strain Vector eypsilon_ij
c      Do 60 K1=1,NTENS
c      STATEV(K1)=STRAN(K1)
c 60   CONTINUE
C  Writing Strain Increment Vector eypsilon_dot_ij
c      Do 70 K2=NTENS+1,2*NTENS
c      STATEV(K2)=DSTRAN(K2)
c 70    CONTINUE


       if (TIME(2).gt.STATEV(98))then
       STATEV(25)=STATEV(13)
       STATEV(26)=STATEV(14)
       STATEV(27)=STATEV(15)
       STATEV(28)=STATEV(16)
       STATEV(29)=STATEV(17)
       STATEV(30)=STATEV(18)
       STATEV(43)=STATEV(37)
       STATEV(44)=STATEV(38)
       STATEV(45)=STATEV(39)
       STATEV(46)=STATEV(40)
       STATEV(47)=STATEV(41)
       STATEV(48)=STATEV(42)
       STATEV(61)=STATEV(19)
       STATEV(62)=STATEV(20)
       STATEV(63)=STATEV(21)
       STATEV(64)=STATEV(22)
       STATEV(65)=STATEV(23)
       STATEV(66)=STATEV(24)
       STATEV(68)=STATEV(33)
       STATEV(70)=STATEV(69)
       endif
       if (KINC.gt.STATEV(73))then
```

```
        STATEV(34)=STATEV(32)
        STATEV(36)=STATEV(35)
        endif
C  EVALUATE DEVIATORIC STRAIN TENSOR e_ij
        STATEV(13)=(2.d0*STRAN(1)-STRAN(2)-STRAN(3))/3.d0
        STATEV(14)=(2.d0*STRAN(2)-STRAN(1)-STRAN(3))/3.d0
        STATEV(15)=(2.d0*STRAN(3)-STRAN(2)-STRAN(1))/3.d0
        STATEV(16)=STRAN(4)
        STATEV(17)=STRAN(5)
        STATEV(18)=STRAN(6)

C  EVALUATE INCREMENTAL DEVIATORIC STRAIN TENSOR de_ij
        STATEV(19)=STATEV(13)-STATEV(25)
        STATEV(20)=STATEV(14)-STATEV(26)
        STATEV(21)=STATEV(15)-STATEV(27)
        STATEV(22)=STATEV(16)-STATEV(28)
        STATEV(23)=STATEV(17)-STATEV(29)
        STATEV(24)=STATEV(18)-STATEV(30)

c  Storing the Old DEVIATORIC STRAIN TENSOR e_ij


C  CALCULATE sqrtJ2e, OCTHEDRAL SHEAR STRAIN
        STATEV(31)=dsqrt(0.5d0*(STATEV(13)**2.d0+STATEV(14)**2.d0
      + +STATEV(15)**2.d0+2.d0*STATEV(16)**2.d0+2.d0*STATEV(17)**
      +  2.d0+2.d0*STATEV(18)**2.d0))
        STATEV(32)=2.d0*dsqrt(2.d0/3.d0)*STATEV(31)
        STATEV(33)=STATEV(32)-STATEV(34)
        if (STATEV(33).lt.0.)then
         STATEV(35)=STATEV(36)-STATEV(33)
         else
         STATEV(35)=STATEV(36)+STATEV(33)
c        STATEV(35)=STATEV(35)
        endif
C  Storing the old sqrtJ2e, OCTHEDRAL SHEAR STRAIN

C    CALCULATE STRESS FROM ELASTIC STRAINS
C
C  EVALUATE STRESS INVARIENTS, IONE and JTWO
        Ione=stress(1)+stress(2)+stress(3)
        rtJtwo=dsqrt((1.d0/6.d0)*
      + ((stress(1)-stress(2))**2.d0
      + +(stress(2)-stress(3))**2.d0
      + +(stress(3)-stress(1))**2.d0)+stress(4)**2.d0
      + +stress(5)**2.d0+stress(6)**2.d0)
        Mises=dsqrt(3.d0)*rtJtwo
        F=-1.d0/3.d0*Ione*dtand(alpha)+kappa
C EVALUATE DEVIATORIC STRESS TENSOR
c          s11=stress(1)-1.d0/3.d0*Ione
c          s22=stress(2)-1.d0/3.d0*Ione
c          s33=stress(3)-1.d0/3.d0*Ione
c          s12=stress(4)
c          s23=stress(5)
c          s31=stress(6)
```

```
C EVALUATE EQUIVALENT PLASTIC STRAIN

       If(Mises .lt. F)then
          depleq=0.

       else
        yield=1.d0
        depleq1=dabs(STATEV(19))
        depleq2=dabs(STATEV(20))
        depleq3=dabs(STATEV(21))
        depleq12=2.d0*dsqrt(3.d0)*dabs(STATEV(22))
        depleq23=2.d0*dsqrt(3.d0)*dabs(STATEV(23))
        depleq31=2.d0*dsqrt(3.d0)*dabs(STATEV(24))
        depleq=dmax1(depleq1,depleq2,depleq3,depleq12,depleq23,depleq31)
       endif
c------------------------------------------------------------------
C EVALUATE INCREMENTAL PLASTIC STRAIN TENSOR
         If(rtJtwo .lt. 1/(10.d30))then
          depl11=0.
          depl22=0.
          depl33=0.
          depl12=0.
          depl23=0.
          depl31=0.
         else
          depl11=depleq*(((5d-1*s11)/rtJtwo)+(1.d0/3.d0*dtand(psi)))
          depl22=depleq*(((5d-1*s22)/rtJtwo)+(1.d0/3.d0*dtand(psi)))
          depl33=depleq*(((5d-1*s33)/rtJtwo)+(1.d0/3.d0*dtand(psi)))
          depl12=depleq*(s12/rtJtwo)
          depl23=depleq*(s23/rtJtwo)
          depl31=depleq*(s31/rtJtwo)
         endif

         deel11=DSTRAN(1)-depl11
         deel22=DSTRAN(2)-depl22
         deel33=DSTRAN(3)-depl33
         deel12=DSTRAN(4)-depl12
         deel23=DSTRAN(5)-depl23
         deel31=DSTRAN(6)-depl31

         STATEV(37)=STATEV(43)+depl11
         STATEV(38)=STATEV(44)+depl22
         STATEV(39)=STATEV(45)+depl33
         STATEV(40)=STATEV(46)+depl12
         STATEV(41)=STATEV(47)+depl23
         STATEV(42)=STATEV(48)+depl31

c ---------------------------------------------------------
c  C  CALCULATE sqrtJ2e, OCTHEDRAL SHEAR STRAIN
       STATEV(49)=dsqrt(0.5d0*(STATEV(37)**2.d0+STATEV(38)
      + **2.d0+STATEV(39)**2.d0+2.d0*STATEV(40)**2.d0+2.d0*
     +  STATEV(41)**2.d0+2.d0*STATEV(42)**2.d0))
       STATEV(50)=2.d0*dsqrt(2.d0/3.d0)*STATEV(49)
```

```
         STATEV(51)=STATEV(50)-STATEV(53)
         STATEV(54)=STATEV(55)+dabs(STATEV(51))
         STATEV(53)=STATEV(50)
         STATEV(55)=STATEV(54)
c ----------------------------------------------------
         epleq=dsqrt(6.25d+1*(STATEV(37)**2.d0+
     +   STATEV(38)**2.d0+
     +   STATEV(39)**2.d0+STATEV(40)**2.d0+
     +   STATEV(41)**2.d0+STATEV(42)**2.d0))
c ------------------------------------------------------
C  EVALUATE GZERO AND GAMMAY
C      calculation of mean pressure
       STATEV(56)=(-1.d0/3.d0)*Ione
       if(STATEV(56) .lt. 0.d0)then
        STATEV(56)=1.d0/(1.d30)
       endif
       dmeanp=STATEV(56)-STATEV(57)
       STATEV(57)=STATEV(56)

       if(option .eq. 1)then
        STATEV(58)=gzeroref
       endif

       if(option .eq. 2)then
           if(TIME(2) .lt. 1.05*DTIME)then
           STATEV(58)=gzeroref
         else
          STATEV(58)=STATEV(59)+5.d-1*
     +     (gzeroref**2.d0)/meanpref
     +    /STATEV(59)*dmeanp
         endif
           if(STATEV(58) .lt. 1.d-1*gzeroref)then
          STATEV(58)=1.d-1*gzeroref
         endif
       endif

       if(option .eq. 3)then
        if(TIME(2) .lt. 1.05*DTIME)then
           STATEV(58)=gzeroref*dsqrt(STATEV(56)/meanpref)
        else
          STATEV(58)=STATEV(59)+5.d-1*(gzeroref**2.d0)/meanpref
     +    /STATEV(59)*dmeanp
        endif
         if(STATEV(58) .lt. 1.d-1*gzeroref)then
          STATEV(58)=1.d-1*gzeroref
         endif
       endif
       if (TIME(1).gt.STATEV(71))then
       STATEV(59)=STATEV(58)
       endif
       tauoctmax=dsqrt(2.d0)/3.d0*(dtand(alpha)*STATEV(56)+kappa)
       gammay= 1.d0/STATEV(58)*tauoctmax
c ---------------------------------------------------------------------
C  CHECK LOAD REVERSAL
```

```
          STATEV(60)=STATEV(19)*STATEV(61)+
        + STATEV(20)*STATEV(62)+STATEV(21)*STATEV(63)
        + +2.d0*STATEV(22)*STATEV(64)
        + +2.d0*STATEV(23)*STATEV(65)
        + +2.d0*STATEV(24)*STATEV(66)
            STATEV(67)=STATEV(33)*STATEV(68)
            STATEV(69)=STATEV(70)


              if(TIME(1) .ge. statictime)then
              if(STATEV(60) .lt. 0.d0)then
c             if(STATEV(68) .gt. 0)then
c              if(STATEV(33) .lt. 0)then
c              STATEV(35)=0.d0 + (STATEV(50)/1.0d02)
c              STATEV(35)=0.d0
               STATEV(69)=STATEV(69)+1.d0
c           if(STATEV(69) .lt. 1.d-1)then
c           STATEV(35)= STATEV(35)

c         else
          if(mod(STATEV(69), 2.d0) .lt. 5.d-1)then
          STATEV(35)=0.d0 - (STATEV(50)/9.5d02)

          else
          STATEV(35)=0.d0 - (STATEV(50)/9.5d01)

c         endif
c         endif
c             endif
            endif
           endif
           endif

c ---------------------------------------------------------------
C  CALCULATE G(tangential) AND K(tangential)

c--------------------------------------------------------------
          if(a .eq. 0.d0)then
          gamratio=1.d0
         else
          if(dabs(STATEV(35)) .lt. 1/(10.d20))then
            gamratio=1.d0+a
          else
           if(dabs(STATEV(35)) .gt. 10.d10)then
             gamratio=1.d0
           else
             gamratio=1.d0+a*dexp(-b*STATEV(35)/gammay)
           end if
          end if
         end if
c
          if(STATEV(69) .lt. 1.d-1)then

          G=STATEV(58)/(1.d0+gamratio*STATEV(35)/gammay)**2.d0
```

```
       else
        if(mod(STATEV(69), 2.d0) .lt. 5.d-1)then
c        if(TIME(1).lt.(50.0*STATEV(69)))then
c        G=STATEV(58)/(1.26d01)
c         G=33500.0
c        else
         G=STATEV(58)/(1.d0+
     +   gamratio*STATEV(35)/gammay/ntwo)**2.d0
c        endif
        else

         G=STATEV(58)/(1.d0+
     +   gamratio*STATEV(35)/gammay/none)**2.d0
        endif
       endif
        STATEV(74)=gamratio
        STATEV(75)=gammay

        STATEV(77)=Ione
        STATEV(78)=rtJtwo
        STATEV(79)=Mises
        STATEV(80)=F
        STATEV(81)=depleq
        STATEV(82)=yield

c        STATEV(83)=((5d-1*s11)/rtJtwo)+(1.d0/3.d0*tand(psi))
c        STATEV(84)=((5d-1*s22)/rtJtwo)+(1.d0/3.d0*tand(psi))
c        STATEV(85)=((5d-1*s33)/rtJtwo)+(1.d0/3.d0*tand(psi))
c        STATEV(86)=s12/rtJtwo
c        STATEV(87)=s11
c        STATEV(88)=s22
c        STATEV(89)=s33
c        STATEV(90)=s12
        STATEV(91)=deel11
        STATEV(92)=deel22
        STATEV(93)=deel33
        STATEV(94)=deel12

       gmin=1.d-2*STATEV(58)
      if(G .le. gmin)then
        G=gmin
       end if
        STATEV(76)=G/STATEV(58)
       K=(2.d0*G*(1.d0+nuzero))/(3.d0*(1.d0-2.d0*nuzero))
c---------------------------------------------------------------
c -----------Updated Jacobian------------------
        DO 100 I1=1,NDI
        DO 200 I2=1,NDI
           DDSDDE(I2,I1)=k-(2.d0*G/3.d0)
200       CONTINUE
        DDSDDE(I1,I1)=k+(2.d0*G/3.d0)
100       CONTINUE
       DO 300 II1=NDI+1,NTENS
        DDSDDE(II1,II1)=2.d0*G
```

```
300       CONTINUE
c----------------Update Stress--------------------------------
       Do 1000 III1=1, NDI
       STRESS(III1)=STRESS(III1)+2.d0*G*DSTRAN(III1)+
     + (K-(2.d0/3.d0)*G)*(DSTRAN(1)+DSTRAN(2)+ DSTRAN(3))
1000    Continue
       Do 2000 III2=NDI+1,NTENS
       STRESS(III2)=STRESS(III2)+2.d0*G*DSTRAN(III2)
2000    Continue

        STATEV(71)=TIME(1)
        STATEV(72)=KSTEP
        STATEV(73)=KINC
        STATEV(98)=TIME(2)

c      Do 1100 J=1,3
c      Do 1200 JJ=1,3
c      write(*,*) TIME(1), DROT(JJ,J)
c1200      continue
c1100      continue

c      Do 1300 JJJ=1,6
c      write(*,*) JJJ,'STRESS',DTIME, STRESS(JJJ)
c1300  CONTINUE

c      Do 1400 JJJ=1,6
c      write(*,*) 'KINC',KINC,'STEP', KSTEP
c1400  CONTINUE



      RETURN
      END
```

APPENDIX E. CONSTITUTIVE MODEL VERIFICATION AND CALIBRATION

E.1 INTRODUCTION

This chapter presents the verification and calibration of the proposed soil constitutive model (Chapter 5). Model verification was performed by simulating laboratory experiments, a quarter-scale bridge test, and a full-scale instrumented bridge. In addition to the full-scale bridge, the scale of experiments ranged from element to laboratory to large-scales tests. Thus the verification was conducted for various stress levels and length scales. All tests used in the model verification were performed as part of this study, except for the element scale tests, which were from published tests in the literature. Simulations of the large-scale tests and the full-scale bridge were used to calibrate the nonphysical parameters of the model.

As discussed in Chapter 5, there are eleven (11) parameters required for the constitutive model; six (6) of which are considered physical parameters (parameters that can be measured) and five (5) of which are fitting parameters (parameters that require calibration or can be estimated based on soil type). The physical parameters include:

1. Small strain reference stiffness ($G_{o,ref}$). Estimated using the Hardin (1978) equation as follows:

$$G_{o,ref} = 625\frac{1}{0.3+0.7e^2}\sqrt{P_a\sigma'_{m,ref}} \tag{E.1}$$

Where,
e=void ratio
P_a=atmospheric pressure
σ_m^{ref}= reference effective mean stress

2. Effective mean reference stress ($\sigma_{m,ref}$). Used to estimate $G_{o,ref}$.
3. Small strain Poisson's ratio (υ). Assumed to be 0.3 for all the cases.
4. Drucker-Prager friction angle (α). A function of the internal angle of friction (ϕ).

For a triaxial state of stresses, α is given by:

$$tan(\alpha) = \frac{2\sqrt{3}sin(\phi)}{3-sin(\phi)} \tag{E.2}$$

For plain-strain, α is given by:

$$sin(\phi) = \frac{tan(\alpha)\sqrt{3(9-tan^2(\psi))}}{9-tan(\alpha)tan(\psi)} \tag{E.3}$$

5. Drucker-Prager cohesion (κ). A function of cohesion (c), which is given by

$$\kappa = \frac{2\sqrt{3}c\ cos(\psi)}{3-sin(\psi)} \tag{E.4}$$

6. Dilation angle (ψ). Assumed to be 1° for all cases.

The fitting parameters include:

1. "a and b" control the shape of the modulus degradation curve of the initial backbone curve and subsequent cycles.
2. "N1 and N2" control the shape of the modulus degradation curves for unloading/reloading (after the first load reversal).
3. "C1" controls the semi-linear response observed during the initial reloading curve in cases of horizontal loading.

All of the fitting parameters were determined through simulation iterations until the measured stress-strain curves were reasonably captured.

Simulation of the element tests and the tests of the physical model with sand are presented in Sections E.2 and E.3, respectively. One test of a laterally loaded pile and two tests of a large-scale specimen (¼-scale bridge) are discussed in Sections E.4 and E.5, respectively. Finally, simulation of an instrumented bridge in Indiana (US 231 over the AEP Railroad Spur) is presented in Section E.6.

E.2 MODEL VERIFICATION: ELEMENT TESTS

The simulated element tests were conventional triaxial and direct simple shear cyclic tests on granular soils. The stress-strain relationships obtained from the simulations were compared to those reported in the literature; more specifically, triaxial test by Yu (2007), and the direct simple shear by Pradhan, Tatsuoka, and Sato (1989). Both tests were modeled in three-dimensional space with general 3D stress elements (volume elements), and the simulations were conducted as displacement-control.

E.2.1 Simulation of Triaxial Test

Yu (2007) performed drained cyclic triaxial tests on Ottawa sand. The tests were modeled with Abaqus© explicit (VUMAT for the material defined subroutine). Yu (2007) reported that the initial void ratio was 0.71, and the test was performed under a confining stress of 3.0 kg/cm^2 (~6300psf). The initial void ratio, along with the confining stress (effective mean reference stress), was used to estimate $G_{o,ref}$, which, based on Equation E.1 was taken as 1.1*10^6 psf. The value was adjusted (within 15%) to capture the initial (small-strain) portion of the stress-strain curve. The Drucker-Prager friction angle (α) was estimated based on a friction angle (ϕ) of 30° using Equation E.2. A very small cohesion was assumed for numerical stability. Table E.1 presents the model parameters used in the simulations.

The comparison between the stress-strain relationship obtained from the Abaqus© simulation and the Cyclic Triaxial test is presented in Figure E.1. As shown, the model has acceptable capabilities in capturing soil behavior under triaxial loading.

E.2.2 Simulation of Direct Simple Shear Test

Pradhan et al. (1989) performed drained direct simple shear Cyclic tests on granular soils (Toyoura sand). The tests were modeled with Abaqus© standard (UMAT for the material defined subroutine). Pradhan et al. (1989) reported that the initial void ratio was 0.83, and the test was performed under a confining stress of 1.0 kg/cm^2 (~2100 psf). The initial void ratio and the confining stress (effective mean reference stress) were used to estimate $G_{o,ref}$ (based on Equation E.1), which resulted in a value of 1.0*10^6 psf; the value was adjusted (within 15%) to capture the initial (small-strain) portion of the stress-strain curve. The Drucker-Prager friction angle (α) was estimated based on a friction angle (ϕ) of 30° using Equation E.3. A

TABLE E.1
Soil Model Parameters—Cyclic Triaxial Test Simulation

$G_{o,ref}$ psf (N/m^2)	$\sigma_{m,ref}$ psf (N/m^2)	υ	α deg	κ psf (N/m^2)	a	b	N_1	N_2	ψ deg
9.4*10^5 (4.5*10^7)	6.3*10^3 (3.0*10^5)	0.3	35	0.02 (1)	−0.06	1.3	2.05	2.4	1

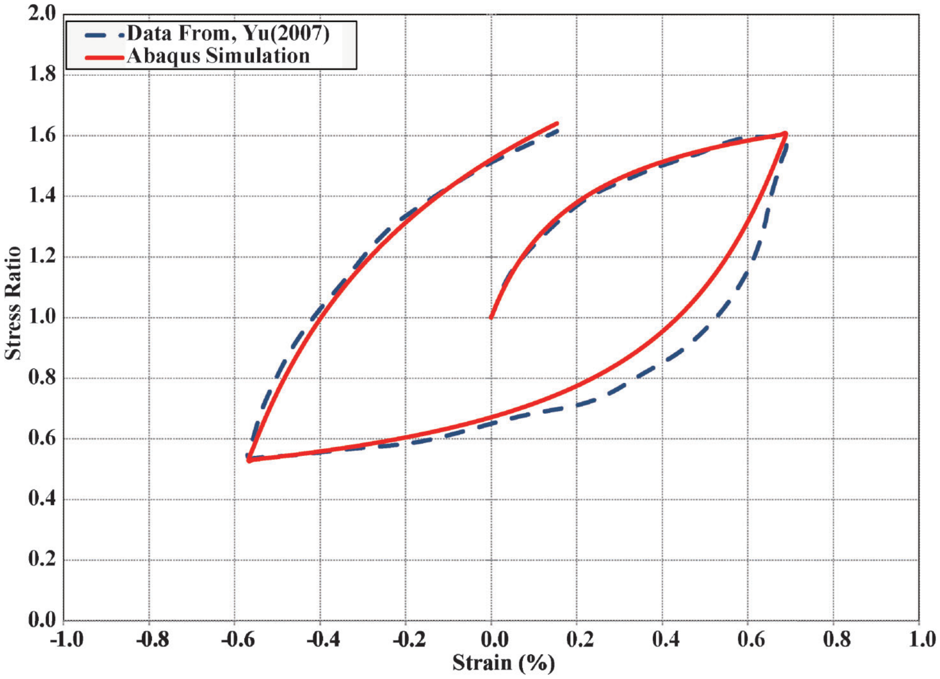

Figure E.1 Comparison of the stress-strain relationship—laboratory cyclic triaxial test.

very small cohesion was assumed for numerical stability. Table E.2 presents the model parameters used in the simulation.

The comparison between the stress-strain relationship obtained from the Abaqus© Simulation and the cyclic direct simple shear test is presented in Figure E.2. It can be concluded that the model has acceptable capabilities in capturing soil behavior under direct shear loading.

E.3 MODEL VERIFICATION: PHYSICAL MODEL

The physical model that simulated abutment movement due to thermal expansion and contraction of the bridge's deck was presented in Chapter 4. Four tests were simulated to cover different wall angles and wall conditions (smooth and rough) and are listed in Table E.3. The objectives of the simulations were to:

1. Evaluate the validity of the model in capturing behavior under shearing conditions different from those of the element tests.
2. Examine model performance under different stress levels.
3. Evaluate the ability of the model to capture rotation of the backbone curve.
4. Evaluate the ability of the model to capture linearity of the observed response upon reloading.
5. Evaluate the performance of the model with various contact conditions.

The tests selected for simulation include those that have a loading sequence similar to what will be used in the parametric study in Chapter 7. The tests with 60° walls were not simulated because the test results were not reliable due to the proximity of the boundaries to the wall in the physical model as discussed in Chapter 4.

The tests were simulated in three-dimensional space with Abaqus© Standard. The dimensions of the model were identical to those of the physical model. The modeled soil was 3-ft long (longest side), 1 ft in width and 1 ft in height. The front and back plates' dimensions in the model were 1.5 ft in height and 1.0 ft in width with a thickness of 0.5 in. The model and sample dimensions are shown in Figure E.3.

Boundary conditions and contacts were simulated such that they replicated the boundaries and contacts of the physical model. Fixed boundaries were assigned to the back plate (far field). Rollers were used to simulate the assumed frictionless condition between the plates and the sand. The contact between the sand and the back plate was assumed as frictionless with a hard-type contact using the surface to surface finite sliding contact algorithm in Abaqus© Standard. A hard contact is used in Abaqus to enforce contact between the two surfaces, which ensures that there is no penetration. The contact between the front plate and the sand was assigned as either smooth (Tests 2 and 9) or rough (Tests 5 and 8) based on the actual test. Abaqus has few friction algorithms mostly derived from classical Coulomb friction ($\tau_{crit}=\mu p$. The enforcement of classical Coulomb friction, which allows slip only when $\tau>\tau_{crit}$ (referred to as the "Lagrange Multiplier" in Abaqus) could cause convergence problems, as the contact will be rigid until the limit shear stress is reached (perfectly plastic at the contact). However, the penalty friction allows for small finite sliding (elastic sliding). The magnitude of the "elastic sliding" changes with each increment based on the stresses at the contact. Therefore, the penalty friction was used in the analysis as it allows for small sliding during each increment. The algorithm used for the contact between the front plate and the sand was similar to the

TABLE E.2
Soil Model Parameters—Cyclic Direct Simple Shear Test Simulation

$G_{o,ref}$ psf (N/m^2)	$\sigma_{m,ref}$ psf (N/m^2)	υ	α (deg)	κ psf (N/m^2)	a	b	N_1	N_2	ψ deg
$8.8*10^5$ ($4.2*10^7$)	$2.1*10^3$ ($1.0*10^5$)	0.3	40	0.02 (1)	−0.5	0.65	1.66	1.82	1

TABLE E.3
Simulated Physical Model Tests

Test #*	Amplitude (in.)	Wall Angle (degrees (°))	Wall Condition
2	±0.1	0	Smooth
5	±0.1	45	Rough
8	±0.1	45	Smooth
9	±0.1	0	Rough

*Test # is the same given in Table 4.3.

one used between the back plate and the sand, except that a penalty friction was assigned for the rough wall condition (μ=0.4, equivalent to a friction angle of 21.3°). The boundary conditions and contacts are presented in Figure E.4.

Cyclic displacement was applied at the front plate in the longitudinal direction. The displacement cycle amplitude was ±0.1 in. (equal to the displacement of the actual test). A total of ten cycles (10) were imposed in each simulation.

The model was discretized using 8-node linear brick, general stress elements. The simulations were performed using Abaqus© Standard. The plates were modeled as a linear-elastic material, and the sand was modeled as an elastoplastic material using the constitutive model developed in this study (UMAT, refer to Chapter 5). The elastic model parameters for the plates are presented in Table E.4.

The elastoplastic model parameters for the sand with the zero degree (0°) wall (Tests 2 and 9), and the forty-five degree (45°) wall (Tests 5 and 8) configurations are presented in Tables E.5 and E.6, respectively. Based on the sand characterization tests and the preliminary test on the sand to calibrate the compaction effort (Chapter 4), maximum and minimum void ratios (e_{max} and e_{min}) were estimated to be 0.77 and 0.5, respectively. The relative density (Dr) was estimated as 32%, given the compaction effort used in sample preparation. The internal angle of friction (ϕ) at Dr=32% was about 31°. Based on the above measured properties, the initial void ratio was about 0.57. Using Equations E.1 and E.3 and at mean effective stress of 110 psf, $G_{o,ref}$ and α were estimated as 1.5*10^5 psf and 41°, respectively. Subsequently, $G_{o,ref}$ was changed by about 30% to capture better the initial portion of the load-displacement curve (small-strain).

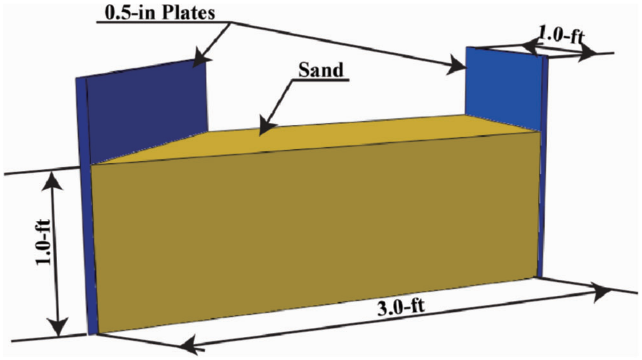

Figure E.3 Numerical model dimensions.

It should be noted that the parameters change with the skew angle of the test. This difference occurs because the stress path imposed to the soil depends on the location of the soil behind the wall (center, obtuse, or acute corners) and on the skew.

E.3.1 Tests with Zero Degree (0°) Wall (Tests 2 and 9)

The results from the simulation of the tests with a zero (0°) degree wall are compared with the laboratory tests in terms of force versus displacement. Two sets of curves are presented; the first set for the smooth wall (Test 2) in Figure E.5, and the second set for the rough wall (Test 9) in Figure E.6. Each set includes four plots for four different cycles (Cycles 1, 2, 5, and 10).

Figure E.5 presents the comparison between the Abaqus simulation and the experimental results for the zero degree (0°) smooth wall case (Test 2). As shown, the model prediction of the

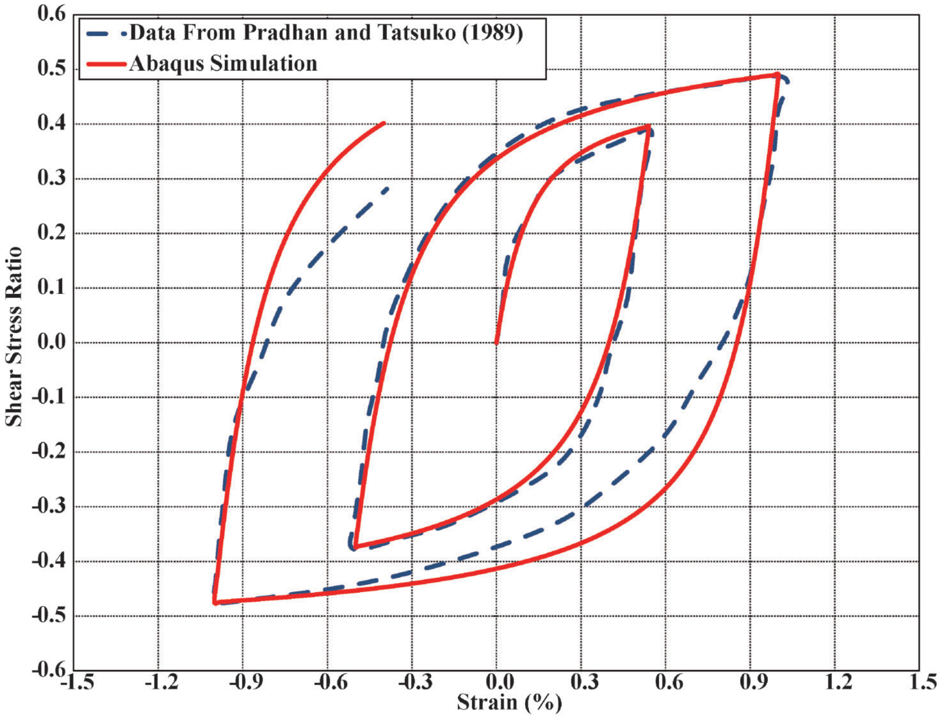

Figure E.2 Comparison of the stress-strain relationship—laboratory cyclic direct simple shear.

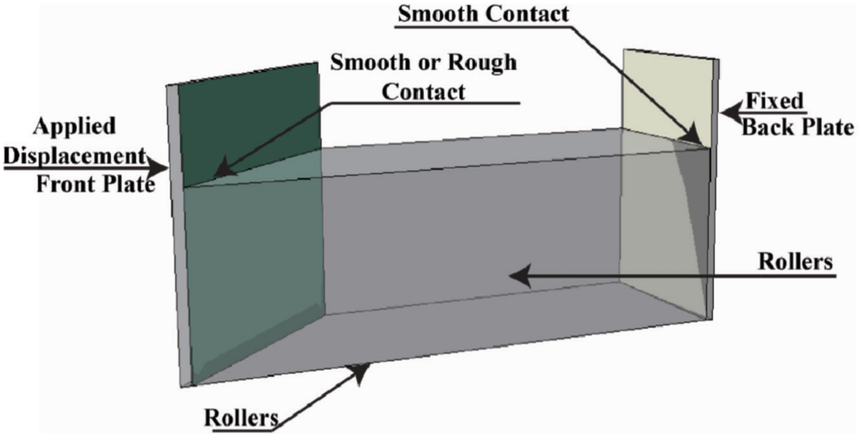

Figure E.4 Boundary conditions and contacts used in the numerical simulation.

observed behavior is reasonable for all cycles. In addition to, in general capturing the force versus displacement response, other features of the observed behavior such as rotation of the backbone curve and the semi-linear response upon unloading were captured by the model.

Figure E.6 presents the comparison between the Abaqus simulation and the experimental results for the zero degree (0°) rough wall case (Test 9). It can be concluded that the observed behavior from the tests was captured well, except for the tenth cycle, where the model provides a stiffer response. However, for the tenth cycle, the simulation results for the magnitude of the force are considered acceptable.

E.3.2 Tests with Forty-Five Degree (45°) Wall (Tests 8 and 5)

The results from the simulation of the tests with a forty-five degree (45°) wall are compared with the laboratory tests, in terms of force versus displacement. Two sets of curves are presented; the first set for the smooth wall (Test 8) in Figure E.7, and the second set for the rough wall (Test 5) in Figure E.8. Each set includes four plots for four different cycles (Cycles 1, 2, 5, and 10 for the smooth wall, and Cycles 1, 2, 5, and 9 for the rough wall. The 9th cycle was selected because the simulation didn't converge at the 10th cycle due to excessive plastic strains).

Figure E.7 presents the comparison between the Abaqus simulation and the experimental results for the forty-five degree (45°) smooth wall (Test 8). As shown, the model is capable of capturing the behavior as observed from the test. It should be noted the rotation of the backbone curve is captured well in Cycles 1, 2, and 5. However, during the tenth cycle, a softer response in the laboratory was observed after reloading. The softer response indicates a rotation of the backbone curve in the opposite direction, which is beyond the capabilities of the model.

Figure E.8 presents the comparisons between the Abaqus simulation and the experimental results for the forty-five degree (45°), rough wall test (Test 5). As shown, the observed behavior from the tests is captured well in Cycles 1, 2, and 5. For the ninth cycle, as in previous cases, the "softening" behavior was not well approximated by the model, which and the response was overestimated by about 15%. One of the reasons for this difference is that the rotation of the backbone curve during the ninth cycle was larger than what was usually observed. However, it should be noted that observed behavior from instrumented bridges in the field showed that "steady-state" is reached between the fifth and seventh year (Frosch & Lovell, 2011). This observation supports the use of the model for actual bridge behavior as it is not necessary to go to cycles beyond five to seven.

TABLE E.4
Model Parameters for the Plates

Material	E psf (N/m^2)	υ
Stainless steel	$4.2*10^9$ ($2.0*10^{11}$)	0.3

E.4 MODEL VERIFICATION: LATERALLY LOADED PILE TEST

As part of this study, a pile was tested under lateral loading (the test report is attached as Appendix E-1). The test results are used in this section for additional validation and calibration of the constitutive model. The amplitudes of the simulated test are presented in Table E.7. The objectives of the simulation were to:

1. Evaluate the validity of the model in capturing behavior under a larger scale test.
2. Examine the model performance under relatively high stress levels.
3. Calibrate the model to obtain the parameters required for foundation soils that will be used in the parametric study (Chapter 7).

The test was simulated in three-dimensional space with Abaqus© Standard. The dimensions of the model were identical to the actual dimensions in the field. The volume of soil modeled had dimensions 5.5 ft wide, 5.5 ft long, and 20 ft deep. The pile was a 0.5 ft diameter, 12.5 ft long concrete filled tube (CFT) with a 2.5 ft stickup above the ground surface. The model dimensions are shown in Figure E.9.

The boundary conditions and contacts were simulated to replicate the boundaries and contacts of the pile test. Roller boundaries were assigned to the sides of the foundation soils. A fixed boundary was used at the bottom of the foundation soils. Cyclic displacement was applied at the top of the pile, and the displacement cycle amplitude was equal to the displacement of the actual test as given in Table E.7. Figure E.10 shows the model with the applied boundary conditions and the displacement-time history.

The contacts and constraints were applied to replicate what is believed to exist in the actual test. The contact between the pile perimeter and foundation was achieved using the finite sliding contact algorithm in Abaqus© Standard. The friction coefficient used was $\mu=0.78$, equivalent to a friction angle of 38°. A tie constraint was applied between the tip of the pile and the foundation soils. The contacts and constraints are shown in Figure E.11.

TABLE E.5
Soil Model Parameters—Zero Degree (0°) Wall Tests (Tests 2 and 9)

$G_{o,ref}$ psf (N/m^2)	$\sigma_{m,ref}$ psf (N/m^2)	υ	α (deg)	κ psf (N/m^2)	a	b	N_1	N_2	ψ (deg)	C_1
$1.0*10^5$ $(4.8*10^6)$	$1.1*10^2$ $(5.3*10^3)$	0.3	41	1 (47.9)	0.25	−0.1	3.0	2.3	1	3.1

TABLE E.6
Soil Model Parameters—Forty-Five Degree (45°) Wall Tests (Tests 5 and 8)

$G_{o,ref}$ psf (N/m^2)	$\sigma_{m,ref}$ psf (N/m^2)	υ	α (deg)	κ psf (N/m^2)	a	b	N_1	N_2	ψ (deg)	C_1
$1.0*10^5$ $(4.8*10^6)$	$1.1*10^2$ $(5.3*10^3)$	0.3	41	1 (47.9)	−0.3	0.3	3.5	1.85	1	3.3

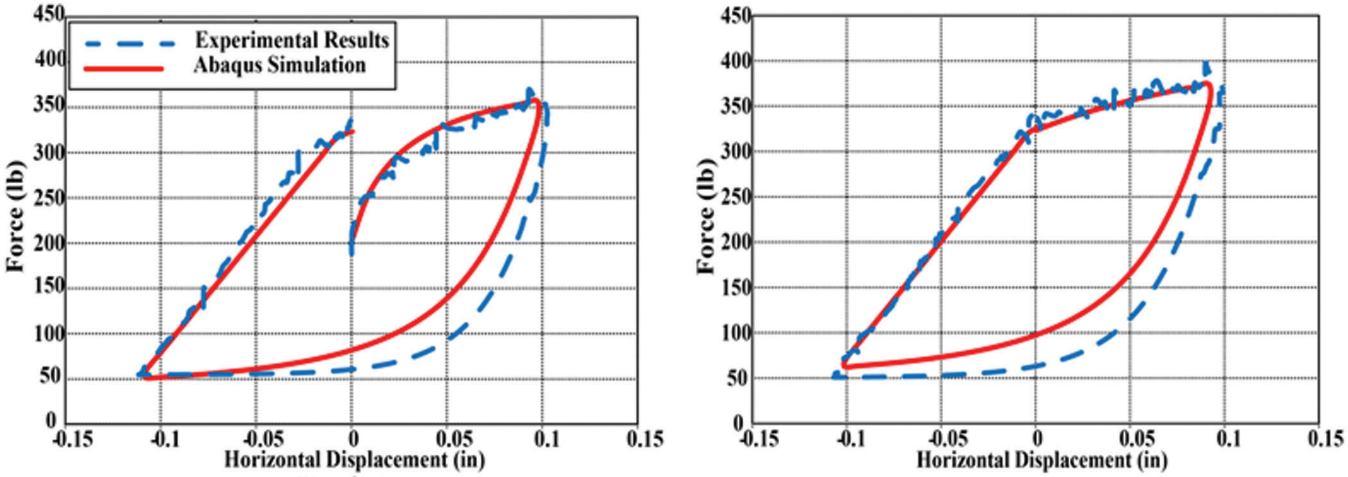

a- First Cycle

b- Second Cycle

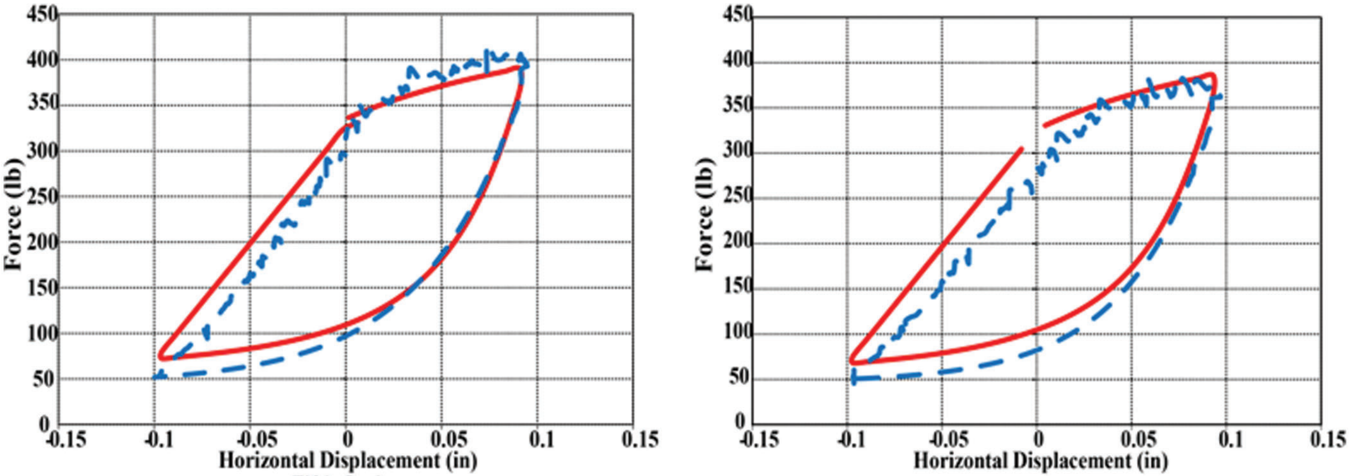

c- Fifth Cycle

d-Tenth Cycle

Figure E.5 Force versus displacement comparison—zero degree (0°), smooth wall case (Test 2).

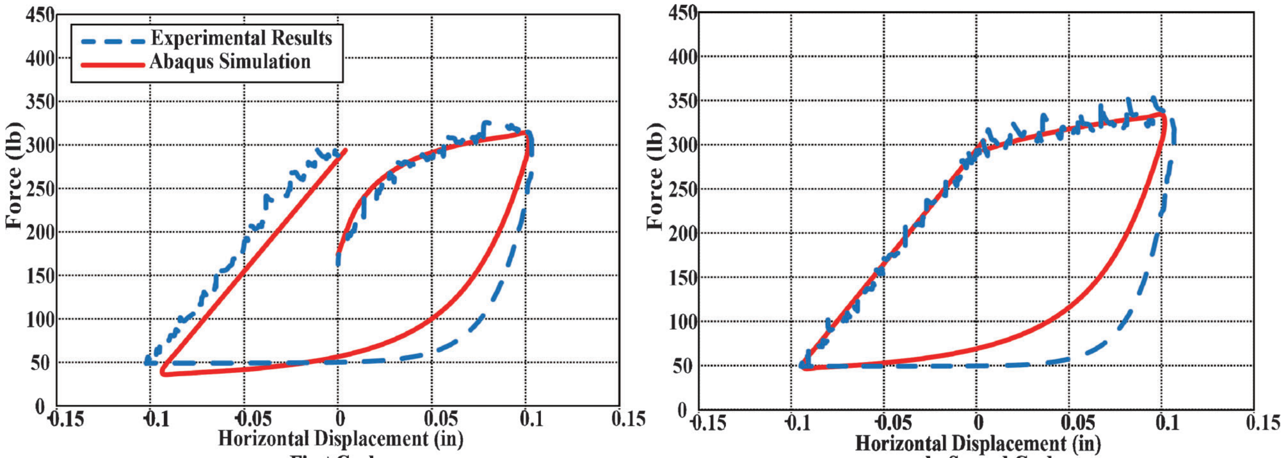

a- First Cycle

b- Second Cycle

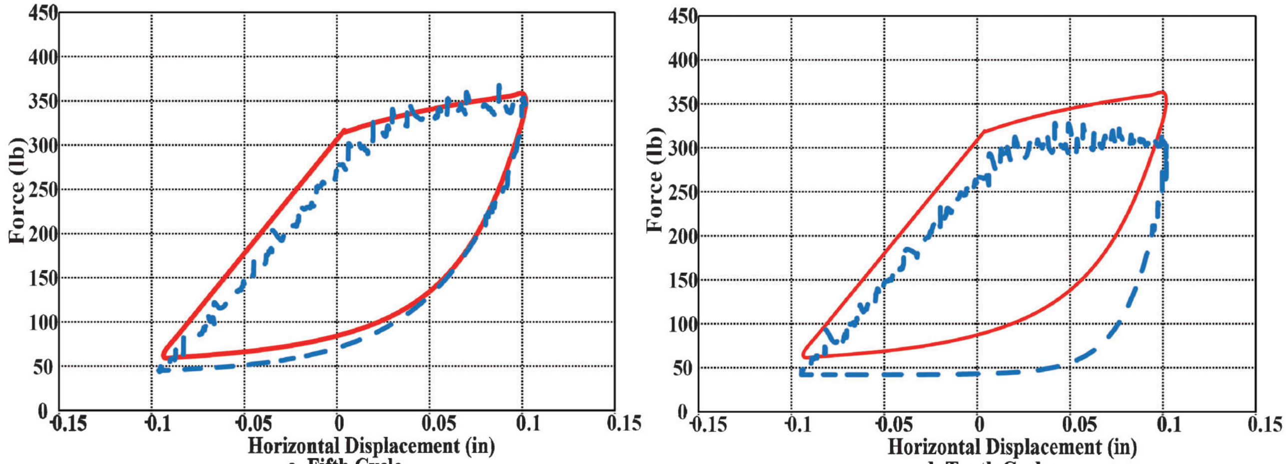

c- Fifth Cycle

d- Tenth Cycle

Figure E.6 Force versus displacement comparison—zero degree (0°), rough wall case (Test 9).

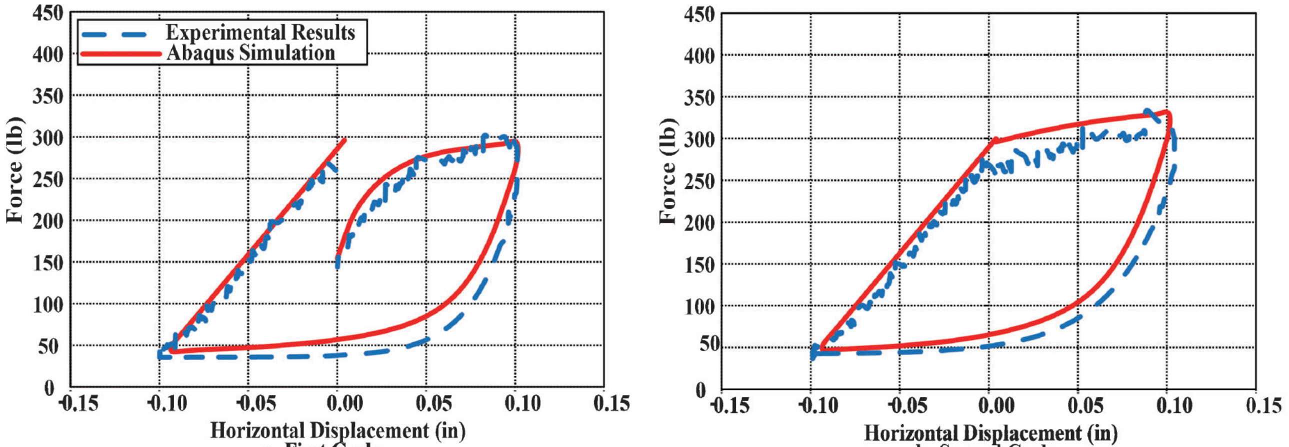

a- First Cycle

b- Second Cycle

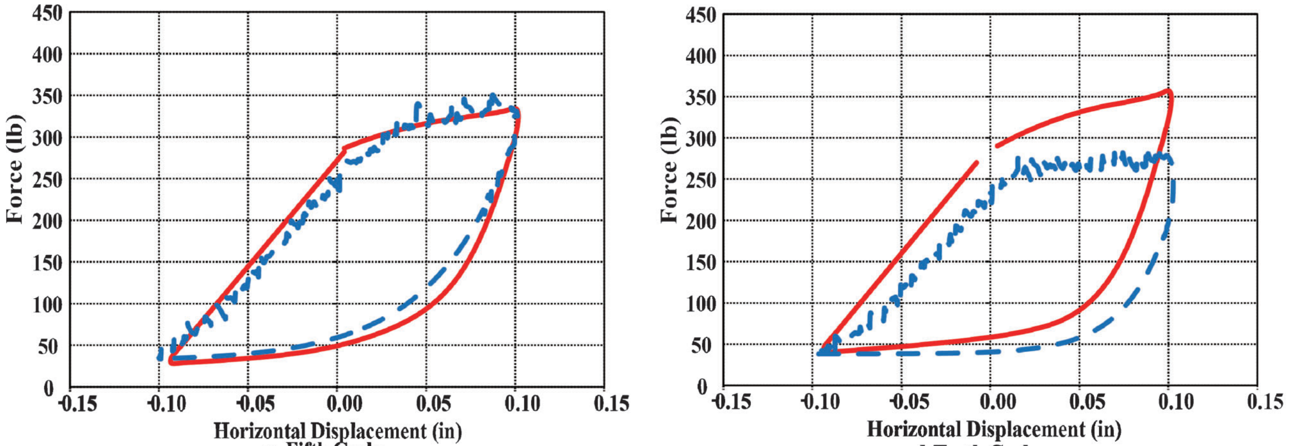

c- Fifth Cycle

d-Tenth Cycle

Figure E.7 Force versus displacement comparison—forty-five degree (45°), smooth wall case (Test 8).

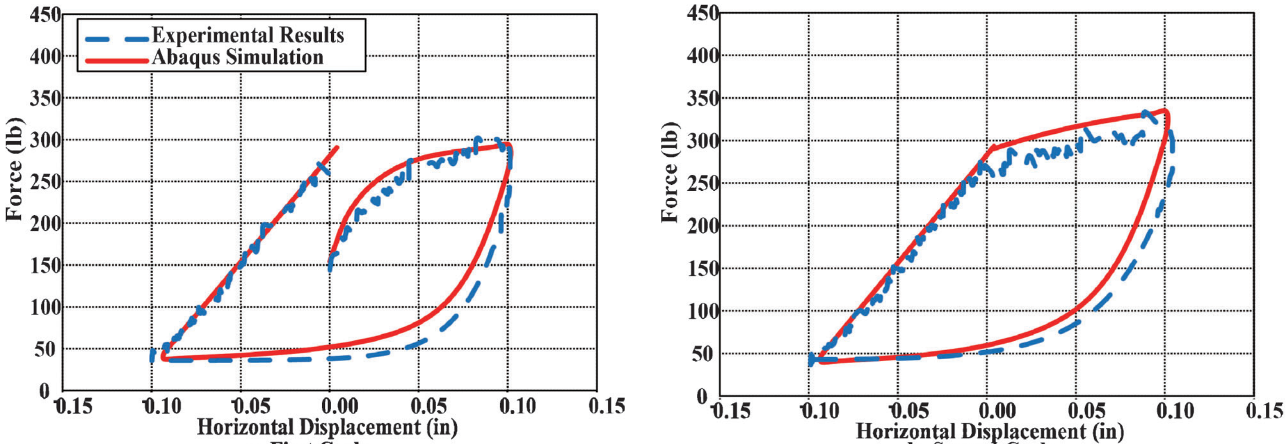

a- First Cycle

b- Second Cycle

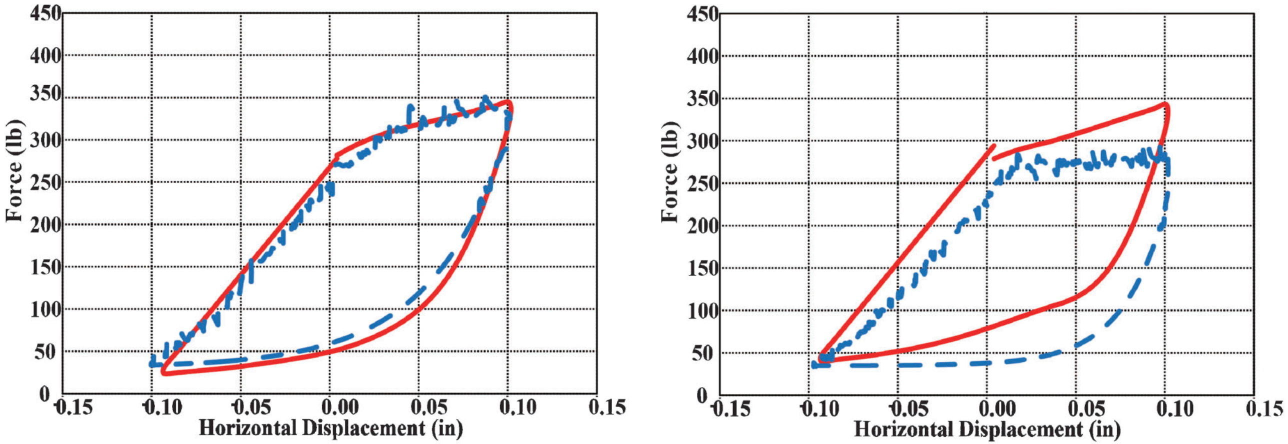

c- Fifth Cycle

d- Ninth Cycle

Figure E.8 Force versus displacement comparison—forty-five degree (45°), rough wall case (Test 5).

TABLE E.7
Amplitude of Displacement Cycles

Cycle #	Amplitude (in.)
1	±0.25
2	±0.5
3	±0.75
4	±1.0
5	±1.5
6	±2.0
7	+ 2.5
8	+ 3.0
9	−2.0/+4.0

All model components were discretized using 4-node linear tetrahedral, general stress elements. The simulation was performed using Abaqus© Standard. The pile was modeled as a linear elastic material, while the foundation soils were modeled as elastoplastic using the constitutive model developed in this study (UMAT, refer to Chapter 5). The elastic model parameters for the pile are presented in Table E.8 (based on Frosch and Lovell (2011)).

The elastoplastic model parameters for the foundation soils are presented in Table E.9. Based on the subsurface conditions at Bowen Laboratory (location of the field test), the soils are mostly granular with blow counts on the order of 20 blows/ft (as discussed in Chapter 3). Empirical correlations were used to estimate the relative density (50%), initial void ratio (0.25) and internal friction angle (31°). Using Equation E.1 with the mean reference effective stress and Equation E.3, the $G_{o,ref}$ and α were estimated to be $7.1*10^5$ psf and 41°, respectively. During the simulations and to fit the observed behavior, the $G_{o,ref}$ was slightly modified (increased by ~15%).

The deformed shape of the pile with depth obtained from the simulation is compared with the measured deformed shape in Figure E.12. Four plots are provided, each showing the deformed shape at a different loading cycle, as indicated below each plot. The results indicate that the model was able to capture the behavior of the pile under lateral loading in terms of deformation and the inflection point.

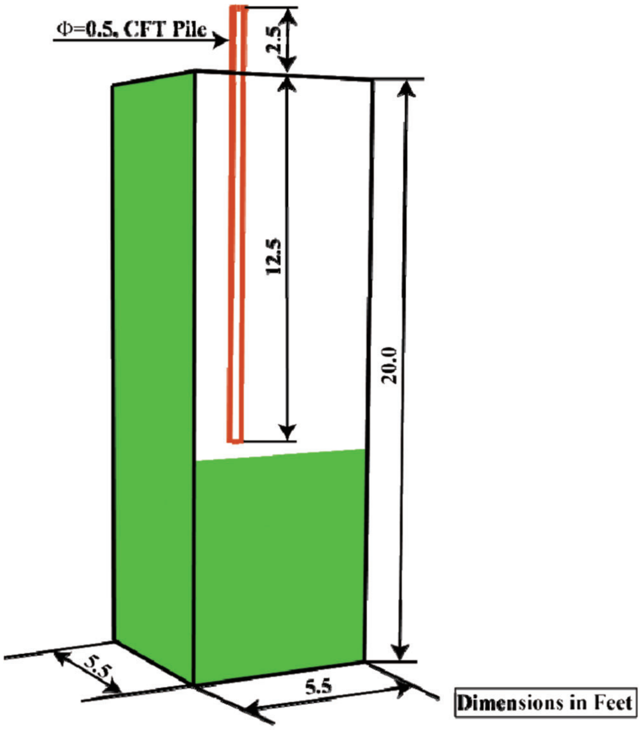

Figure E.9 Numerical model dimensions.

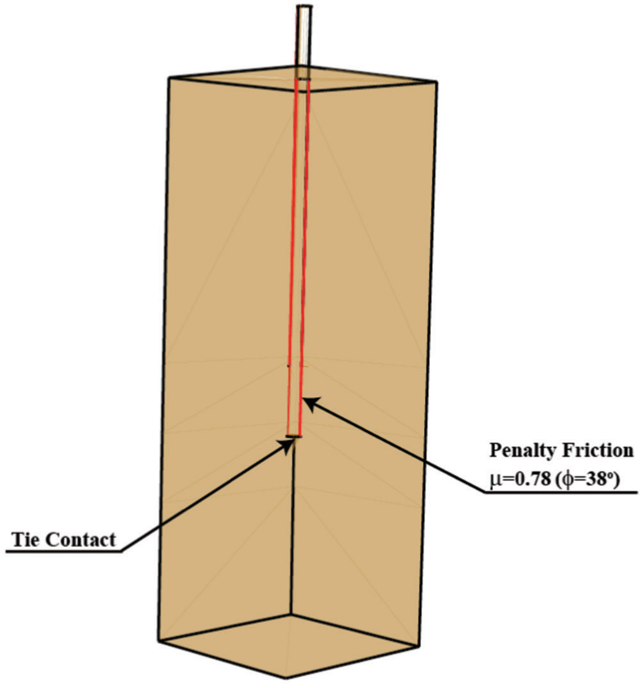

Figure E.11 Contacts used in the numerical simulation.

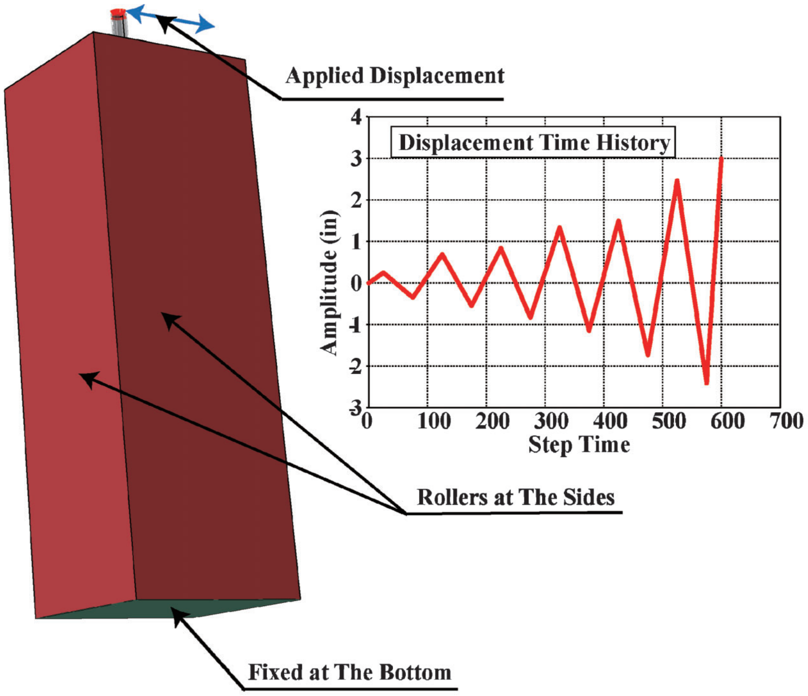

Figure E.10 Applied boundary conditions.

TABLE E.8
Model Parameters for the Pile

Part	Material	E psf (N/m^2)	υ
Piles	Concrete filled steel tube transformed Section EI	4.2*10^9 (2.0*10^{11})	0.2

TABLE E.9
Soil Model Parameters for the Foundation Soils

$G_{o,ref}$ psf (N/m^2)	$\sigma_{m,ref}$ psf (N/m^2)	υ	α (deg)	κ psf (N/m^2)	a	b	N_1	N_2	ψ (deg)	C_1
8.5*10^5 (4.1*10^7)	1250 6*10^4	0.3	41	1 (47.9)	−0.35	0.1	2.0	1.8	1	NA$^{(1)}$

[1] Not applicable since the linear option upon reloading was not used for the foundation soils.

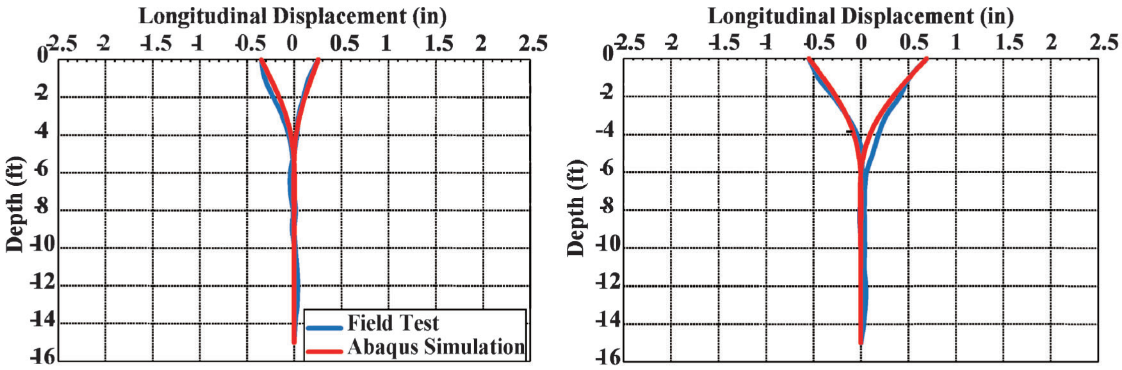

a- 0.25-in Cycle

b- 0.5-in Cycle

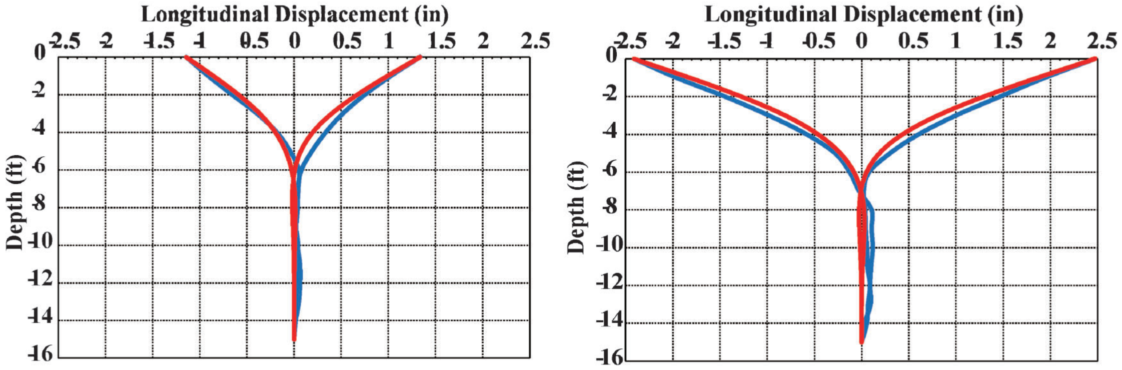

c- 1.0-in Cycle

d- 2.0-in Cycle

Figure E.12 Comparison of the pile's deformed shape between Abaqus© simulations and experimental results.

E.5 MODEL VERIFICATION: LARGE SCALE BRIDGE TEST

A large-scale bridge test (¼ scale) that simulated thermal expansion and contraction of the bridge deck and associated movement of the abutment and piles was presented in Chapter 3. Two tests were carried out to evaluate different boundary conditions (without and with backfill). The simulated tests are presented in Table E.10. The objectives of this simulation were to:

1. Evaluate the validity of the model in capturing the behavior of a larger scale test.
2. Examine the model performance under relatively high stress levels.
3. Evaluate the ability of the model to capture rotation of the backbone curve.
4. Evaluate the performance of the model with various contact conditions.
5. Calibrate the model to obtain the parameters required for a parametric study.

The tests were simulated in three-dimensional space with Abaqus© Standard. The simulations were performed for only half of the bridge, which is considered reasonable because the displacements were applied at the gap in the middle of the bridge (Chapter 3). The dimensions of the model were identical to those of the large-scale bridge dimensions. The modeled half bridge dimensions were 17 ft wide and 11.9 ft long, with 45° skew. The abutment wall was 2.1 ft wide and 3 ft deep. The bridge deck was supported on three girders (12 in. × 10 in.). The deck was 4 in. thick. Five 6 in. diameter, 17-ft long concrete-filled tube (CFT) piles were included in the simulations. The foundation soils were 43.7 ft long, 27 ft wide and 25 ft deep. The backfill dimensions (Test 3) were 43.7 ft long, 27 ft wide, and 3 ft deep. The model dimensions are shown in Figure E.13.

The boundary conditions and contacts were simulated to replicate the boundaries and contacts of the large-scale test. Roller boundaries were assigned to the back and sides of the foundation soils. Rollers were also applied to the back and two sides of the backfill for Test 3. A pinned boundary was used at the bottom of the foundation soils. Cyclic displacement was applied at the front of the bridge (mid span gap) in the longitudinal direction and with amplitude equal to the actual test, as shown in Table E.10. Figure E.14 shows the model with the applied boundary conditions as well as the displacement-time history. To enhance model stability, a uniform load (35 psf) was applied at the top of the backfill and to the front of the backfill next to the abutment walls.

The contacts and constraints were applied to replicate what is believed to exist in the actual tests. The contacts between the abutment wall and the backfill, abutment wall base, and foundation soils, the perimeter of the piles and foundation soils, and between the backfill and foundation soils were modeled using the surface to surface finite sliding contact algorithm in Abaqus© Standard. The friction coefficient used in each contact was as follows:

1. Abutment wall-backfill: $\mu=0.2$, equivalent to a friction angle of 11.3°.
2. Abutment wall base-foundation soils: $\mu=0.2$, equivalent to a friction angle of 11.3°.
3. Piles perimeter-foundation soils: $\mu=0.78$, equivalent to a friction angle of 38°.
4. Backfill-foundation soils: $\mu=0.27$, equivalent to a friction angle of 15°.

TABLE E.10
Simulated Large Scale Bridge Test

Test 1		Test 3	
No Backfill		With Backfill	
Cycle #	Amplitude (in.)[1]	Cycle #	Amplitude (in.)[1]
1	±0.25	1	±0.5
2	±0.5	2	±1.0
3	±0.75	3	±1.5
4	±1.0	4	±2.0
5	±1.5	5	±2.0
6	±2.0	6	±2.5
7	±2.5	7	+3.0

[1] Displacement amplitude measured at the gap.

A tie constraint was applied between the top of the piles and the abutment wall (fixity connection). In addition, the tie constraint was applied at the tip of the pile, between the pile and the foundation soils. The contacts and constraints are presented in Figure E.15.

All model components were discretized using 4-node linear tetrahedral, general stress elements. The simulations were performed using Abaqus© Standard. The bridge superstructure, abutments, and piles were modeled as linear-elastic. The foundation soil and backfill were modeled as elastoplastic materials using the constitutive model developed in this study (UMAT, refer to Chapter 5). For the backfill, the linear response upon reloading option was used; this option was turned off for the foundation soils. The elastic model parameters for the bridge and piles are presented in Table E.11 (based on Frosch and Lovell (2011)).

The elastoplastic model parameters for the foundation soils and the granular backfill are presented in Tables E.12 and E.13, respectively. The foundation soil parameters are identical to those used for the foundation soils in the laterally loaded pile simulation (Section E.4). No field testing was conducted on the backfill soils, therefore, the initial void ratio, of approximately 0.66, was estimated using phase relations. Using Equation E.1, with the mean effective reference stress of 320 psf, $G_{o,ref}$ is estimated to be $3.1*10^5$ psf.

E.5.1 Test 1: No Backfill

The test of the ¼ scale bridge with no backfill was simulated to evaluate the ability of the model to capture the behavior of the foundation soils. The response of the foundation soils affects the movement of the bridge and the shape of the deformed piles. The simulation replicated the applied displacement time history of the actual test (Table E.10). Figure E.16 shows the deformed (amplified 50 times) and undeformed meshes during active and passive loading and the longitudinal displacement contours (obtuse and acute corners are based on the bridge angle in plan view). From Figure E.16, two rotations are observed: rotation along the vertical axis (rotation in the horizontal plane) and rotation along the transverse axis (horizontal axis parallel to abutment wall). Rotation along the vertical axis is clockwise during passive (expansion) loading (towards the obtuse corner) and counterclockwise during active (contraction) loading (towards the acute corner). In addition, rotation along the transverse axis shows larger displacements at the top compared to the bottom of the abutment wall. Finally, the point of fixity of the piles is in the upper third to half the depth of the piles.

As discussed in Chapter 3, due to the skew angle and constraints applied by the piles, the bridge undergoes longitudinal and transverse displacements as well as rotation in the horizontal plane due to application of displacement at the gap. Figure E.17 presents a comparison between simulation and measurements of the longitudinal and transverse displacements of the deck. It is clear that the displacements were captured well.

Figure E.18 provides an additional comparison between predictions and observations where the deformation of the piles with depth at the acute and obtuse corners are shown. The constitutive model performed well in capturing the behavior of the soil-pile system, both in terms of deformation and inflection point (approximately 6–8 ft below ground surface). It should be noted that stress levels in the foundation soils are much higher than the earlier simulated tests presented in Section E.3.

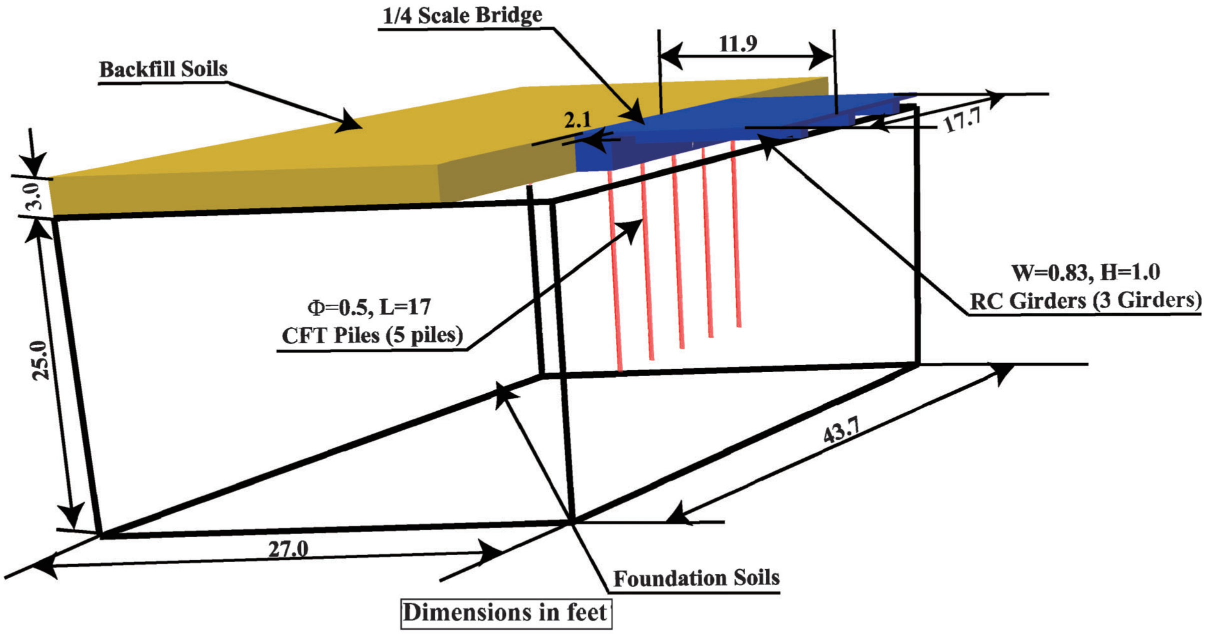

Figure E.13 Numerical model dimensions.

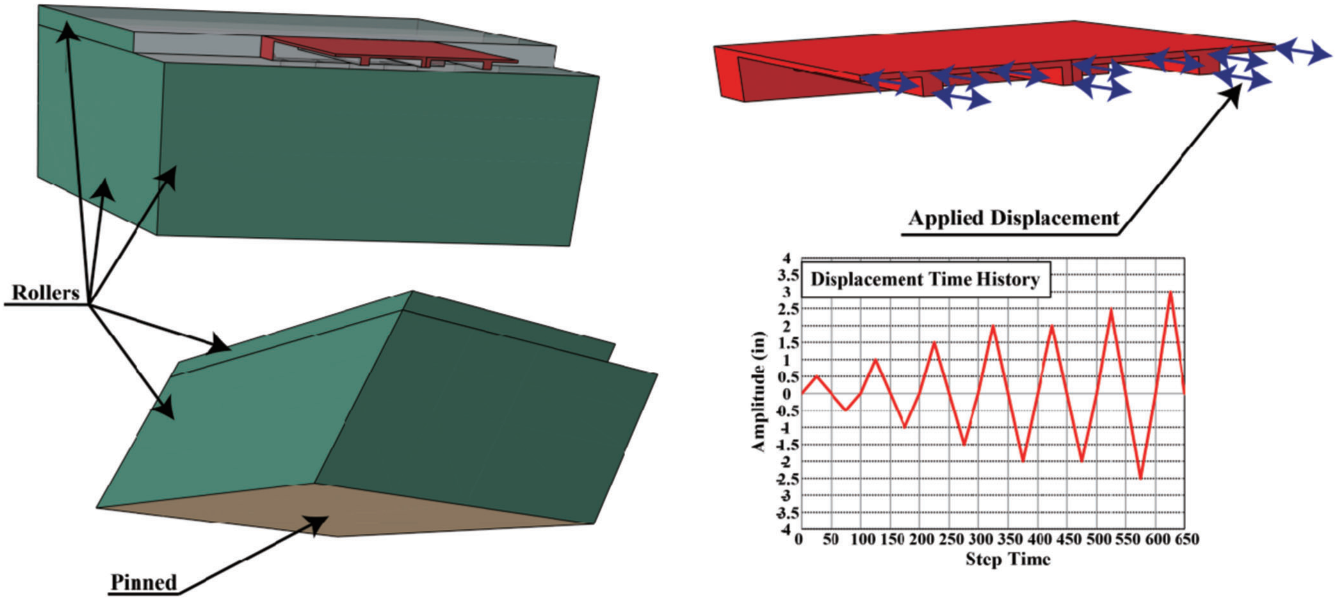

Figure E.14 Applied boundary conditions.

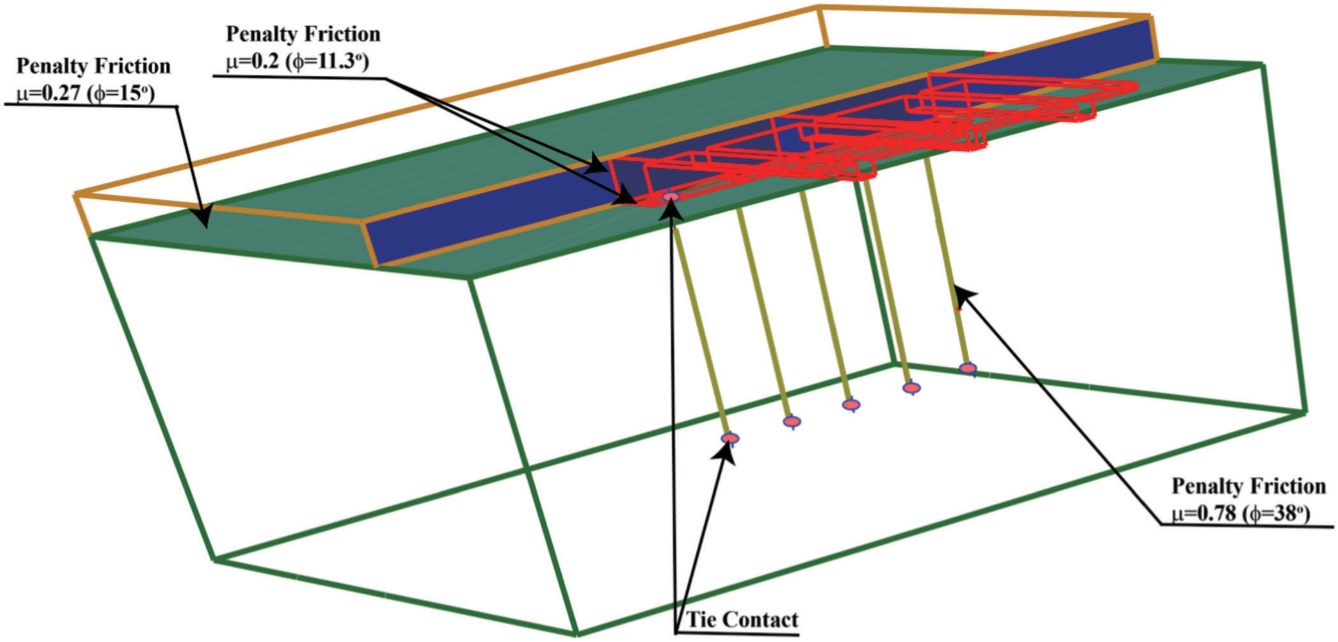

Figure E.15 Contacts used in the numerical simulation.

TABLE E.11
Model Parameters for the Bridge Superstructure, Abutment Wall, and Piles

Part	Material	E psf (N/m^2)	υ
Deck and girders	Concrete[1]	$2.6*10^8$ ($1.2*10^{10}$)	0.3
Abutment qall	Concrete[1]	$2.6*10^8$ ($1.2*10^{10}$)	0.3
Piles	Concrete filled steel tube transformed Section EI	$1.4*10^9$ ($6.7*10^{10}$)	0.2

[1] Reduced elastic modulus is used to account for cracked section.

TABLE E.12
Soil Model Parameters for the Foundation Soils

$G_{o,ref}$ psf (N/m^2)	$\sigma_{m,ref}$ psf (N/m^2)	υ	α (deg)	κ psf (N/m^2)	a	b	N_1	N_2	ψ (deg)	C_1
$8.5*10^5$ ($4.1*10^7$)	1250 ($6*10^4$)	0.3	41	1 (47.9)	−0.35	0.1	2.0	1.8	1	NA(1)

[1] Not applicable because the linear option upon reloading was not used for the foundation soils.

TABLE E.13
Soil Model Parameters for the Granular Backfill

$G_{o,ref}$ psf (N/m^2)	$\sigma_{m,ref}$ psf (N/m^2)	υ	α (deg)	κ (psf (N/m^2)	a	b	N_1	N_2	ψ (deg)	C_1
$3.5*10^5$ ($1.7*10^7$)	320 ($1.5*10^4$)	0.3	41	1 (47.9)	−0.1	0.1	2.0	1.8	1	3.1

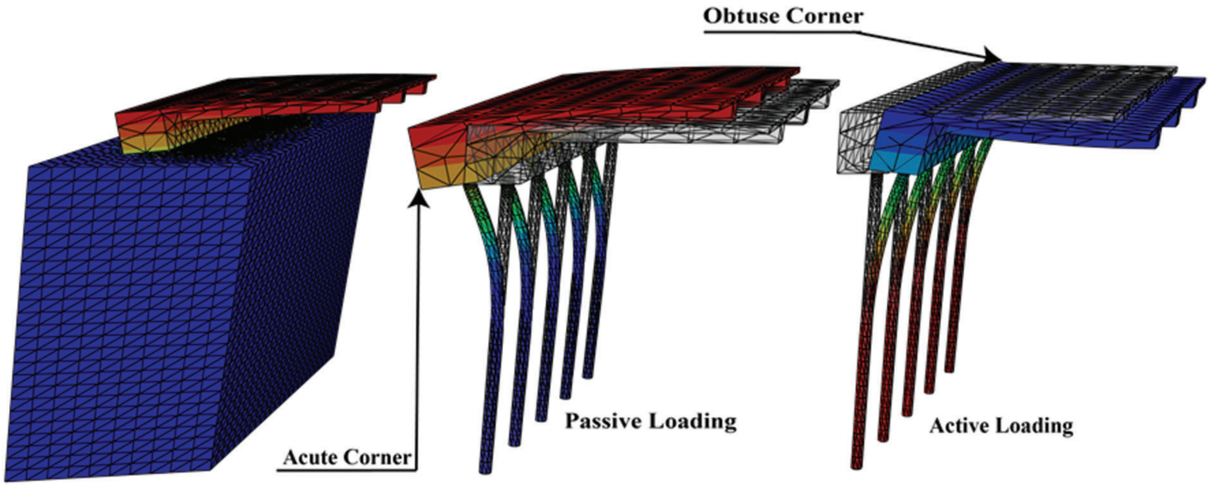

Figure E.16 Deformed shape of the simulated bridge (Test 1).

E.5.2 Test 3: With Backfill

The test of the ¼ scale bridge with backfill was simulated to evaluate the ability of the model to capture response of a granular backfill due to loading/unloading cycles imposed by the bridge deck. Two important features of such response observed in the field are higher lateral earth pressures at the obtuse corner relative to the acute corner and escalation of pressures behind the abutment with repeated cycles of constant amplitude. The simulation was designed to replicate the applied displacement time history of the actual test (Table E.10). Figure E.19 shows the deformed mesh (amplified 50 times) during active and passive loading, and longitudinal displacement contours. As shown in Figure E.19, rotation along the transverse axis (horizontal axis parallel to abutment wall) is observed, which shows larger displacement at the top compared to the bottom of the abutment wall. Furthermore, the point of fixity of the piles is located in the upper third to half of the pile depth.

The lateral earth pressure obtained from the simulations is compared to the lateral earth pressure measured from the model test in Figure E.20. Two plots are provided: one for the obtuse corner (Figure E.20(a)) and the other for the acute corner (Figure E.20(b)). The field measurements (diamond symbols) indicate that the lateral earth pressure increases with increasing amplitude up to an expansion of 2 in. at the obtuse corner and 1.5 in. at the acute corner. Subsequently, lower pressures are developed. It is also observed that yielding occurred during contraction after the 0.5 in. cycle. For a repeated cycle at amplitude of 2 in. (data inside the), a larger lateral earth pressure is observed. Finally, the observed earth pressures (amplitudes larger than 1 in.) at the obtuse corner are higher than at the acute corner during expansion. These behaviors are all captured by the analytical model.

In summary, based on the results presented in Figure E.20, the model successfully captured the behavior of the granular backfill in the following aspects:

1. The magnitude of the lateral earth pressures versus displacement agreed well with the lateral earth pressure recorded during the test.
2. The lateral earth pressure at the obtuse corner was higher than at the acute corner.
3. Lateral earth pressure escalation at two successive cycles with the same amplitude was captured well.
4. Yielding of the soil during active loading was replicated by the constitutive model.

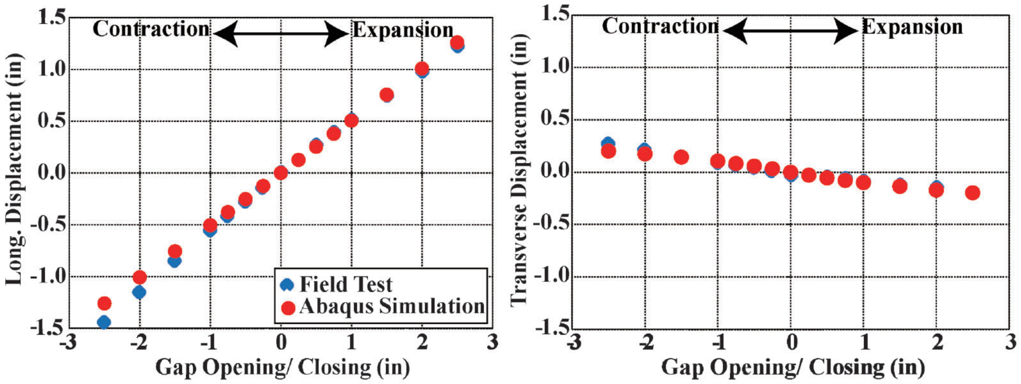

a- Longitudinal Displacement

b- Transverse Displacement

Figure E.17 Bridge deck rigid body movement comparison between Abaqus© simulations and experimental results for the test with no backfill (Test 1).

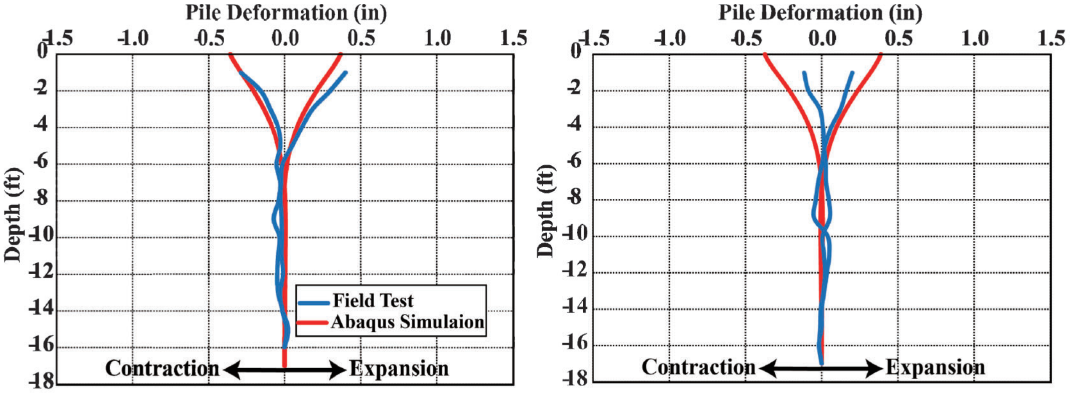

a- Acute Corner, 1.0-in Cycle

b- Obtuse Corner, 1.0-in Cycle

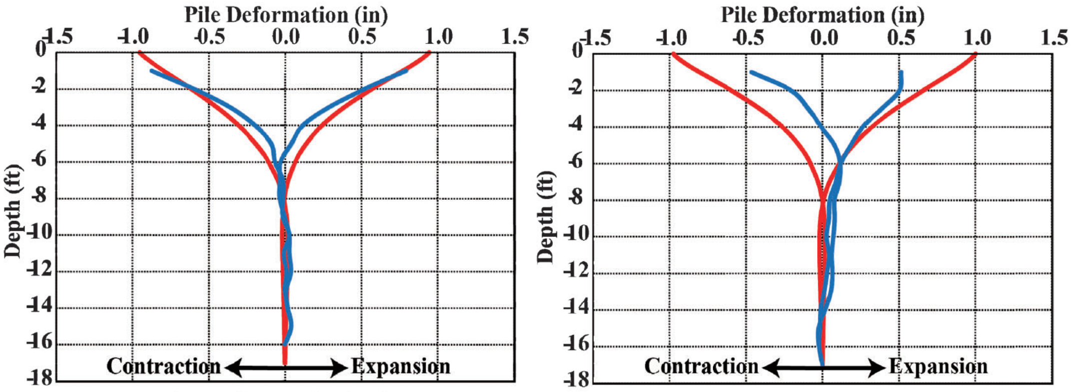

c- Acute Corner, 2.5-in Cycle

d- Obtuse Corner, 2.5-in Cycle

Figure E.18 Comparison of the pile's deformed shape between Abaqus$^{\copyright}$ simulations and experimental results for the test with no backfill (Test 1).

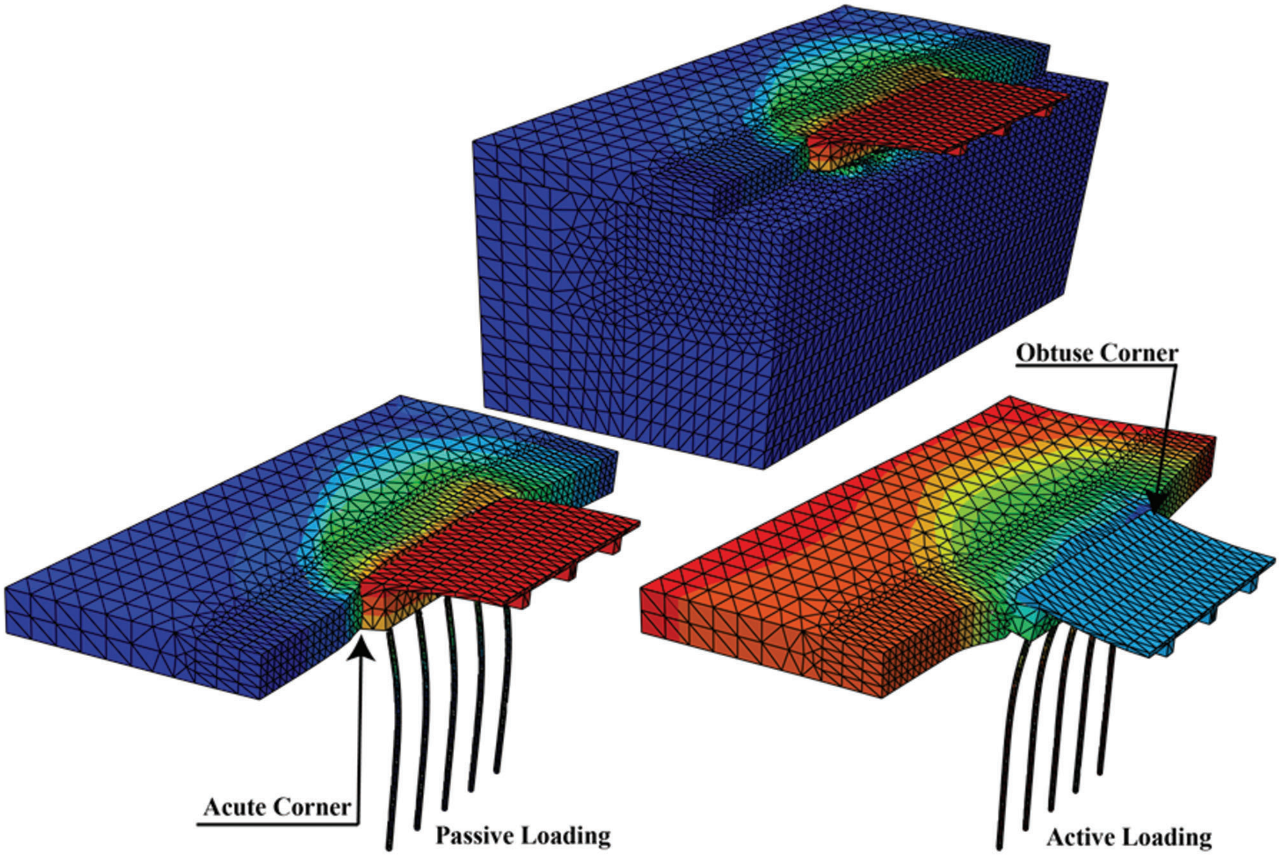

Figure E.19 Deformed shape of the simulated bridge with backfill (Test 3).

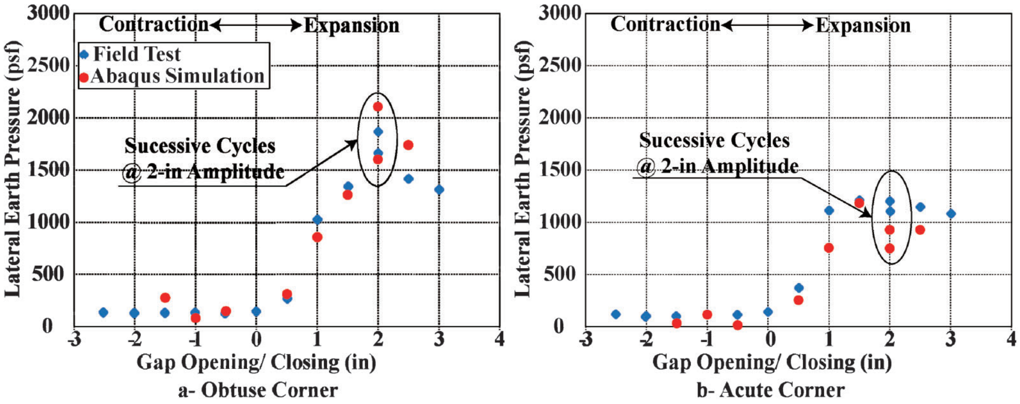

a- Obtuse Corner

b- Acute Corner

Figure E.20 Comparison of the lateral earth pressure obtained from Abaqus© simulation and experimental results for the test with backfill (Test 3).

E.6 MODEL VERIFICATION (FULLY COUPLED THERMAL SOIL-STRUCTURE INTERACTION): FULL-SCALE INSTRUMENTED BRIDGE (US 231 OVER AEP RAILROAD SPUR)

The US 231 over AEP Railroad Spur bridge is one of the full-scale instrumented bridges in Indiana described by Frosch and Lovell (2011). This bridge, which was monitored for 3.5 years after construction, was selected for simulation using the constitutive model developed in this study. It was decided to simulate the entire bridge length, along with the abutment, piles, foundation soils, and backfill soil using thermal loading/unloading of the superstructure (fully coupled thermal soil-structure interaction). The recorded temperature at the bridge site is shown in Figure E.21. The objectives of this simulation were to:

1. Evaluate the validity of the model in capturing the behavior of a full scale bridge.
2. Examine the model performance under the anticipated stress levels for actual bridge foundations.
3. Evaluate the ability of the model to capture the lateral earth pressure of the backfill soils measured during a number of expansion and contraction cycles.
4. Evaluate the model predictions using the calibrated model parameters from Section E.5.

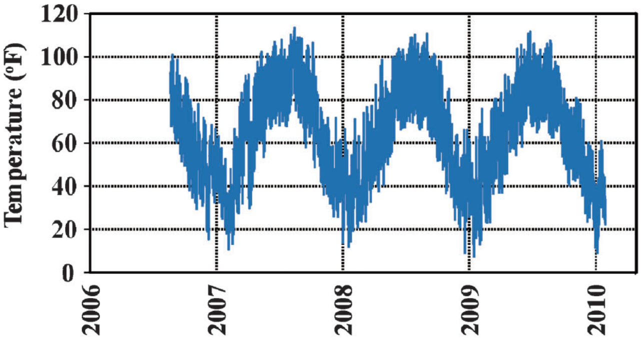

Figure E.21 Recorded temperature at US 231 bridge's deck (Frosch & Lovell, 2011).

5. Perform a fully coupled thermal-displacement simulation incorporating soil-structure interaction.

The bridge was simulated in three-dimensional space with Abaqus© Standard. The simulations were evaluated by coupling thermal and mechanical response. The dimensions of the model were identical to those of the instrumented US 231 bridge, which were 55.1 ft wide and 221 ft long, with a 33.8° skew angle. The abutment wall was 3 ft wide and 8.4 ft deep. The bridge deck was supported on seven girders, the girders type is Type III Prestressed I-Beam, due to the difficulty in modeling the shape of the Type III beam, an equivalent section of 4.3 ft × 1.1 ft was used for the girders. Equivalent section dimensions were calculated by matching the EI and EA of the Type III beam and the equivalent section. Seven 14 in. diameter, 80 ft long concrete-filled tube (CFT) piles, supporting each abutment, were included in the simulations. The foundation soils were 75.1 ft long, 42 ft wide and 85 ft deep. The backfill dimensions were 75.1 ft long, 42 ft wide and 8.4 ft deep. The model dimensions are shown in Figure E.22.

The boundary conditions and contacts were simulated to replicate the boundaries and contacts of the full scale instrumented bridge. Roller boundaries were assigned to the back and sides of the foundation soils. Rollers were also applied to the back and two sides of the backfill. A pinned boundary was used at the bottom of the foundation soils. The temperature-time history was applied to the superstructure with amplitudes similar to the actual recorded temperature, as shown in Figure E.21. Figure E.23 shows the model with the applied boundary conditions, and the temperature-time history. To enhance model stability, a uniform load (100 psf) was applied at the top of the backfill and to the front of the backfill next to the abutment walls.

The contacts and constraints were applied to replicate what is believed to exist in the actual bridge. The contacts between the abutment wall and the backfill, abutment wall base and foundation soils, and the piles perimeter and foundation soils were approximated using the surface to surface finite sliding contact algorithm in Abaqus© Standard (penalty friction algorithm). The friction coefficient used in each contact was as follows:

1. Abutment wall-backfill: $\mu=0.2$, equivalent to a friction angle of 11.3°.
2. Abutment wall base-foundation soils: $\mu=0.2$, equivalent to a friction angle of 11.3°.
3. Piles perimeter-foundation soils: $\mu=0.78$, equivalent to a friction angle of 38°.

A tie constraint was applied between the top of the piles and the abutment wall (fixed connection). In addition, a tie constraint was applied at the tip of the piles, between the pile and the foundation soils. The contacts and constraints are presented in Figure E.24.

The substructure components (abutment walls and piles), foundation soils, and backfill soils were discretized using 4-node linear tetrahedral, general stress elements. The superstructure components (deck and girders) were discretized using 4-node thermally coupled tetrahedral linear displacement and temperature elements. The element type distribution is presented in Figure E.25.

Simulations were performed using Abaqus© Standard. The bridge abutments wall and piles were modeled as linear-elastic. The superstructure was modeled as a coupled thermal-mechanical elastic material. The foundation soil and backfill were modeled as elastoplastic materials using the constitutive developed in this study (UMAT, refer to Chapter 5). For the backfill, the linear response upon reloading option was used; this option was turned off for the foundation soils. The elastic and thermal model parameters for the bridge and piles are presented in Table E.14 (based on Frosch and Lovell (2011)).

The elastoplastic model parameters for the foundation soils and the granular backfill are presented in Tables E.15 and E.16, respectively. The foundation soil parameters used are identical to those used for the foundation soils in the laterally loaded pile simulation (Section 5.4). The model parameters for the backfill soils were identical to those used for the backfill soils in the large-scale bridge simulation (Section 5.5), except for some slight modifications of some of the fitting parameters (parameter "a" changed from −0.1 to −0.2, parameter N_1 changed from 2.0 to 2.2, and parameter N_2 changed from 1.8 to 1.7), to achieve a better fit of the recorded soil pressures. These changes in the fitting parameters are justified, because compaction controls and type of backfill soils are not identical between the backfill of the large-scale test and the full-scale bridge. It is more reasonable to use the backfill parameters from the modeling of the full-scale in a parametric study.

The simulation was designed to replicate the applied temperature-time history recorded at the instrumented bridge (Figure E.21). Figure E.26 shows the deformed mesh (amplified 50 times) during active and passive loading and the longitudinal displacement contours. The longitudinal displacement at the acute corner, during expansion, is larger than at the obtuse corner, with an outward direction (towards the backfill) which results in rotation in the horizontal plane towards the obtuse corner. During contraction, the longitudinal displacement at the acute corner is also larger than at the obtuse corner but in the opposite direction (away from the backfill soils) which results in rotation in the horizontal plane towards the acute corner. The point of fixity of the piles is approximately 10 ft from the ground surface.

The lateral earth pressure obtained from the simulation was compared with the measured lateral earth pressure in Figure E.27 at the obtuse corner, acute corner, and centerline of the abutment. The temperature-time history is also plotted in Figure E.27. As shown, the lateral earth pressure was largest at the obtuse corner and smallest at the center of the abutment. The model also captured escalation of the soil pressure with time. In general, the simulation performed reasonably well in capturing the recorded earth pressure for the US 231 bridge. The minimum lateral earth pressure that a soil can develop is at its active state (shown in Figure E.27 by the horizontal green line), which is captured well by the simulations. The small differences between the model and the theoretical active state are due to three-dimensional effects, which are included in the model and not in the computation of the active pressure. The measured values at low temperatures, however, show pressures close to or at zero. This situation is unlikely in a granular fill unless the fill is frozen and a gap develops between the soil and the abutment. This is precisely what was observed during the test of the large scale bridge (Test #2 in Chapter 3) performed during winter. The behavior of the frozen backfill was not modeled, because the soil model doesn't capture such behavior.

The displacements from the simulation without and with adding concrete shrinkage strains were compared with the measured displacements in Figure E.28 at the obtuse and acute corners.

As shown in Figure E.28, the simulation with shrinkage strains captured the larger displacement at the acute corner. The model also captured well the net inward movement of the bridge deck.

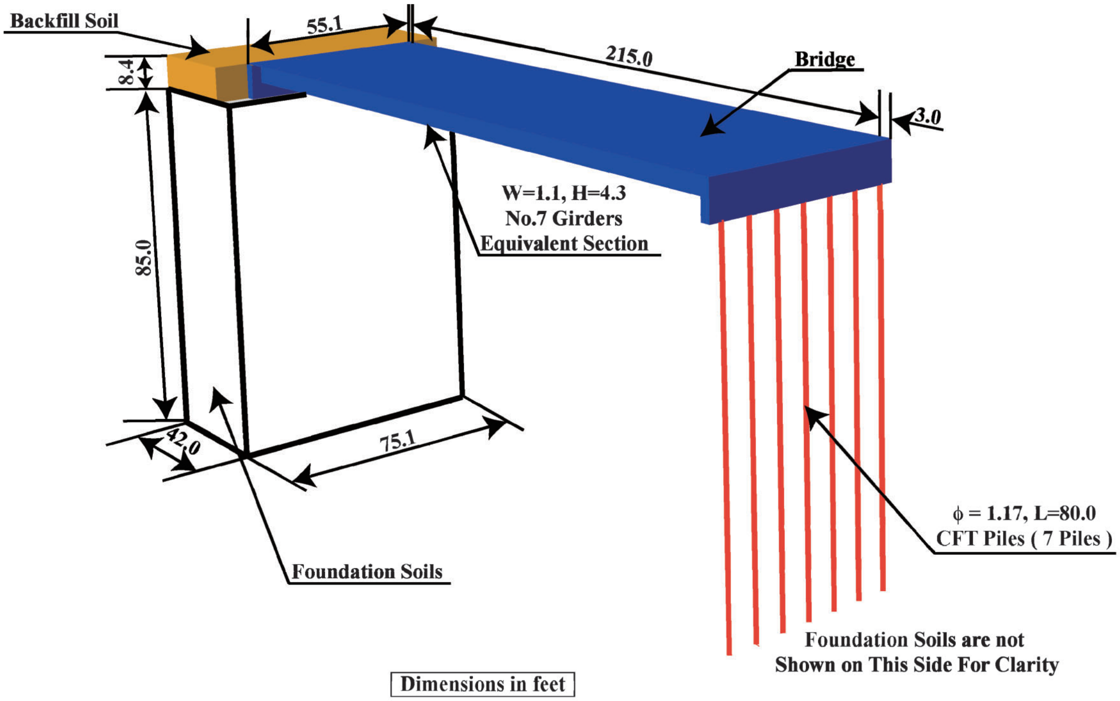

Figure E.22 Numerical model dimensions.

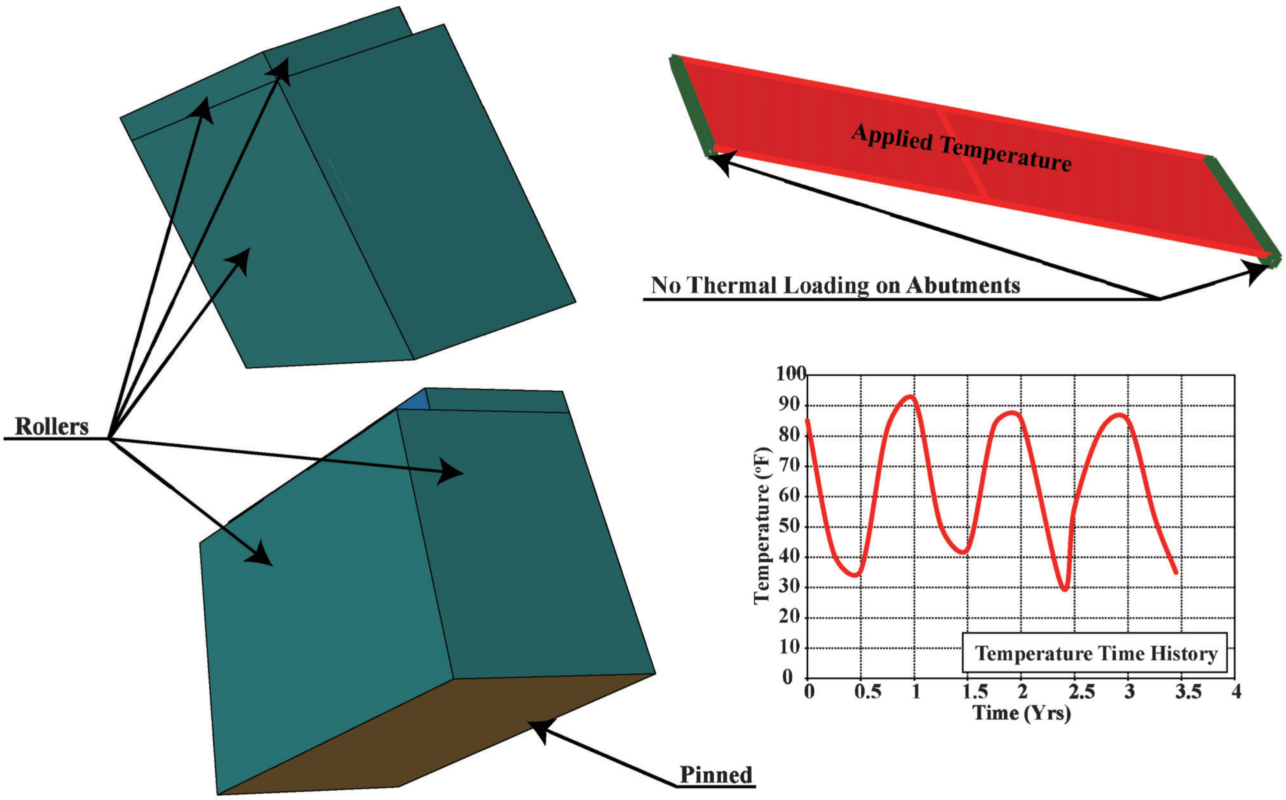

Figure E.23 Applied boundary conditions.

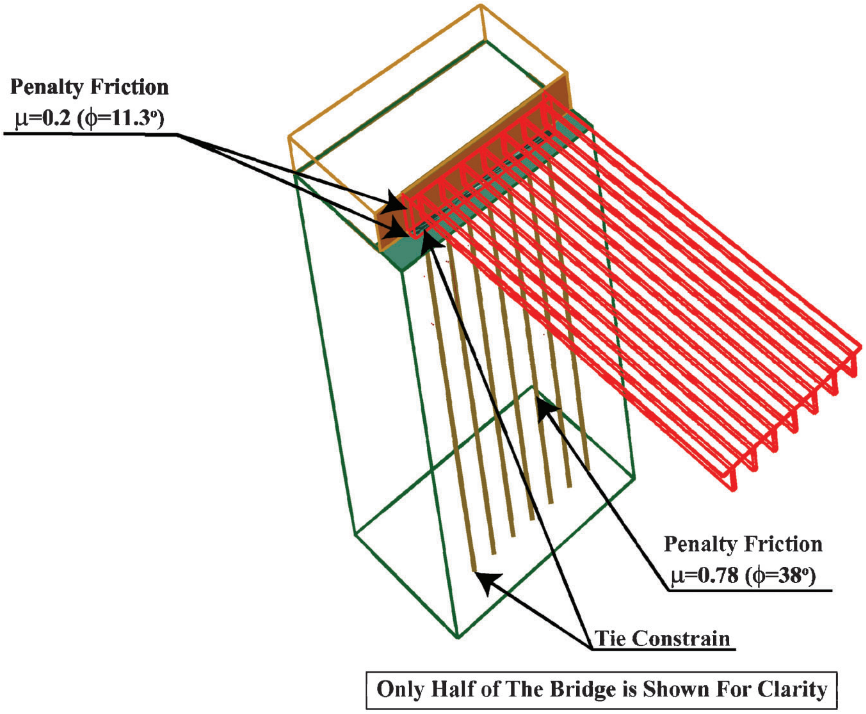

Figure E.24 Contacts used in the numerical simulation.

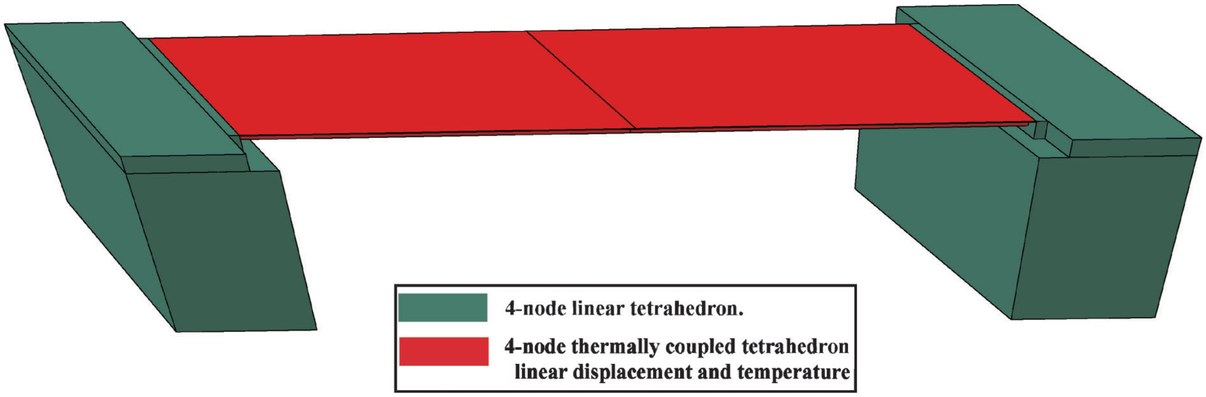

Figure E.25 Element type distribution.

TABLE E.14
Model Parameters for the Bridge Superstructure, Abutment Wall, and Piles

Part	Material	E psf (N/m^2)	υ	α 1/°F
Deck and girders	Concrete	$5.2*10^8$ ($2.4*10^{10}$)	0.3	$5.5*10^{-6}$
Abutment wall	Concrete	$5.2*10^8$ ($2.4*10^{10}$)	0.3	NA
Piles	Concrete filled steel tube transformed Section (EI matching EI)	$1.4*10^9$ ($6.7*10^{10}$)	0.2	NA

TABLE E.15

Soil Model Parameters for the Foundation Soils

$G_{o,ref}$ psf (N/m^2)	$\sigma_{m,ref}$ psf (N/m^2)	υ	α (deg)	κ psf (N/m^2)	a	b	N_1	N_2	ψ (deg)	C_1
$8.5*10^5$ $(4.1*10^7)$	1250 $(6*10^4)$	0.3	41	1 (47.9)	−0.35	0.1	2.0	1.8	1	NA(1)

[1] Not applicable since the linear option upon reloading was not used for the foundation soils.

TABLE E.16

Soil Model Parameters for the Granular Backfill

$G_{o,ref}$ psf (N/m^2)	$\sigma_{m,ref}$ psf (N/m^2)	υ	α (deg)	κ psf (N/m^2)	a	b	N_1	N_2	ψ (deg)	C_1
$3.5*10^5$ $(1.7*10^7)$	320 $(1.5*10^4)$	0.3	41	1 (47.9)	−0.2	0.1	2.2	1.7	1	3.1

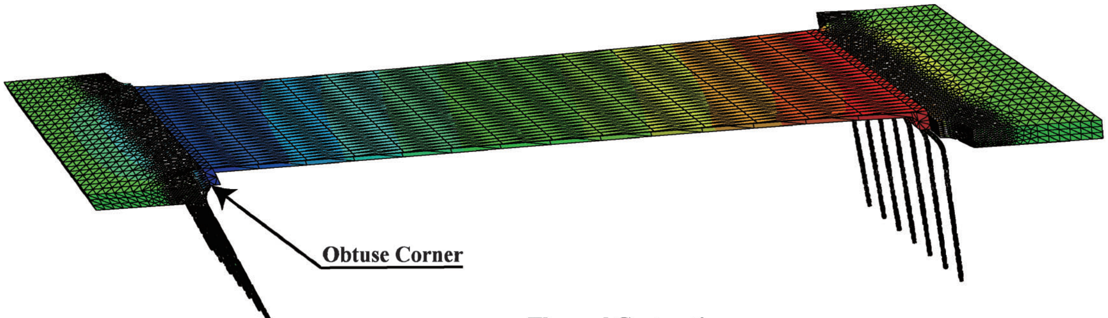

a- Thermal Contraction

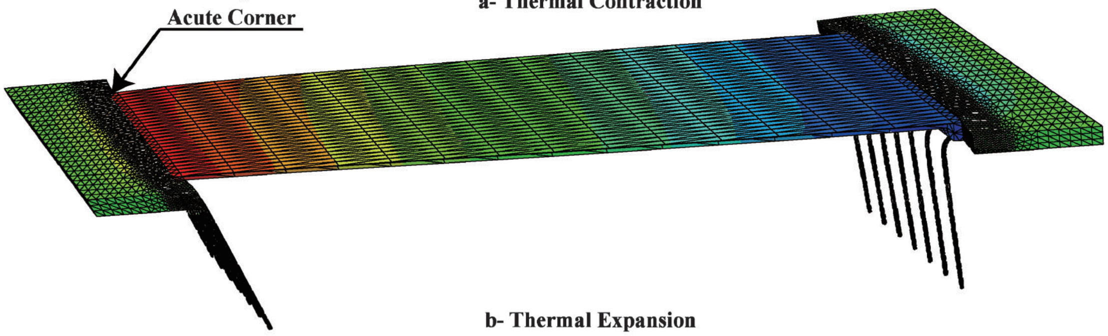

b- Thermal Expansion

Figure E.26 Deformed shape of the simulated instrumented bridge.

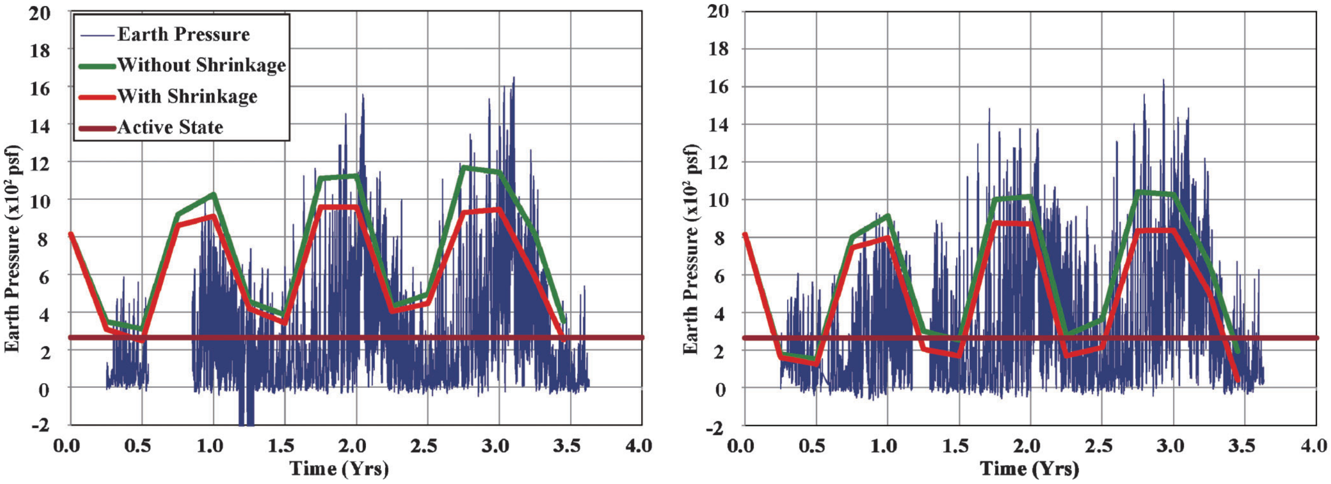

a- Obtuse Corner

b- Acute Corner

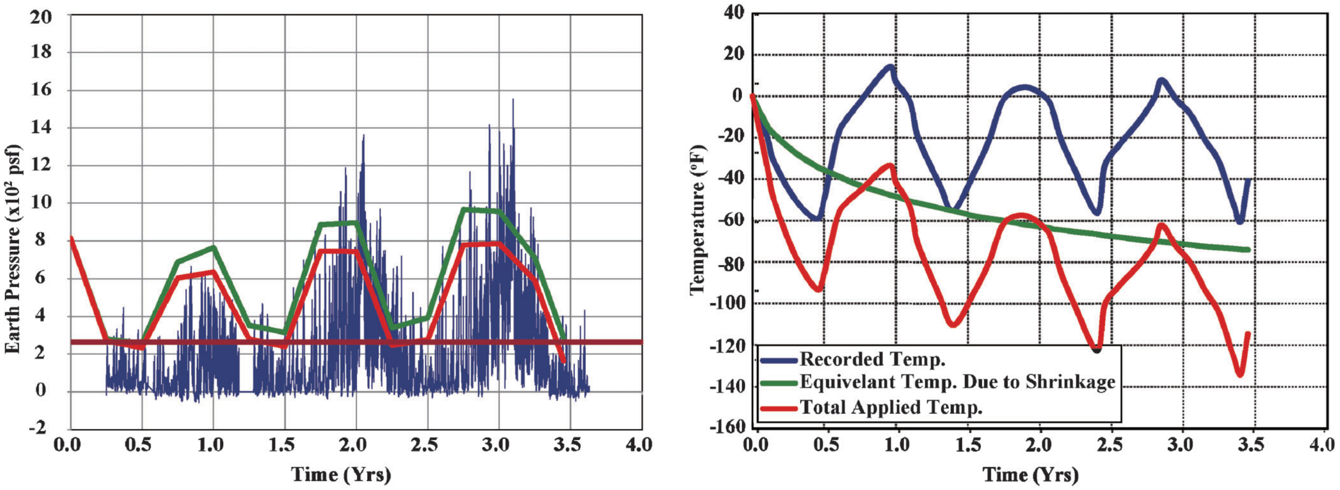

c- Center Line

d- Thermal Loading

Figure E.27 Comparison of the lateral earth pressure.

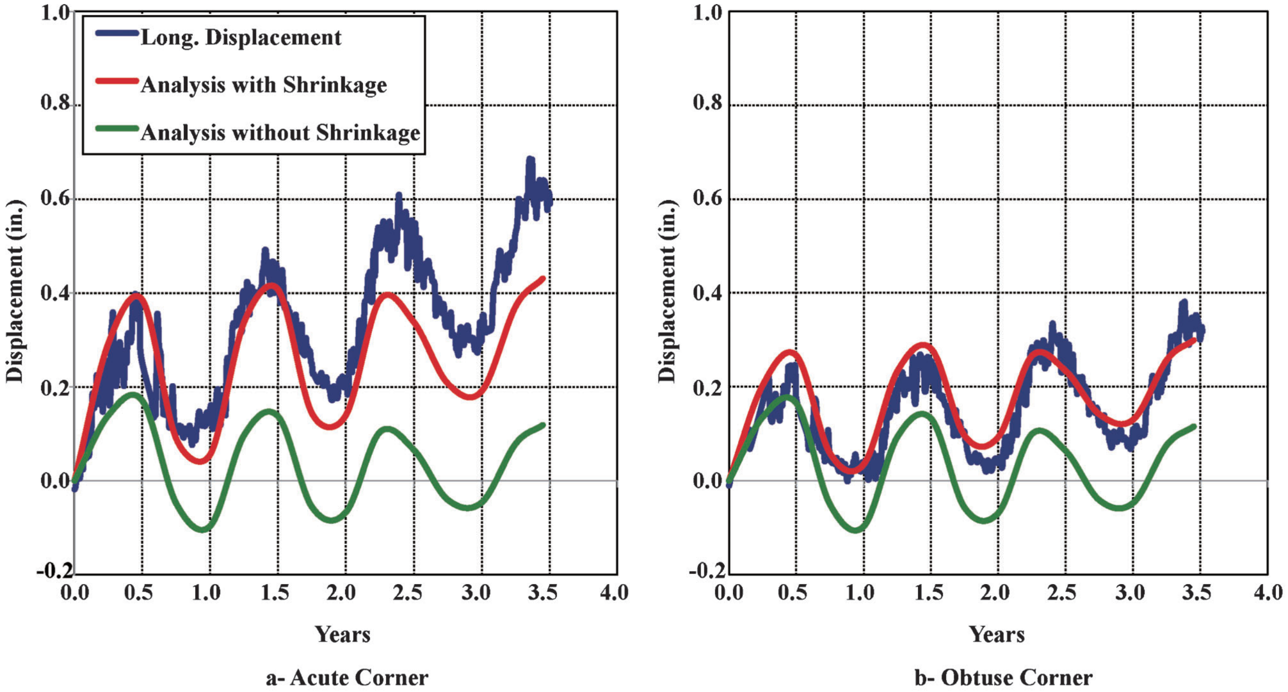

a- Acute Corner

b- Obtuse Corner

Figure E.28 Comparison of the abutment wall movement.

E.7 CONCLUSIONS FROM THE VERIFICATION AND CALIBRATION OF THE SOIL'S MODEL

Based on the results from the simulations and their comparison with both laboratory and field tests, the following can be concluded:

1. The model performed well under a very wide range of stress levels and various length scales.
2. The model has acceptable predictive capabilities.
3. Escalation of earth pressure behind the abutment with an increasing number of cycles is captured.
4. The close to linear response of earth pressure upon reloading under lateral loading is captured.
5. The model performed well replicating the magnitude of pile deformations and inflection points.
6. The parameters obtained from the model calibration for the foundation soils and backfill (Section E.6) can be used in the parametric analysis of Chapter 7 given the scale of the tests simulated.

E.8 REFERENCES

Frosch, R. J., & Lovell, M. D. (2011). *Long-term behavior of integral abutment bridges* (Joint Transportation Research Program Publication No. FHWA/IN/JTRP-2011/16). West Lafayette, IN: Purdue University. http://dx.doi.org/10.5703/1288284314640

Hardin, B. O. (1978). The nature of stress-strain behavior for soils. In *Earthquake Engineering and Soil Dynamics—Proceedings of the ASCE Geotechnical Engineering Division Specialty Conference* (pp. 3–90), June 19–21, 1978, Pasadena, CA.

Pradhan, T. B., Tatsuoka, F., & Sato, Y. (1989). Experimental stress-dilatancy relations of sand subjected to cyclic loading. *Soils and Foundations*, *29*(1), 45–64.

Yu, H., Khong, C., & Wang, J. (2007). A unified plasticity model for cyclic behavior of clay and sand. *Mechanics Research Communications*, *34*, 97–114.

APPENDIX E-1

E-1.1 INTRODUCTION

This chapter presents and documents the results of a lateral pile load test. The pile was installed at Bowen Laboratory at Purdue University. The purpose of the study was to evaluate the pile response under various displacement cycles.

The pile was installed as part of a previous JTRP study (SPR-3223) by Frosch and Lovell (2011). An obstruction was encountered during the pile installation, which prevented the pile from reaching the final depth. The pile was about 4.5 ft shallower than the rest of the piles presented in SPR-3223. The pile instrumentation was designed to capture the pile translational and rotational movements, the force applied by the hydraulic jack's pressures at each cycle, and the deflection shape of the pile. The instrumentation is discussed in Section III. The details of the test are included in Section IV.

The test results show the translational and rotational pile movement at the pile cap, the force applied at the hydraulic jacks to generate the required displacement, and the deformed shape of the pile. The test results are presented in Section V. The results are discussed in Section VI and preliminary conclusions are presented in Section VII.

E-1.2 PILE GEOMETRY AND SUBSURFACE CONDITIONS

The pile is a concrete filled steel tune (CFT). The pile geometrical properties were estimated by Frosch and Lovell (2011) based on section transformation from the SR 18 bridge's piles. As mentioned earlier this pile was about 4.5 ft shorter than the other piles installed at the site (driven to about 12.5 ft below the ground surface). The piles were driven into the ground first and then filled with 5000 psi concrete. The cross sectional properties are presented in Table E-1.1.

There was no geotechnical investigation program conducted at the bridge site. We established the subsurface conditions at the site based on the borings that were drilled for the Bowen Laboratory structure in 2002 by Alt & Witzig Engineering, Inc. (Borings B-4 and B-7). The subsurface conditions consist of an upper layer of medium dense to dense sand, down to an approximately depth of 20 ft. The blow counts are about 25 blows/ft. The sand layer is inter-bedded with silty clay and silt layers in boring B-4. The sand layer is underlain by medium compact silt down to an approximate depth of 42 ft; the blow counts are of the order of 30 blows/ft. A very compact silt layer (blow counts larger than 50) was encountered below the medium compact silt down to the explored depth of 51 ft. The water table was encountered in boring B-7 at a depth of about 9 ft.

E-1.3 PILE INSTRUMENTATION

Instrumentation was installed to monitor displacements, applied pressure to the load jacks and pile deformation.

The displacements of the pile cap were recorded using strain gauge-based potentiometers (UniMeasure Model PA-10-DS). Four potentiometers were installed to monitor the longitudinal movement and two potentiometers were installed to monitor transverse displacements of the pile's cap.

TABLE E-1.1
Pile Cross Sectional Properties, after Frosch and Lovell (2011)

Outer diameter (in.)	6
Inner diameter (in.)	5.5
Wall thickness (in.)	0.25
Composite effective area (in.^{2})	7.80
Composite effective moment of inertia (in.^{4})	24.9

The deformed shape of the piles was recorded by accelerometer-based (Microelectromechanical Systems) rope gauge (Measurand Model: SAAF). Four records of the deformed pile shape were recorded during each loading-unloading cycle.

The applied pressures to the jacks used to induce the required inward/outward displacements to the pile's cap were monitored by strain gauge-based pressure transducers (Omegadyne Inc. Model Number: PX409). Two pressure transducers were used for the hydraulic pump; one for the inward phase and the other for the outward phase. The monitoring locations are shown in Figure E-1.1.

E-1.4 TESTS DESCRIPTION

One test was completed. The test consisted of applying a displacement at the pile's cap and recording the cap's displacements, the pressure applied to the hydraulic jacks and the deformation shapes of the piles. The displacement at the cap was applied in steps, each with a different maximum magnitude. The displacements consisted of cycles of outward and inward movements. Table E-1.2 shows the amplitude of each cycle.

During the tests, the displacements from all potentiometers and pressures at the hydraulic jacks were continuously recorded. The deformed shape of the pile was taken at maximum, minimum amplitudes and at zero cap displacement.

The sign convention for displacements used throughout this report is positive for outward longitudinal movement and clockwise for rotational movements.

E-1.5 TEST RESULTS

Rigid Body Movement of the Pile's Cap

The overall longitudinal movement of the pile cap for in cycles is plotted in Figure E-1.2.

The figure shows the modulus degradation as a function of the cycles' amplitude. In addition, it appears that the soil-pile system had a stiffer response during the inward movement. Also, the pile cap had about 0.6 in of residual displacement at the end of the test, after all the pressure was released.

The horizontal force and the horizontal longitudinal displacement at the end of each cycle are plotted in Figure E-1.3.

The figure shows the degradation of the modulus; at larger amplitude (>+2.5 in) the modulus reached close to a constant value.

The rigid movement in the transverse direction is plotted in Figure E-1.4.

The transverse horizontal displacement was negligible at small amplitudes up to (+/−1.5 in); at larger amplitudes, the transverse movement was about 10% of the cycle amplitude.

The rotation around the three axis (X,Y,Z) is plotted in Figure E-1.5 as a function of the cycle's amplitude. X, Y, and Z in the figure denote the direction of the longitudinal, transverse and vertical directions, respectively.

The pile's cap showed insignificant rotations along the X and Z directions and significant rotation along the Y-direction. It is observed that the rotation during the outward movement was larger than the rotation during the inward movement. In addition, the relation between the rotation and the horizontal longitudinal movement was close to linear.

Pile Deformation

The pile deformations were recorded at the maximum, minimum and zero of each cycle. The longitudinal deformations of the pile at the depth of the potentiometers agree well with the potentiometer readings, as shown in Figure E-1.6.

The inflection point of the pile is at about 5 ft below the ground surface. The pile's deformed shape in the transverse direction was small compared to the longitudinal direction.

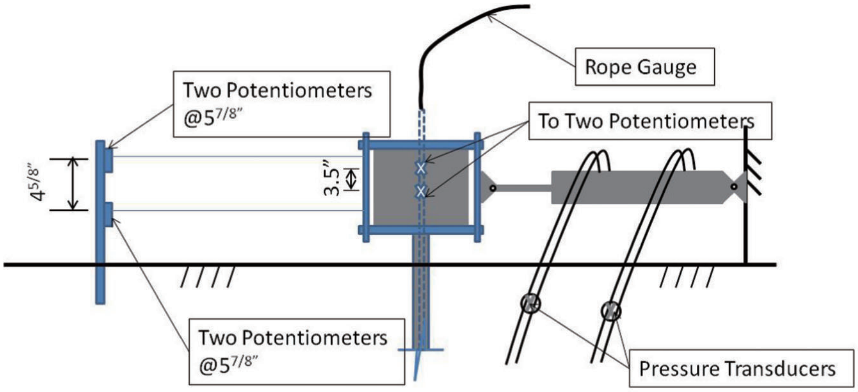

Figure E-1.1 Bridge displacement monitoring locations with potentiometers.

TABLE E-1.2
Amplitude of each Displacement Cycle

Cycle #	Amplitude (in)*
1	+/−0.25
2	+/−0.5
3	+/−0.75
4	+/−1.0
5	+/−1.5
6	+/−2.0
7	+ 2.5
8	+3.0
9	−2.0/+4.0
10	Pressure release

*Displacement amplitude measured at the cap's longitudinal direction (+ve: Outward movements and –ve: inward movement).

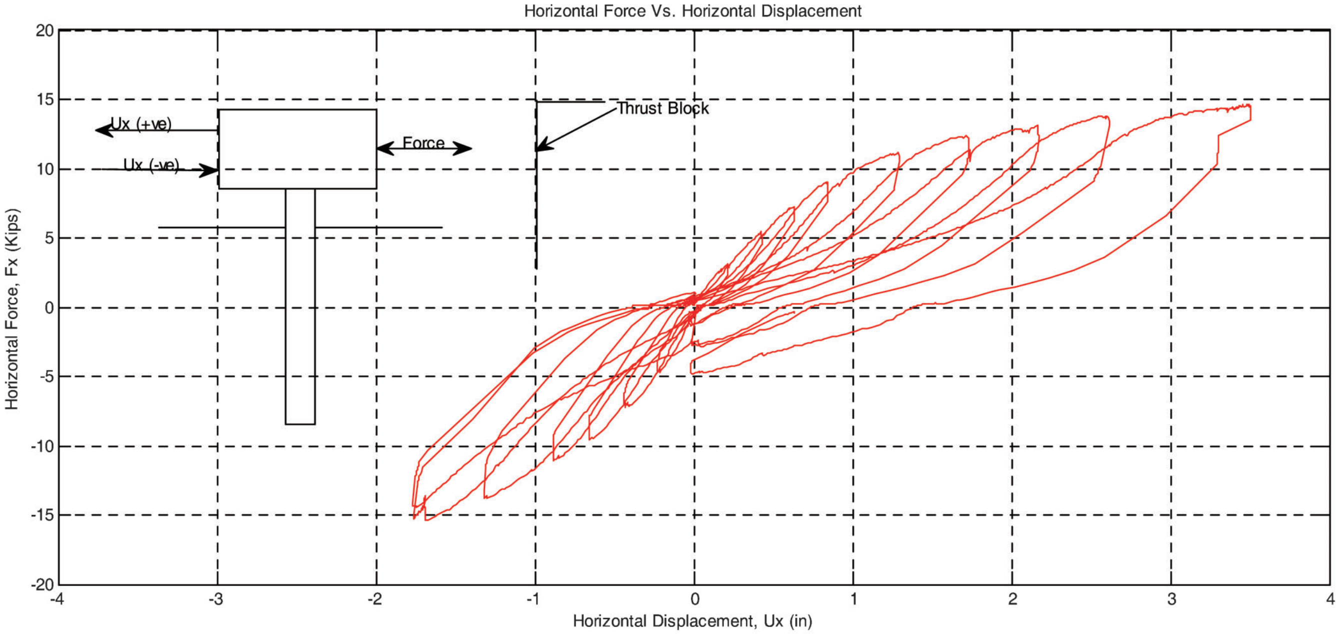

Figure E-1.2 Horizontal force versus horizontal longitudinal displacement.

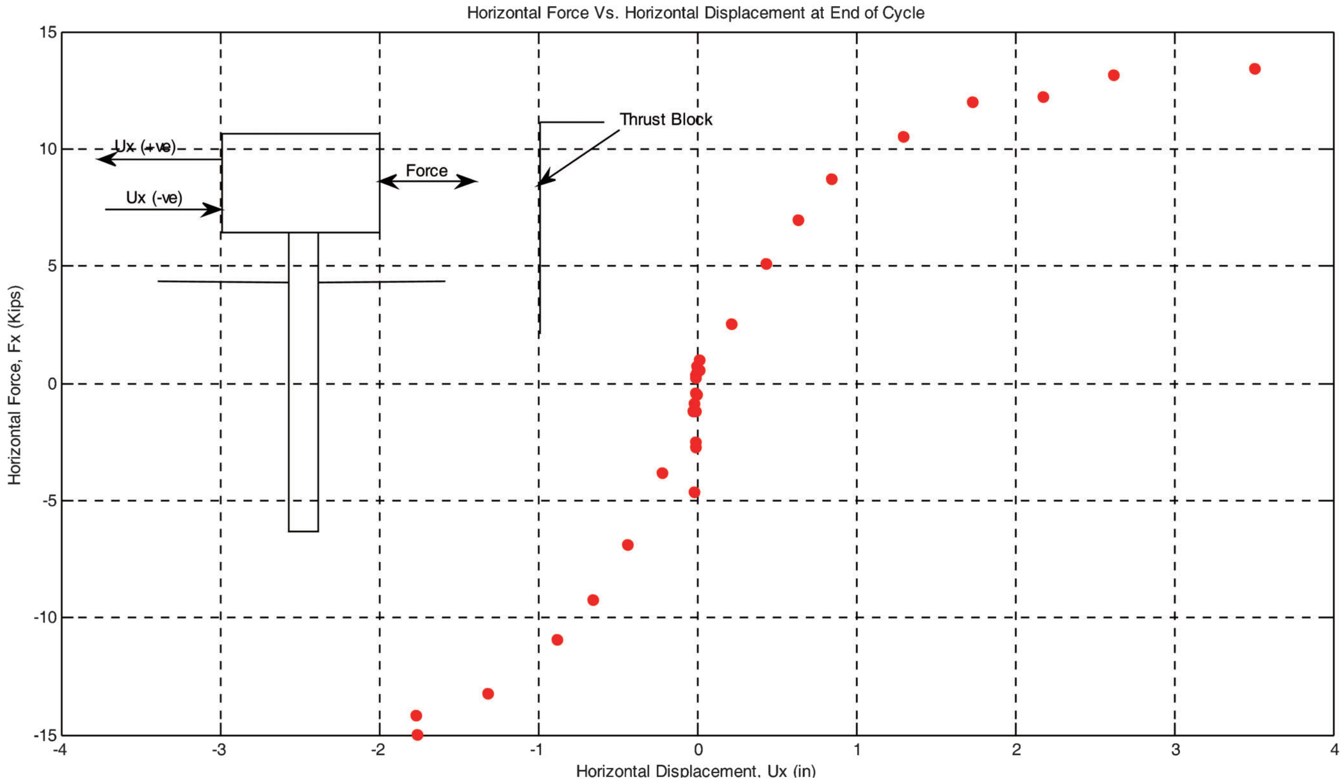

Figure E-1.3 Horizontal force versus horizontal longitudinal displacement at end of cycle.

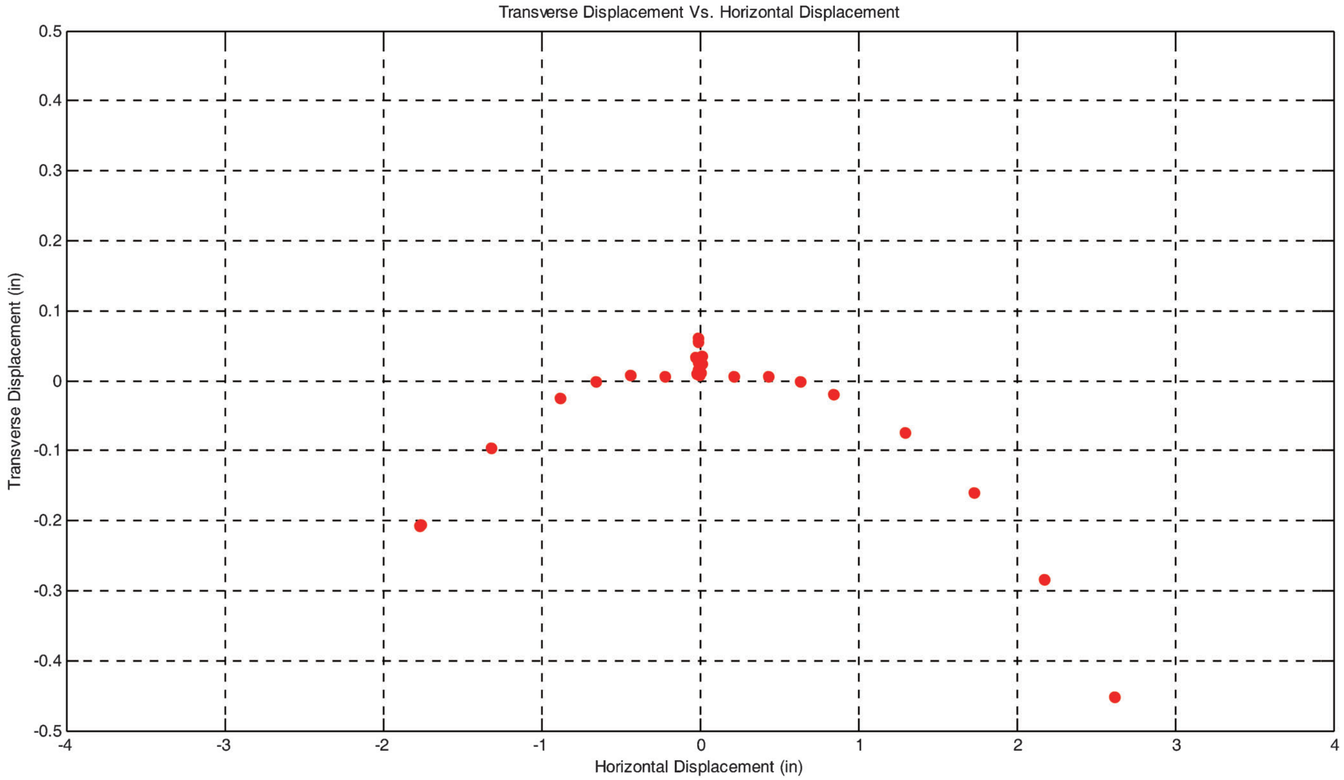

Figure E-1.4 Transverse displacement versus horizontal longitudinal displacement.

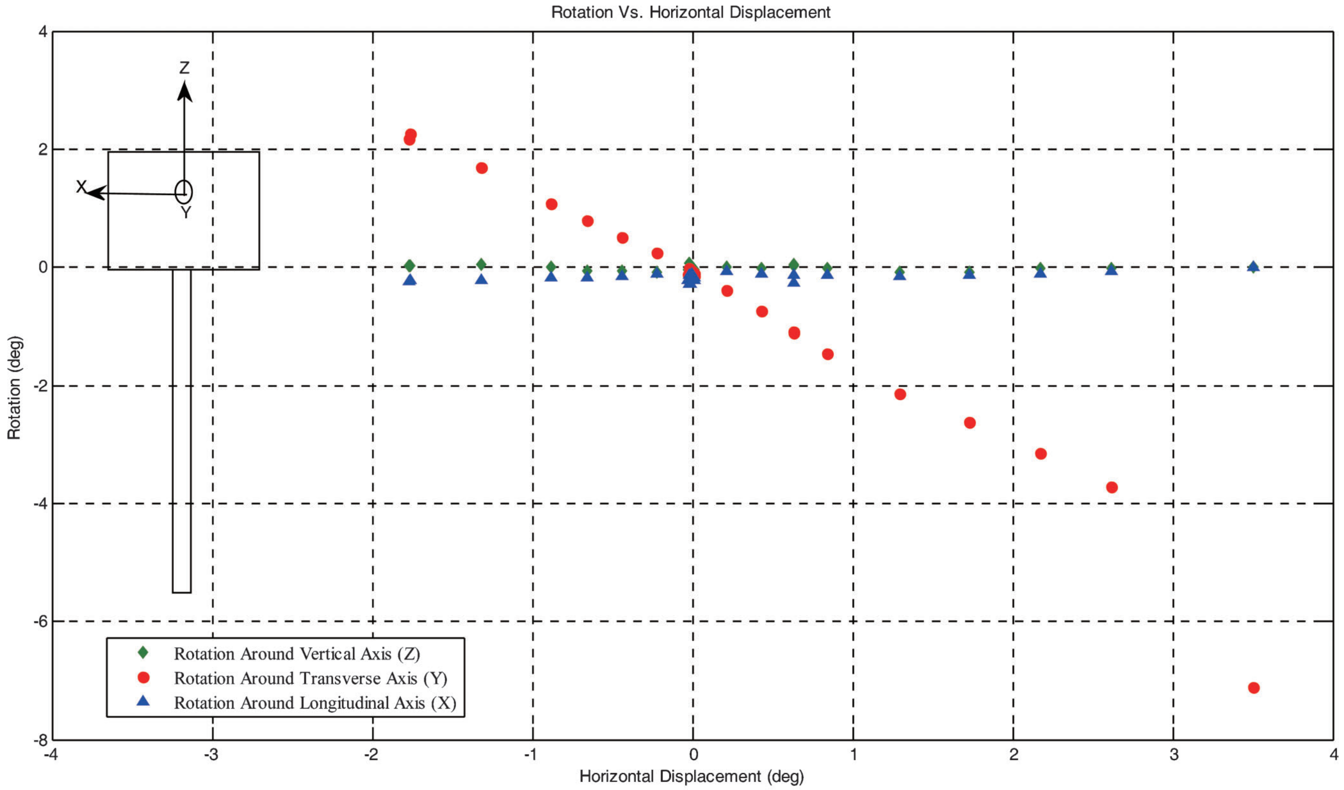

Figure E-1.5 Rotation versus horizontal longitudinal displacement.

E-1.6 DISCUSSION OF THE RESULTS

Rigid Body Response of the Pile's Cap

The pile's response at the cap is presented in Figures E-1.2 through E-1.5. The horizontal applied force as a function of the horizontal displacement showed hysteresis loops with stiffness degradation with displacement. From Figure E-1.2, it is clear that at cycle N, the response is softer than at cycle N-1, until the maximum amplitude of cycle N-1 is reached then a stiffer response is observed, this observation agrees well with the anticipated behavior, due to the "softening" of the soil around the pile at cycle N-1.The end of cycle force versus displacement (Figure E-1.3) shows a clear hyperbolic relation, which means that the modulus degradation is a function of displacement. The degradation of the secant modulus is presented in Figure E-1.7.

Figure E-1.7 shows that the modulus degrades as a function of displacement. It is interesting to note that during pulling (inward movement) the pile towards the bridge (Thrust Block) a stiffer response is observed than pushing (outward movement) the pile away from the bridge (This is also clear in Figure E-1.7). The secant modulus for the first cycle (0.25 in. amplitude) and for the outward movement was about 70% of the secant modulus corresponding to the inward movement of the same cycle. The reason may be attributed to densification of the soil between the bridge and the pile during the bridge's construction activities and during the bridge testing.

The transverse movement presented in Figure E-1.4 was insignificant during the first cycles, then became more significant. This is may be attributed to the accumulation of strains in the soil; that is, as the amplitudes became larger the soil showed less resistance to the movement in the transverse direction.

The rotational movement was only significant in the direction of loading (Figure E-1.5), which is anticipated from the test setup, which replicates a horizontal force applied at the pile's cap. The small rotations along the two other axes are a good indication that the pile was loaded mostly in the longitudinal direction.

Piles Response

The longitudinal and transverse deformed shapes of the pile are shown in Figure E-1.6 along with the potentiometer readings at their corresponding depth. There was a good agreement between the potentiometer readings and the pile's deformed shape; this observation confirms that the fixity (about 5 ft below the ground surface) observed in the deformed shape corresponds to that of a long pile (even if it was shorter than in previously tested piles). It is also observed that at large amplitudes (3 in and 4 in) the inflection point was about a 1 ft lower than for the smaller amplitudes. The plot for the transverse deformed shape was not conclusive.

The initial and final shapes (after releasing all the pressure in the testing system) of the pile are presented in Figure E-1.8.

The figure shows that the displacements were not recoverable, from the ground surface to about 2 ft below the ground surface.

E-1.7 CONCLUSIONS

It can be concluded that:

1. The pile behaved as long pile with a fixity point at about 5 ft below the ground surface.
2. The sub-grade modulus in the longitudinal direction degraded significantly with the displacement amplitude; it reached less than 50% of its initial value at large amplitudes.
3. Increasing the number of cycles resulted in modulus degradation.
4. The plastic deformations extended below the ground surface to a depth of about 2 ft.

E-1.8 REFERENCE

Frosch, R. J., & Lovell, M. D. (2011). *Long-term behavior of integral abutment bridges* (Joint Transportation Research Program Publication No. FHWA/IN/JTRP-2011/16). West Lafayette, IN: Purdue University. http://dx.doi.org/10.5703/1288284314640

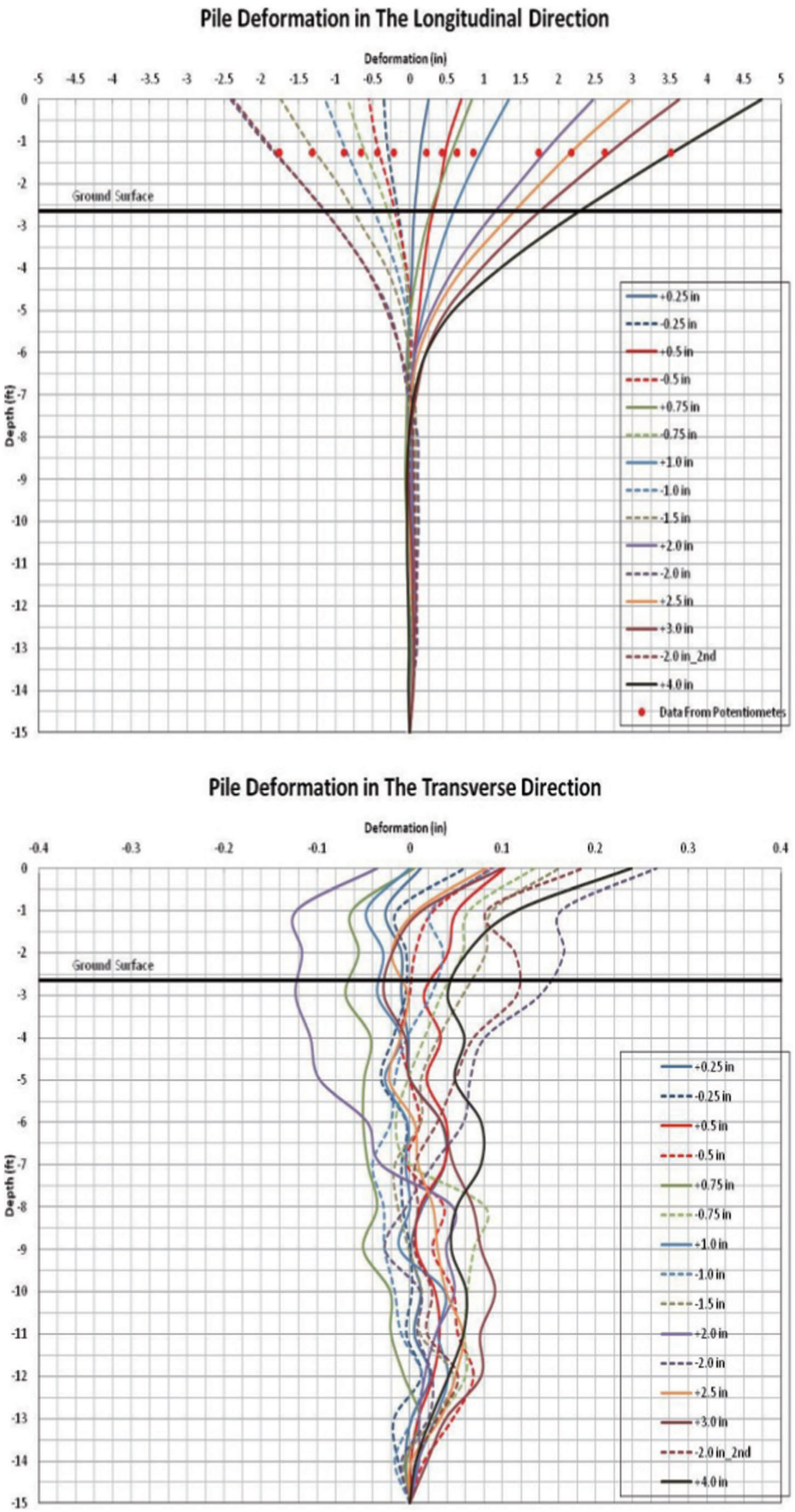

Figure E-1.6 Longitudinal and transverse deformations of the pile.

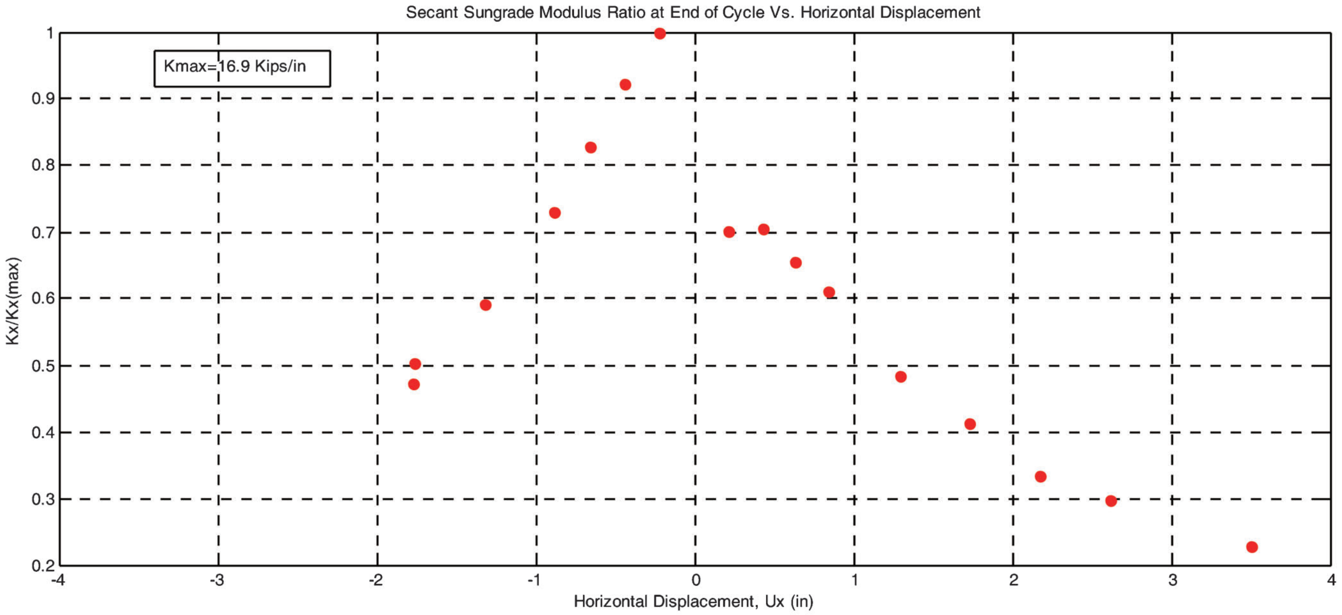

Figure E-1.7 Secant modulus as a function of displacement.

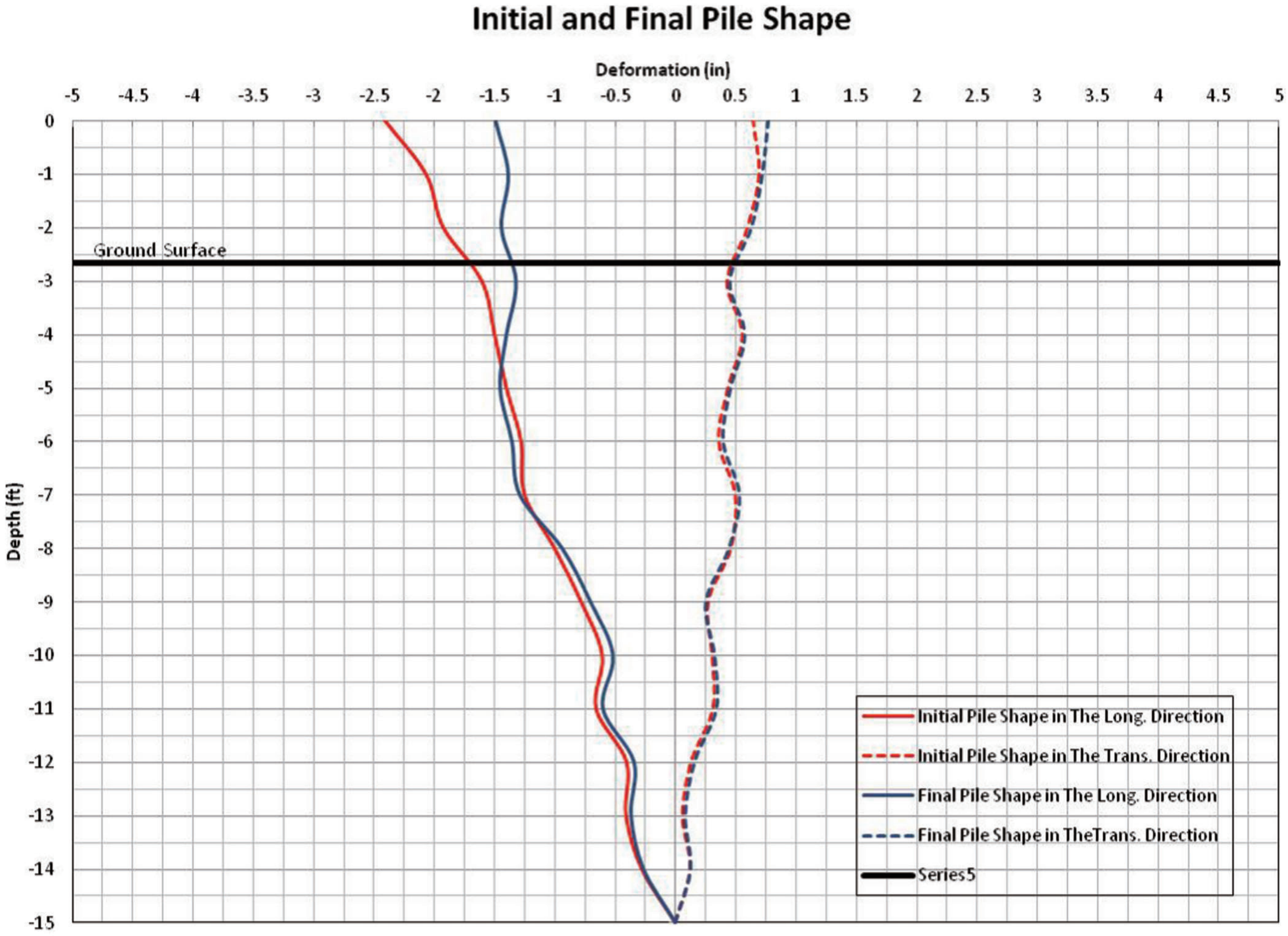

Figure E-1.8 Initial and final pile's shape.

APPENDIX F. PARAMETRIC STUDY

F.1 INTRODUCTION

The objective of the parametric study is to develop guidelines for selecting the combined maximum length and maximum skew angle of an integral abutment bridge given the range of soil properties and bridge geometries that can be considered common in Indiana. The understanding of the integral abutment bridge behavior (movement and backfill response) was established based on results from the ¼ scale bridge test (Chapter 3). Understanding of the backfill response due to low frequency cyclic loading was developed based on laboratory tests (Chapter 4). Laboratory and field tests were simulated in Abaqus© Standard with the soil's constitutive model developed in this study (Chapters 5 and 6).

To develop guidelines, a series of three-dimensional numerical simulations were completed for different bridge geometry configurations and foundation soil properties. The simulations were based on coupled thermal displacement analysis with soil-structure interaction. The commercially available Abaqus© Standard software with a user-defined subroutine for the soil's constitutive model was used.

An extreme case in terms of geometry (combination of large skew angle and length) was used as the base case and as reference to provide comparisons with other bridge geometries and soil properties. The base case was a 1000 ft long and 45.75 ft wide bridge with a 60° skew angle. The abutment wall was 8.4 ft deep and 3 ft thick. Two cases (L=1000 ft and L=500 ft with 60° skew) were analyzed (Cases 19 and 20) with thermal loading oscillating between 0°F and −75°F with shrinkage. A total of twenty (20) cases were analyzed to cover a wide-enough range of geometries and properties to develop design guidelines. Table F.1 presents the analyzed cases and the associated geometry and mechanical parameters. Note that the base case is Case #3.

The effect of bridge length was investigated by analyzing three cases in addition to the "base" case: Cases 1, 2, and 6. All the parameters presented in Table F.1 remained the same as the base case (Case 3), except for the length. The thermal response of concrete structures is directly proportional to the structure's length. The range of selected bridge dimensions covered typical bridge lengths, between 200 ft to 500 ft (Cases 1 and 2). Two additional cases were included, a 1000 ft long bridge (Case 3—base case) and a 1500 ft long bridge (Case 6), to explore the upper bound of bridge lengths. In particular, Case 6 was analyzed to investigate the response of integral abutment bridge, backfill soils and the foundation due to large displacements.

The effect of skew angle on bridge response was investigated by analyzing Cases 4 (30° skew angle) and 5 (45° skew angle) in addition to the base case (60° skew angle). All bridges had the same 1,000 ft length, and all of the other parameters as presented in Table F.1 remained the same as the base case (Case 3), except for the skew angle. The selected range of skew angles was larger than what is typically observed in integral abutment bridge (<35°). The selection of larger skew angles was necessary to explore the limits of existing design guidelines.

The effect of foundation stiffness was investigated by varying the small-strain shear modulus of the foundation soils. The small-strain shear modulus (G_{max}) for the "base" case (Case 3) was 850 ksf, which was in the range of medium stiffness granular soils at the reference effective mean stress. Two additional foundation soils were investigated: a "soft" and a "stiff" soil. The soft foundation soil had G_{max} of 425 ksf (half the stiffness of the base case), while the stiff foundation soil had G_{max} of 1700 ksf (double the stiffness of the base case). Five cases were analyzed in addition to the base case (Cases 1, 7, 8, 11, and 12) to provide understanding on the effects of the foundation soils on bridges with different lengths but with the same skew angle. Cases 7 and 8 (soft and stiff soils, respectively) were compared to the base case to investigate the effect of soil stiffness for a constant bridge length (1000 ft) and skew (60°). A comparison between Cases 11 (soft soil) and 12 (stiff soil) with Case 1 provided the effects of the foundation soils on a bridge 200 ft long with 60° skew.

The effect of abutment wall thickness was examined by analyzing two cases in addition to the base case: Case 13 with a 2 ft wall thickness and Case 14 with a 4 ft wall thickness, both

TABLE F.1
Analyzed Cases

Case	L (ft)	Skew (°)	Foundation Stiffness[1]	Wall (ft)	Wing Wall[2]	Shrinkage[3]	Starting Load[4]	Notes
1	200	60	Medium	3	No	No	Passive	±50°F
2	500	60	Medium	3	No	No	Passive	±50°F
3*	1000	60	Medium	3	No	No	Passive	±50°F
4	1000	30	Medium	3	No	No	Passive	±50°F
5	1000	45	Medium	3	No	No	Passive	±50°F
6	1500	60	Medium	3	No	No	Passive	±50°F
7	1000	60	Soft	3	No	No	Passive	±50°F
8	1000	60	Stiff	3	No	No	Passive	±50°F
9	1000	60	Medium	3	Yes	No	Passive	±50°F
10	1000	60	Medium	3	No	Yes	Active	±50°F
11	200	60	Soft	3	No	No	Passive	±50°F
12	200	60	Stiff	3	No	No	Passive	±50°F
13	1000	60	Medium	2	No	No	Passive	±50°F
14	1000	60	Medium	4	No	No	Passive	±50°F
15	200	60	Medium	3	No	Yes	Active	±50°F
16	500	60	Medium	3	No	Yes	Active	±50°F
17	1000	30	Medium	3	No	Yes	Active	±50°F
18	1000	45	Medium	3	No	Yes	Active	±50°F
19	1000	60	Medium	3	No	Yes	Active	0 to −75°F
20	500	60	Medium	3	No	Yes	Active	0 to −75°F

*Base case.

1. Foundation stiffness refers to the small strain shear modulus of the foundation soils.
2. Wing wall refers to whether abutment wing walls were included in the model.
3. Shrinkage refers to whether shrinkage deformation of the bridge deck with time was included in the analysis.
4. "Passive" indicates that the first loading cycle is expansive (the backfill soil is loaded), while "Active" means that the first loading cycle is contractive (the backfill soil is unloaded).

TABLE F.2
Model Parameters—Bridge Superstructure, Abutment Wall, and Piles

Part	Material	E psf (N/m^2)	υ	α 1/°F
Deck and girders	Concrete	$5.2*10^8$ ($2.4*10^{10}$)	0.3	$5.5*10^{-6}$
Abutment wall	Concrete	$5.2*10^8$ ($2.4*10^{10}$)	0.3	NA
Piles	(Equivalent Section matching EI)	$1.4*10^9$ ($6.7*10^{10}$)	0.2	NA

having a thickness within the typical range used in practice for a wall 8.4 ft high. The investigation was conducted to observe the influence of the capacity of the wall to deform in bending and in torsion on the overall response of the deck, backfill, and foundation piles. In addition to the potential restraint that the abutment might place on deformations of the backfill and piles, the effect of a similar restraint that could be induced by wing walls at the end of the abutment was investigated by comparing the results from Case 9 (with 90° wing walls) with the base case (no wing walls).

All cases were examined starting with passive loading (starting with thermal expansion) with no consideration of the deformations resulting from concrete shrinkage. To examine a different loading sequence (starting with thermal contraction) and the effect of shrinkage deformations, a case was analyzed starting with active loading and including shrinkage deformations (Case 10). In addition, the effect of bridge length and skew angles with shrinkage deformations and starting with active loading was examined in Case 10 and Cases 15 through 18.

In this chapter, the finite element modeling is summarized in Section F.2; results from the base case are presented in Section F.3, and the acceptable integral abutment bridge behavior criteria are discussed in Section F.4. The effect of length, skew angle, foundation soils stiffness, abutment wall stiffness, wing wall, and loading sequence and shrinkage are discussed in Sections F.5 through F.10. Conclusions are included in Section F.11.

F.2 FINITE ELEMENT MODELING

All cases used in the parametric study were modeled with Abaqus© Standard. The finite element models were based on the same techniques and assumptions discussed in Section 6.6 (element types, contacts, constraints, etc.).

The bridge superstructure configuration (deck thickness, girder dimensions, girder spacing and girder number) and the pile configuration (diameter, depth, and number) were identical to the full scale bridge (US 231 over AEP Railroad Spur) that was discussed and simulated in Section 6.6. The bridge length and skew angle were changed depending on each case analyzed. For most of the cases, the other dimensions remained the same as the US 231 bridge model. The bridge structure width was 45.75 ft. The abutment wall was 3 ft wide (except for Cases 13 and 14 in Table F.1) and 8.4 ft deep. The bridge deck was supported on seven girders (4.3 ft × 1.1 ft equivalent section, refer to Section 6.6). Seven 14 in. diameter, 80 ft long concrete-filled tube (CFT) piles, supporting each abutment, were included in the simulations. The foundation soils were 75.1 ft long, 42 ft wide and 85 ft deep. The backfill dimensions were 75.1 ft long, 42 ft wide (except for the case with wing wall, Case 9) and 8.4 ft deep. The dimensions and bridge superstructure configuration are shown in detail in Section F.3.2.

The material parameters are also identical to those discussed in Section 6.6, except for the cases where the foundation stiffness was changed (Section F.7). The techniques and assumptions used in developing the finite element model and the material parameters incorporated into the model are summarized in the following paragraphs.

The bridge was simulated in three-dimensional space with Abaqus© Standard. The simulations were conducted including thermal and mechanical response as well as soil-structure interaction. Contacts and constraints between structural elements and soil or at the boundaries were applied in the model to replicate what is believed to exist in an actual bridge. The contacts between the abutment wall and the backfill, abutment wall base and foundation soils, and between the pile perimeter and foundation soils were approximated using the surface to surface finite sliding contact algorithm in Abaqus© Standard (penalty friction algorithm).

The substructure components (abutment walls and piles), foundation soils, and backfill soils were discretized using 4-node linear tetrahedral, general stress elements. The superstructure components (deck and girders) were discretized using 4-node coupled tetrahedral linear displacement and temperature elements.

The bridge abutment walls and piles were modeled as linear-elastic. The superstructure was modeled as a coupled thermal-mechanical elastic material. The foundation and backfill soils were represented as elastoplastic materials using the constitutive model developed in this study (refer to material model in Chapter 5). The elastic and thermal model parameters for the bridge and piles are presented in Table F.2 (based on Frosch and Lovell (2011)).

The elastoplastic model parameters for the foundation soils and granular backfill are presented in Tables F.3, and F.4, respectively (refer to Chapter 5 for definition of input parameters).

As discussed in Chapter 6, roller boundaries were placed at the back and sides of the foundation soils. Rollers were also placed at the back and sides of the backfill. A pinned boundary was used at the bottom of the foundation soils. To enhance model stability, a small uniform load (100 psf) was applied at the top of the backfill and to the front of the backfill next to the abutment walls (Figure 6.23).

The temperature time history input into the simulation is shown in Figure F.1. It consisted of constant cycles with amplitude of ±50°F and period of 1 yr. In all simulations, a ten (10) cycle thermal loading was imposed only to the bridge deck and girders. The temperature loading shown in Figure F.1 was used in all cases except for the case with shrinkage (Case 10 presented in Section F.10).

F.3 GENERAL BEHAVIOR OF INTEGRAL ABUTMENT BRIDGE WITH TEMPERATURE CYCLES

The rigid body response of the superstructure due to thermal expansion and contraction is one of the factors controlling the demand on the foundation piles and the resulting lateral earth

TABLE F.3
Model Parameters—Foundation Soils

$G_{o,ref}$ psf (N/m^2)	$\sigma_{m,ref}$ psf (N/m^2)	υ	α (deg)	κ psf (N/m^2)	a	b	N_1	N_2	ψ (deg)	C_1
$8.5*10^5$ ($4.1*10^7$)	1250 ($6*10^4$)	0.3	41	1 (47.9)	−0.35	0.1	2.0	1.8	1	NA(1)

[1] Not applicable because the linear option upon reloading was not used for the foundation soils.

TABLE F.4
Model Parameters—Backfill

$G_{o,ref}$ psf (N/m^2)	$\sigma_{m,ref}$ psf (N/m^2)	υ	α (deg)	κ psf (N/m^2)	a	b	N_1	N_2	ψ (deg)	C_1
$3.5*10^5$ ($1.7*10^7$)	320 ($1.5*10^4$)	0.3	41	1 (47.9)	−0.2	0.1	2.2	1.7	1	3.1

pressure of the backfill soils (Chapter 3). This is one of the key observations made during the ¼ scale bridge test, where displacements imposed at a gap to simulate displacements from thermal loading, resulted in translational and rotational movements of the bridge deck. During the expansion phase, the bridge deck moved towards the backfill soil and rotated towards its obtuse corner. During contraction, the bridge deck moved away from the backfill soil and rotated towards the acute corner. A conceptual understanding of the movements of the bridge deck is presented in Section F.3.1. Such understanding is thought to be instrumental in the analysis of the results obtained from the base case, which are presented in Section F.3.2.

F.3.1 Rigid Body Response

A simple coupled thermal-displacement model was analyzed using Abaqus©. The model consisted of the deck, girders, and abutment wall. The bridge was 1000 ft long and 45.75 ft wide, and the abutment dimensions were 10 ft high and 3 ft in thickness. The skew angle was 45°. The support for the bridge structure was provided by linear springs (instead of piles) in the two horizontal directions. The material properties for the bridge deck and abutment walls are those provided in Table F.2. The stiffness of the linear springs used in the analysis was 132 kips/ft^3, which was based on the results of the laterally loaded pile test (Appendix D). Temperature was imposed to the bridge deck and girders with a full cycle of expansion and contraction and amplitude of ±50°F.

Figure F.2 presents the displacements and rigid body response of the bridge during expansion. Contour plots of the transverse displacements on the deformed shape of the bridge deck are given in Figure F.2(a), together with the undeformed shape of the deck superimposed to the contour plots. A side view of the deformed shape of the deck and abutment (showing the entire bridge length) is shown in Figure F.2(b). An elevation view of the deformed shape of the abutment wall is shown in Figure F.2(c), together with the magnitudes of the transverse displacements. A more detailed plot of the abutment transverse displacements is shown in Figure F.2(d).

Figure F.2(a) shows an overall expansion of the bridge deck, which is the result of the increase of temperature. As expected, the abutment corners move outwards. However, larger longitudinal and transverse displacements occurred at the acute corner than at the obtuse corner. This is supported by Figure F.2(b) which shows the deformed shape of the bridge, with contours of the transverse deformations. It is important to notice the deformation of the abutment due to the overall thermal expansion of the deck. As shown in Figure F.2(c) and in more detail in Figure F.2(d), the abutment deforms in bending along a vertical and a horizontal axis, as well as in torsion. Of all these deformations, because of the stiffness of the abutment along the three different axes, the largest deformation occurs in bending along the vertical dimension of the abutment. The deformed shape of the abutment wall in Figure F.2(c), shows that the vertical bending of the abutment wall is not uniform along the abutment, with larger bending at the acute corner than at the obtuse corner (notice the larger gradient of horizontal displacements at the acute corner along the abutment height in Figure F.2(c)). Furthermore, it is observed from the contours of the lateral displacement on the deformed shape of the abutment wall in Figure F.2(d) that the lateral displacements are primarily toward the obtuse corner (positive (+) displacement). However, approximately at the bottom third of the abutment wall (primarily between the center of the abutment and the obtuse corner), the lateral displacements are toward the acute corner (negative (-) displacement) as a result of torsion on the wall. This illustrates that bending deformations are largest at the acute corner. Due to the skew of the abutment, the abutment bending results in both longitudinal and transverse displacements (with respect to the longitudinal axis of the bridge) at the top of the abutment. The largest longitudinal and transverse displacements occur at the acute corner as previously discussed (if there is no skew, bending of the abutment results in only longitudinal displacements). Figure F.3 provides a conceptual schematic of the displacements at the corners of the deck due to bending of the abutment; the upper portion shows the corners and abutment wall from Figure F.2(a), while the lower portion shows an outline of the plan view of the bridge deck. The displacement vectors are added to the schematic to help illustrate the displacements of the bridge deck induced by the thermal deformations and the skew of the bridge.

As seen in the upper portion of Figure F.3(a), the bridge deck is subjected to horizontal bending as a result of thermal expansion. This horizontal bending results in a larger displacement at the acute corner as indicated by the displacement vector acting on the

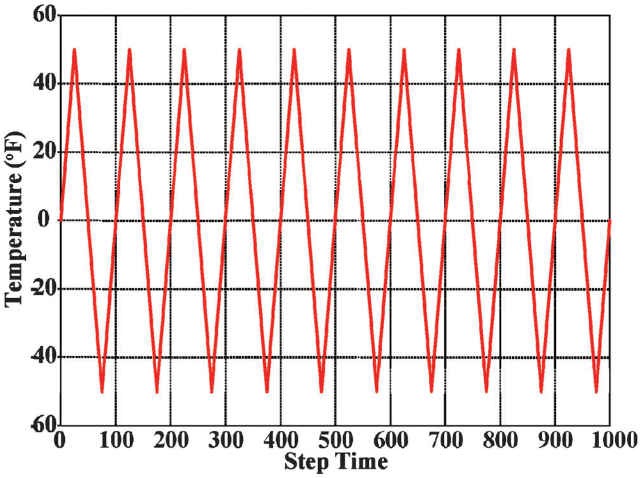

Figure F.1 Initial and final pile's shape.

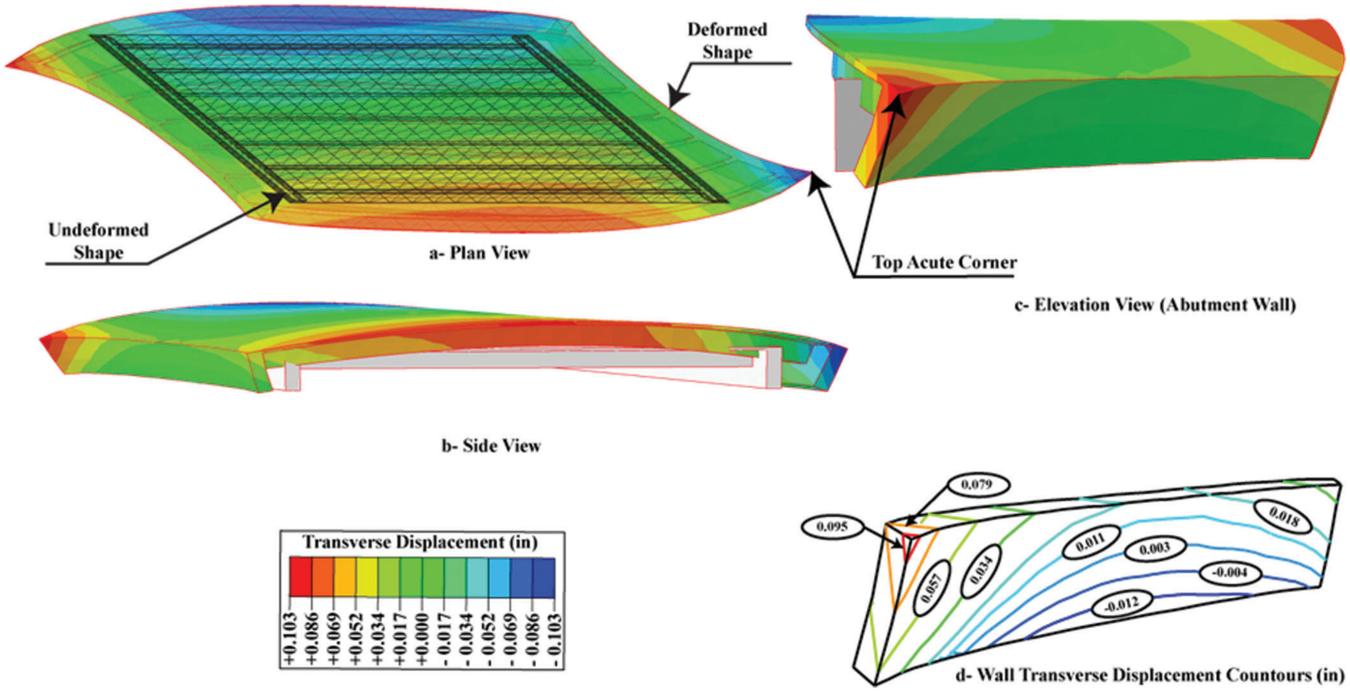

Figure F.2 Bridge deformations during expansion.

undeformed shape (UR_{acute}). To provide a better understanding of the rigid body modes of displacements, the displacement vectors are added to the schematic of the bridge plan view, as shown on the lower portion of Figure F.3(a). The bridge deck geometry is anti-symmetric, which means that the opposite corners at a diagonal are subjected to the same displacement (acute corners have the same displacement and obtuse corners have the same displacement). The resultant displacements are decomposed in two directions: the longitudinal (UL) and the transverse (UR) directions, as shown in Figures F.3(b) and F.3(c). The longitudinal displacement vectors are larger at the acute corner (UL_{acute}) than at the obtuse corners (UL_{obtuse}). The direction of the longitudinal displacements results in elongation of the bridge during expansion. The transverse displacements (Figure F.3(c))

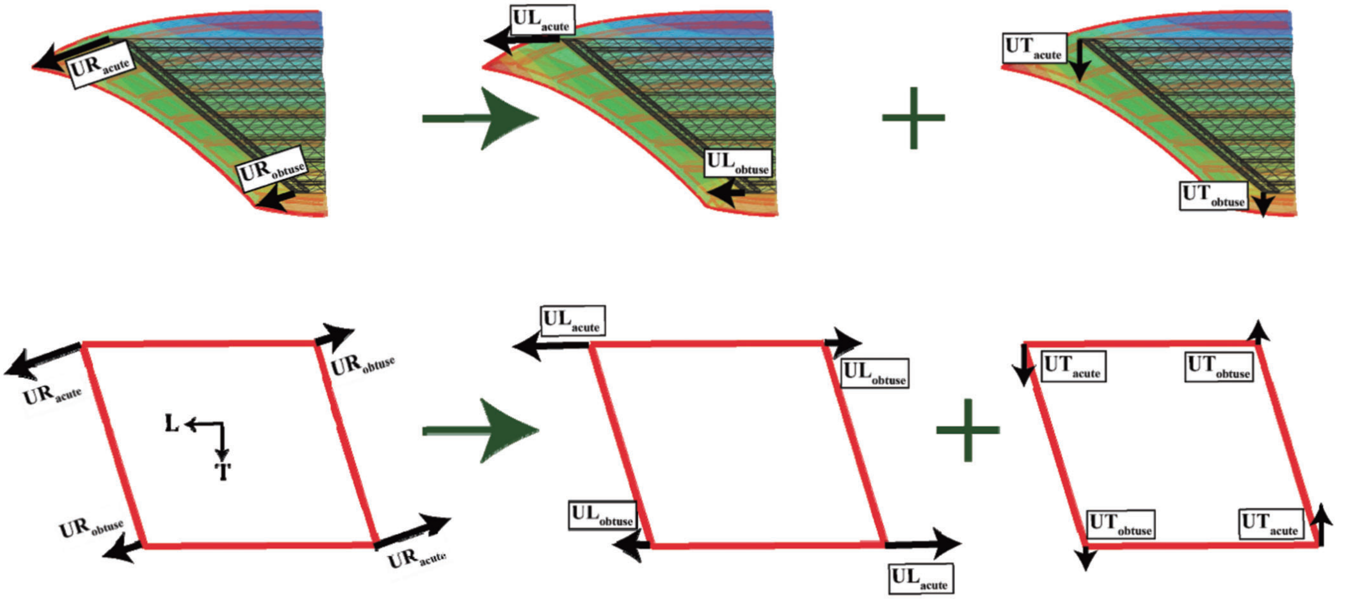

a- Resulting Displacement

b- Longitudinal Displacement

c- Transverse Displacement

Figure F.3 Bridge deformations during expansion.

result in a counterclockwise rotation of the bridge deck. This behavior is consistent with the results of the numerical models as well as the ¼ scale test results.

F.3.2 "Base" Case—Case 3

The base case was simulated in the manner described in Section F.2. The general view of the model is shown in Figure F.4(a) which illustrates the bridge deck, abutment walls, girders, backfill and foundation soils, and piles (piles shown on one side of the bridge and soil on the other). The dimensions of the model are 45.75 ft wide and 1000 ft long with a 60° skew angle as shown in the plan view (Figure F.4(b)). The bridge deck is supported on seven girders (4.3 ft × 1.1 ft) as shown in Figure F.4(c). Details of the abutment are shown in Figure F.4(d); the abutment wall was 3 ft wide and 8.4 ft deep. The piles (number and dimensions) are shown in Figure F.4(e) which includes seven 14 in. diameter, 80 ft long concrete-filled tubes (CFT), supporting each abutment. The foundation soils were analyzed as 75.1 ft long, 42 ft wide and 85 ft deep and the backfill dimensions were 75.1 ft long, 42 ft wide and 8.4 ft deep as shown in Figures F.4(a) and F.4(f).

The thermal loading time history presented in Figure F.1 was applied to the bridge superstructure and the deformed shape is presented in Figure F.5. Three plots are shown: the general view of the deformed shape (Figure F.5(a)), the deformed shape of the abutment wall and piles (Figure F.5(b)), and a close up of the deformed abutment and piles (Figure F.5(c)). The deformed shape of the bridge indicates elongation of the bridge with larger displacements at the acute corner. The longitudinal displacements are enlarged in Figure F.5(b), which shows that the displacement demand on the piles is larger at the acute corner than at the obtuse corner with a larger depth of fixity at the acute corner. The transverse displacement demand on the piles can be observed in the close-up view of the abutment and piles (Figure F.5(c)). It is interesting to note that the transverse displacements of the top of the piles are in the opposite direction of the displacements of the corresponding points at the top of the abutment. This behavior is a result of the complex deformations that occur at the abutment, with bending along two axes and torsion. Figure F.2(d) illustrated this behavior. While this figure is the result of a different case, it still represents what occurs in Case 3. Figure F.2(d) shows the expected transverse deformations at the top of the abutment, but because of bending and torsion, the transverse deformations are in the opposite direction at the bottom of the abutment. Note also that the negative transverse deformations at the bottom of the abutment in Figure F.2(d) are small compared to those at the top and are about one order of magnitude smaller than at the acute corner. This is also the case in Figure F.5(c), where the transverse deformations of the piles are grossly exaggerated, about 800 times, with transverse displacement at the top of the pile about 7 times smaller than the transverse displacement at top of the wall.

The total horizontal displacements of the abutment wall, which are the resultant of the longitudinal and transverse displacements, are plotted for the top and bottom of the abutment wall at three locations: the acute and obtuse corners and at the centerline of the abutment (note that the locations at the bottom of the abutment also represent the displacements of the top of the piles). The displacements are plotted in Figure F.6 as a function of the cycle number, where Figure F.6(a) shows displacements at the top of the wall and Figure F.6(b) shows displacements at the bottom of the wall. The following observations can be made:

1. Displacements reached an approximately steady state after the fifth cycle.
2. Largest displacement was observed at the acute corner.
3. Displacements at the upper part of the wall are larger than at the lower part, which supports vertical bending of the abutment.
4. The difference between displacements at the upper part of the wall and the lower part of the wall is greater at the acute corner than at the obtuse corner, which supports a previous observation (Figure F.2) that the vertical rotation/bending of the abutment wall is larger at the acute corner than at the obtuse corner.

The deformed shape of the piles with depth is plotted for the first, second, fifth, and tenth cycles in Figures F.7 and F.8, in the longitudinal and transverse directions, respectively. The following observations can be made:

1. Displacement demands on the acute piles are larger than the obtuse piles in both the longitudinal and transverse directions.
2. Displacement demands on the piles are larger during thermal expansion when compared with the displacement demand during contraction for both the longitudinal and transverse directions.
3. Points of fixity of the piles are at a depth of approximately 15 ft. However, for the pile at the acute corner, the point of fixity appears deeper during the fifth and tenth cycles.
4. The deformed shape of the piles in the transverse direction tends to the vertical in the upper 3 ft, which agrees with the recorded pile's deformed shape obtained from the ¼ scale bridge test discussed in Chapter 3.
5. The deformed shape of the piles in the transverse direction during expansion indicates a transverse displacement towards the acute corner which agrees with the discussion regarding the transverse displacement at bottom of the abutment wall in Section F.3.1 (Figure F.2(d)).

Lateral earth pressures on the abutment wall as a function of the number of cycles are plotted in Figure F.9 for the obtuse corner, the centerline of the abutment wall, and the acute corner. All plots show the lateral earth pressures at 0 ft, 4.2 ft, and 8.4 ft below the top of the bridge deck.

From Figure F.9, the following observations are made:

1. The lateral earth pressure is higher at the obtuse corner than at the acute corner this behavior was observed on the ¼ scale bridge discussed in Chapter 3. In addition, the lateral earth pressure at the acute corner is higher than at the centerline of the abutment wall.
2. The maximum lateral earth pressure (during expansion) increases with the number of cycles, up to the fifth cycle, after which steady state is approached.
3. Active stress is reached during the first cycle at most locations behind the abutment.
4. At the obtuse corner, the lateral earth pressure is higher at a depth of 4.2 ft than at 8.4 ft, after the third cycle. This behavior is somewhat counterintuitive, as pressures are expected to increase with depth and is attributed to the accumulation of plastic strains in the soil adjacent to the abutment.

Earth pressures with depth at the acute corner, obtuse corner, and center of the abutment are shown in Figure F.10 for the first, second, fifth, and tenth cycles. The observations made from those plots are similar to those based on the results presented in Figure F.9. The increase of the lateral earth pressure at the obtuse corner at a depth of 4.2 ft (mid-depth of the abutment) is observed as the number of cycles increases. The pressure distribution along a vertical section through the abutment is a function of the displacement demand on the soil and on its confinement. Thus, pressures at the surface are limited due to the low confinement of the soil, while pressures at the bottom may be constrained by the connection between the abutment and the piles that restricts horizontal displacements of the bottom of the abutment and thus of the adjacent soil. Pressures at the corners are larger than at the center, and it is hypothesized that this behavior is due to larger confinement at the extremes of the abutment than at the center. To inspect this hypothesis, the deformed shape of the abutment wall during the first expansion cycle is shown in Figure F.11. It can be seen in Figure F.11 that lower confinement at the center is caused by the deformed shape of the abutment wall. As discussed in Section F.3.1 and shown in Figure F.11, bending around the vertical axis (bending in the horizontal direction) is larger at the

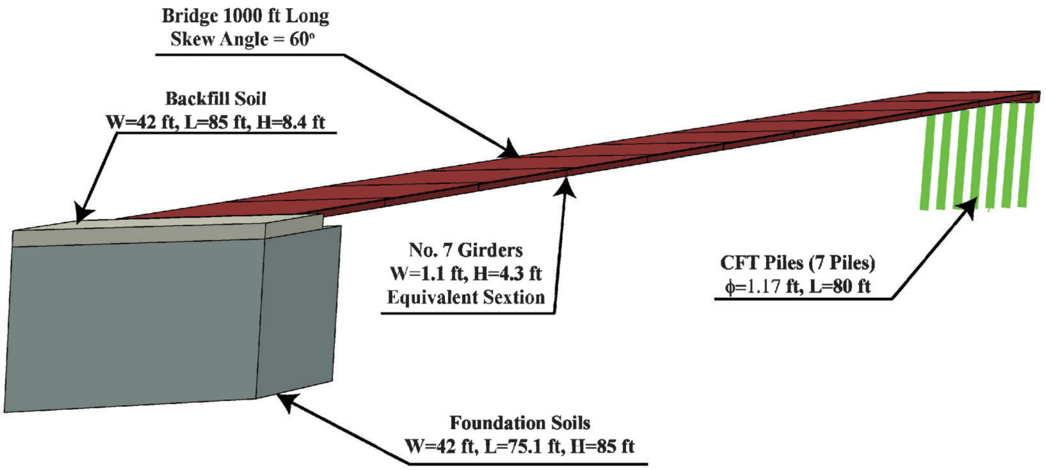

a- General View

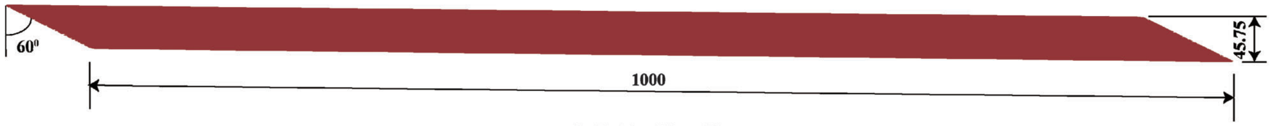

b- Bridge Plan View

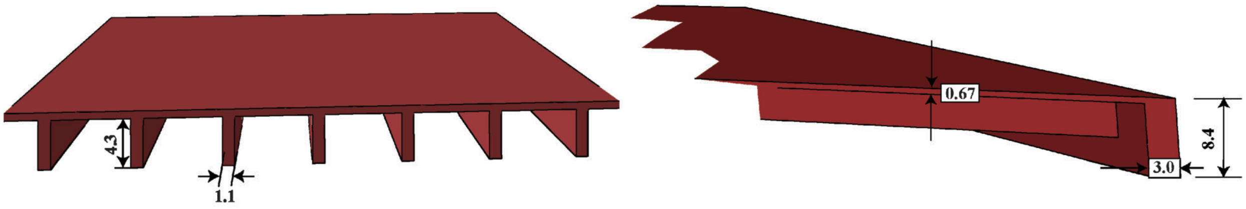

c- Section (Bridge Deck and Girders)

d- Abutment (Close Up View)

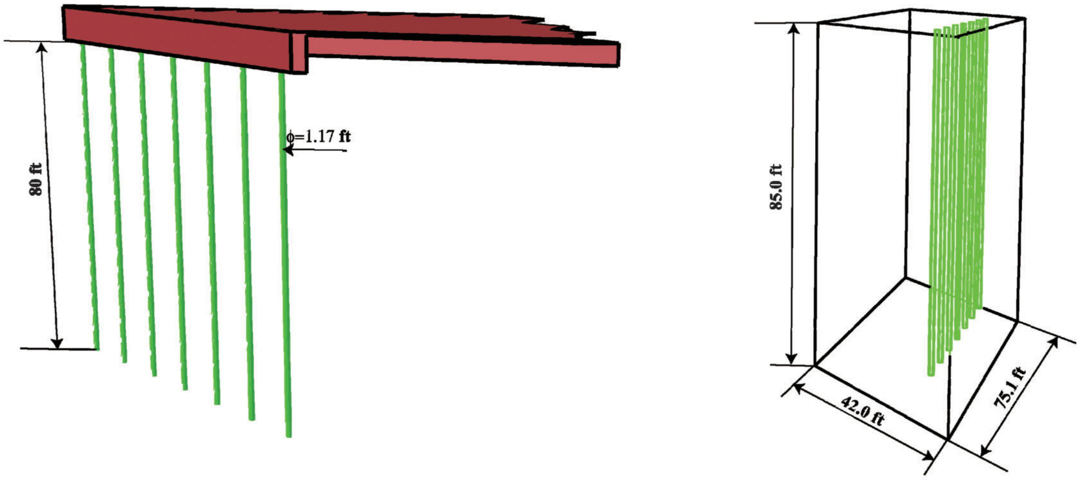

e- Abutment Wall and Piles

f- Piles and Foundation Soil

Figure F.4 Numerical model dimensions.

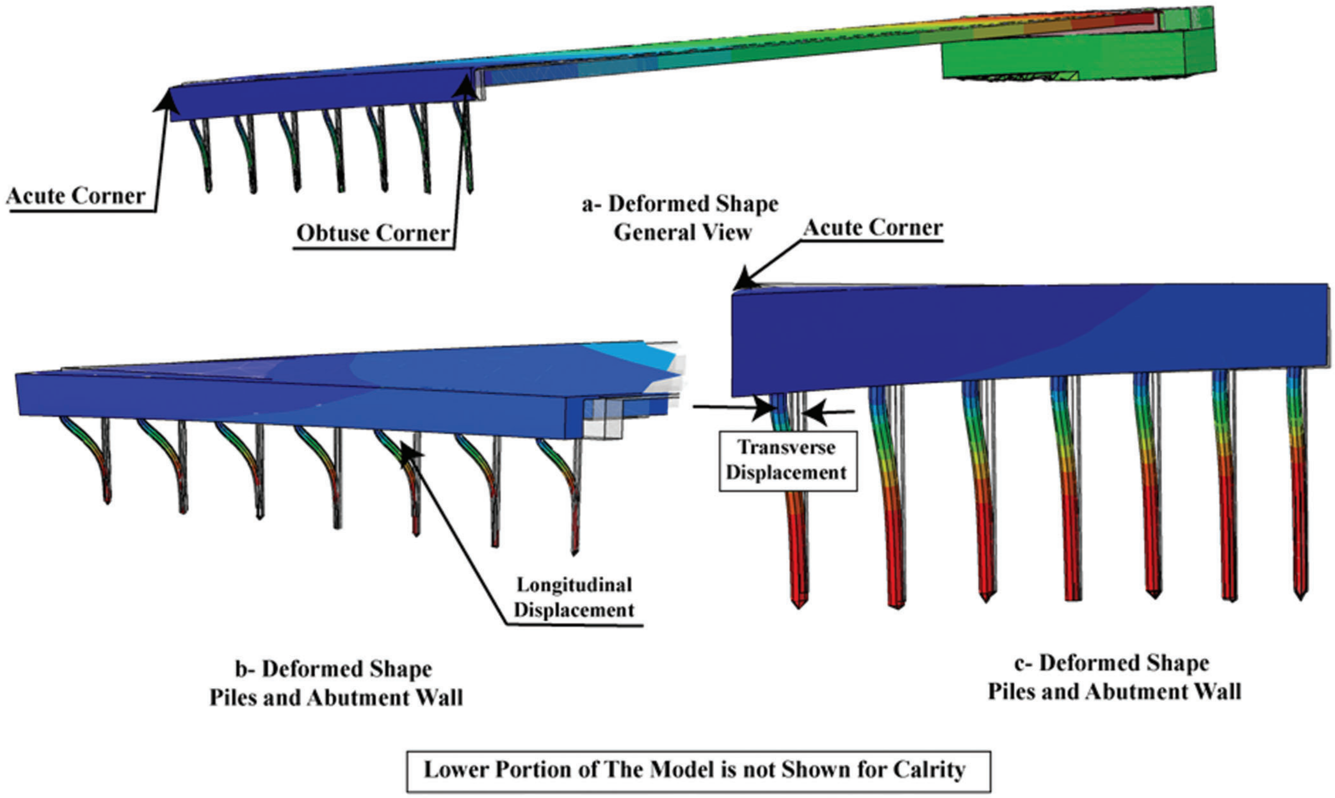

Figure F.5 Deformed shape of the bridge for Case 3 (first expansion cycle).

corners than at the center which results in arching at the center of the abutment, a smaller displacement at the centerline, and consequently a smaller earth pressure.

The lateral earth pressure distribution along the abutment wall at a depth of about 6.4 ft (above the pile-abutment wall connection) and the associated lateral earth pressure coefficient during thermal expansion (passive loading) are plotted in Figures F.12 and F.13, respectively.

It is observed from Figure F.12 that the lateral earth pressure is approximately uniform along the majority of the abutment wall. An increase of the lateral earth pressure above the average is observed at the acute and obtuse corners (higher at the obtuse than at the acute). The higher earth pressure at the corners is attributed to the larger confinement as discussed earlier. The earth pressure distribution agrees with the observations from field tests reported in Frosch and Lovell (2011). Along most of the wall, the lateral earth pressure reaches a steady state between the fifth and seventh cycles.

Figure F.13 shows that high lateral earth pressures, $K>3$, observed at the obtuse corner only act along about 3% of the abutment wall length. The lateral earth pressure coefficient is between 1.2 and 2 along most of the abutment length.

The abutment wall displacement, as presented in Figure F.6, shows that the displacements are higher at the acute corner than at the obtuse corner. However, the earth pressure is higher at the obtuse corner (Figures F.9, F.10, and F.12) than at the acute corner, which seems to be counterintuitive. To investigate this finding, the horizontal displacement (in the horizontal plan) distribution of the backfill is plotted in Figure F.14 for the first, second, fifth, and tenth cycles (note that the shading scale used in different cycles is not the same to prevent masking the displacement distribution). As shown in Figure F.14, the resultant horizontal displacement is higher at the obtuse corner, which is opposite to what was observed from the displacement distribution of the abutment wall. This difference in the displacement magnitude and distribution between the abutment wall and the backfill soil during expansion is attributed to the rotational movement of the abutment wall. Part of the displacement of the abutment wall is caused by wall rotation, which doesn't exist in the displacement observed at the backfill. Furthermore, it can be concluded that rotation of the acute corner is higher than the obtuse corner because more displacement was transferred from the obtuse corner to the backfill soil than from the acute corner to the backfill.

To inspect the earth pressure distribution with depth (Figure F.10), the depth scale is added to the backfill in Figure F.14. It can be seen that at a depth of 8.4 ft, the restraint imposed by the piles is reflected in a smaller displacement than at the top of the backfill. However, confinement at top of the wall is smaller than at the bottom. Thus, with depth, the confinement controls as earth pressure increases to a depth of about 4 ft (Figure F.10), after which the displacement constraint imposed by the piles becomes the controlling factor, resulting in a smaller earth pressure (clearer at the 2nd and 5th cycles).

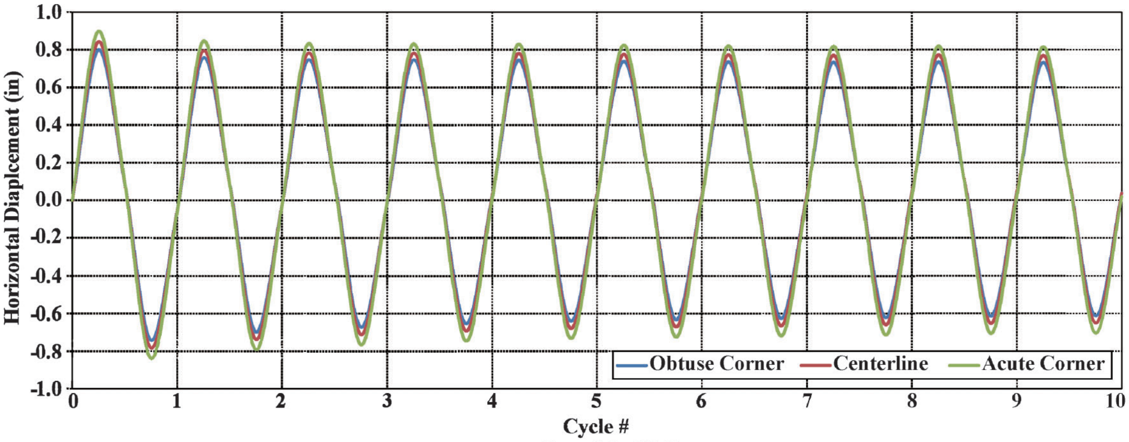

a- Top of the Wall

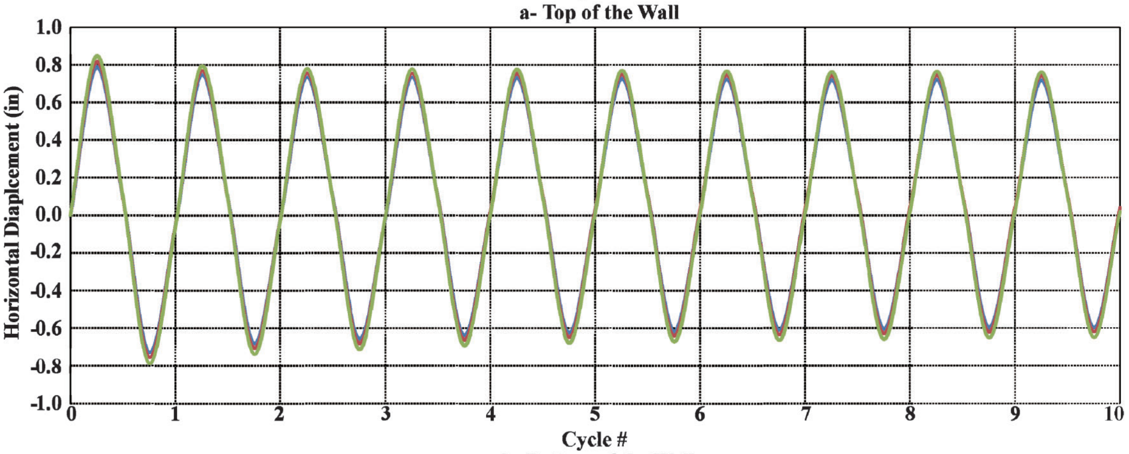

b- Bottom of the Wall

Figure F.6 Horizontal displacements of abutment wall.

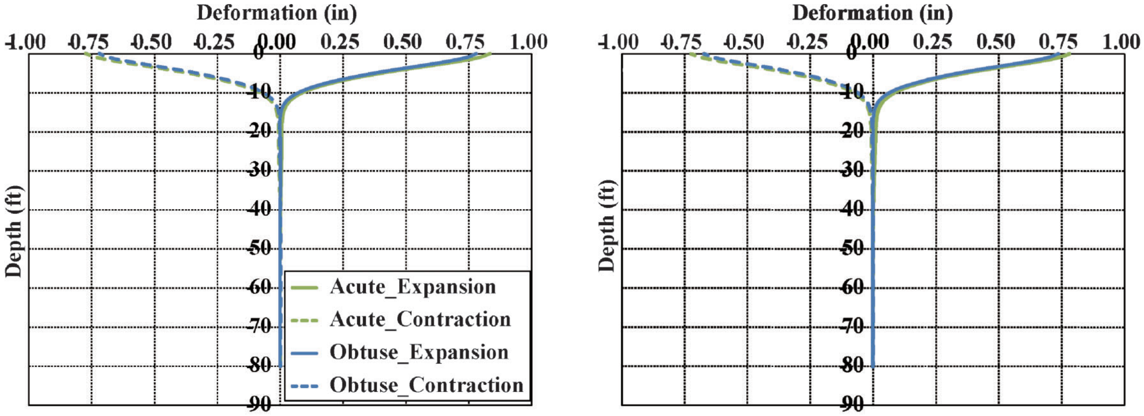

a- First Cycle

b- Second Cycle

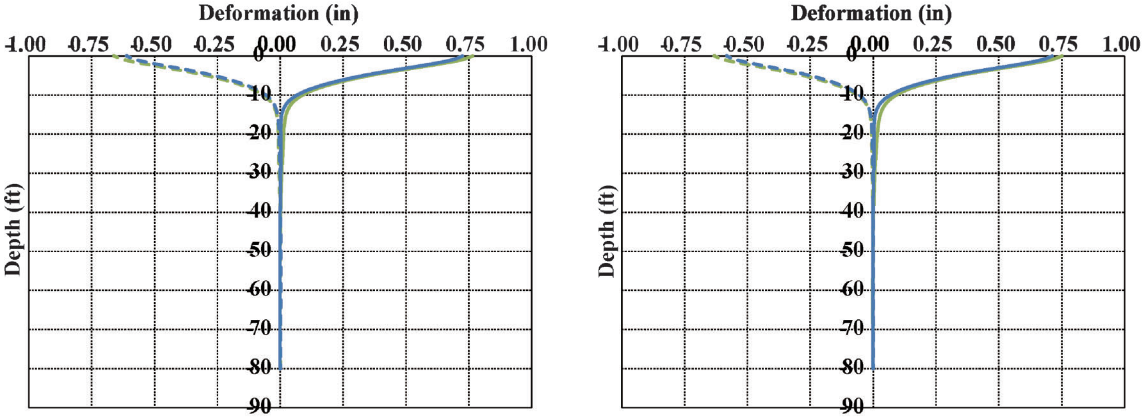

c- Fifth Cycle

d- Tenth Cycle

Figure F.7 Displacements of the piles with depth—longitudinal.

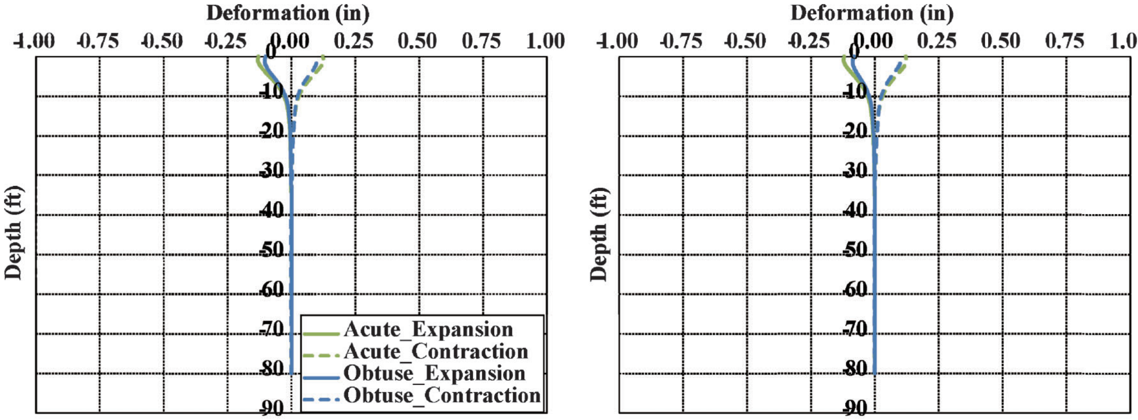

a- First Cycle

b- Second Cycle

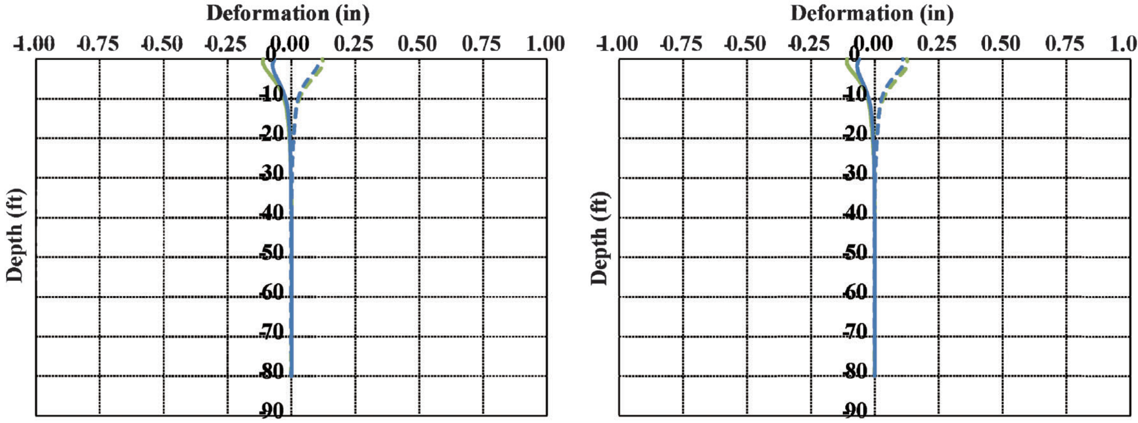

c- Fifth Cycle

d- Tenth Cycle

Figure F.8 Displacements of the piles with depth—transverse.

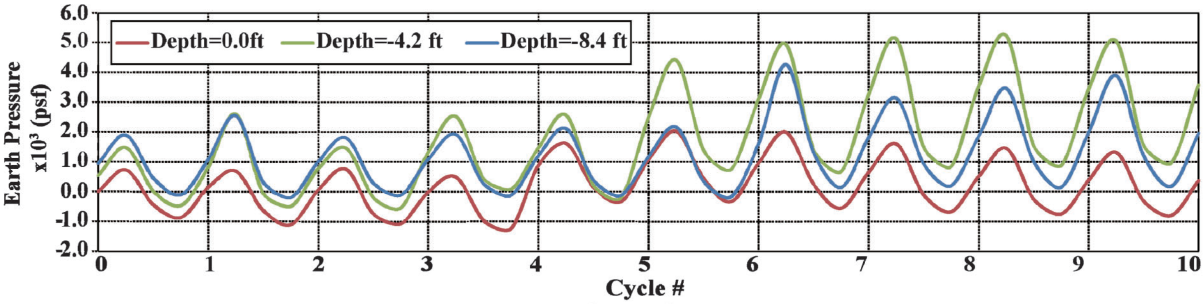

a- Obtuse Corner

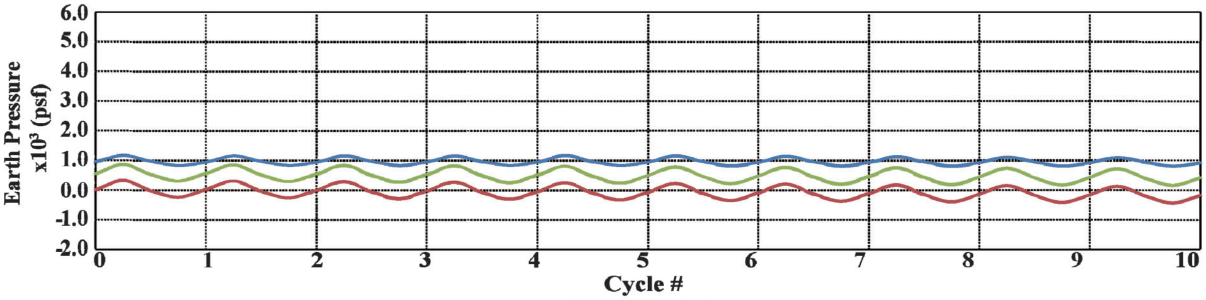

b- Bridge Centerline

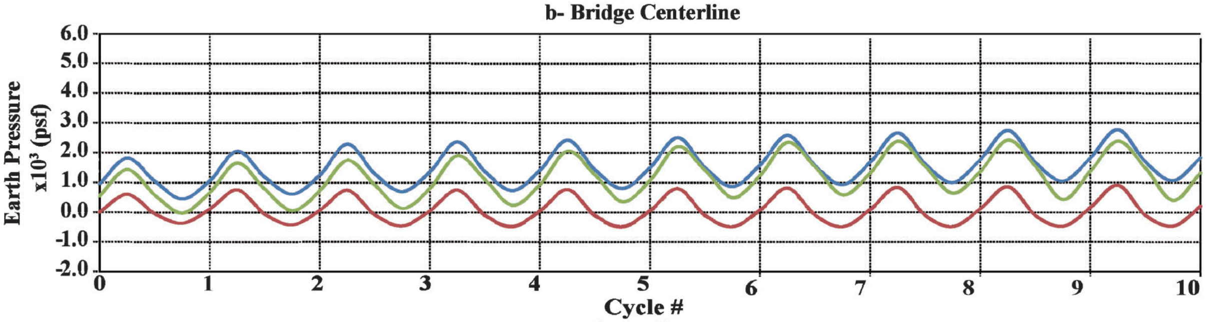

c- Acute Corner

Figure F.9 Earth pressure as a function of number of cycles.

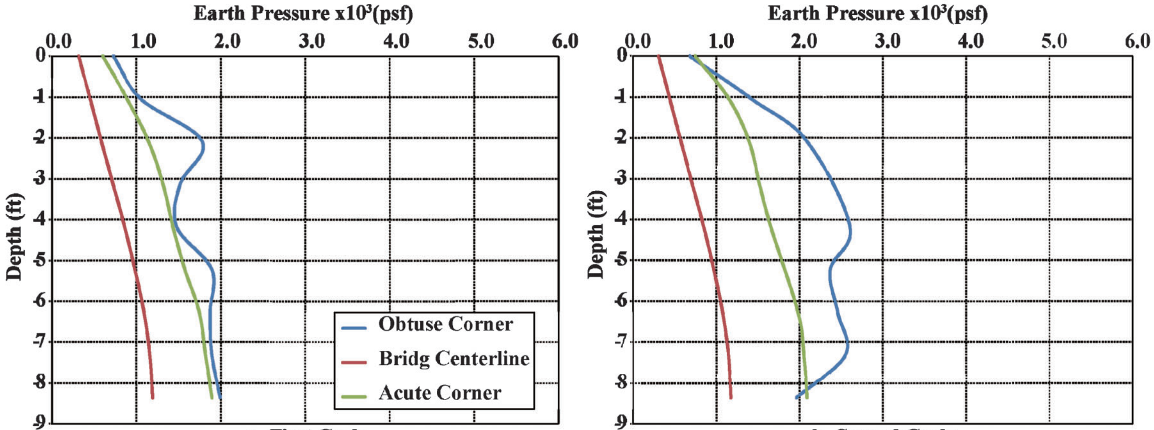

a- First Cycle

b- Second Cycle

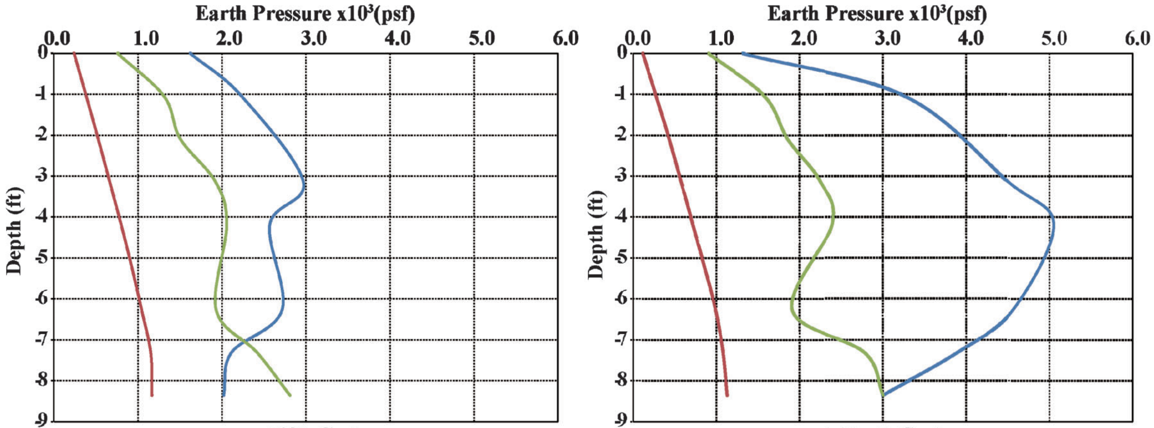

c- Fifth Cycle

d- Tenth Cycle

Figure F.10 Soil Pressure along a vertical section at the acute and obtuse corners, and at the center of the abutment.

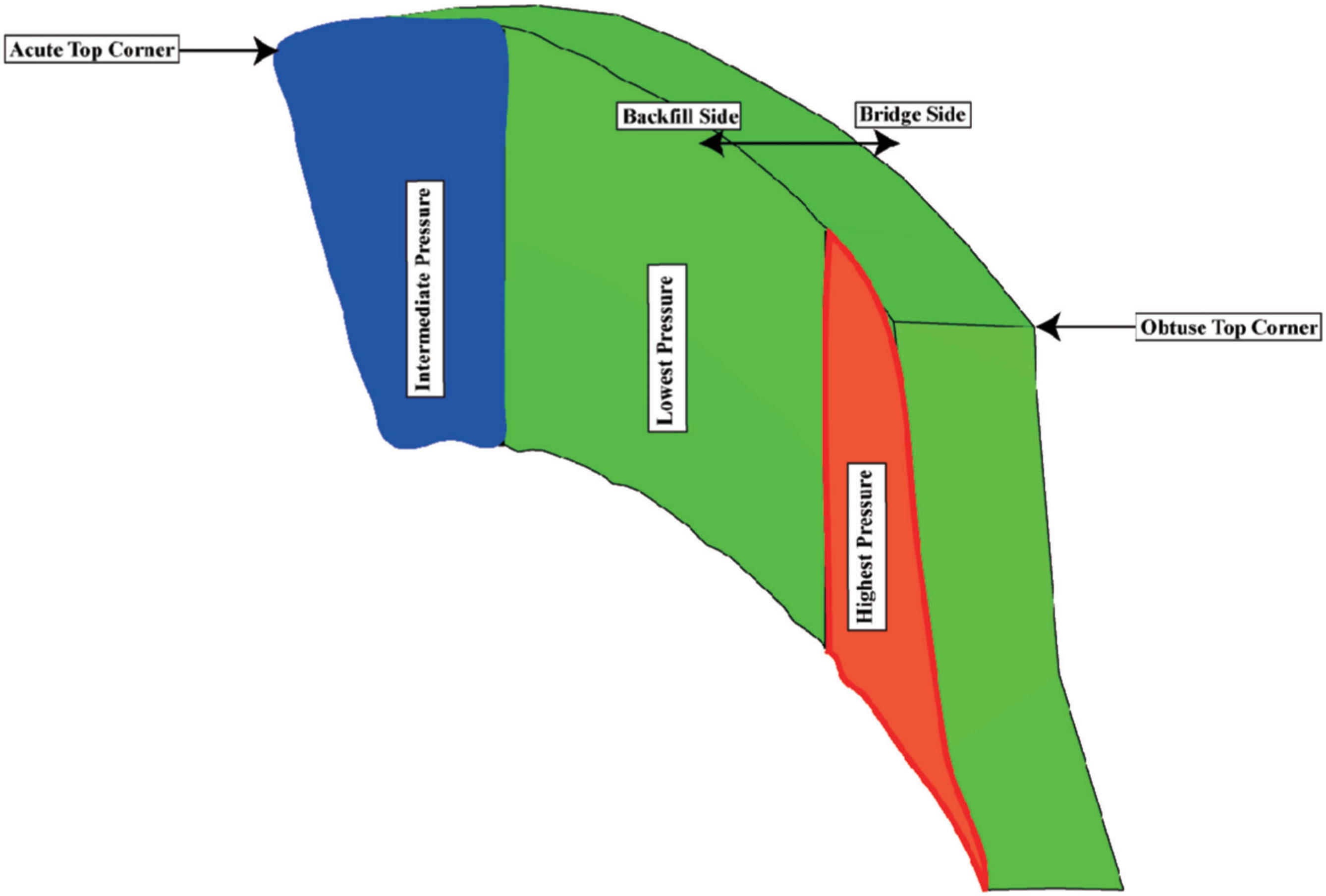

Figure F.11 Deformed shape of the abutment wall during the first expansion cycle.

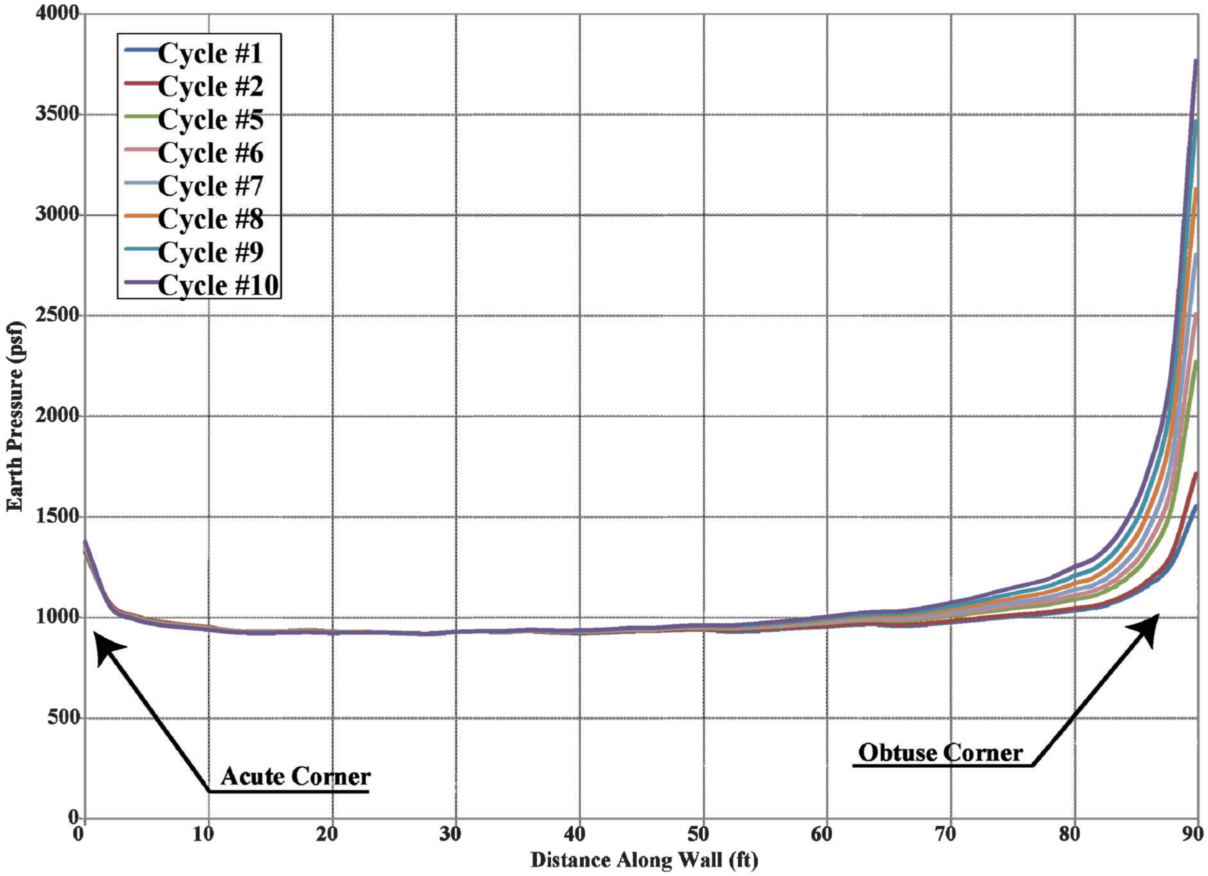

Figure F.12 Earth pressure along the abutment (6.4 ft from top of abutment wall).

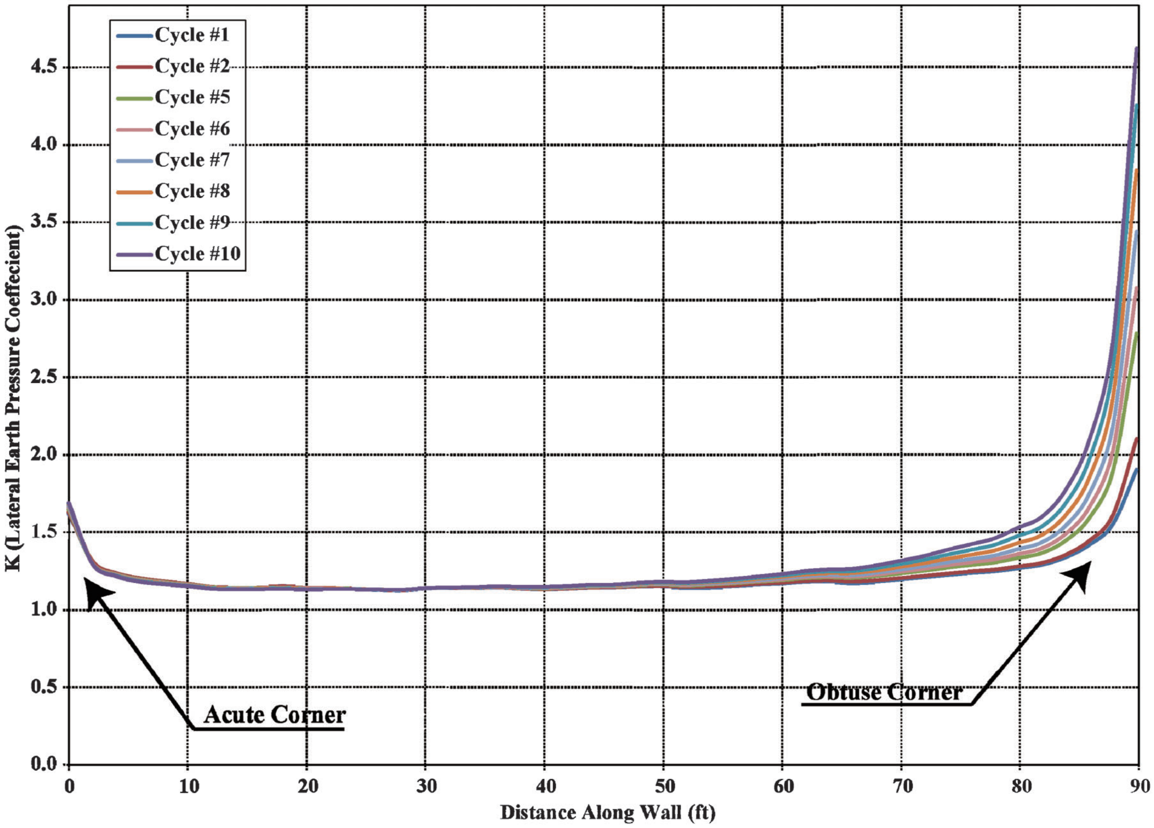

Figure F.13 Earth pressure coefficient along the abutment (6.4 ft from top of abutment wall).

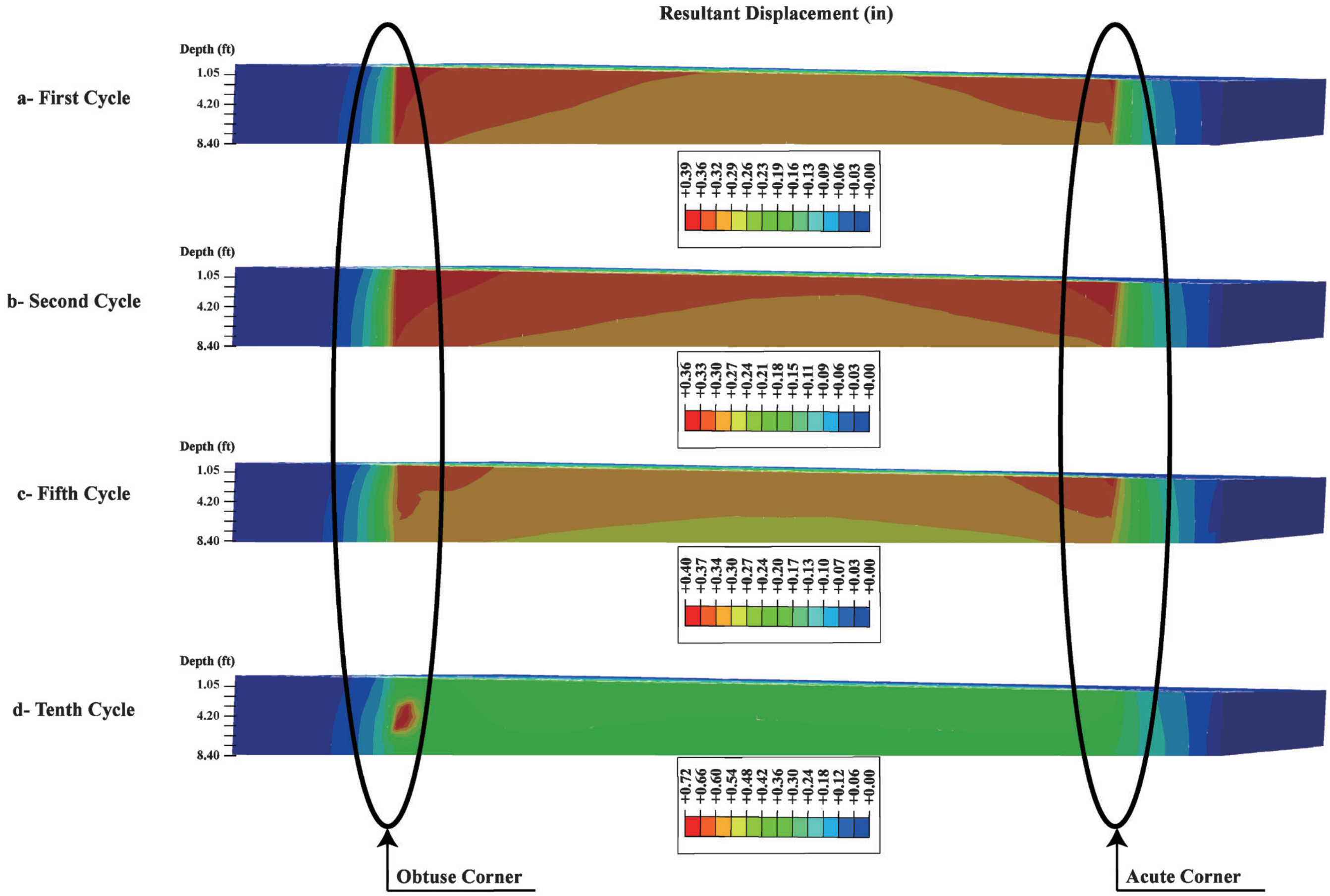

Figure F.14 Resultant displacement distribution on the backfill during expansion.

F.4 ACCEPTABLE IAB PERFORMANCE

Two factors were considered to establish acceptance criteria for the performance of IABs. The first is based on the magnitude of the lateral earth pressure of the backfill soils, and the second is based on the maximum displacement at the top of the piles.

The lateral earth pressure criterion was included given reports from the literature and what was observed from the test of the ¼ scale bridge. The nonuniform lateral soil pressure distribution behind the abutment wall and the escalation of lateral earth pressure with number of cycles (years) were of particular concern. However, the data in Figures F.12 and F.13 show that the lateral earth pressure is almost uniform along the abutment wall with lateral earth pressure coefficients between 1.2 and 2. Therefore, this factor is not considered significant in imposing limits to the geometry of the integral abutment bridge.

The maximum displacement was included considering the potential of damage to the piles. The criterion adopted was based on a comprehensive study conducted by Frosch et al. (2006). The study by Frosch et al. presented results from testing laterally loaded pile-abutment connections. As part of the testing program, three concrete filled tube (CFT) piles were tested under large amplitude and low frequency lateral displacements while maintaining the axial load. The tests were conducted to examine the deterioration of the pile-abutment connection. The pile-abutment connections were tested using a large number of cycles (100 cycles). Frosch et al. concluded that for an 8 in. and 10 in. diameter CFT piles (under 9 ksi vertical stress), the lateral displacement capacity was 1.75 in. and 2 in., respectively. First buckling of the 8 in. and 10 in. diameter CFT piles was observed at 1.5 in. and 1.75 in., respectively.

Most of the piles in integral abutment bridges in Indiana are usually larger than 10 in. diameter (14 in. typically used). Considering the research performed by Frosch et al. (2006) and Frosch, Kreger, & Talbott (2009), it was decided to adopt a 2 in. maximum lateral displacement capacity threshold for acceptable performance (Robert Frosch, personal communication, 2013). Because CFT piles are circular in cross-section (axisymmetric) the resultant of the horizontal displacement (resultant from the longitudinal and transverse displacements) was used for the comparison with the 2 in. allowable displacement. Summary and details of Frosch et al. (2006) testing program is summarized in Chapter 2.

F.5 BRIDGE LENGTH EFFECTS

To investigate the effect of bridge length on the behavior of integral abutment bridge, four different finite element models were analyzed using Abaqus© as discussed in Section F.2. The selected lengths were 200 ft, 500 ft, 1000 ft, and 1500 ft with a 60° skew angle; all the other parameters remained the same. A summary of the analyzed cases is presented in Table F.5.

The resultant horizontal displacement (resultant of displacement in the longitudinal and transverse directions) at the top of the piles is plotted for each of the four cases as a function of the number of cycles (Figure F.15) at the top of the piles at the acute corner, at the center of the abutment, and at the obtuse corner. As anticipated, the displacement demands on the piles increased as

TABLE F.5
Cases for Length Effect

Case #	Length (ft)	Skew (deg)	Foundation Stiffness	Abutment Wall Thickness (ft)	Wing Wall	Shrinkage	Starting Load
1	200	60	Medium	3	No	No	Passive
2	500	60	Medium	3	No	No	Passive
3	1000	60	Medium	3	No	No	Passive
6	1500	60	Medium	3	No	No	Passive

the length of the bridge increased. The displacement was largest at the acute corner, which agrees with the results presented in Section F.3.2 (base case) and observations from the tests on the ¼ scale bridge (Chapter 3). It is also observed that a steady state pile displacement was achieved after the sixth cycle.

Figure F.16 plots the soil pressure behind the abutment for each of the cases analyzed. The results are shown along a vertical cross section at the center of the abutment and for select cycles (1, 2, 5, and 10). A number of observations can be made:

1. As the length of the bridge increased, the lateral earth pressure increased. This behavior is due to the increase of the displacement applied to the abutment wall because of the thermal loading.
2. Lateral earth pressures for all lengths reached approximately the same value after the tenth cycle. This behavior can be attributed to a significant accumulation of plastic strains because a larger number of cycles will cause more rotation of the backbone curve. For the first few cycles, backbone curve rotation causes an increase in the earth pressure (plastic strains are still relatively small) for the same applied displacement. However, with a larger number of cycles, more plastic strains are accumulated resulting in a reduction of the earth pressure for the same applied displacement. A schematic of stress-strain cycles is shown in Figure F.17. During initial loading in the first cycle the stress evolves with increasing strain following the assumed hyperbolic relationship. Upon unloading and reloading, the stress-strain curve follows the relationship and rules explained in Chapter 5. In subsequent cycles, the backbone curve rotates to allow the increase in stress with number of cycles, but the rotation is a function of the plastic strain ε_{pi} (cycle i in Figure F.17). For a larger number of cycles, more plastic strains are accumulated (ε_{pn}) and more rotation of the backbone curve is achieved; however, the larger plastic strains result in shifting the stress-strain cycle in the opposite direction of loading which results in a net reduction of the developed earth pressure, as indicated in Figure F.17 for the nth cycle. It should be noted that this schematic was prepared using actual test results from the laboratory scale tests presented in Chapter 4. The actual cycles were used from the test results, but the backbone rotation and cycles shifting have been exaggerated for clarity.
3. Longer bridges tend to have a larger gradient of stresses towards the bottom of the abutment. This behavior occurs because of the additional resistance to deformation provided by the piles. As increased deformation demands on the piles are imposed by longer bridges, the pile-soil system provides

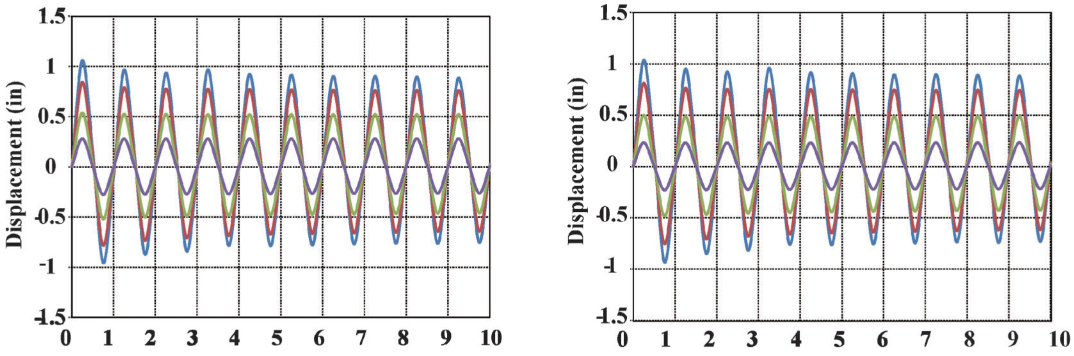

a- Acute Corner

b- Bridge Centerline

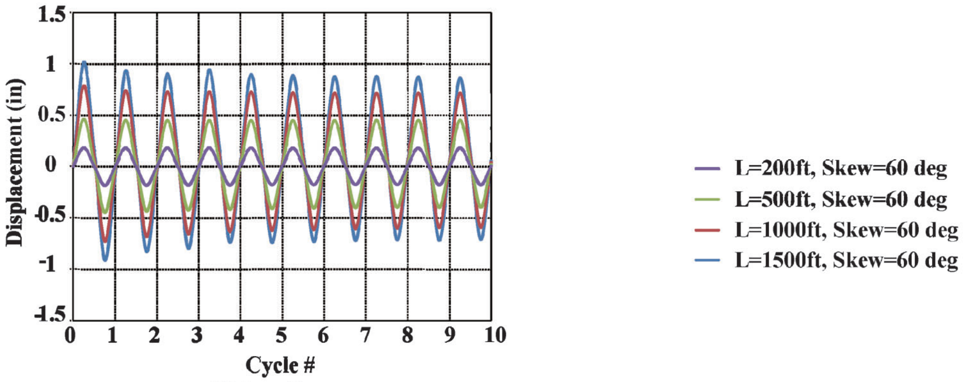

c- Obtuse Corner

Figure F.15 Effect of bridge length—displacement at top of the pile as a function of the number of cycles.

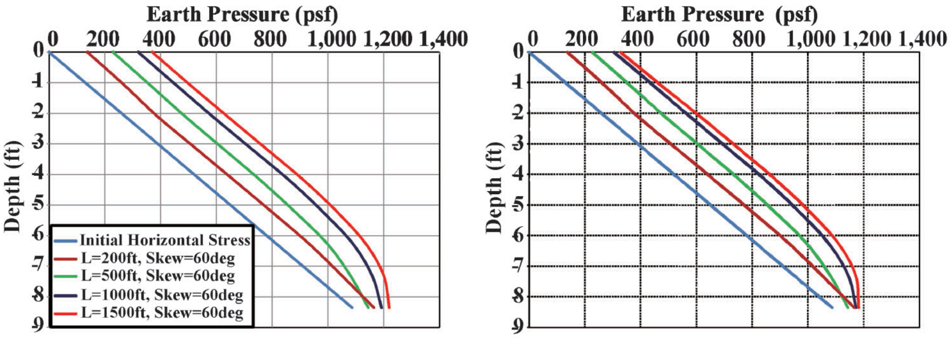

a- First Cycle

b- Second Cycle

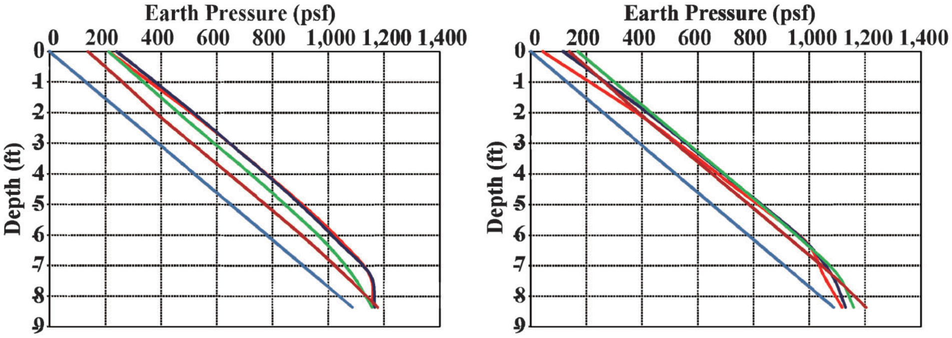

c- Fifth Cycle

d- Tenth Cycle

Figure F.16 Effect of bridge length—soil pressure along a vertical section at the center of the abutment.

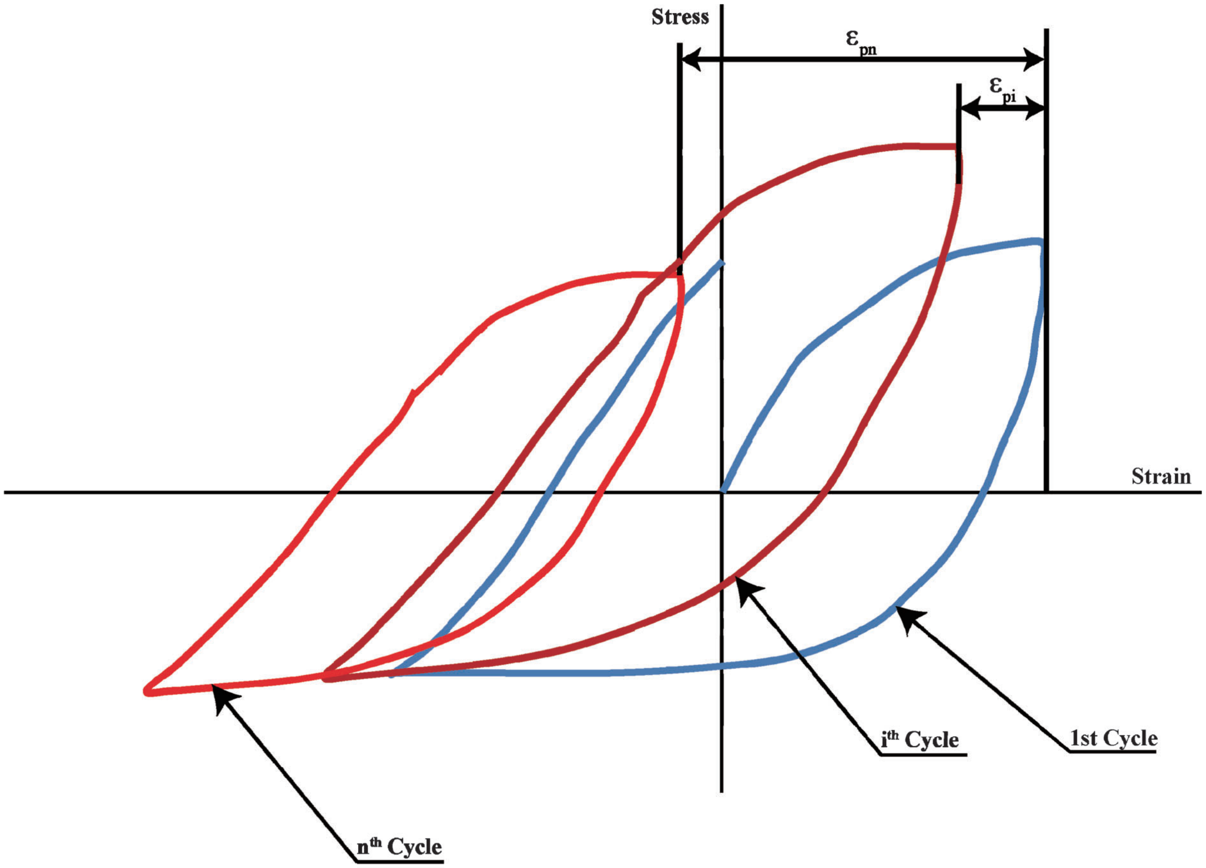

Figure F.17 Backbone curve rotation with cycles of loading.

TABLE F.6
Cases for Skew Angle

Case #	Length (ft)	Skew (deg)	Foundation Stiffness	Abutment Wall Thickness (ft)	Wing Wall	Shrinkage	Starting Load
3	1000	60	Medium	3	No	No	Passive
4	1000	30	Medium	3	No	No	Passive
5	1000	45	Medium	3	No	No	Passive

more resistance to deformation (higher pressure developed by the soil around the pile).

F.6 BRIDGE SKEW ANGLE EFFECTS

To investigate the effect of the bridge skew angle on the behavior of the integral abutment bridge, three different finite element models were analyzed using Abaqus© as discussed in Section F.2. The selected skew angles were 30°, 45°, and 60° with a 1000-ft long bridge; all the other parameters remained the same. A summary of the analyzed cases is presented in Table F.6.

The resultant horizontal displacements at the top of the piles at the acute corner, obtuse corner, and at the center of the abutment are plotted in Figure F.18. The results are similar, which is somewhat expected given the cross section of the piles and the constant length of the bridge.

Figure F.18 shows that displacements are largest at the acute corner, which agrees with the discussion of the abutment movement in Section F.3.1 (base case) and observations from the tests on the ¼ scale bridge (Chapter 3). It is also observed that a steady-state for pile displacements was achieved after the sixth cycle for all skew angles.

The soil pressures behind the abutment are shown in Figure F.19 for Cycles 1, 2, 5, and 10 on a vertical section through the center of the abutment. It can be observed that as the skew angle increased, the lateral earth pressure decreased. For the same bridge length, the thermal demand is the same. However, as discussed in Section F.3.1, the skew of the bridge is associated with transverse displacements and a rotation of the bridge deck in addition to the longitudinal displacements. As the skew angle increases, and for the same bridge expansion, larger transverse displacements are induced, which in turn results in larger rotations. As the transverse and rotation rigid body movements increase, a smaller portion of the thermal expansion is transferred to the longitudinal displacements and thus a smaller lateral earth pressure occurs. To evaluate the hypothesis of a smaller longitudinal displacement applied to the backfill soil with a lager skew angle, plots of the longitudinal displacement distribution on backfill for the first expansion cycle for the three skew angles are presented in Figure F.20.

It can be seen from Figure F.20 that the abutment wall of the 60° skewed bridge transferred the lowest longitudinal displacements at all locations in the backfill. On the other hand, the abutment wall of the 30° skewed bridge transferred the largest longitudinal displacements. The longitudinal displacement distribution along the backfill also shows largest longitudinal displacement at the obtuse corner which decreases gradually towards the acute corner and then increases slightly at the acute corner (note the distribution at the corners). This longitudinal displacement distribution results in the largest earth pressures at the obtuse corner which decrease towards the acute corner and then increase slightly at the acute corner. The longitudinal displacement for the 60° skew angle case (which is the same as the base case discussed in Section F.3.2), showed the smallest displacement gradients along the backfill (except at the corners),

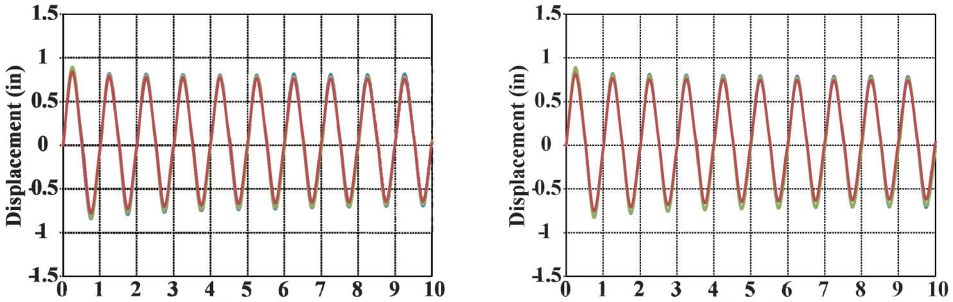

a- Acute Corner

b- Bridge Centerline

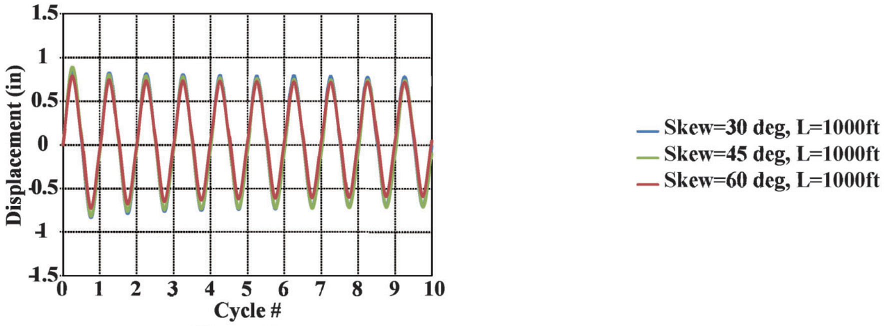

c- Obtuse Corner

Figure F.18 Effect of skew angle—displacement at the top of the piles.

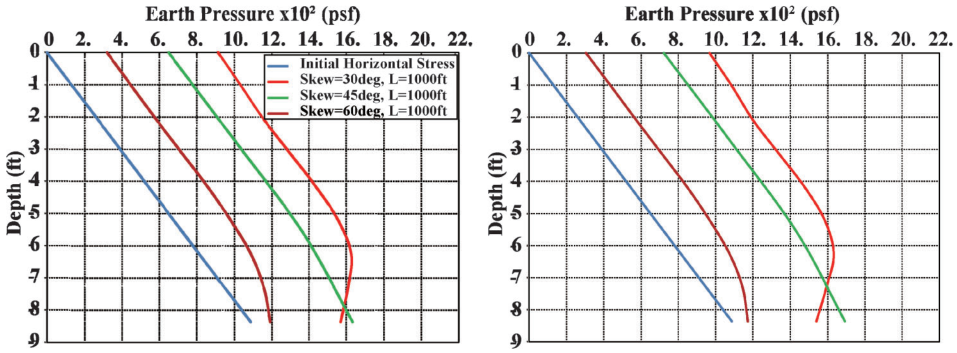

a- First Cycle

b- Second Cycle

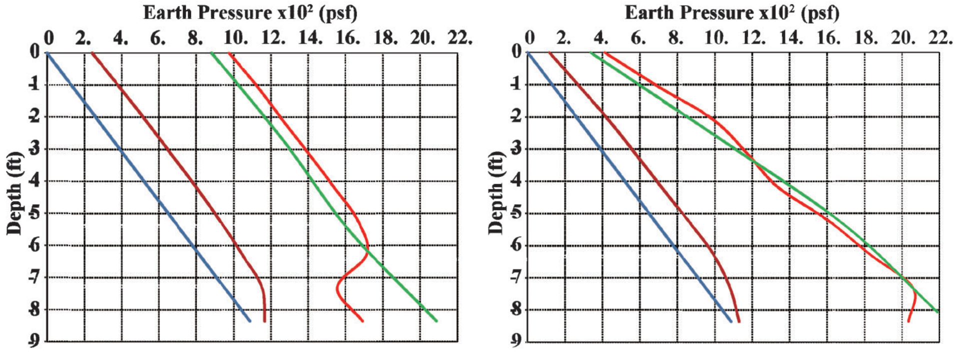

c- Fifth Cycle

d- Tenth Cycle

Figure F.19 Effect of skew angle—soil pressure along a vertical section at the center of the abutment.

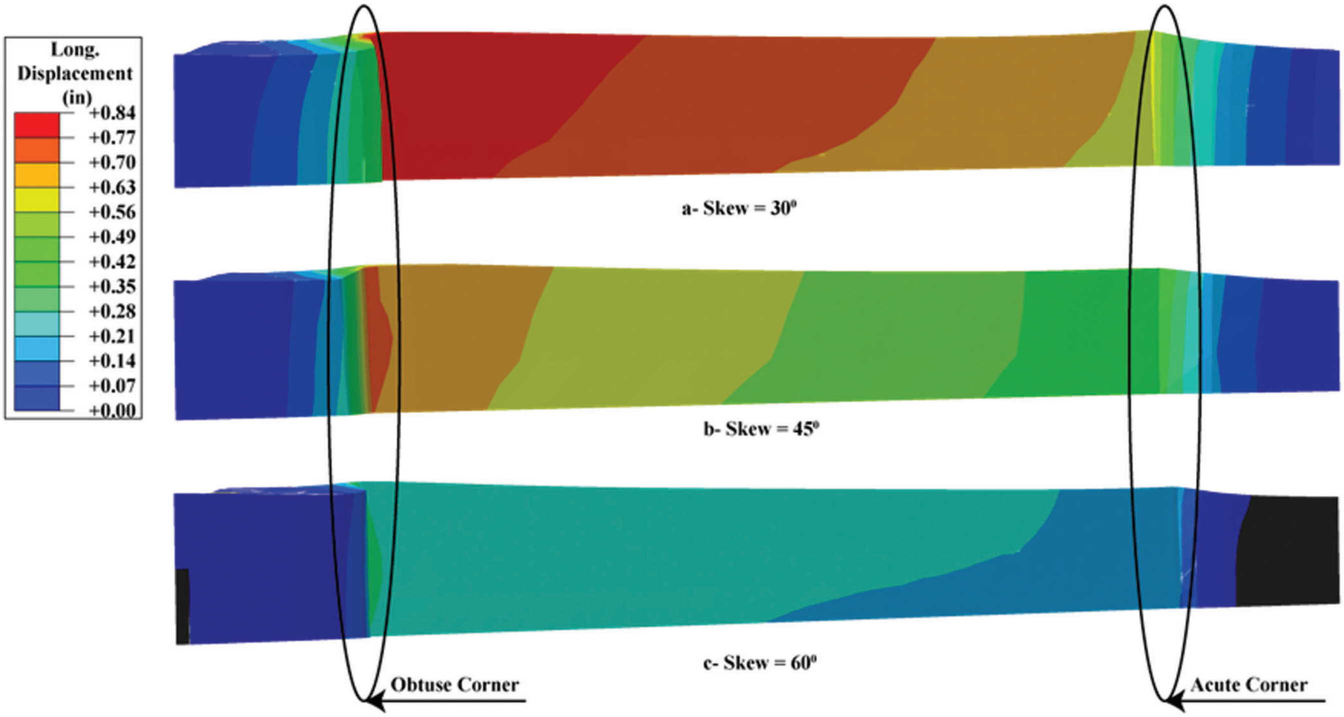

Figure F.20 Longitudinal displacement distribution on the backfill during the first expansion cycle.

which results in a relatively uniform earth pressure in the area between the corners, and agrees with the lateral earth pressure distribution presented in Figure F.12.

F.7 FOUNDATION STIFFNESS EFFECTS

To investigate the effect of the foundation stiffness on behavior six different cases were analyzed using Abaqus© as discussed in Section F.2. The small strain shear stiffness of the foundation was 425 ksf, 850 ksf, and 1700 ksf to simulate soft, typical (base case), and stiff soils. To examine the significance of the foundation stiffness as a function of length, two bridge lengths were used in the analysis: 200 and 1000 ft. All the other parameters remained the same. A summary of the analyzed cases is presented in Table F.7.

The pile displacements are presented in Figures F.21 and F.22. Figure F.21 presents the results of the displacements at the top of the piles at the corners and at the center of the abutment for the 1000 ft long bridge while Figure F.22 contains similar plots for the 200 ft bridge. As anticipated, with a softer foundation, the displacement demand on the piles increased because for a softer soil, there is less resistance to deformation of the piles. Because the other parameters in the soil model remained the same, a smaller initial small-strain modulus resulted in smaller pressures in the soil acting on the piles for the same displacement demand.

As observed in Figures F.21 and F.22, the increase in the displacement demand of the piles with the softer foundation is larger for the longer bridge.

The soil pressure on the abutment is presented in Figure F.23 for the 1000 ft bridge and in Figure F.24 for the 200 ft long bridge. Results are shown for Cycles 1, 2, 5 and 10 and for the pressure distribution along a vertical section across the center of the abutment. As shown, the effect of the foundation soil stiffness is small for early cycles. For the 1000 ft long bridge, at cycle 10, the pressures decreased as the soil stiffness decreased. The differences in pressures for the shorter bridge are negligible.

F.8 ABUTMENT WALL STIFFNESS EFFECT

To investigate the effect of wall stiffness on behavior, three different cases were analyzed with Abaqus© as discussed in Section F.2. The selected wall thicknesses were 2-ft, 3-ft, and 4-ft, which are within the range of practical dimensions. All the other parameters remained the same. A summary of the analyzed cases is presented in Table F.8. Wall thicknesses less than 2 ft were not analyzed because it does not provide area required to accommodate a 14 in. pile diameter.

The resultant horizontal displacement at the top of the piles is plotted for the three cases as a function of the number of cycles in Figure F.25 for the top of the piles at the acute corner, centerline of the abutment and at the obtuse corner. It is observed that there was no effect of the abutment wall thickness on the response of piles.

The pressures behind the backfill are plotted in Figure F.26 for Cycles 1, 2, 5, and 10. As shown, all cases produced similar pressure distributions along the wall, except at the base of the wall. The wall with the smallest stiffness (2 ft thick wall) showed the lowest pressure at its base. It is hypothesized that this is the result of a larger rotation of the wall that results in an unloading at its base. To evaluate this hypothesis, the deformed shape of the abutment walls for the three cases is presented in Figure F.27.

Because of the smaller resistance to bending provided by the 2 ft thick wall, the relative longitudinal displacement between the base and top of the wall is much larger than for the thicker walls as shown in Figure F.27. The softer wall bends more than the stiffer walls and imposes reduced displacement demands on the piles. As the displacement demands reduce, the soil pressures at the bottom of the wall also reduce. While wall stiffness may be considered as the most significant factor, there are other factors that affect the pressure distribution with depth such as the accumulation of plastic strains in the backfill soil, interaction between the soil and the structure, rigid body movements of the bridge, etc. These factors may play a role and influence the soil pressure distributions at large cycles.

TABLE F.7
Cases for the Foundation Stiffness Effect

Case #	Length (ft)	Skew (deg)	Foundation Stiffness	Abutment Wall Thickness (ft)	Wing Wall	Shrinkage	Starting Load
1	200	60	Medium	3	No	No	Passive
3	1000	60	Medium	3	No	No	Passive
7	1000	60	Soft	3	No	No	Passive
8	1000	60	Stiff	3	No	No	Passive
11	200	60	Soft	3	No	No	Passive
12	200	60	Stiff	3	No	No	Passive

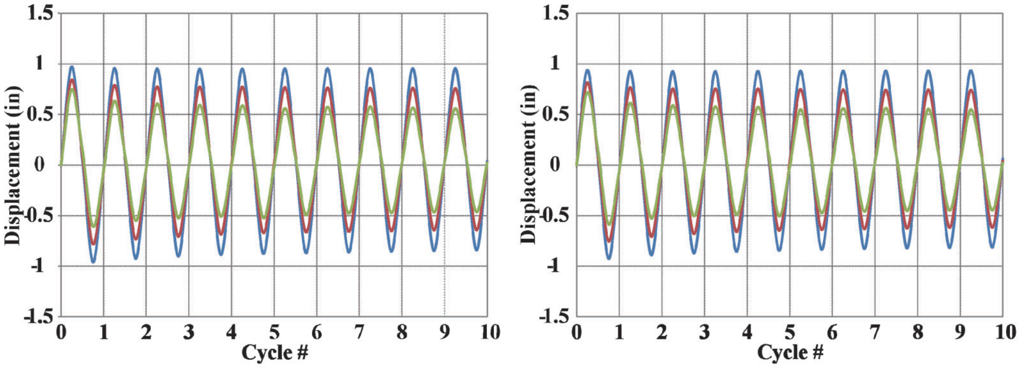

a- Acute Corner b- Bridge Centerline

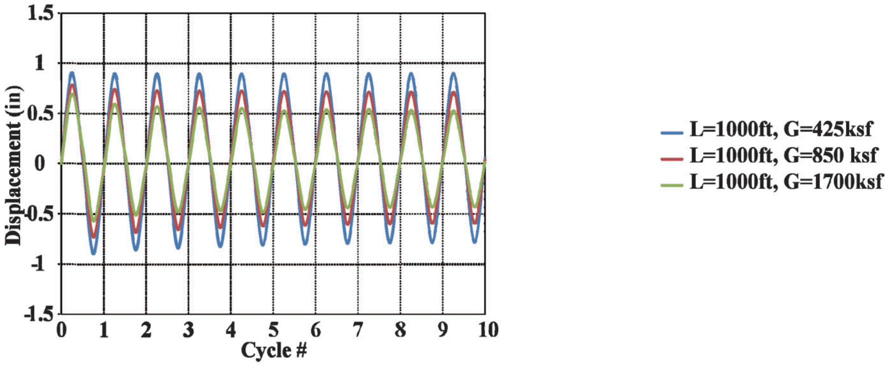

c- Obtuse Corner

Figure F.21 Effect of soil foundation stiffness—displacement at top of the pile—1000 ft long bridge.

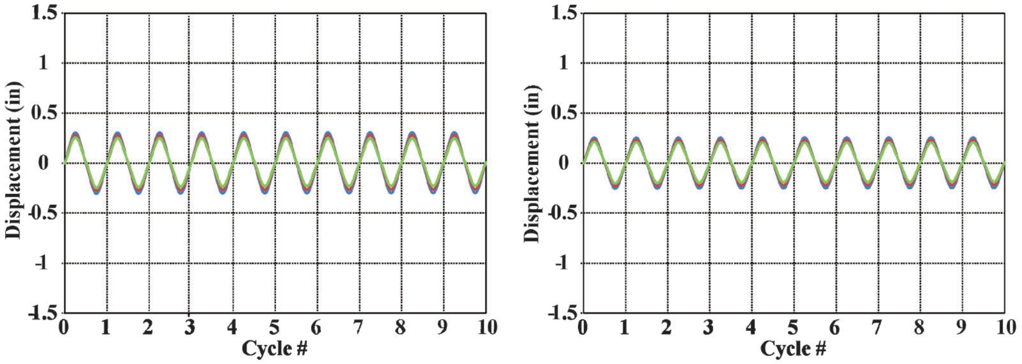

a- Acute Corner b- Bridge Centerline

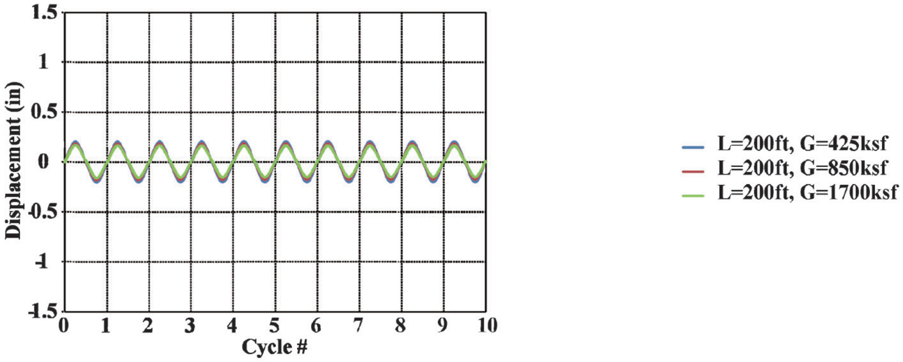

c- Obtuse Corner

Figure F.22 Effect of soil foundation stiffness—displacement at top of the pile—200 ft long bridge.

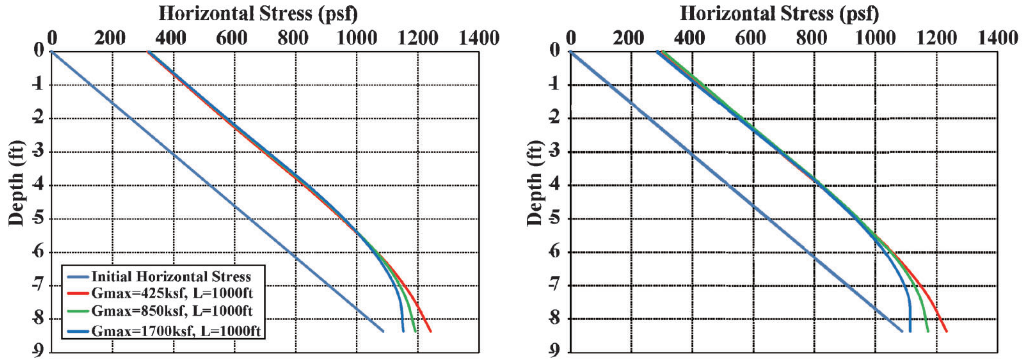

a- First Cycle b- Second Cycle

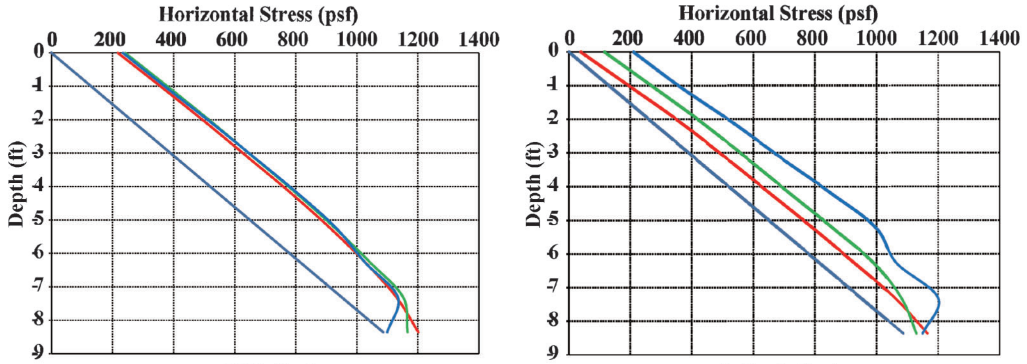

c- Fifth Cycle d- Tenth Cycle

Figure F.23 Effect of foundation soil stiffness—soil pressure along a vertical section at the center of the abutment—1000 ft bridge.

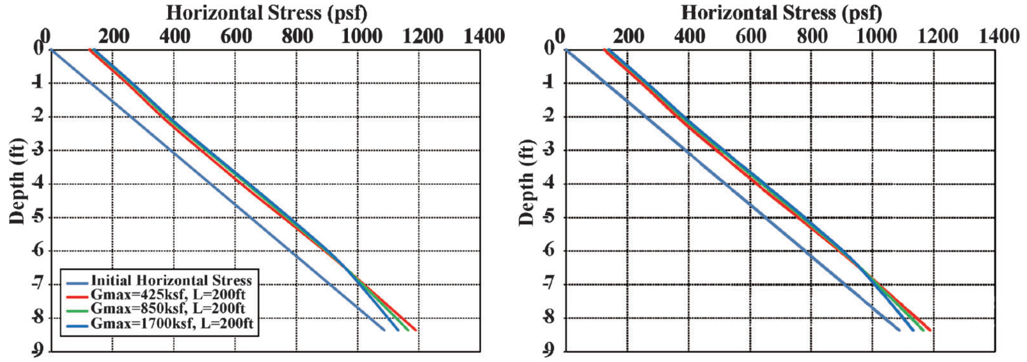

a- First Cycle b- Second Cycle

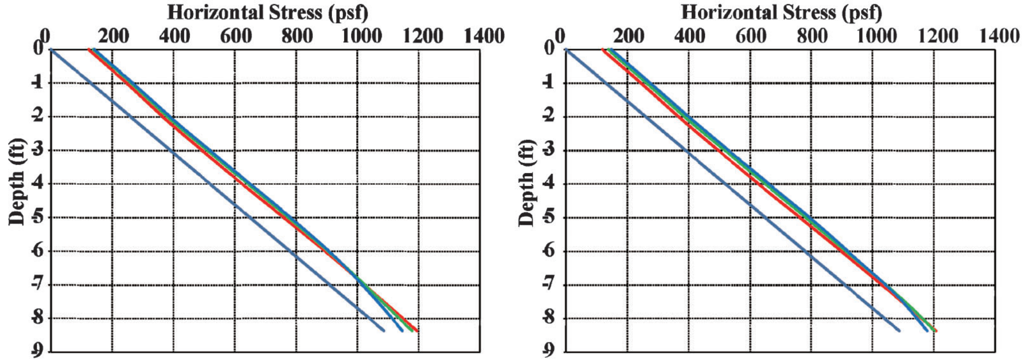

c- Fifth Cycle d- Tenth Cycle

Figure F.24 Effect of foundation soil stiffness—soil pressure along a vertical section at the center of the abutment—200 ft bridge.

TABLE F.8
Cases for Abutment Wall Stiffness

Case #	Length (ft)	Skew (deg)	Foundation Stiffness	Abutment Wall Thickness (ft)	Wing Wall	Shrinkage	Starting Load
3	1000	60	Medium	3	No	No	Passive
13	1000	60	Medium	2	No	No	Passive
14	1000	60	Medium	4	No	No	Passive

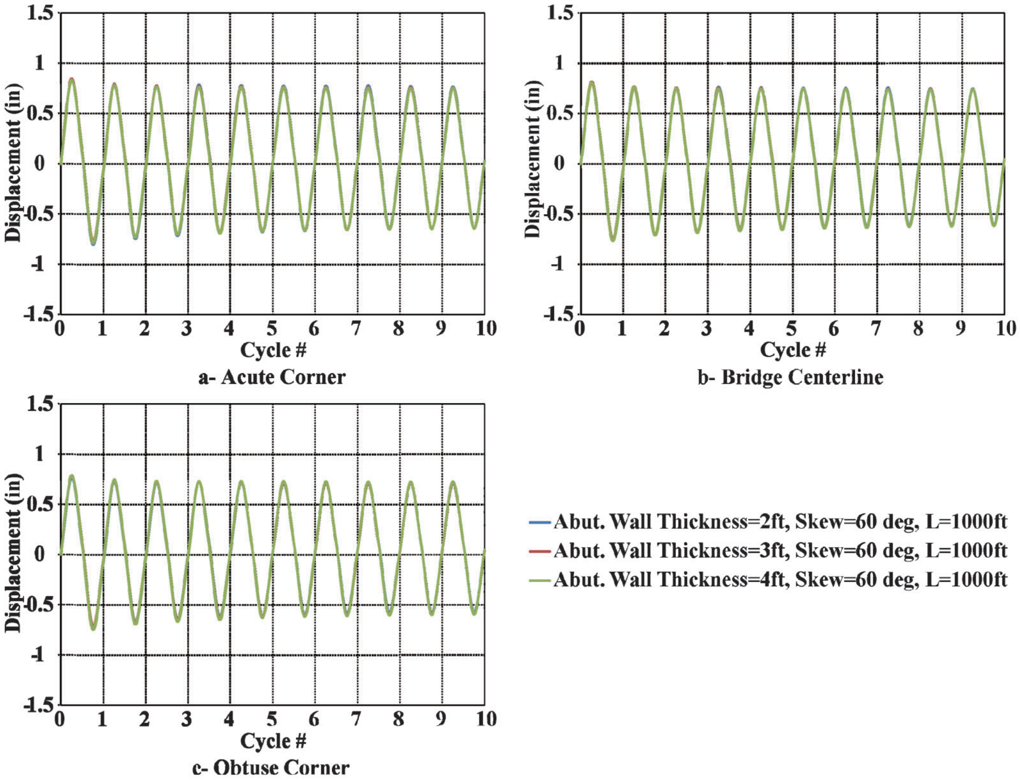

Figure F.25 Effect of abutment wall thickness—displacement at top of the pile as a function of the number of cycles.

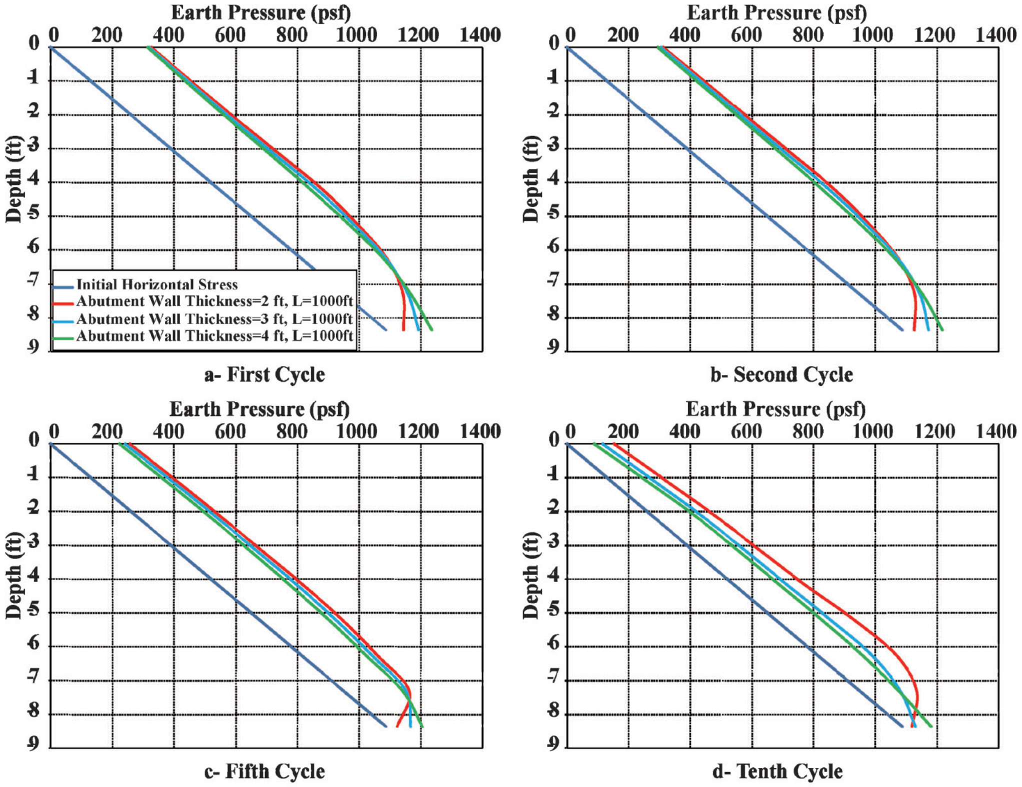

Figure F.26 Effect of abutment wall thickness—soil pressure along a vertical section at the center of the abutment.

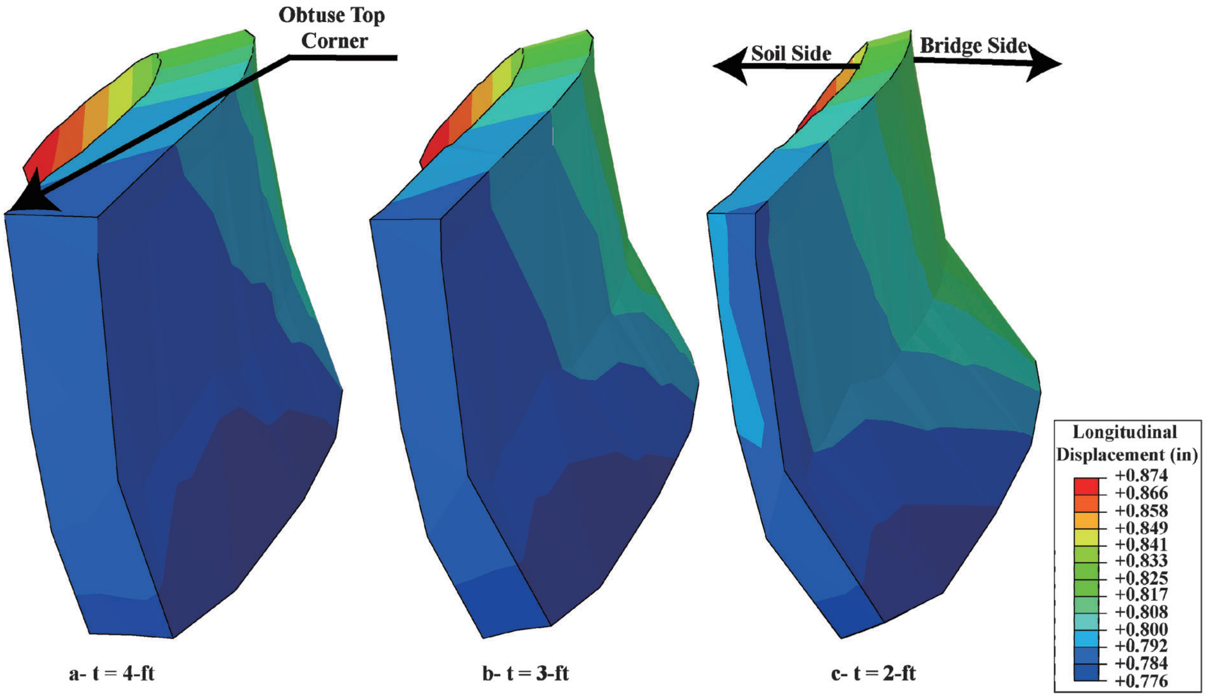

Figure F.27 Deformed shape of abutment wall.

F.9 WING WALL EFFECTS

To investigate the effect of wing walls on behavior, two different cases were analyzed: one with wing walls and the other without. One wall was placed at each end of the abutment in the direction of bridge axis, with a tie connection (moment connection) to the abutment wall. The wall dimensions were 42 ft long, 8 ft high and 1.5 ft thick. The wing walls were modeled as linear elastic with the same properties as the abutment wall. Figure F.28 shows a general view of the wing wall configuration in the model and the associated contact properties. A summary of the analyzed cases is presented in Table F.9.

Figure F.29 presents the displacements at the top of the piles at the acute corner, centerline of the abutment, and the obtuse corner. The displacements were obtained for two cases: with and without a wing wall. The results from the analysis show that the presence of the wing wall has no effect on the piles.

Figure F.30 shows the soil pressure distribution with depth behind the abutment wall for a vertical cross section through the center of the wall and for Cycles 1, 2, 5, and 10. The lateral earth pressure for the case with wing wall was higher than without the wing wall. This behavior occurs due to the additional confinement provided by the wing wall (relative rigid when compared to the backfill soil). As the soil tends to deform towards the wing wall, additional pressure is applied to the soil, which increases confinement to the soil and thus increase the pressure on the abutment. To verify the larger confinement, a plot of the effective mean stress is shown in Figure F.31.

Figure F.31 shows that the mean effective stress (pressure) is larger for the case including the wing wall. The differences are small, but justify the small increase in pressures shown in Figure F.30. As the mean effective stress increases, the stiffness of the soil increases. Therefore, the pressures from the soil should be larger for similar imposed displacements. The differences between the two cases presented in Figure F.30 increase with the number of cycles and become significant at the 10th cycle.

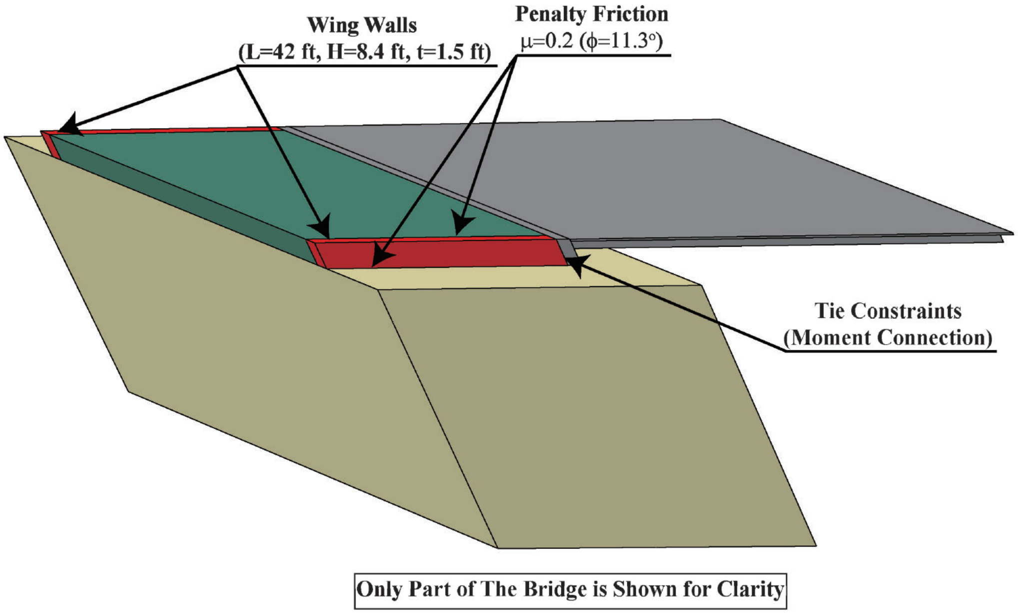

Figure F.28 General view of the wing walls and contact properties.

TABLE F.9
Cases for the Wing Wall Effect

Case #	Length (ft)	Skew (degree (°))	Foundation Stiffness	Abutment Wall Thickness (ft)	Wing Wall	Shrinkage	Starting Load
3	1000	60	Medium	3	No	No	Passive
9	1000	60	Medium	3	Yes	No	Passive

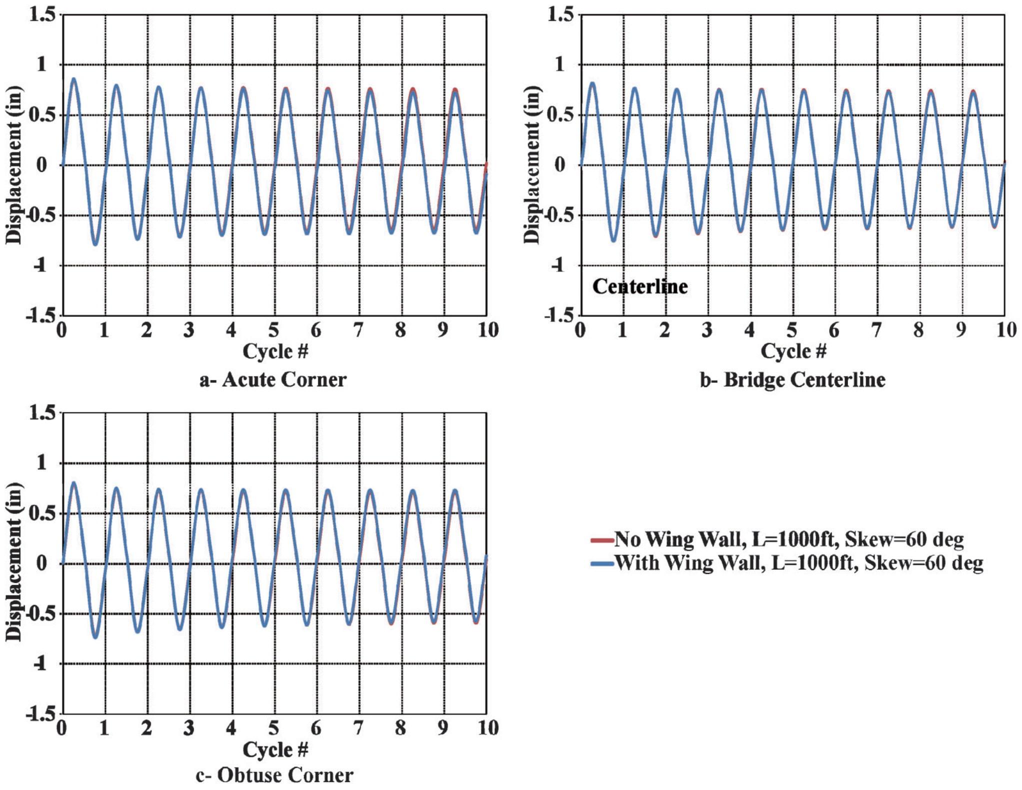

a- Acute Corner

b- Bridge Centerline

c- Obtuse Corner

Figure F.29 Wing wall effect—displacement at top of the pile as a function of the number of cycles.

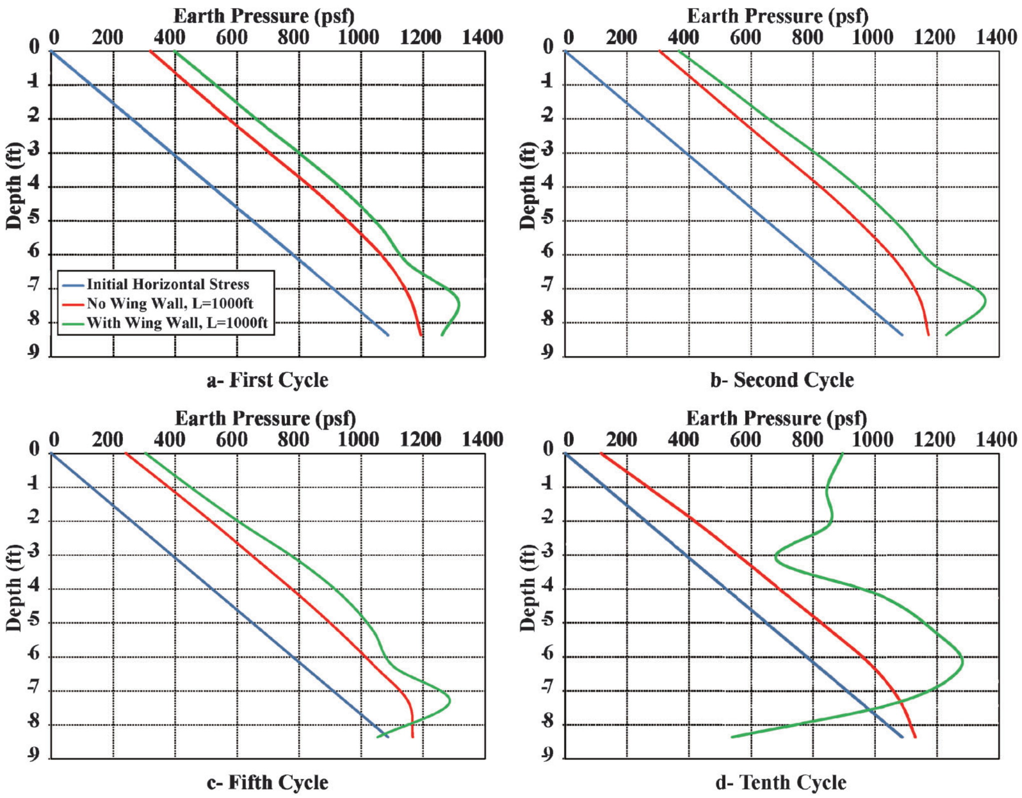

a- First Cycle

b- Second Cycle

c- Fifth Cycle

d- Tenth Cycle

Figure F.30 Effect of wing wall—soil pressure along a vertical section at the center of the abutment.

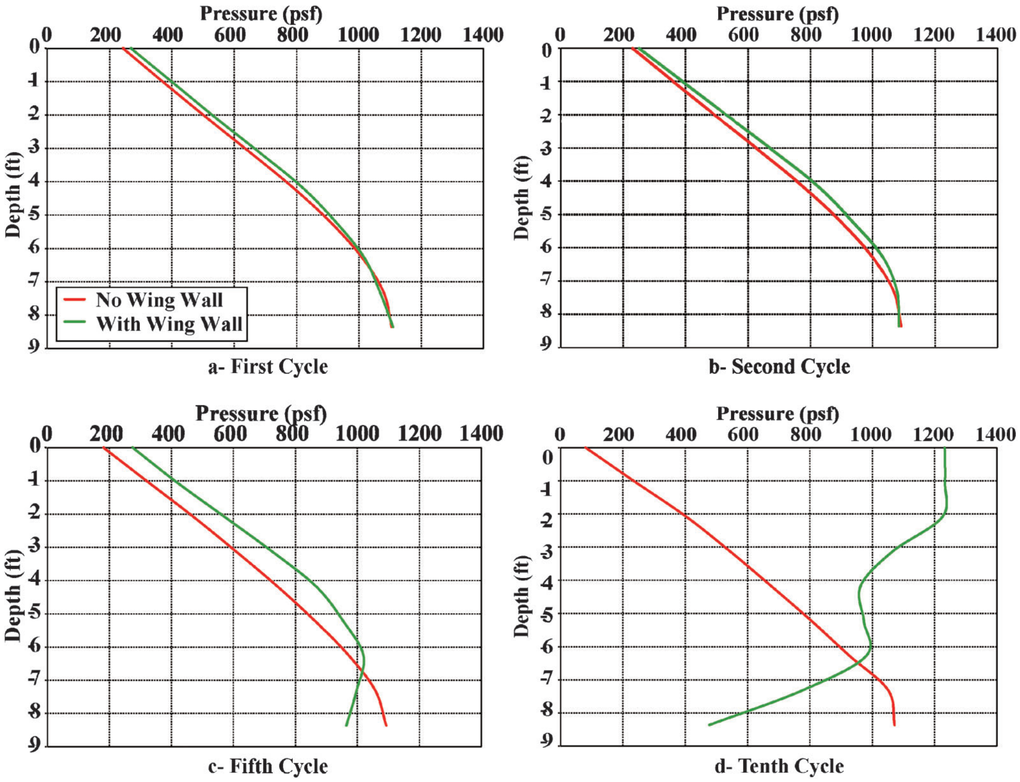

Figure F.31 Effective mean stress (pressure) along a vertical section at the center of the abutment.

F.10 SHRINKAGE AND LOADING SEQUENCE EFFECTS

To investigate the effect of concrete shrinkage with time and loading sequence (starting with contraction), six cases were analyzed. One case included shrinkage, starting with contraction (active loading) to allow comparison with the base case (without shrinkage but starting with expansion (passive loading)). The other four cases were analyzed to examine the influence of bridge length and skew angle considering shrinkage and loading sequence. A summary of the analyzed cases is presented in Table F.10.

Frosch and Lovell (2011) used the concrete properties of one of the integral abutment bridges (US 231 in Indiana), with the concrete mix design parameters (water cement ratio and compressive strength) along with the environmental conditions and length of curing, to calculate shrinkage strains based on the CEB MC90 Model. In the present study, the calculated shrinkage strains by Frosch and Lovell (2011) were adopted and are shown in Figure F.32 as a function of time.

Shrinkage was imposed to the bridge deck as thermal loading to provide the volumetric expansion without the generation of unwanted stresses. The change of temperature that will generate the shrinkage strain was calculated based on the following equation:

$$\Delta T = \frac{\Delta L}{L}\frac{1}{\alpha} \tag{F.1}$$

Where,

$$\frac{\Delta L}{L} = \textit{the shrinkage strain based on figure } F.32$$

α=coefficient of thermal expansion for concrete, 5.5×10^{-6}, 1/°F

TABLE F.10
Cases for Shrinkage and Loading Sequence

Case #	Length (ft)	Skew (deg)	Foundation Stiffness	Abutment Wall Thickness (ft)	Wing Wall	Shrinkage	Starting Load
3	1000	60	Medium	3	No	No	Passive
10	1000	60	Medium	3	No	Yes	Active
15	200	60	Medium	3	No	Yes	Active
16	500	60	Medium	3	No	Yes	Active
17	1000	30	Medium	3	No	Yes	Active
18	1000	45	Medium	3	No	Yes	Active

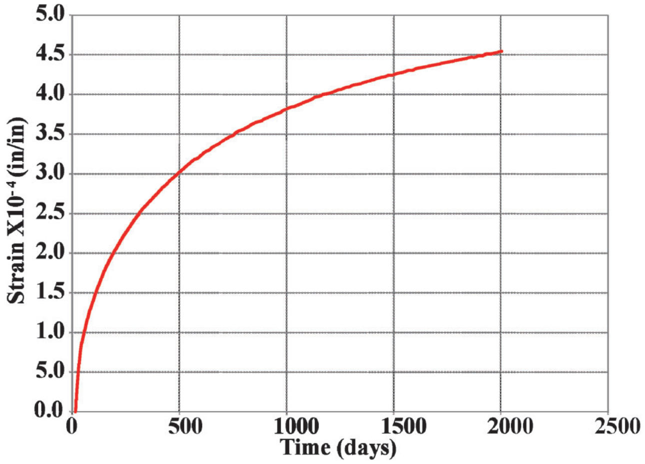

Figure F.32 Shrinkage strains (after Frosch and Lovell (2011)).

The "equivalent temperature" (temperature decrease to simulate shrinkage) was added to the yearly temperature cycle. The final temperature is shown in Figure F.33 that presents cycles of amplitude ±50°F with decreasing average to simulate shrinkage.

F.10.1 Comparison with the Base Case

The resultant horizontal displacement at the top of the piles is plotted in Figure F.34 for the acute corner, center of abutment, and obtuse corner. As shown, shrinkage results in larger displacement demands on the piles during contraction and smaller displacement demand during expansion. The deformation of the piles reach a steady-state after approximately 5.5 years (2,000 days) which coincides with the tapering off of the shrinkage deformations (Figure F.32).

The pressure distribution behind the abutment was computed for different cycles, (Cycles 1, 2, 5, and 10). Figure F.35 plots of the results for the two cases, along a vertical section through the center of the abutment. It should be noted that the pressures presented in Figure F.35 were obtained at the point of maximum expansion for the cycle. Note that in Figure F.34, maximum expansion does not occur at the same time for the two cases analyzed. Table F.11 shows the time of year at which the earth pressures are plotted.

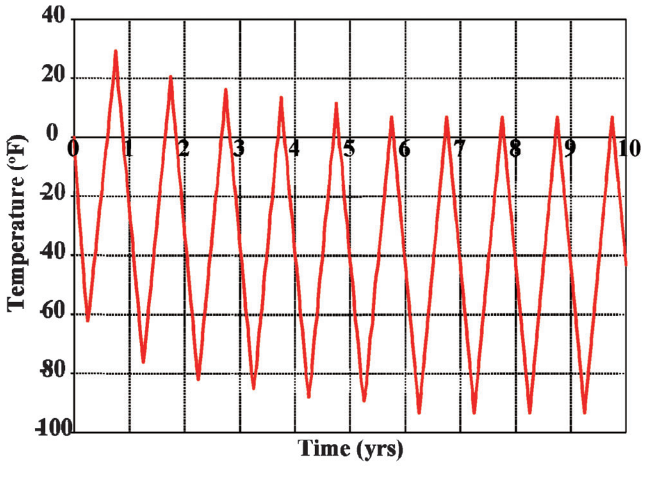

Figure F.33 Thermal load time history to include shrinkage with initial contraction.

Figure F.35 shows that the pressures for the case with shrinkage tend to be larger on the top two 2 ft of the abutment and lower below this dimension as compared with the base case. To investigate this behavior, the displacement of the backfill soil adjacent to the abutment is plotted relative to the abutment wall in Figure F.36.

Figure F.36 plots the positions of the soil and abutment during the first cycle (Case 11) at maximum expansion and at maximum contraction. During contraction, the soil detaches from the abutment between a depth of 2 ft and 6 ft. During expansion, the backfill soil and the abutment wall are attached. Detachment of the soil (loss of confinement) induces large unloading and thus large plastic deformations in the soil. This behavior is reflected during the expansion in Figure F.35a where significant stress gradients are observed between depths of 2 and 6 ft. A similar phenomenon occurs during the contraction phase in subsequent cycles that are associated with the unloading observed in Figure F.36 at depths below 2 ft. Figure F.37 is a plot of the side of the abutment in contact with the backfill depicting the areas where the soil detaches from the abutment during contraction. As evident, detachment is produced in all cycles, but stabilizes after cycles 5 or 6 considering the loading of Figure F.33.

F.10.2 Effect of Bridge Length

The resultant horizontal displacement at the top of the piles is plotted in Figure F.38 for the acute corner, center of abutment, and obtuse corner. Different bridge lengths (Cases 10, 15 and 16) were considered. Similar to the observation made in Section F.10.1, shrinkage results in larger displacement demands on the piles during contraction and smaller displacement demands during expansion.

Due to the detachment between backfill and abutment wall, as discussed in Section F.10.1, earth pressures were not plotted for these cases.

F.10.3 Effect of Skew Angles

The resultant horizontal displacement at the top of the piles is plotted in Figure F.39 for the acute corner, center of abutment, and obtuse corner. Different skew angles (Cases 10, 17, and 18) were considered. Similar to the observation made in Section F.10.1, shrinkage results in larger displacement demands on the piles during contraction and smaller displacement demands during expansion. Similar to the discussion in Section F.6, the resultant horizontal displacements at the top of the piles at the acute and obtuse corners as well as at the center of the abutment are similar, which is somewhat expected given the cross section of the piles and the constant length of the bridge in all the cases.

F.10.4 Thermal Loading Oscillates between 0°F and −75°F

Two cases were analyzed with thermal time history oscillating between 0°F and −75°F to reflect end of construction by the end of summer, concrete shrinkage effect was included in the analysis. The resulting temperature time history is shown in Figure F.40.

The resultant horizontal displacement at the top of the piles is plotted in Figure F.41 for the acute and obtuse corners. Two bridge lengths (Cases 19 and 20) were considered. Similar to the observation made in Section F.10.1, shrinkage results in larger displacement demands on the piles during contraction and smaller displacement demands during expansion.

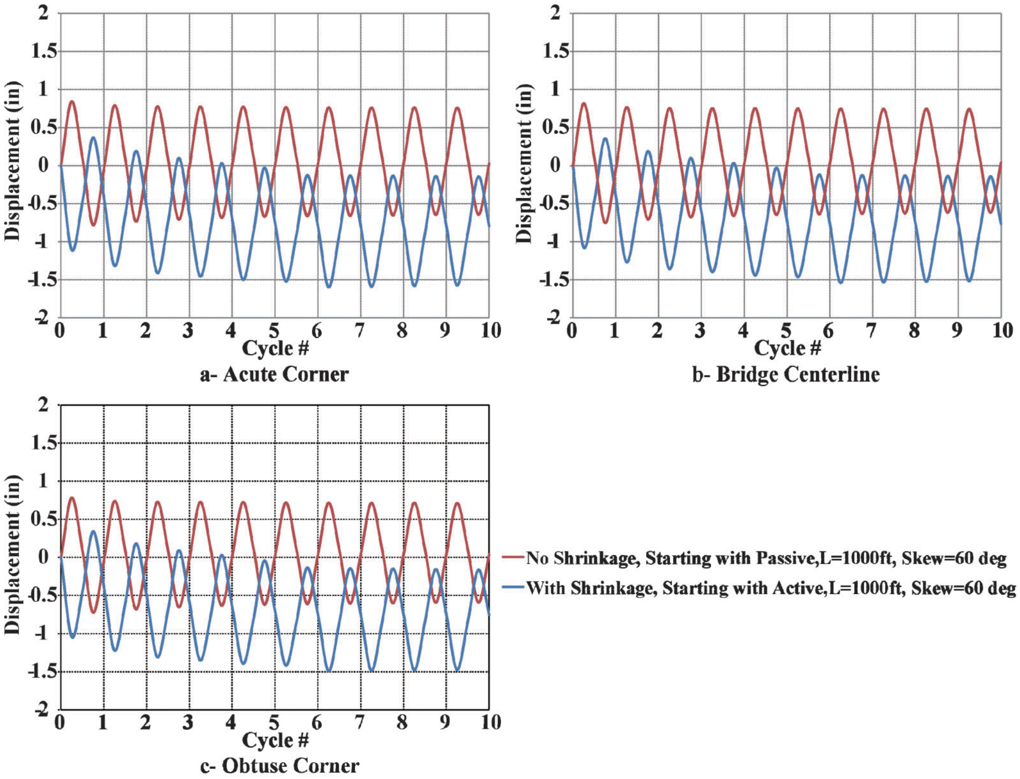

a- Acute Corner

b- Bridge Centerline

c- Obtuse Corner

Figure F.34 Shrinkage and load history—displacement at top of the pile as a function of the number of cycles.

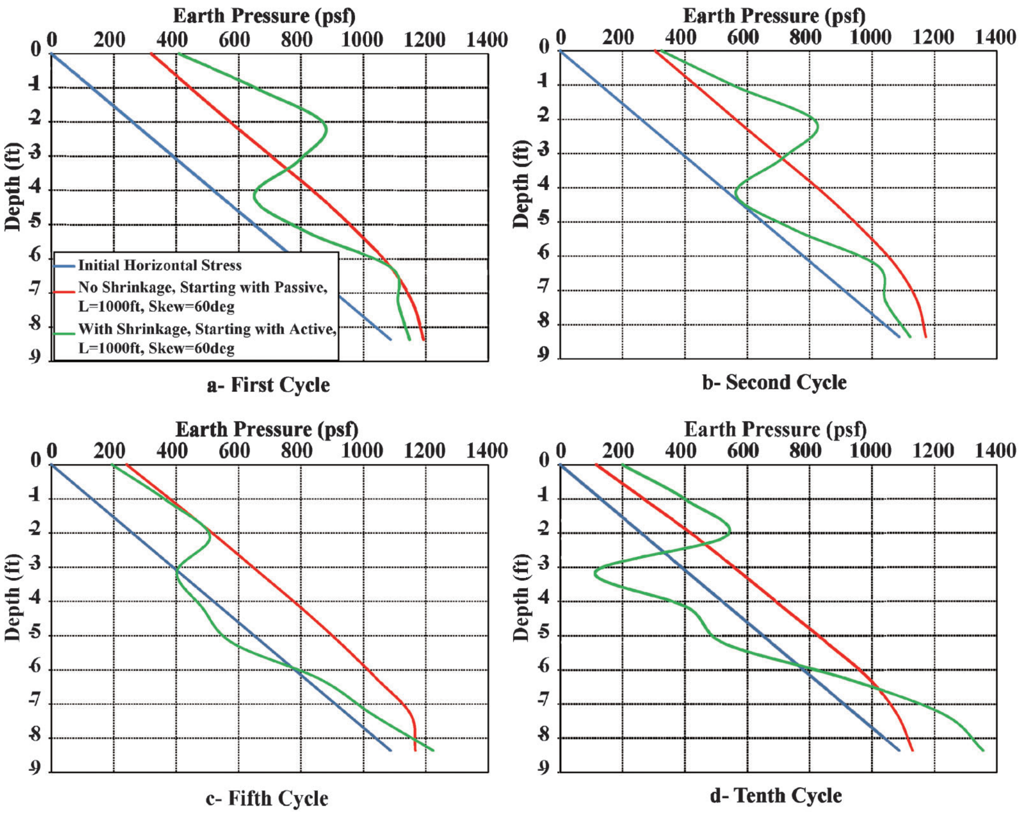

a- First Cycle

b- Second Cycle

c- Fifth Cycle

d- Tenth Cycle

Figure F.35 Effect of shrinkage and load history on soil pressures along a vertical section at the center of the abutment.

TABLE F.11
Times Corresponding to Earth Pressure Plots in Figure F.30

Cycle #	No Shrinkage Starting with Passive Loading	With Shrinkage Starting with Active Loading
1	0.25	0.75
2	1.25	1.75
5	4.25	4.75
10	9.25	9.75

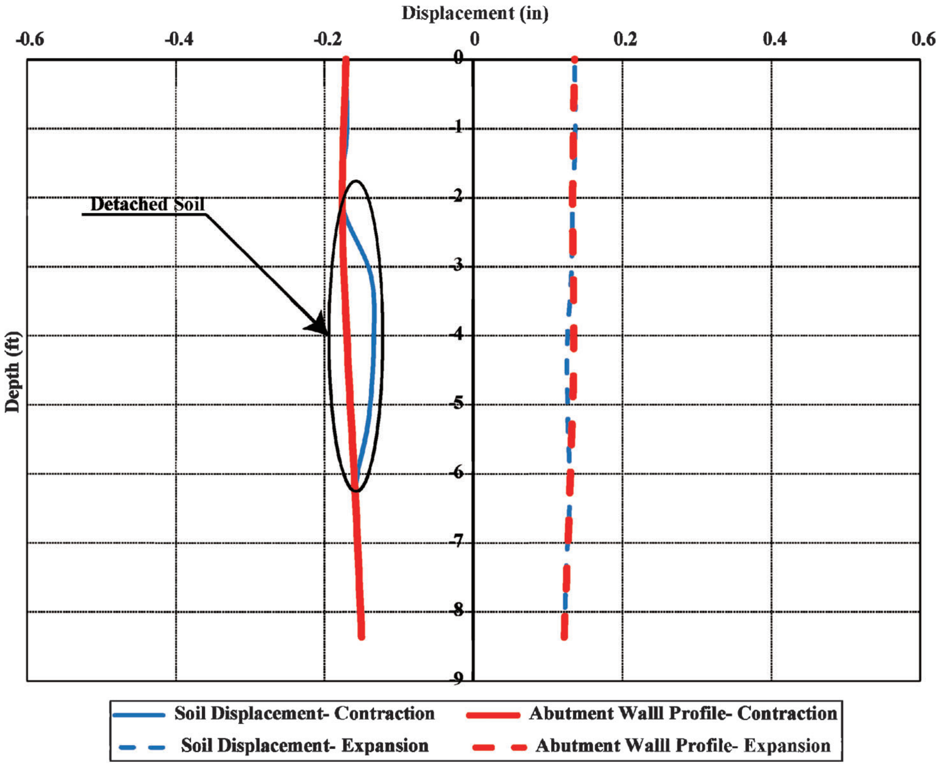

Figure F.36 Backfill displacement adjacent to the abutment wall along a vertical section through the center of the abutment (1st cycle).

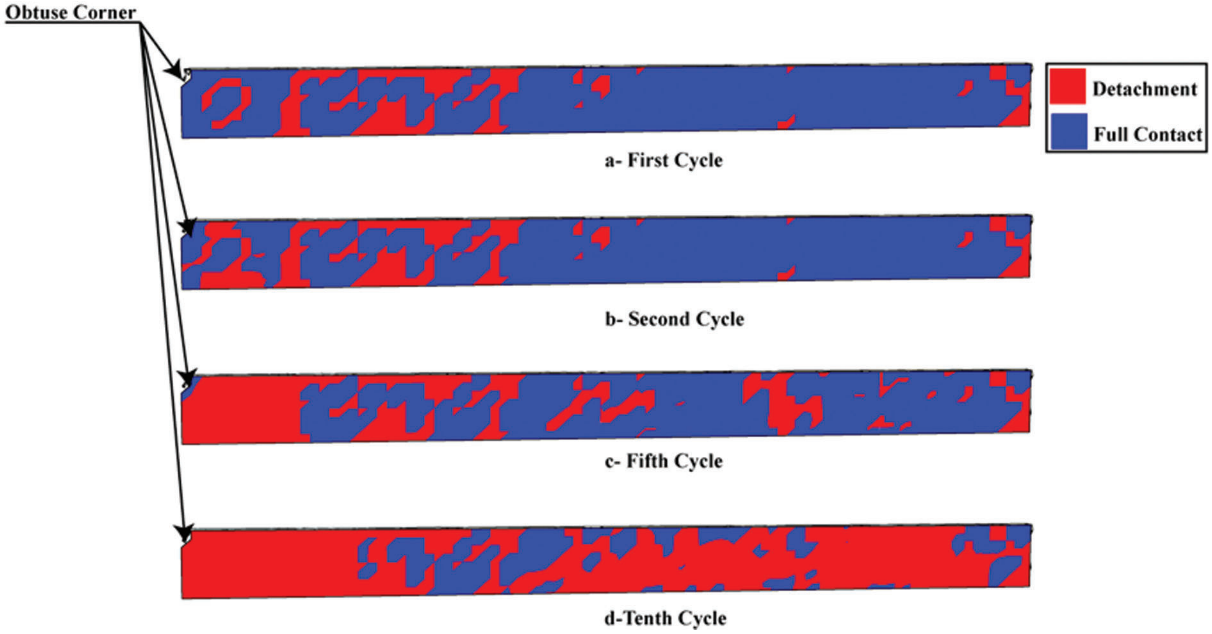

Figure F.37 Detachment between abutment and backfill (Case 11).

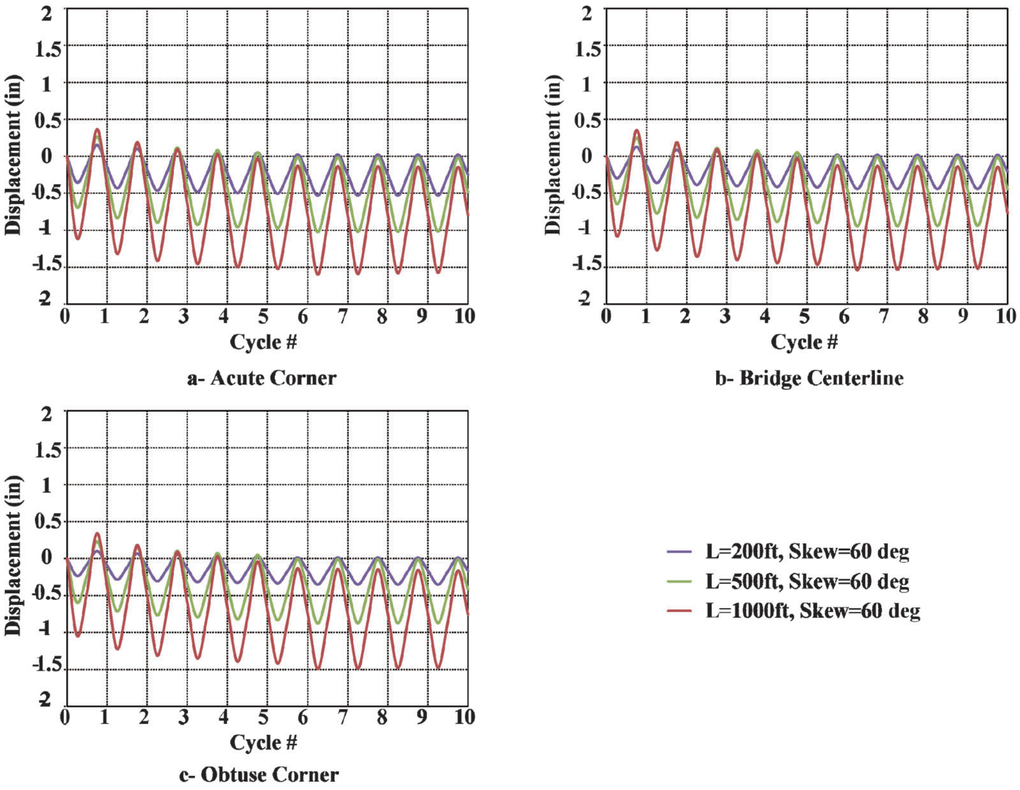

Figure F.38 Shrinkage and load history—displacement at top of the pile as a function of the number of cycles for different bridge lengths.

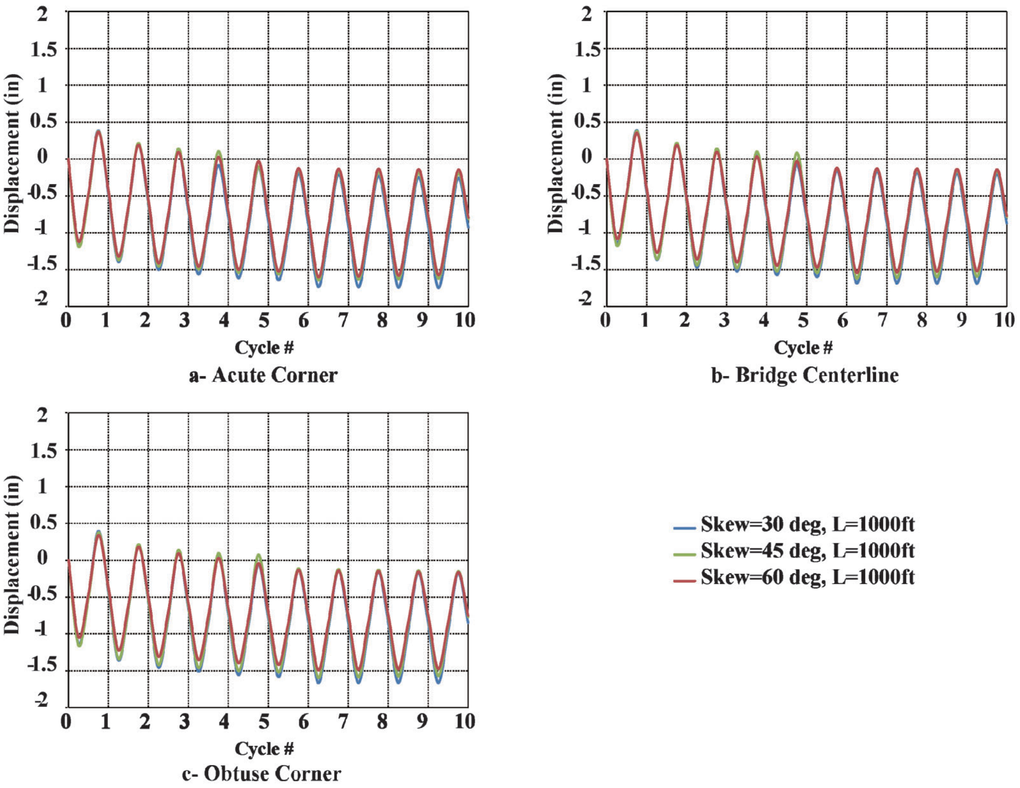

a- Acute Corner

b- Bridge Centerline

c- Obtuse Corner

Figure F.39 Shrinkage and load history—displacement at top of the pile as a function of the number of cycles for different skew angles.

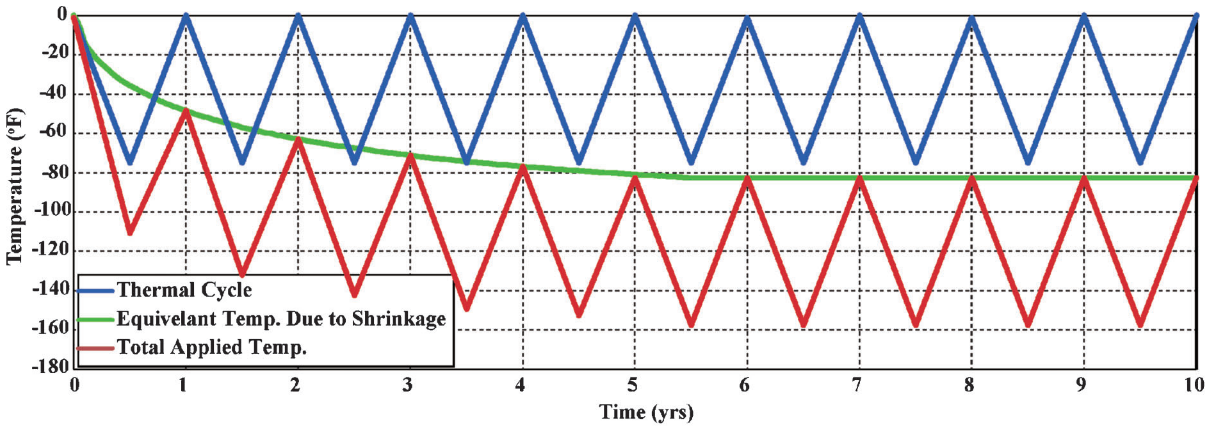

Figure F.40 Thermal load oscillating between 0°F and −75°F time history with shrinkage.

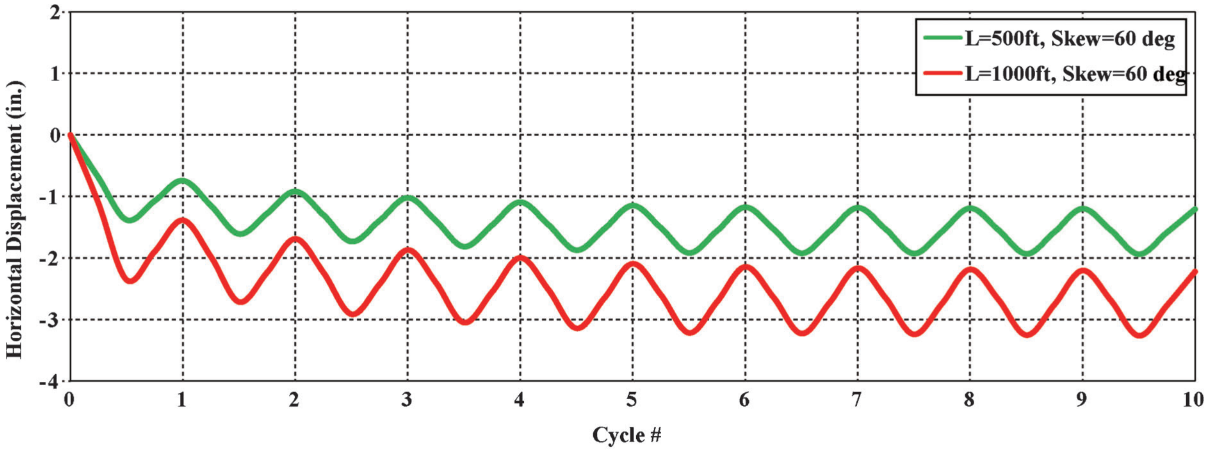

a- Acute Corner

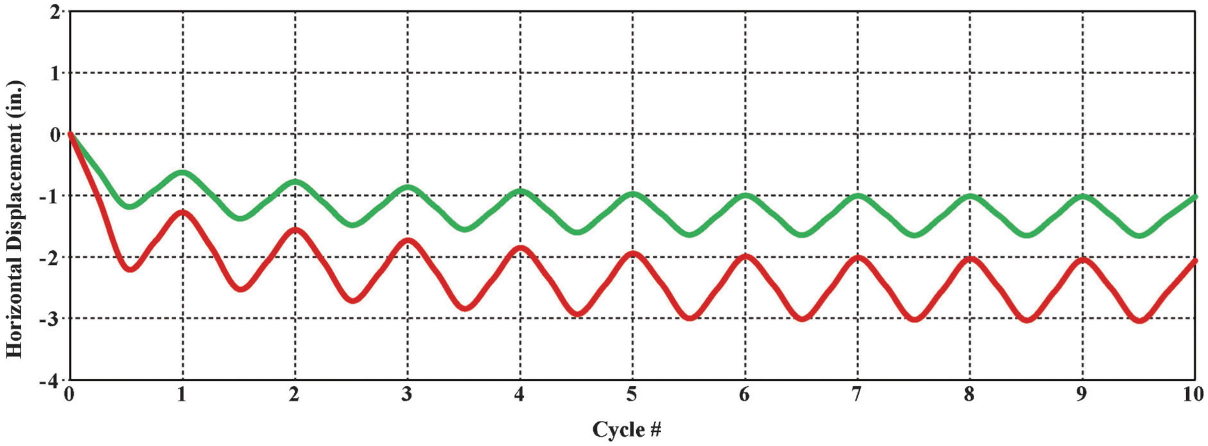

b- Obtuse Corner

Figure F.41 Shrinkage and load history—displacement at top of the pile as a function of the number of cycles for different bridge lengths.

F.11 CONCLUSIONS

Based on the parametric study, the following conclusions are reached:

1. The maximum length and skew angle for integral abutment bridge with medium to stiff foundation soils can be as high as 500 ft and 60°.
2. The stiffness of the foundation may have an adverse effect on the displacement demand on the piles in the case of long bridges (>1000 ft) on soft foundation soils. In this case, a full soil-structure analysis should be conducted.
3. The effect of the abutment wall stiffness, for the range of practical wall thickness typically used in integral abutment bridge, is not significant.

F.12 REFERENCES

Frosch, R. J., Chovichien, V., Durbin, K., & Fedroff, D. (2006). *Jointless and smoother bridges: Behavior and design of piles* (Joint Transportation Research Program Publication No. FHWA/IN/JTRP-2004/24). West Lafayette, IN: Purdue University. http://dx.doi.org/10.5703/1288284313379

Frosch, R. J., Kreger, M. E., & Talbott, A. M. (2009). *Earthquake resistance of integral abutment bridges* (Joint Transportation Research Program Publication No. FHWA/IN/JTRP-2008/11). West Lafayette, IN: Purdue University. http://dx.doi.org/10.5703/1288284313448

Frosch, R. J., & Lovell, M. D. (2011). *Long-term behavior of integral abutment bridges* (Joint Transportation Research Program Publication No. FHWA/IN/JTRP-2011/16). West Lafayette, IN: Purdue University. http://dx.doi.org/10.5703/1288284314640

About the Joint Transportation Research Program (JTRP)

On March 11, 1937, the Indiana Legislature passed an act which authorized the Indiana State Highway Commission to cooperate with and assist Purdue University in developing the best methods of improving and maintaining the highways of the state and the respective counties thereof. That collaborative effort was called the Joint Highway Research Project (JHRP). In 1997 the collaborative venture was renamed as the Joint Transportation Research Program (JTRP) to reflect the state and national efforts to integrate the management and operation of various transportation modes.

The first studies of JHRP were concerned with Test Road No. 1—evaluation of the weathering characteristics of stabilized materials. After World War II, the JHRP program grew substantially and was regularly producing technical reports. Over 1,500 technical reports are now available, published as part of the JHRP and subsequently JTRP collaborative venture between Purdue University and what is now the Indiana Department of Transportation.

Free online access to all reports is provided through a unique collaboration between JTRP and Purdue Libraries. These are available at: http://docs.lib.purdue.edu/jtrp

Further information about JTRP and its current research program is available at:
http://www.purdue.edu/jtrp

About This Report

An open access version of this publication is available online. This can be most easily located using the Digital Object Identifier (doi) listed below. Pre-2011 publications that include color illustrations are available online in color but are printed only in grayscale.

The recommended citation for this publication is:

Frosch, R. J., Bobet, A., & Khasawneh, Y. (2014). *Reduction of bridge construction and maintenance costs through coupled geotechnical and structural design of integral abutment bridges* (Joint Transportation Research Program Publication No. FHWA/IN/JTRP-2014/06). West Lafayette, IN: Purdue University. http://dx.doi.org/10.5703/1288284315500